

**Multiscale Modeling of Self-assembled  
Nanoparticle Superstructures**

BY

HENRY CHAN

B. Sc. in Chemistry, University of Illinois at Chicago, 2009

THESIS

Submitted as partial fulfillment of the requirements  
for the degree of Doctor of Philosophy in Chemistry  
in the Graduate College of the  
University of Illinois at Chicago, 2016

Chicago, Illinois

Defense Committee:

Prof. Petr Král, Chair and advisor  
Prof. Mark Schlossman, Physics  
Prof. Preston Snee  
Prof. Cynthia Jameson  
Prof. Justin Lorieau

## ACKNOWLEDGMENTS

I acknowledge my advisor, Prof. Petr Král, for his guidance and support throughout my graduate studies. He has emphasized the importance of curiosity, creativity, and thoroughness in research.

I acknowledge all my collaborators, whom I worked with during my graduate studies – Prof. Rafal Klajn, Prof. Nicholas Kotov, Prof. Mark Schlossman, Prof. Heinrich Jaeger, Dr. Arnaud Demortiere, and Dr. Sanja Tepavcevic – for their guidance and support in our collaborative research. Through working with the projects, I learned how to apply computational methods to study different self-assembled systems.

I acknowledge Prof. Cynthia Jameson for the discussions on the Monte Carlo method. I appreciate the time and effort she spent, and all her helpful advice.

I am grateful to Prof. Preston Snee for introducing me to nanoscience research during my undergraduate years. I express my gratitude to the staff members of the UIC chemistry department – Dr. George Papadantonakis, Rhonda Staudohar, Silvia Solis, Mary Ann Borjal, Jennifer Kazin, and Pat Ratajczyk – for their effort and indirect support.

I am very fortunate to have worked and shared offices with my colleagues and former members of the group – Dr. John Russell, Dr. Alexey Titov, Prof. Lela Vukovic, Dr. Niladri Patra, Dr. Artem Baskin, Antonett Madriaga, Irena Yzeiri, Soumyo Sen, Nikita Repnin, Ishai Strauss, Marilyn Gaske, Mena Poonaki, and Shanshan Wu.

Lastly, I express my deepest appreciation to my parents and family members for their constant support and personal guidance.

# TABLE OF CONTENTS

<u>CHAPTER</u>		<u>PAGE</u>
<b>1</b>	<b>INTRODUCTION . . . . .</b>	<b>1</b>
1.1	Self-assembly of nanoscale objects . . . . .	2
1.2	Modeling of nanoscale systems . . . . .	3
1.3	Layout of this thesis . . . . .	6
<b>2</b>	<b>SIMULATION METHODS . . . . .</b>	<b>8</b>
2.1	Phase space and ensembles . . . . .	8
	Ergodic hypothesis . . . . .	9
2.2	Molecular dynamics simulations . . . . .	9
	Derivation of force fields . . . . .	10
	Bonded interactions . . . . .	12
	Nonbonded interactions . . . . .	15
	Initial and spatial boundary conditions . . . . .	20
	Newtonian mechanics . . . . .	21
	Integration algorithms . . . . .	22
	Thermostats and barostats . . . . .	23
	Additional approximations . . . . .	24
2.3	Monte Carlo methods . . . . .	25
	Metropolis sampling algorithm . . . . .	25
	Trial moves . . . . .	28
<b>3</b>	<b>MODELING OF NANOPARTICLE SYSTEMS: SELF-ASSEMBLY, STRUCTURES, AND MATERIAL PROPERTIES . . . . .</b>	<b>30</b>
3.1	Self-Standing NP Membranes and their mechanical properties . . . .	31
	Introduction . . . . .	31
	Coarse-grained modeling of NPs . . . . .	32
	Stretching dynamics of NP membranes . . . . .	34
	Structural analysis of NP capsules . . . . .	38
	Conclusions . . . . .	42
3.2	Filtration properties of NP membranes . . . . .	44
	Introduction . . . . .	44
	Filtration experiments . . . . .	45

## TABLE OF CONTENTS (Continued)

<u>CHAPTER</u>		<u>PAGE</u>
	Atomistic modeling of the NP membranes . . . . .	48
	Free energy calculations . . . . .	50
	Filtration mechanism . . . . .	52
	Conclusions . . . . .	53
3.3	Interfacial Localization and Voltage-Tunable Arrays of Charged NPs	54
	Introduction . . . . .	54
	Probing the interfacial position of NPs by experiments . . . . .	55
	Self-assembly of voltage-tunable arrays . . . . .	58
	MD simulations of a submerging NP . . . . .	61
	Conclusions . . . . .	68
3.4	Stabilization and Self-assembly of Nanoparticles in Lipid Bilayers . .	69
	Introduction . . . . .	69
	Modeling of NP-lipid layered systems . . . . .	70
	Insertion of NPs into lipid bilayers . . . . .	71
	Nanoparticles self-assembly inside bilayers . . . . .	73
	Intercalation of nanorods and nanodiscs . . . . .	76
	Conclusions . . . . .	79
3.5	Self-assembly of Platinum Nanocubes into Superlattices . . . . .	80
	Introduction . . . . .	80
	Superlattices observed in experiments . . . . .	81
	Analysis of the supercrystal growth . . . . .	83
	Microscopic modeling of bulk vdW coupling between NC cores . .	85
	Atomistic modeling of couplings between NC ligands . . . . .	87
	Conclusions . . . . .	95
3.6	Cadmium Sulfide NP Nanocapsules . . . . .	96
	Introduction . . . . .	96
	Experiment: Self-assembly of nanocapsule . . . . .	97
	Analysis of the formation of a nanoshell . . . . .	101
	Models of the CdS NPs . . . . .	102
	Atomistic MD simulations of nanoshells. . . . .	105
	Conclusions . . . . .	108
3.7	Self-Assembly of NPs into Chiral Twisted Nanoribbons . . . . .	109
	Introduction . . . . .	109
	CPL-induced transformations observed in experiments . . . . .	110



## TABLE OF CONTENTS (Continued)

<u>CHAPTER</u>		<u>PAGE</u>
	Mechanism of light-induced self-assembly . . . . .	116
	Atomistic MD simulations . . . . .	119
	Conclusions . . . . .	122
3.8	Field-Induced Self-Assembly of Magnetite Nanocubes . . . . .	123
	Introduction . . . . .	123
	Superstructures observed in experiments . . . . .	124
	Modeling the NCs and their interactions . . . . .	129
	MC simulations of belt structures . . . . .	134
	MC simulations of superhelices . . . . .	139
	MC simulations of NC self-assembly . . . . .	141
	Finding the origin of chirality . . . . .	144
	Conclusions . . . . .	147
4	<b>CONCLUDING REMARKS . . . . .</b>	149
	<b>CITED LITERATURE . . . . .</b>	152
	<b>APPENDIX . . . . .</b>	185
	<b>CURRICULUM VITAE . . . . .</b>	192

## LIST OF ABBREVIATIONS

ABF	Adaptive biasing force
AFM	atomic force microscopy
BO	Born-Oppenheimer
BTPPA	bis(triphenyl-phosphoranylidene)-ammonium
CD	circular dichroism
CG	coarse-grained
CPL	circularly polarized light
DCE	1,2-dichloroethane
DEG	diethylene glycol
DNA	deoxyribonucleic acid
EM	electron microscopy
FEM	finite element method
fcc	face-centered cubic
GISAXS	grazing-incidence small-angle X-ray scattering
hcp	hexagonal close packing
LCP	left-handed circularly polarized
LH	left-handed
LJ	Lennard-Jones
LP	linearly polarized
MA	magnetocrystalline anisotropy
MC	Monte Carlo
MD	molecular dynamics

## LIST OF ABBREVIATIONS (Continued)

NAMD	Nanoscale Molecular Dynamics
NC	nanocube
NP	nanoparticle
OA	oleic acid
PDF	probability distribution function
PES	potential energy hyper-surface
PME	Particle mesh Ewald
RCP	right-handed circularly polarized
RH	right-handed
SAED	selected area electron diffraction
sc	simple cubic
SEM	scanning electron microscopy
SPM	superparamagnetic
STM	scanning tunneling microscopy
TEM	transmission electron microscopy
TGA	thioglycolic acid
TPFB	tetrakis-pentafluorophenyl-borate
TTMA	trimethylammonium
UnP	unpolarized
vdW	van der Waals
VMD	Visual Molecular Dynamics

## ABSTRACT

This thesis describes the computational modeling work performed during my graduate studies (two of my works related to Mg-ion battery [1] and water-graphene [2] systems are not included). The thesis is based on 7 original papers [3–9] and 2 submitted manuscripts [10, 11]. These studies focused on different self-assembled nanoparticle systems, including nanoparticle membranes and arrays, nanoparticle–lipid hybrid systems, superlattices, nanoshells, nanoribbons, and superhelices.

The first part of this thesis gives an introduction to the nanoscience field, self-assembly concepts, and multiscale modeling approaches. In a separate chapter, classical simulation methods such as molecular dynamics and Monte Carlo are described. The chapter also provides a description of classical force fields, specifically, how bonded and nonbonded interactions are related to quantum first principles.

The second part of this thesis describes the performed modeling studies. These studies are separated into sections, and arranged by the types of self-assembled structures. Mean-field calculations, Monte Carlo simulations, and molecular dynamics simulations at the atomistic and coarse-grained levels were used to perform these studies.

## CHAPTER 1

### INTRODUCTION

The fast economic and population growth anticipated in developing countries is expected to put a high demand on natural resources such as water and energy. To meet this demand while keeping a low impact on the environment, new generations of materials with highly tunable properties need to be developed. One possibility to make these materials is to compose them from nanoscale ( $< 100$  nm) components. In this way, structured materials with nanoscale features can be prepared, resulting in unique and tunable properties that are not present in bulk materials. The earliest examples of materials with nanoscale features were found in the pre-modern era, in the form of dichroic glass [12], stained glass [13], Islamic lusterware [14], and Damascus sabre steel [15]. These ancient materials have unique appearances and properties that were not understood until the nanoscience field was established in the past few decades.

Nanotechnology was a term defined by Norio Taniguchi in 1974 [16]. It was later associated with the idea of manipulating matter at the nanoscale level with ultrahigh precision, and ultimately performing atom-by-atom manipulations, as introduced by Richard Freymann in 1959 [17]. Most nanoscience studies were triggered by the development of microscopy equipment, such as the scanning tunneling microscope (STM) [18] and the atomic force microscope (AFM) [19]. Many researchers came with exciting discoveries of new materials, such as fullerene [20] and carbon nanotubes [21]. Practical applications of nanotechnology were fueled by governmental grants, such as the National Nanotechnology Initiative (NNI) [22], and funding from the private sector.

Photolithography is a widely used approach in the preparation of materials with nanoscale features. However, such a **top-down technique** is associated with a high cost [23]. Alternative **bottom-up techniques** that build materials from small individual subunits are arguably more scalable and efficient in making robust nanoscale structures [24–27]. However, nanoscale or even molecular and atomic constituents cannot be mechanically assembled by robotic fingers, as Eric Drexler proposed [28]. Their preparation could instead be achieved by “self-assembly”, just as Nature assembles proteins and other molecular components in cells.

### 1.1 Self-assembly of nanoscale objects

Self-assembly is a process where units of the same or similar types spontaneously form ordered structures [29]. It is a concept that is applicable across a wide range of length scales [30], but we typically associate it with microscopic units forming macroscopic structures. There are many examples of self-assembled systems in biology – viral capsids [31], globular proteins [32], lipid bilayers [33], and fibrils [34]. Many different man-made structures have been also self-assembled, such as clusters, capsules, layers, superlattices, and liquid crystals [35]. They can be formed by atoms [36], molecules [37], and colloidal nanoparticles (NPs) [38], often in analogy to sophisticated biological systems. For instance, the extraordinary strength of elastic proteins [39], present in collagen [40] and spider silk [41], is a result of nature-designed structures that, in principle, can be man-made through a hierarchy of finely tuned self-assembly processes [42]. Hybrid natural and man-made self-assembled systems are of great interest in medicine and material sciences, due to their rich potential applications in the preparation of multi-functional materials [43].

The self-assembly of nanoscale units into ordered structures is a process of Gibbs free energy minimization, which depends on both enthalpic and entropic contributions, i.e.,  $\Delta G = \Delta H - T\Delta S$ . In principle, such processes can be **thermodynamically** or **kinetically** driven, thus affecting the

long-term stability of the formed structures. In nanoscale systems, the outcomes of self-assembly processes are often difficult to predict because these processes depend on a delicate competition of different forces – originating in van der Waals, Coulombic, and magnetic interactions, etc, between the nanoscale subunits [44]. From the point of equilibrium, we can distinguish two types of self-assembled systems [30]: one that requires a constant energy flow from external sources to maintain its ordered structure, and the other that does not require energy input. The first type of systems are self-organizing (dynamical self-assembly) [45]. These self-organized structures cease to exist once the source of energy disappears (equilibrium). Notable examples of such systems are Rayleigh-Bénard convection cells and biological cells (life itself). The second type of systems are stable in equilibrium (static self-assembly). We will study such systems in the context of NP self-assembled structures.

The self-assembly of NPs in heterogeneous medium, such as suspensions [46] or liquid interfaces [47,48] are of particular interest, since the assembled structures can be involved in various molecular activities and transport processes, such as molecular filtration [4]. Charge transport across interfaces of two immiscible ionically conductive medium is very important both in natural systems and in designed applications [49]. Examples include selective transport or exchange of ions across biological membranes [50], delivery of charged drugs in cells [51,52], and development of ion-selective electrodes and biosensors [53–55]. The role of NP-assemblies as unique platforms for interfacial processes remains largely unexplored.

## 1.2 Modeling of nanoscale systems

Since the last decade, experimental procedures have allowed crafting NPs of different sizes [56–60], shapes [61–65], and surface chemistry (ligands) [44, 66, 67]. Metallic [68–72] and semiconducting [73, 74] NPs as well as NPs made from oxides [56, 75], inorganic salts [76, 77], and polymers [78, 79] can be prepared as nanospheres, [80] polyhedra [81, 82], rods [81–84], ellipsoids [85], plates [86–89],

dipods, tripods or tetrapods [90,91], core/shell [68,92–94], nanocages [95–97], dumbbells [98–100], and capsules [101–105].

This rich spectrum of available NPs can be used to prepare functional meta-materials with unique characteristics [38,106,107]. Colloidal NPs have been self-assembled into many types of superlattices [108–110] and other structures, such as chains [111], rings [112], nanowires [113,114], and sheets [115], typically stabilized on solid substrates [116,117]. Charges [118], dipoles [44,63], surface chemistry [119,120], and other material parameters of the NPs endow the self-assembled meta-materials [121–126] a rich spectrum of properties, such as photoactivity [127,128], magnetic activity [129–132], thermoelectric properties [133], catalytic activity [134], and specific toxicological properties [135].

To design NP-based systems for applications, we need to develop reproducible, controllable, and scalable NP self-assembly techniques, which is based on understanding of the conditions which limit the NP self-assembly. The passivation of NPs [136,137] and their further protection and functionalization by a variety of organic [138], inorganic [139,140], and biological capping ligands [141–144] can be used to impart desired properties to them. They can control various NP properties such as solubility [145], specificity towards various molecules [146,147], resistance to nonspecific adsorption [148], net electric charge [118,149,150], and electrochemical activity [151–154].

The packing of colloidal NPs in superlattices is largely controlled by forces originating from the NP core, ligands, solvent, and substrate used. The ligands are of great importance, since they determine the NP charges, strength of ligand-NP and ligand-ligand binding, surface chemistry, etc. Therefore, they can determine the type of NP-packing and the potential activity of the formed superstructures. The solvent type can also determine the type of formed structures through its ionic strength, pH, hydrophobic/philic nature, etc. Electron microscopy (EM) and tomography techniques can be used to image self-assembled structures in great detail, even during their growth in solution



inside silicon nitride or graphene cells [155, 156]. However, these techniques have limitations, which prevent complete information about a self-assembled system to be obtained. For example, high resolution TEM can provide atomic resolution images of the metallic cores of NPs, but their ligands are not visible due to the low contrast of organic molecules. All this shows that deciphering the self-organization and potential activity of self-assembled materials is a challenging problem that requires close integration of many experimental and theoretical approaches [157–166].

Multiscale simulation methods can in principle be used to model all types of nanoscale systems, and retrieve information that is difficult to obtain from experiments. First principle density functional and *ab initio* methods can model atomic systems in full detail. These methods describe both electrons and atomic nuclei, and precisely account for their interactions. However, their complexity limits them to systems of few hundred or at most few thousand atoms. Atomistic or coarse-grained molecular dynamics simulation methods extend this limit to many million of atoms by modeling only the nuclear positions and describing their interactions using simplistic force fields derived from first principle calculations and/or experimental data. Although these methods can describe large nanoscale systems, they require a proper choice of potential functional forms and parameters.

The current availability of powerful supercomputers and highly scalable simulation codes has made it possible to perform microsecond time scale simulations of systems having a few million atoms. Millisecond time scale molecular dynamics simulations of biomolecular systems have also been achieved using specialized computer hardware [167]. Therefore, computer simulations can mimic experiments, thus the terms virtual or *in silico* experiments have come into common use, and as such they can revolutionize our knowledge of complex biological and material systems. Simulations can guide experiments and account for unexpected results which might lead to new discoveries.

### 1.3 Layout of this thesis

The goal of this thesis is to model superstructures and clusters of self-assembled nanoparticles using multiscale simulation techniques. Chapter 2 describes classical simulation methods, such as molecular dynamics (MD) and Monte Carlo (MC) methods. The chapter also briefly describes the derivation of empirical force fields from first principles. Chapter 3 describes systems studied in this thesis – NP membranes (section 3.1, 3.2) and arrays (section 3.3), NP-lipid hybrid systems (section 3.4), superlattices (section 3.5), nanoshells (section 3.6), nanoribbons (section 3.7), and NP superhelices (section 3.8). These studies can be grouped according to the method used, and are summarized as follows:

#### 1. Atomistic modeling

**Section 3.2:** Study of molecular filtration through alkanethiol ligated gold NP membranes, performed in collaboration with Prof. Heinrich Jaeger (U. Chicago). Gibbs free energy profiles of different tryptophan species were calculated from atomistic MD simulations to study the filtration mechanism.

**Section 3.3:** Study of supercharged trimethylammonium ligated gold NP arrays at aqueous-organic liquid interfaces, performed in collaboration with Prof. Mark Schlossman (Physics, U. Illinois Chicago). Transport mechanism and ion-NP correlations were studied using atomistic MD simulations.

**Section 3.6:** Study of nanoshells formed by cadmium sulfide NPs, performed in collaboration with Prof. Nicholas Kotov (U. Michigan). The stabilization mechanism and self-assembly process of nanoshells at different pH conditions was studied using atomistic MD simulations of different charged NPs.

**Section 3.7:** Study of nanoribbons formed by cadmium sulfide NPs, performed in collaboration with Prof. Nicholas Kotov (U. Michigan). The arrangement of NPs and their chirality transfer in self-assembled twisted nanoribbons were studied using atomistic MD simulations.

## 2. Coarse-grained modeling:

**Section 3.1:** Theoretical study of alkanethiol ligated gold NP membranes and capsules. Structural analysis of these membranes focusing on the effect of ligands was performed using coarse-grained MD simulations.

**Section 3.4:** Theoretical study of hybrid structures of alkanethiol ligated gold NP and 1-palmitoyl-2-oleoyl-sn-glycero-3-phosphocholine lipid bilayer. The inclusion and stabilization of these small hydrophobic NPs in the interior of the lipid bilayer were simulated using coarse-grained MD simulations.

## 3. Mean-field modeling:

**Section 3.5:** Study of octylamine ligated platinum nanocube superlattices, performed in collaboration with Dr. Arnaud Demortière (Argonne National Laboratory). Analytical mean-field modeling of the NP core-core interaction, and precise calculations of the ligand-ligand interactions were used to study the stabilization mechanism of two types of superlattices formed of regular and truncated octylamine ligated platinum nanocubes.

**Section 3.8:** Study of oleic acid ligated magnetite nanocube superhelices, performed in collaboration with Prof. Rafal Klajn (Weizmann Inst. of Science). Complex organization of magnetic dipole moments in these superstructures, and the delicate balance of different magnetic interactions were studied using MC simulations.

## CHAPTER 2

### SIMULATION METHODS

This chapter briefly describes the concepts of a classical phase space and ensembles used in statistical mechanics. These concepts permit characterization of complex equilibrated interacting systems at the atomic scale, such as superstructures of self-assembled nanoparticles. Then, we discuss two classical simulation methods – molecular dynamics and Monte Carlo. The MD method allows us to prepare equilibrated trajectories of the systems, which are statistically identical to their ensembles (Ergodic theorem).

#### 2.1 Phase space and ensembles

In this PhD thesis, I describe nanoscale systems classically without considering them to undergo any significant chemical modifications caused by reactions. A microstate of such a classical system with  $N$  atoms is fully described by the atom positions,  $\vec{r} = (x_1, y_1, z_1, \dots, x_N, y_N, z_N)$ , and momenta,  $\vec{p} = (p_{x,1}, p_{y,1}, p_{z,1}, \dots, p_{x,N}, p_{y,N}, p_{z,N})$ . The positions and conjugate momenta  $(\vec{r}, \vec{p})$  form vectors in a  $6N$ -dimensional phase space. Statistical mechanics assumes that a macroscopic system in equilibrium is populated by a set of microstates, which is characterized as an ensemble (a subset of phase space). A self-assembled system composed of molecular or nanoscale components at equilibrium can be treated by a canonical ensemble (NVT) for which the number of particles  $N$ , the volume  $V$ , and the temperature  $T$  are constant.

Any observables of a canonical system in thermal equilibrium can be evaluated using

$$\langle A \rangle = \frac{\int \int A(\vec{r}, \vec{p}) e^{-E(\vec{r}, \vec{p})/k_B T} d\vec{r} d\vec{p}}{\int \int e^{-E(\vec{r}, \vec{p})/k_B T} d\vec{r} d\vec{p}}, \quad (2.1)$$

where  $\langle A \rangle$  is the expectation value of an observable  $A$ ,  $E$  is the energy of a microstate,  $k_B$  is the Boltzmann constant,  $T$  is temperature, and  $Q = \int \int e^{-E(\vec{r}, \vec{p})/k_B T} d\vec{r} d\vec{p}$  is the canonical partition function. Therefore,  $Q^{-1} e^{-E(\vec{r}, \vec{p})/k_B T}$  gives the probability of the system to be in a particular microstate given by the point  $(\vec{r}, \vec{p})$  and energy  $E(\vec{r}, \vec{p})$ .

### Ergodic hypothesis

A dynamical system evolves along a trajectory in phase space. The ergodic hypothesis [168] assumes that time averaging of an observable over the phase space trajectory of an equilibrated system gives the same expectation value as averaging over the microstates in the ensemble of the system.

$$\langle A \rangle = \lim_{t_{total} \rightarrow \infty} \frac{1}{t_{total}} \int_0^{t_{total}} A(t) dt, \quad (2.2)$$

where  $\langle A \rangle$  is the expectation value of an observable  $A$ ,  $t_{total}$  is the total time of measurement. We can use the Ergodic theorem to obtain expectation values of an equilibrated system by averaging them over sufficiently long trajectories obtained in molecular dynamics simulations. The long trajectories will be run in such a way that correspond to the appropriate equilibrium ensembles.

## **2.2 Molecular dynamics simulations**

Molecular dynamics (MD) simulations can be used to describe our self-assembled systems. Classical atomistic MD simulations model atoms as points, with pre-assigned masses and partial charges. Each atom moves according to the forces generated by all other atoms and external fields, if any,

imposed on the system.. The forces are evaluated using a parameterized interatomic interaction energy function (called a force field), with parameters that can be derived from first principles.

### Derivation of force fields

A quantum description of a molecular system is given by a wave function that describes all its nuclei and electrons. The Hamiltonian,  $\hat{H}$ , of a system containing  $N$  atomic nuclei with coordinates  $\vec{R} = (\vec{R}_1, \dots, \vec{R}_N)$ , and  $l$  electrons with coordinates  $\vec{r} = (\vec{r}_1, \dots, \vec{r}_l)$ , can be written as

$$\hat{H} = -\frac{\hbar^2}{2} \sum_{\alpha=1}^N \frac{1}{m_{\alpha}} \nabla_{\alpha}^2 - \frac{\hbar^2}{2m_e} \sum_{i=1}^l \nabla_i^2 + \sum_{\alpha=1}^N \sum_{\beta>\alpha}^N \frac{Z_{\alpha} Z_{\beta} e^2}{|\vec{R}_{\alpha} - \vec{R}_{\beta}|} - \sum_{\alpha=1}^N \sum_{i=1}^l \frac{Z_{\alpha} e^2}{|\vec{r}_i - \vec{R}_{\alpha}|} + \sum_{i=1}^l \sum_{j>i}^l \frac{e^2}{|\vec{r}_i - \vec{r}_j|} , \quad (2.3)$$

where  $m_{\alpha}$ ,  $m_e$  are masses of nucleus  $\alpha$  and an electron, respectively,  $\nabla^2$  is the Laplacian,  $Z_{\alpha}$  and  $Z_{\beta}$  are partial charges of nuclei  $\alpha$  and  $\beta$ , respectively, and  $e$  is the elementary charge of an electron. The first two terms in this expression are kinetic energy operators of nuclei and electrons, respectively, and the last three terms are electrostatic potential energy operators of nucleus-nucleus repulsions, nucleus-electron attractions, and electron-electron repulsions, respectively.

The non-relativistic time evolution of such system is described by the Schrödinger equation:

$$i\hbar \frac{\partial \Psi(\vec{R}, \vec{r}, t)}{\partial t} = \hat{H} \Psi(\vec{R}, \vec{r}, t) , \quad (2.4)$$

where  $\Psi(\vec{R}, \vec{r}, t)$  is the wave function containing all the information about nuclei and electrons, which depends on their coordinates  $\vec{R}$ ,  $\vec{r}$ , and time,  $t$ . This wave function cannot be separated into nuclear and electronic contributions due to the coupling of its constituents.

Since the Hamiltonian,  $\hat{H}$ , does not depend on time, the spatial and time coordinates of the wave function is  $\Psi_n(\vec{R}, \vec{r}, t) = \Psi_n(\vec{R}, \vec{r})e^{-iE_n t/\hbar}$ . The stationary states of the system are described by the time-independent Schrödinger equation:

$$\hat{H}\Psi_n(\vec{R}, \vec{r}) = E_n\Psi_n(\vec{R}, \vec{r}) , \quad (2.5)$$

where  $n = 0$  and  $n \geq 1$  corresponds to the ground state and excited states, respectively,  $\Psi_n(\vec{R}, \vec{r})$  are the stationary eigenstates, which depend on the coordinates of nuclei and electrons in a non-separable way, and  $E_n$  are the eigenvalues of  $\hat{H}$ .

Since electrons are a few orders of magnitude lighter than nuclei ( $M_n/m_e \approx 10^3$  to  $10^4$ ), their motions are much faster. They adjust almost instantaneously to any changes in the nuclear coordinates, while the motions of nuclei are practically frozen when compared to the motions of electrons. The **Born-Oppenheimer (BO) approximation** freezes nuclei fully. As a consequence, 1) the kinetic energy of nuclei (1st term in Equation 2.3) can be neglected, and 2) the total wave function can be separated into wave functions of nuclei and electrons,  $\Psi_{nucl,n}(\vec{R})$  and  $\Psi_{elec,n}^{\vec{R}}(\vec{r})$ , respectively. The Hamiltonian for motions of electrons is parameterized by the coordinates of frozen nuclei,  $\vec{R}$ , and it is written as

$$\hat{H}_{elec} = -\frac{\hbar^2}{2m_e} \sum_{i=1}^N \nabla_i^2 + \sum_{\alpha=1}^N \sum_{\beta>\alpha}^N \frac{Z_\alpha Z_\beta e^2}{|\vec{R}_\alpha - \vec{R}_\beta|} - \sum_{\alpha=1}^N \sum_{i=1}^l \frac{Z_\alpha e^2}{|\vec{r}_i - \vec{R}_\alpha|} + \sum_{i=1}^l \sum_{j>i}^l \frac{e^2}{|\vec{r}_i - \vec{r}_j|} , \quad (2.6)$$

where  $\hat{H}_{elec}$  consists of kinetic energy of electrons, and electrostatic potential energy of nucleus-nucleus repulsions, nucleus-electron attractions, and electron-electron repulsions, respectively.

The wave function of the electrons is parameterized by the coordinates of the nuclei. The time-independent Schrödinger equation (Equation 2.5) can be solved for motions of electrons around frozen nuclei,

$$\hat{H}_{elec}\Psi_{elec,n}^{\vec{R}}(\vec{r}) = U_n(\vec{R})\Psi_{elec,n}^{\vec{R}}(\vec{r}) , \quad (2.7)$$

where, for the  $n^{th}$  electronic state,  $U_n(\vec{R}) = E_{elec,n}(\vec{R}) + E_{nu-nu}(\vec{R})$  is the electrostatic potential energy as a function of the coordinates of frozen nuclei, which has an electronic contribution,  $E_{elec,n}(\vec{R})$ , and a constant additive nucleus-nucleus coupling energy (2nd term in Equation 2.6).

$U_n(\vec{R})$  defines the **potential energy surface (PES)** for different  $n$  and  $\vec{R}$ , and it can be used to solve the Schrödinger equation for motions of nuclei:

$$\begin{aligned} \hat{H}_{nucl}\Psi_{nucl}(\vec{R}) &= E_{sys,n}\Psi_{nucl}(\vec{R}) , \\ \hat{H}_{nucl} &= -\frac{\hbar^2}{2} \sum_{\alpha=1}^N \frac{1}{m_{\alpha}} \nabla_{\alpha}^2 + U_n(\vec{R}) , \end{aligned} \quad (2.8)$$

where  $E_{sys,n}$  is the system energy on the  $n$ -th electronic surface, which can be approximately separated into translational, rotational, vibrational, and electronic energy contributions, i.e.,  $E_{sys,n} = E_{tran} + E_{rot,n} + E_{vib,n} + E_{elec,n}$ . In this manner a fully quantum description of a single isolated molecule is feasible, but such a description for a large collection of molecules without additional approximations is not practical.

### Bonded interactions

Bonded interactions account for the chemical bonds between atoms of a molecule (derived from Equation 2.7). In classical force fields, these bonded interactions are associated with molecular



vibrations around the equilibrium positions of atoms, defined by bond lengths and bond frequencies.

To find these parameters, we first define an internal coordinate of a  $N$ -atom molecule as

$$\vec{R}_{com} = \frac{\sum_{i=1}^N m_i \vec{R}_i}{\sum_{i=1}^N m_i}, \quad (2.9)$$

where  $\vec{R}_{com}$  is the center-of-mass,  $m_i$  and  $\vec{R}_i$  are the mass and coordinates of atom  $i$ , respectively. The relative positions of all atoms in the molecule can be described with respect to  $\vec{R}_{com}$ . Since these relative positions do not depend on the translation of center-of-mass or the rotation around it, the total number of internal vibrational degrees of freedom associated with these relative coordinates is  $3N - 5$  for diatomic molecules, and  $3N - 6$  for polyatomic molecules. In particular, the single vibration mode ( $3N - 5 = 1$ ) of a diatomic molecule is associated with the change of a single bond length.

The internal vibrational degrees of freedom of a molecule is associated with independent normal modes of vibrations, which are obtained from the PES. The PES,  $U_n(\vec{R})$ , can be expanded around its local minima by a Taylor series

$$U_{local,n}(\vec{R}) = U_n(\vec{R}_e) + \sum_{i=1}^N \left. \frac{\partial U_n}{\partial \vec{R}_i} \right|_{\vec{R}_i=\vec{R}_e} (\vec{R}_i - \vec{R}_e) + \frac{1}{2} \sum_{i=1}^N \sum_{j>i}^N \left. \frac{\partial^2 U_n}{\partial \vec{R}_i \partial \vec{R}_j} \right|_{\vec{R}_i, \vec{R}_j=\vec{R}_e} (\vec{R}_i - \vec{R}_e)(\vec{R}_j - \vec{R}_e) + \dots \quad (2.10)$$

where  $U_{local,n}(\vec{R})$  is the potential energy around the local minima,  $\vec{R}_e$  is the equilibrium positions of nuclei,  $\vec{R}_i$ ,  $\vec{R}_j$  are the coordinates of nuclei  $i$  and  $j$ . The first term is an additive constant, the second term (1st derivative) is zero at the local minima, and the third term has a 2nd derivative component,  $\left. \frac{\partial^2 U_n}{\partial \vec{R}_i \partial \vec{R}_j} \right|_{\vec{R}_i, \vec{R}_j=\vec{R}_e}$ , which is the generalised force constant, elements of a Hessian matrix,

associated with the local PES curvatures around the minima, and the remaining higher order terms which describe anharmonicities of vibrations are neglected. The Hessian matrix,  $[k_{ij}]$ , is written as

$$\begin{bmatrix} k_{11} & k_{12} & \dots & k_{1(3N-6)} \\ k_{21} & k_{22} & \dots & k_{2(3N-6)} \\ \vdots & \vdots & \ddots & \vdots \\ k_{(3N-6)1} & k_{(3N-6)2} & \dots & k_{(3N-6)(3N-6)} \end{bmatrix} \xrightarrow{\text{diagonalize}} \begin{bmatrix} k'_{11} & 0 & \dots & 0 \\ 0 & k'_{22} & \dots & 0 \\ \vdots & \vdots & \ddots & \vdots \\ 0 & 0 & \dots & k'_{(3N-6)(3N-6)} \end{bmatrix}$$

Nonzero off-diagonal elements in the left matrix implies correlated intra-molecular vibrations. Diagonalizing  $[k_{ij}]$  gives  $3N - 6$  independent **normal modes of vibrations** related to the frequencies of classical or quantum harmonic oscillators representing vibrations. Since vibrations are defined in classical simulations by redundant internal coordinates, which include all the 2-, 3-, and 4- body motions (bonds, angles, and dihedrals), the  $3N - 6$  normal modes of vibrations has to be projected onto individual bond, angle, and dihedral. The direct mapping of Hessian matrix to internal force constants has been done for an isolated molecule in vacuum [169], but fitting procedures based on stochastic methods are needed for a molecule in a solvent environment [170]. Once the force constants for every type of bonds is determined, they can be used in the force field to describe the proper molecular geometry.

The parameters for angles, dihedrals, and improper dihedrals are also determined using a similar fitting procedure used for bonds. In the CHARMM force field [171], angles and improper dihedrals have the same functional form (harmonic potential) as bonds:

$$\begin{aligned}
U_{bond}(b) &= k_b(b - b_0)^2, \\
U_{angle}(\theta) &= k_\theta(\theta - \theta_0)^2 + k_{ub}(r - r_{ub})^2, \\
U_{dihedral}(\phi) &= \begin{cases} k_{\phi,n} [1 + \cos(n\phi - \delta_n)], & \text{if } n > 0, \\ k_{\phi,n} (\phi - \delta_n)^2, & \text{if } n = 0, \end{cases} \\
U_{improper}(\varphi) &= k_\varphi (\varphi - \varphi_0)^2,
\end{aligned} \tag{2.11}$$

where  $U_{bond}$ ,  $U_{angle}$ ,  $U_{dihedral}$ ,  $U_{improper}$  are the potential energies for a single bond, angle, dihedral, and out-of-plane distortion (improper),  $k_b$ ,  $k_\theta$ ,  $k_{\phi,n}$ ,  $k_\varphi$  are the force constants associated with the interaction strengths, and  $b_0$ ,  $\theta_0$ ,  $\delta_n$ ,  $\varphi_0$  are the equilibrium values for bond, angle, etc.

### Nonbonded interactions

The most common nonbonded interactions in nanoscale systems include electrostatic interactions (charge–charge, charge–dipole, dipole–dipole, etc...), van der Waals (vdW) interactions, and hydrogen bonding. To evaluate the electrostatic interactions between molecules (one of the nonbonded interactions), we need to first calculate the effective charges of atoms. In classical force fields, charge densities of electrons obtained from their wave functions are mapped onto point charges located on the nuclei of atoms. In the CHARMM force field, such procedures involve 1) evaluation of an electric field of a molecule generated by the precise charge distribution obtained in high level (MP2) quantum calculations done with an implicit solvent, and 2) assignment of point charges to atomic nuclei, which are adjusted iteratively to minimize the least square error of the electric field generated by these point charges and the electric field evaluated in step 1. Once we know these charges, we can calculate the forces between the molecules and other nanoscale objects. Then, we can often

cumulatively add these charges for nanoparticles or molecules and evaluate the effective (mean-field) coupling between them.

**1. Electrostatic interactions.** The electrostatic potential energy between two point charges,  $q_i$  and  $q_j$ , at  $\vec{r}_i$  and  $\vec{r}_j$ , is

$$U_{q_i q_j} = \frac{1}{4\pi\epsilon_0\epsilon} \frac{q_i q_j}{|\vec{r}_i - \vec{r}_j|} , \quad (2.12)$$

where  $|\vec{r}_i - \vec{r}_j|$  is the distance between the two charges,  $\epsilon_0$  is the dielectric permittivity of vacuum, and  $\epsilon$  is a dielectric constant which accounts for an implicit solvent medium. The functional form of electrostatic interaction energy in the CHARMM force field [171] is equivalent to Equation 2.12 with different constants.

For a group of  $l$  charges ( $l > 2$ ), the total electrostatic potential energy can be obtained by

$$U_{elec} = \sum_{i=1}^l \sum_{j>i}^l U_{q_i q_j} . \quad (2.13)$$

The strength of  $U_{q_i q_j}$  has the  $1/r$  dependence given in Equation 2.12. This long distance dependence of  $U_{q_i q_j}$  requires the inclusion of many surrounding atoms during the evaluation of the electrostatic potential energy. The need to consider many pairwise computations of  $U_{q_i q_j}$  between these atoms greatly affect the efficiency of MD simulations. Therefore, MD simulation codes split  $U_{q_i q_j}$  into a short- and long- range contributions based on a predefined cutoff distance, where the short-range portion is evaluated explicitly in the simulations, and the long-range (tail) portion is approximated using methods such as Particle Mesh Ewald (PME) [172], which performs mesh-based Ewald sums using Fourier transforms in the reciprocal space of a periodic system.

When the atomistic description of charges is not needed, a **mean-field approach** can be used. For a cluster of  $l$  closely located charges with coordinates  $(\vec{r}_1, \dots, \vec{r}_l)$  around the origin, a multipole

expansion can be used to approximate their long-range electrostatic potential observed at point  $\vec{\mathcal{R}}$ .

The electrostatic potential

$$V(\vec{r} - \vec{\mathcal{R}}) = \frac{1}{4\pi\epsilon_0\epsilon} \sum_{i=1}^l \frac{q_i}{|\vec{r}_i - \vec{\mathcal{R}}|} \quad (2.14)$$

can be expanded (in Cartesian coordinates) around the origin  $\vec{r} = 0$  as a Taylor series

$$V(\vec{r} - \vec{\mathcal{R}}) = V(-\vec{\mathcal{R}}) - \sum_{\alpha=x,y,z} r_\alpha \left. \frac{\partial V(-\vec{\mathcal{R}})}{\partial r_\alpha} \right|_{\vec{r}=0} + \frac{1}{2} \sum_{\alpha=x,y,z} \sum_{\beta=x,y,z} r_\alpha r_\beta \left. \frac{\partial^2 V(-\vec{\mathcal{R}})}{\partial r_\alpha \partial r_\beta} \right|_{\vec{r}=0} + \dots, \quad (2.15)$$

where  $r_\alpha$  is the  $\alpha$  component of  $\vec{r}$ . After this expression is re-written in terms of a traceless Cartesian second rank tensor using the Laplace equation, the expression can be differentiated and we obtain the following:

$$V(\vec{r} - \vec{\mathcal{R}}) = \frac{1}{4\pi\epsilon_0\epsilon} \left( \frac{q_{total}}{R} + \frac{\sum_{\alpha=x,y,z} \mu_\alpha R_\alpha}{R^3} + \frac{\sum_{\alpha=x,y,z} \sum_{\beta=x,y,z} Q_{\alpha\beta} (3R_\alpha R_\beta - \delta_{\alpha\beta} R^2)}{6R^5} + \dots \right), \quad (2.16)$$

where  $q_{total} = \sum_{i=1}^l q_i$ ,  $\mu_\alpha = \sum_{i=1}^l q_i r_{i\alpha}$ , and  $Q_{\alpha\beta} = \sum_{i=1}^l q_i (3r_{i\alpha} r_{i\beta} - \delta_{\alpha\beta} r_i^2)$  are defined as monopole, dipole, and quadrupole, respectively,  $\delta_{\alpha\beta} = 1$  if  $\alpha = \beta$  and 0 otherwise,  $R$  is the distance between origin and the observation point,  $R_\alpha$  is the  $\alpha$  component of  $\vec{\mathcal{R}}$ . This multipole mean-field definition can also be applied to magnetostatic potentials, except that magnetic analog of electric monopole does not exist. The monopole (effective charge) and dipole obtained can be directly used to compute the electrostatic potential energy between any two nanoparticles or with other charges.

This mean-field approach can simplify the interaction between nanoparticles by replacing them with an effective charge and/or dipole. Electrostatic interaction energy between two effective charges

follows the same definition as two charges (Equation 2.12), whereas the interaction energy between two electric dipoles is

$$U_{dd} = \frac{1}{4\pi\epsilon_0\epsilon} \frac{\vec{\mu}_i \cdot \vec{\mu}_j - 3(\hat{r}_{ij} \cdot \vec{\mu}_i)(\hat{r}_{ij} \cdot \vec{\mu}_j)}{|\vec{r}_i - \vec{r}_j|^3}, \quad (2.17)$$

where  $\vec{\mu}_i, \vec{\mu}_j$  are dipoles,  $|\vec{r}_i - \vec{r}_j|$  is the distance between them, and  $\hat{r}_{ij}$  is the unit vector of  $\vec{r}_i - \vec{r}_j$ .

This formula with modified constants can also be applied to interaction energy between two magnetic dipoles.

Ions present in an electrolyte solution can screen electrostatic interactions (Debye screening), reducing their strength and length scale. The Debye length formula gives the effective screening distance as a function of ionic strength (ion concentrations),

$$\lambda_D = \sqrt{\frac{\epsilon_0\epsilon k_B T}{2N_A E^2 I}} \quad , \quad I = \frac{1}{2} \sum_{i=1}^n C_i Z_i^2, \quad (2.18)$$

where  $\lambda_D$  is the Debye length,  $\epsilon_0$  is the dielectric permittivity of vacuum,  $\epsilon$  is the dielectric constant,  $k_B$  is the Boltzmann constant,  $T$  is temperature,  $N_A$  is the Avogadro's number,  $e$  is the elementary charge of an electron,  $I$  is the ionic strength of the electrolyte,  $n$  is the number of ion types,  $C_i$  is molar concentration of the  $i^{th}$  ion, and  $Z_i$  is charge of the ion.

**2. van der Waals interactions.** We now describe the van der Waals (vdW) interactions between atoms (another one of the nonbonded interactions). We first discuss how vdW interactions are represented in classical force fields, and then we expand the discussion to vdW interactions between bulk materials.

vdW interactions are time-independent correlations between many-electron wave functions, which originate from the non-separable solution of several Slater determinants with different distribution of

electrons. The vdW interaction energy,  $U_{vdW}$ , between two not chemically bonded atoms is described by

$$U_{vdW}(\vec{r}_i, \vec{r}_j) = -\frac{C_{vdW}}{|\vec{r}_i - \vec{r}_j|^6}, \quad (2.19)$$

where  $r_i, r_j$  are the coordinates of the two atoms,  $C_{vdW}$  is a positive constant associated with the interaction strength, and  $|\vec{r}_i - \vec{r}_j|$  is the distance between atoms  $i$  and  $j$ .

vdW interactions can sometimes be viewed as a combination of Keesom, Debye, and London dispersion forces [173]. In classical simulations, the Lennard-Jones (LJ) 6-12 potential is used to account for the dispersion vdW contribution. LJ potential has a  $1/r^6$  term which accounts for vdW attractions, and a  $1/r^{12}$  term which accounts for repulsive exchange interactions, which originates from the overlapping of the electron distributions of the two non-bonded atoms:

$$U_{LJ}(r) = 4\varepsilon \left[ \left( \frac{\sigma}{r} \right)^{12} - \left( \frac{\sigma}{r} \right)^6 \right], \quad (2.20)$$

where  $U_{LJ}$  is the LJ potential energy,  $\varepsilon$  is the maximum depth of the function, associated with the interaction strength,  $\sigma$  is the minimum distance from which there is no interaction, i.e.,  $U_{LJ} = 0$ , which defines the vdW radius of an atom, and  $r$  is the distance between the centers of the atoms.

In classical force fields, LJ parameters between same atom types is obtained by nontrivial fittings (e.g., lattice energies from experiments), and the LJ parameters between different atom types is typically extrapolated using mixing rules such as  $\sigma_{ij} = (\sigma_{ii} + \sigma_{jj})/2$  and  $\varepsilon_{ij} = \sqrt{\varepsilon_{ii}\varepsilon_{jj}}$  (Lorentz-Berthelot rules). The LJ interactions between atoms are typically employed with a cutoff distance of around  $10 - 14 \text{ \AA}$  for improving the efficiency of a simulation. This cutoff might not be sufficient for vdW interactions between bulk polarizable materials. The nature of bulk vdW interactions

depend on the shapes of the interacting objects, and also the solvent medium in between them. Such interactions can be approximated instead by using the Hamaker pairwise summation [174]

$$U_{vdW,ij} = -\frac{A}{\pi^2} \int_{V_i} \int_{V_j} \frac{1}{r_{ij}^6} d\vec{r}_i d\vec{r}_j. \quad (2.21)$$

where  $A/\pi^2 = C_{vdW}$  (in Equation 2.19),  $A$  is the Hamaker constant which has a value on the order of  $10^{-19}$  to  $10^{-20}$  J depending on the medium,  $r_{ij}$  is the distance between microscopic volume elements of the two interacting objects, and the expression is integrated over their total volumes  $V_i$  and  $V_j$ .

### Initial and spatial boundary conditions

**1. Atom coordinates and velocities.** After we have obtained a force field that describe the bonded and nonbonded interactions of all atoms in the system, the initial coordinates of these atoms have to be provided to set up a MD simulation. This set of initial coordinates are typically relaxed by running energy minimization. The initial velocities of these atoms can be assigned from the thermalized distribution of velocities given by the Maxwell-Boltzmann distribution:

$$f_{MB}(\vec{v}_i) = \left( \frac{m_i}{2\pi k_B T} \right)^{3/2} e^{-m_i \vec{v}_i^2 / 2k_B T} 4\pi \vec{v}_i^2, \quad (2.22)$$

where  $T$  is temperature,  $m_i$  and  $\vec{v}_i$  are mass and velocity of atom  $i$ , respectively,  $k_B$  is the Boltzmann constant. The sampled initial velocities can be rescaled to ensure the conservation of momenta, i.e.,  $\sum_i p_i = 0$ , and to produce kinetic energy that corresponds to the desired  $T$ .

**2. Spatial boundary conditions.** A simulation box is defined by fixed or periodic boundary conditions. Fixed boundary conditions are used in a constant volume setup, whereas periodic boundary conditions (PBCs) are needed for simulating a bulk solvent environment, or infinite solid



layers/superlattices that are formed by repeating units. PBCs replicate the simulation box in all directions to avoid artifacts caused by vacuum boundaries. When a barostat is used, PBCs can be set to use flexible boundaries that either adjust isotropically or anisotropically, depending on the type of systems (typical solvent box vs membrane systems). PBCs are required for the particle mesh Ewald algorithms (PME) [172] briefly discussed in section 2.2.

### Newtonian mechanics

MD simulation of a system in a microcanonical ensemble (NVE) is based on Newtonian mechanics. Here, we first describe this mechanics, later, we introduce thermostats and barostats for fixing temperature and pressure in simulations of a canonical ensemble (NVT) and an isothermal-isobaric ensemble (NPT). The time evolution of a system in a microcanonical ensemble is described by the Hamilton equations of motion

$$\frac{d\vec{p}}{dt} = -\frac{\partial\mathcal{H}}{\partial\vec{r}} \quad , \quad \frac{d\vec{r}}{dt} = \frac{\partial\mathcal{H}}{\partial\vec{p}} \quad (2.23)$$

where  $\vec{p}$  is momentum,  $\vec{r}$  is atomic position,  $t$  is time, and  $\mathcal{H}$  is the Hamiltonian, which is the sum of kinetic and potential energy terms,

$$\mathcal{H}(\vec{r}, \vec{p}) = \frac{\vec{p}^2}{2m} + U(\vec{r}) \quad (2.24)$$

Hamiltonian systems conserve energy throughout its time evolution, i.e.,  $d\mathcal{H}/dt = 0$ . Equation 2.24 and Equation 2.23 gives

$$\frac{d\vec{p}}{dt} = -\vec{\nabla}U(\vec{r}) \quad , \quad \frac{d\vec{r}}{dt} = \frac{\vec{p}}{m} \quad (2.25)$$

The right equation defines momentum as  $\vec{p} = m\vec{v}$ , and the left equation equates to the Newton's equation of motion since  $\vec{F} = -\vec{\nabla}U(\vec{r})$ . For each of the  $N$  atoms, we get

$$\vec{F}_i = m_i \frac{d^2 \vec{r}_i}{dt^2}, \quad i = 1..N \quad (2.26)$$

where  $\vec{F}_i$ ,  $m_i$ , and  $\vec{r}_i$  are the force, mass, and position of atom  $i$ .

Given atomic positions  $\vec{r}(t)$  at time  $t$ , the forces on each atom can be evaluated using the force field, i.e.,  $\vec{F}_i = -\vec{\nabla}U(\vec{r}_i)$ . Integration of Equation 2.26 gives the velocities and positions of the next time step,  $t + \Delta t$ :

$$\vec{v}_i(t + \Delta t) = \vec{v}_i(t) + \frac{\vec{F}_i(t)}{m_i} \Delta t \quad (2.27)$$

$$\vec{r}_i(t + \Delta t) = \vec{r}_i(t) + \vec{v}_i(t) \Delta t + \frac{1}{2} \frac{\vec{F}_i(t)}{m_i} (\Delta t)^2 \quad (2.28)$$

### Integration algorithms

There are several different integration schemes of varying efficiency, accuracy, and numerical stability. For MD simulations of microcanonical systems, a class of symplectic integrators are used due to their time-reversibility, stability, and ability to conserve the system energy.

**Velocity-Verlet** is currently the most common symplectic integrator used in large scale MD simulation software, including NAMD [175], Amber [176], and LAMMPS [177]. The method updates positions using Equation 2.28, and obtain velocities of the same time step by

$$\vec{v}_i(t + \Delta t) = \vec{v}_i(t) + \frac{\vec{F}_i(t) + \vec{F}_i(t + \Delta t)}{2m_i} \Delta t \quad (2.29)$$

### Thermostats and barostats

Real systems are more appropriately simulated using a canonical ensemble (NVT) or an isothermo-isobaric ensemble (NPT). These ensembles require temperature and pressure controls. Temperature in MD simulations is defined in terms of thermal contact with a large thermal reservoir. Velocity rescaling type thermostats, such as Berendsen thermostat, can quickly warm up a system to a target temperature preceding an energy minimization, but they do not produce the correct distribution of temperature of a canonical ensemble.

Stochastic type thermostats, such as Anderson thermostat and Langevin thermostat, produce the correct temperature distribution of a canonical ensemble. The Langevin thermostat modifies the force term in Equation 2.26 such that

$$m \frac{d^2 \vec{r}}{dt^2} = \vec{F} - \gamma \frac{d\vec{r}}{dt} + \sqrt{\frac{2\gamma k_B T}{m}} \quad (2.30)$$

where  $\vec{F}$  is the normal conservative force computed from atom interactions,  $-\gamma \vec{v}$  is the frictional damping term proportional to velocities of atoms, which is scaled by a damping factor,  $\gamma$ , and  $\sqrt{\frac{2\gamma k_B T}{m}}$  is the Gaussian random force due to solvent atoms, which is proportional to temperature,  $T$ , inverse mass of the atom,  $m^{-1}$ , and also scaled by the damping factor,  $\gamma$ . Since the random force is not correlated with position,  $\vec{r}$ , it disappears upon averaging.

Pressure control in MD simulations is done by changing the simulation box size and rescaling the coordinates of atoms within it. The barostat algorithm is typically the same or compatible with the thermostat algorithm used.

## Additional approximations

The applicability of MD simulations is limited by its length scale and time scale. These limitations can be extended by approximations. Here, we have listed some of the common ones.

**1. Interaction cutoff.** Most of the nonbonded interactions reasonably decay with distance. A cutoff distance is usually set in MD simulations to limit the number of pairwise computations. A cutoff value of 10 to 14 Å is sufficient for vdW interactions. The same cutoff is also applied to Coulombic interactions, but the long range portion (tail) of the potential can be accounted for using algorithms such as PME [172]. Setting an abrupt cutoff for nonbonded interactions can lead to problems related to conservation of momentum and energy, or affect the dynamics of the system. Using a switching distance function minimizes this issue by modifying the potential energy function from that point on and smoothly bringing it to zero at the cutoff distance.

**2. Constraints.** The largest time step usable in a MD simulation is limited by the fastest motions in the system. These motions typically corresponds to vibrations. Constraint algorithms, such as RATTLE and SHAKE, can be used to replace high frequency bonds by rigid bonds. Constraints can also be used to restrict or steer the movements of certain atom groups.

**3. Coarse-graining.** Coarse-graining (CG) is used to perform simplifications to the spatial resolution of the system (typically by a mapping ratio that ranges from 1:1 to 4:1). The mapping procedure groups atoms into beads. The interactions between beads have to be re-parameterized. The beads typically have bonded interactions and nonbonded LJ interactions (Equation 2.20), but electrostatic interactions are often not explicitly included. The center of the beads are usually located at the center-of-mass of the atoms that they contain. Similarly, the bead radii can be approximated by the radius of gyration of the group of atoms constituting a bead. The reduction in resolution removes

high frequency vibrations, which allows a significant 10 to 50 times increase in the simulation time step. The grouping of atoms also reduces the number of computation of pairwise interactions, and provides a smoothing of the PES, which leads to faster dynamics.

### 2.3 Monte Carlo methods

Additional speed up can be obtained through Monte Carlo (MC) methods. The methods sample the phase space stochastically, and disregard information about the dynamics of a system. MC methods directly compute ensemble averages using a numerical evaluation of the multi-dimensional phase space integral (Equation 2.1). The numerical procedure is performed by replacing the phase space integral by summation over microstates with weighted probabilities.

#### Metropolis sampling algorithm

The Metropolis algorithm [178] belongs to a class of importance sampling techniques. The effectiveness of this algorithm comes from the realization that the value of a measurable quantity  $A$  is only significant in a very small subset of points in an ensemble. Therefore,  $\langle A \rangle$  can be quickly computed if there is a way to selectively pick out these significant points. When such selection is achieved, the expectation value of  $A$  can be obtained without having to compute  $A$  for every point in the ensemble.

With this principle in mind, the numerical integration of the phase space integral (Equation 2.1) has now turned into a problem of sampling configurations that are significant. For example, if we consider the configuration space, i.e., phase space with momentum dimensions neglected, the configurations should be chosen based on the following probability distribution function (pdf)

$$f_M(\vec{r}) = \frac{e^{-E(\vec{r})/k_B T}}{\int \int e^{-E(\vec{r})/k_B T} d\vec{r}} \quad (2.31)$$

where  $f_M(\vec{r})$  gives the probability of configuration  $\vec{r}$ , and  $E(\vec{r})$  is the energy of the configuration.

Assuming that we start with a system in one of its possible configurations,  $\vec{r}_0$ , i.e., with no overlaps between atoms, etc. A new trial configuration,  $\vec{r}_1$ , can be generated by adding a small random displacement to  $\vec{r}_0$  of a randomly chosen atom. The important issue here is to derive the rules for accepting or rejecting the trial configuration such that it is proportional to Equation 2.31. Metropolis has shown a general approach to achieve this goal.

The probability to transition from a configuration,  $\vec{r}_i$ , to another configuration in the ensemble,  $\vec{r}_j$ , can be denoted as  $\mathcal{P}_{ij}$ , an element of the transition probability matrix,  $\mathcal{P}$ . This matrix must eventually lead the system to an equilibrium that is characterized by a stationary distribution, e.g.,  $f_M(\vec{r})$ . The equilibrium condition implies that the average number of trial moves going from  $\vec{r}_i$  to  $\vec{r}_j$  must equate to the average number of moves coming back to  $\vec{r}_i$  from all the other states,  $\vec{r}_{j \neq i}$ . However, a stronger restriction called the “detailed balance” condition can be imposed on  $\mathcal{P}$ . Such condition states that the average number of trial moves going from  $\vec{r}_i$  to  $\vec{r}_j$  equates to the average number of moves coming back to  $\vec{r}_i$  from  $\vec{r}_j$ . This statement can be shown as

$$f_M(\vec{r}_i) \mathcal{P}_{ij} = f_M(\vec{r}_j) \mathcal{P}_{ji} \quad (2.32)$$

where  $f_M(\vec{r}_i)$  and  $f_M(\vec{r}_j)$  are the equilibrium probability distributions of being in configuration  $\vec{r}_i$  and  $\vec{r}_j$ , respectively, and  $\mathcal{P}_{ij}$  and  $\mathcal{P}_{ji}$  are transition probabilities of  $\vec{r}_i$  to  $\vec{r}_j$  and  $\vec{r}_j$  to  $\vec{r}_i$ , respectively.

In the MC method, a transition from  $\vec{r}_i$  to  $\vec{r}_j$  is comprised of two separate processes: 1) the generation of a trial move, and 2) the acceptance or rejection of the trial move. Therefore, the

transition probability,  $\mathcal{P}_{ij}$ , can be formed of the combined probability of these two processes, which leads to a more specific detailed balance condition

$$f_M(\vec{r}_i) \alpha_{ij} \rho_{ij} = f_M(\vec{r}_j) \alpha_{ji} \rho_{ji} \quad (2.33)$$

where  $\alpha_{ij}$  is the probability to generate the trial move,  $\vec{r}_j$ , at the current configuration,  $\vec{r}_i$  (vice versa for  $\alpha_{ji}$ ), and  $\rho_{ij}$  and  $\rho_{ji}$  are the probabilities of accepting or rejecting the trial moves,  $\vec{r}_j$  and  $\vec{r}_i$ , respectively. Since the trial moves can be generated randomly with no bias, we can take  $\alpha_{ij} = \alpha_{ji}$  and leave them out. Then, it follows that

$$\frac{\rho_{ij}}{\rho_{ji}} = \frac{f_M(\vec{r}_j)}{f_M(\vec{r}_i)} \quad (2.34)$$

where the right side equates to  $e^{-(E(\vec{r}_j)-E(\vec{r}_i))/K_B T}$  (from Equation 2.31). The probability of accepting or rejecting a trial move,  $\rho$ , can be set in multiple ways, as long as it satisfies Equation 2.34. However, the scheme chosen by Metropolis as shown below seems to work well in most of the cases.

$$\rho_{ij} = \begin{cases} 1 & \text{if } E(\vec{r}_j) \leq E(\vec{r}_i) \\ e^{-(E(\vec{r}_j)-E(\vec{r}_i))/K_B T} & \text{otherwise} \end{cases} \quad (2.35)$$

Therefore, a trial configuration is accepted if its potential energy is decreased (or remained the same), otherwise, it is accepted with a probability that is inversely proportional to the difference in their potential energies. In a MC simulation, the second condition can be performed by generating a random number, *rand*, in the range of 0 and 1, and then accept the trial configuration if *rand* is less than the acceptance probability.

### Trial moves

In our discussion of the Metropolis sampling algorithm, we simplified the detailed balance condition by equating two probabilities of trial move selection, i.e.,  $\alpha_{ij} = \alpha_{ji}$ . This implies that the probability of making the trial configuration  $\vec{r}_j$  at current configuration  $\vec{r}_i$  is the same as the probability of the reverse. To fulfill this requirement, one need to make sure that the trial move is symmetrical (non-bias).

For trial moves involving **translations of the center of mass**, the symmetry condition can be achieved by adding a random displacement vector to the center of mass vector, and allow the displacement to be made equally in both forward and backward directions.

$$(x_1, y_1, z_1) = (x_0, y_0, z_0) + \Delta s \hat{s} \quad (2.36)$$

where  $(x_1, y_1, z_1)$  is the new proposed com vector,  $(x_0, y_0, z_0)$  is the current com vector,  $\hat{s}$  is a uniformly chosen displacement unit vector that points in a random direction, and  $\Delta s$  is the displacement step size. Sampling efficiency of the spatial region depends on value of  $\Delta s$ . A large step size would lead to a higher rejection rate due to the increased chances of overlapping with other objects and a larger difference in potential energy as a result of a bigger configuration change.

For trial moves involving **orientational changes** (rigid body rotations), careful attention is needed to avoid introducing bias to its sampling. For example, sampling random orientation of a vector using uniformly sampled polar angle,  $\theta \in [0, 2\pi)$ , and uniformly sampled azimuthal angle,  $\phi \in [0, \pi)$ , would lead to more vectors pointing in the direction of the two poles, due to the area element being a function of  $\phi$ . Furthermore, representation of orientation using Eulerian angles can



lead to complications due to the intensive use of computationally expensive trigonometric functions, and also a well-known problem called “Gimbal lock” related to the loss of degrees of freedom.

Matrix and quaternion representations are good alternatives for handling orientations and rotations. Both representations are easily inter-convertible, which makes any matrix operations possible for quaternions. Since quaternions operate on a 4D unit sphere, it is easy to do a uniform sampling of rotations. Furthermore, it is straight forward to compose any 3D rotations in form of a quaternion, using the simple axis-angle representation. Similar to translations, rotations are also associated with a rotational angle size. Its optimal value also depends on many factors, and it can affect the MC sampling efficiency.

## CHAPTER 3

### MODELING OF NANOPARTICLE SYSTEMS: SELF-ASSEMBLY, STRUCTURES, AND MATERIAL PROPERTIES

This chapter describes computational studies of different self-assembled systems, including NP membranes (section 3.1, 3.2) and arrays (section 3.3), NP-lipid hybrid systems (section 3.4), superlattices (section 3.5), nanoshells (section 3.6), nanoribbons (section 3.7), and NP superhelices (section 3.8). The sections are arranged based on the types of self-assembled structures.

Different multiscale simulation techniques were used in these studies. They include mean-field electrostatic and van der Waals energy calculations (section 3.5), mean-field Monte Carlo (MC) simulations (section 3.8), and classical molecular dynamics (MD) simulations performed at the atomistic level (section 3.2, 3.3, 3.6, 3.7) and the coarse-grained level (section 3.1, 3.4).

### 3.1 Self-Standing NP Membranes and their mechanical properties

Adapted from Ref. [3] (*Nanoscale* 2011, 3 (4), 1881–1886. DOI: 10.1039/C0NR00912A) with permission from The Royal Society of Chemistry.

In this work, we performed microscopic modeling of self-standing membranes and capsules formed by alkanethiol ligated gold NPs. We studied their structures, stabilities, and mechanical properties using coarse-grained molecular dynamic simulations. All the simulations and their analyses in this study were performed by me.

#### Introduction

Colloidal nanoparticles (NP) can self-assemble into many types of superlattices [109, 110], with packing controlled by forces originating from the NP cores, NP ligands, and solvent molecules. Even monodisperse gold NPs covered by simple alkylthiol ligands can form *fcc* and *bcc* superlattices, respectively, when  $R_{LC} < 0.8$  and  $R_{LC} > 0.8$ , where  $R_{LC} = l_{ligand}/r_{core}$  is the ratio between NP core radius,  $r_{core}$ , and the length of ligand,  $l_{ligand}$  [179]. The anisotropic forces responsible for this fcc-bcc transition and the formation of NP chains originate from ligands forming bundles at large  $R_{LC}$  [180, 181]. Colloidal NPs can also form monolayers on solid substrates [116, 117] and solvent interfaces [47, 48], with electrical [182–184] and optical properties [185, 186] dependent on the NP sizes, NP materials, ligands [187], and substrate [188, 189].

Recently, self-standing NP monolayers with highly ordered hexagonal packing have been prepared through a drying-mediated self-assembly of gold NPs covered by dodecanethiol ligands ( $r_{core} \approx 3$  nm,  $l_{ligand} \approx 1.3$  nm,  $R_{LC} \approx 0.44$ ) at an interface of air and toluene solvent [48]. AFM indentation experiments have shown that these NP membranes have robust mechanical strength and remain elastic up to  $T = 370$  K [190]. The mechanical strength of NP membranes depends on the types of

NPs [191]. NP membranes have potential applications in electronics [192–194], molecular filtering, sensing [195], and drug delivery.

### Coarse-grained modeling of NPs

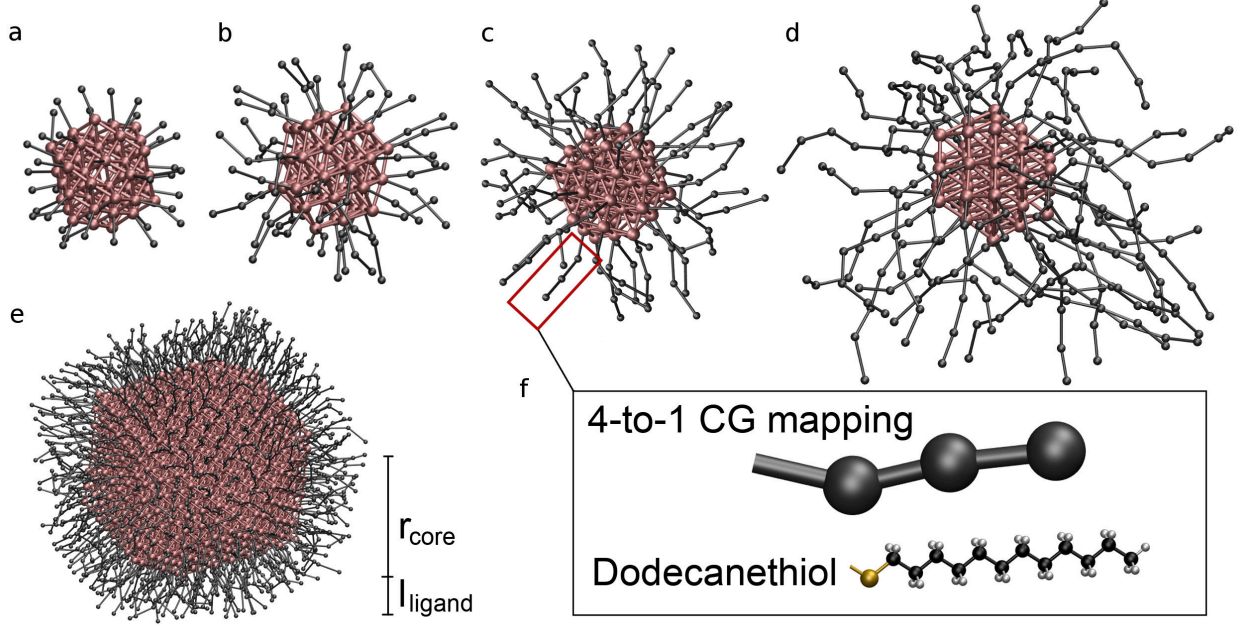


Figure 1: CG model of gold NPs. a-d)  $r_{core} = 0.8$  nm with increasing  $l_{ligand}$  (0.5, 0.9, 1.3, 2.6 nm, respectively), which correspond to  $l_{ligand}$ -to- $r_{core}$  ratio of  $R_{LC} = 0.62, 1.12, 1.62$ , and  $3.24$ . e) Model with same dimension as the NPs used in experiment ( $r_{core} = 3$  nm,  $R_{LC} = 0.44$ ). f) Coarse-graining scheme shown using dodecanethiol as an example. Every CG bead is roughly four methylene groups.

We prepared our CG model based on a CG lipid model [196]. In the model, every four heavy atoms is mapped to one CG bead. The bonded and non-bonded interactions between CG beads are described using the MARTINI 2.0 force field [196]. Non-bonded vdW interactions between CG beads are evaluated using Lennard-Jones potential, Equation 3.1.

$$V_{LJ}(i, j) = \epsilon_{ij} \left\{ \left( \frac{\sigma_{ij}}{r_{ij}} \right)^{12} - \left( \frac{\sigma_{ij}}{r_{ij}} \right)^6 \right\}. \quad (3.1)$$

where  $i, j$  are non-covalently bonded CG beads,  $\epsilon_{ij}$  is the depth of the potential well (strength of interaction),  $r_{ij}$  is the distance between CG bead  $i$  and  $j$ , and  $\sigma_{ij}$  is the closest distance of approach between bead  $i$  and  $j$ .

The NP cores are formed by gold atoms labeled as SC<sub>4</sub>-type beads, where each SC<sub>4</sub>-type bead is roughly four gold atoms. Since these beads are not in the original force field, the lattice constant of the gold atoms (4.08 Å) is assigned as the SC<sub>4</sub>-SC<sub>4</sub> equilibrium bond distance, and 60° is assigned as the SC<sub>4</sub>-SC<sub>4</sub>-SC<sub>4</sub> equilibrium angle. The bond strength and angle bending strength are chosen to be 15.0 kcal/mol/Å<sup>2</sup> and 2.988 kcal/mol/rad<sup>2</sup>, respectively, which give rigid bonds and angles. Alkanethiol ligands are modeled by nonpolar C<sub>1</sub>-type beads as described in the original force field, where each C<sub>1</sub>-type bead except the first and last beads is four methylene groups. This mapping scheme is illustrated in Figure 1f using dodecanethiol ligand as an example.

The SC<sub>4</sub>-type beads are arranged in *fcc* lattice with bonding distances of  $\approx 0.4$  nm to form a cuboctahedral gold core. Note that gold NP cores can be of other shapes. For instance, very small gold clusters typically form shapes of five-fold symmetries [197,198], such as an icosahedron. Different core shapes can give facets which might influence the organization of NPs at low temperature. However, given that our systems are at room temperature and our NPs are mostly covered by long ligands, we neglect the shape factor. We have also neglected the relatively weak bulk vdW interactions between NP cores due to the presence of strong interactions between ligands.

Self-standing NP membranes in experiments, such as the ones prepared by the research group of Prof. Heinrich Jaeger from University of Chicago [190], are made of NPs with  $r_{core} \geq 3$  nm. With a ligand layer thickness  $l_{ligand} \approx 1.3$  nm, these NPs have a  $l_{ligand}$ -to- $r_{core}$  ratio of  $R_{LC} \approx 0.44$  (see Figure 1e). In our studies, due to the constraint of computational resources, smaller NPs with  $r_{core} \approx 0.8$  nm are used to simulate the dynamics of free-standing membranes. From the point

of mechanical properties, membranes made of NPs with similar  $R_{LC}$  ratio should behave similarly. Therefore, our NPs are covered by ligands with length of 1, 2, 3, and 6 CG beads (shown in Figure 1 a-d), which corresponds to  $l_{ligand} \approx 0.5, 0.9, 1.3$ , and  $2.6$  nm and  $R_{LC} \approx 0.62, 1.12, 1.62$ , and  $3.24$ , respectively. Ligand density of 1 ligand per surface  $SC_4$ -type gold bead ( $\approx 15.4 \text{ \AA}^2$  per ligand) is used for these small NPs due to their high surface curvature. Our NPs are labeled by the length (number of beads) of their ligands, i.e., NPs with  $n$ -beads ligands are labeled as  $n$ -bead NPs.

All the MD simulations in this study were performed using the NAMD code [175], and the simulation trajectories were visualized in VMD [199]. The simulations were set to run in a canonical (NVT) ensemble at a temperature of  $T = 310$  K, maintained by Langevin dynamics with a damping coefficient of  $\gamma_{Lang} = 1 \text{ ps}^{-1}$ . The timestep of all simulations was set to  $20 \text{ fs/step}$ .

### Stretching dynamics of NP membranes

*Preparation of NP monolayer:* NP monolayers were prepared by equilibrating 91 NPs whose centers-of-mass were confined in the  $z = 0$  plane using the following force constraint:

$$\vec{F}_{plane} = -k_1 \vec{z}/|\vec{z}|, \quad (3.2)$$

where  $k_1 \approx 200 \text{ pN}$  (a strong confinement). In this way, the NP monolayer remains flat and the distances between NPs are spontaneously optimized by the vdW coupling of the ligands (enthalpic and entropic contributions). After  $\approx 30 \text{ ns}$ , we have spatially disabled the center-of-mass translation motions of all NPs at the edge boundaries of the monolayer and then subsequently removed  $\vec{F}_{plane}$ .

As shown in Figure 2 a,c,e, obtained for the (1–3)-bead NPs, respectively, the relaxed membranes with fixed border NPs reorganize into more or less perturbed planar structures. 1-bead NPs ( $R_{LC} = 0.62$ ) form wavy monolayers, 2-bead NPs ( $R_{LC} = 1.12$ ) sometimes form partial double-layers (two

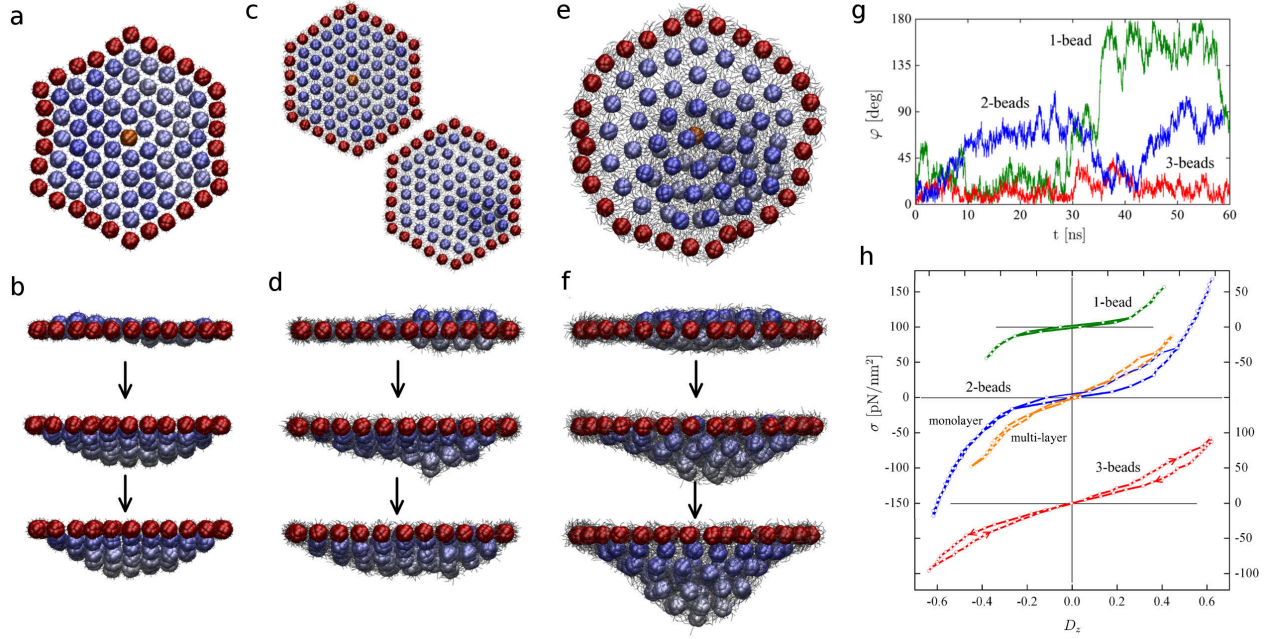


Figure 2: (a, c, e) Relaxed membranes formed by the NPs with (1–3)-bead ligands, respectively. Two membranes are shown for the system with 2-bead ligands, where one is a monolayer and the other is a partial doublelayer (smaller scale). Central beads of NPs on the edge of the membrane (in red) are fixed while the rest of the NPs are free. (b, d, f) 1-bead membrane under different level of stretching. When  $\sigma = 0.0, 25.4$ , and  $44.6$  pN/nm<sup>2</sup>,  $D_z = 0.0, -0.37$ , and  $-0.45$  respectively. 2-bead membrane monolayer under  $\sigma = 0.0, 26.5$ , and  $50.0$  pN/nm<sup>2</sup> with  $D_z = 0.0, -0.26$ , and  $-0.33$  respectively. 3-bead membrane when  $\sigma = 0.0, 46.8$ , and  $105.5$  pN nm<sup>-2</sup> with  $D_z = 0.0, -0.34$ , and  $-0.65$ . (g) Rotational motion of the NP (highlighted in orange in a–c) placed at the center of the 1–3-bead relaxed membranes. The random NP-rotation with the azimuthal angle  $\varphi$  is very different in the three systems. (h) Stress-strain curves for the stretching of NP-membranes with  $R_{LC} = 0.62$ , (top),  $R_{LC} = 1.12$  (middle), and  $R_{LC} = 1.62$  (bottom).  $\sigma$  is the applied stretching force per unit area of the membrane,  $D_z$  is the average NP-displacement divided by the average radius  $R_m$  of the membrane. Regions with loops reflect multilayer formation. The scales for 1-bead and 3-bead are placed on the right while the scale for 2-bead is on the left.

cases shown), while 3-bead NPs ( $R_{LC} = 1.62$ ) always form a partial double-layer. The morphology of the membranes is determined by the ligand type and the initial stretching. For NPs with short ligands, the ligands just provide coupling of the cluster cores that dominate the whole structure. The 1-bead NPs tend to rotate more, which can average out any potential effects due to the core shape. These membranes are highly organized and form monolayers, in analogy to the experimental systems ( $R_{LC} \approx 0.44$ ) [48]. On the other hand, the morphology of membranes formed of NPs with long ligands is mostly controlled by the ligands (negligible core size). These membranes are less

organized, form multilayers, and behave like short cross-linked polymers. The stability and strength of the three types of membranes is also different, and given by the vdW coupling coming from ligand interdigitation.

The NPs in the membranes have fast rotational motion, but very slow translational lateral diffusion, practically absent in the stretched membranes. In Figure 2g, we show random angular rotation in the azimuthal angular direction of the NP located in the center of the relaxed (non-stretched) membranes. It turns out that the NP rotation rate dramatically decreases with  $R_{LC}$ . The 1-bead NP rotates by  $180^\circ$  in 30 ns, the 2-bead NP turns from time to time by  $90^\circ$ , and the 3-bead NP is almost static. The 1-bead NP has almost  $180^\circ$  inversion in  $27 \leq t \leq 36$  ns, which results in a sharper transition and indicates that reorientation takes place sooner than NP with longer ligands.

*Stretching of the Membrane:* We stretch the NP-membranes by a “virtual probe” that locally pushes on the membranes, in analogy to an AFM. The probe is defined by the stretching force, applied to the central bead of every NP, oriented in the  $z$ -direction, and having the  $(x, y)$ -profile

$$\vec{F}_{stretch} = -k_2 \exp(-(x^2 + y^2)/2c^2) \vec{z}/|\vec{z}|. \quad (3.3)$$

Here,  $c = \sqrt{21} = 4.58$  nm is the effective half-width of the probe, and  $k_2$  is the force magnitude.  $c$  is chosen to produce a “virtual tip” that is not too sharp to easily penetrate the membrane, which happens at  $c \geq \sqrt{5}$  nm. It should not be too flat for the used membrane, in order to avoid a significant “collision” (force applied to it) with the fixed border of the membrane, which happens at  $c \geq \sqrt{50}$ . The probe is positioned in the center of the membrane.



We study how the NP-membranes behave in stretch-release cycles going in upward and downward directions. The stress is measured by the average force,  $\vec{F}_{stretch}$ , per unit area of the membrane, and the strain is measured by the average  $z$ -displacement relative to the  $z = 0$  plane.

$$D_z = \frac{1}{NR_m} \sum_{i=1}^N d_{zi}. \quad (3.4)$$

Here,  $d_{zi}$  is the average displacement of the  $i$ th NP ( $N = 91$ ), and  $R_m \approx 11$  nm is the membrane radius.

In Figure 2h, we show the stress-strain curves for the membranes in Figure 2 a,c,e, with  $R_{LC} = 0.62, 1.12$  and  $1.62$ . The force constant  $k_2$  in Equation 3.3 is increased or decreased in steps of 69.5 pN, and after each step the system is equilibrated for  $\approx 20$  ns. Then, we calculate the membrane stretching by averaging it over a trajectory of the length of  $\approx 20$  ns. At low stresses, the strain of the NP-membranes increases linearly with the stress, according to the Hooke's law, with the slope of 38.1, 54.3, 120.6, and 98.0 pN/nm<sup>2</sup> (relative displacement) for the 1-bead, 2-bead (monolayer), 2-bead (multilayer), and 3-bead, respectively. At larger stresses,  $\sigma > 25$  pN/nm<sup>2</sup>, the strain deviates from the linear dependence, and the membranes eventually rupture without recovery. In general, membranes with larger  $R_{LC}$  can be stretched more. Figure 2 b,d,f shows the (1–3)-bead membrane in their half-stretched and fully stretched states.

The stretched 1-bead membrane is always in the form of a monolayer. The 2-bead membrane switches between a monolayer and partial double-layer, giving two different stress-strain dependencies. The formation of double-layers in the (2–3)-bead membranes causes the appearance of hysteresis loops in their stress-strain curves, reflecting memory effects.

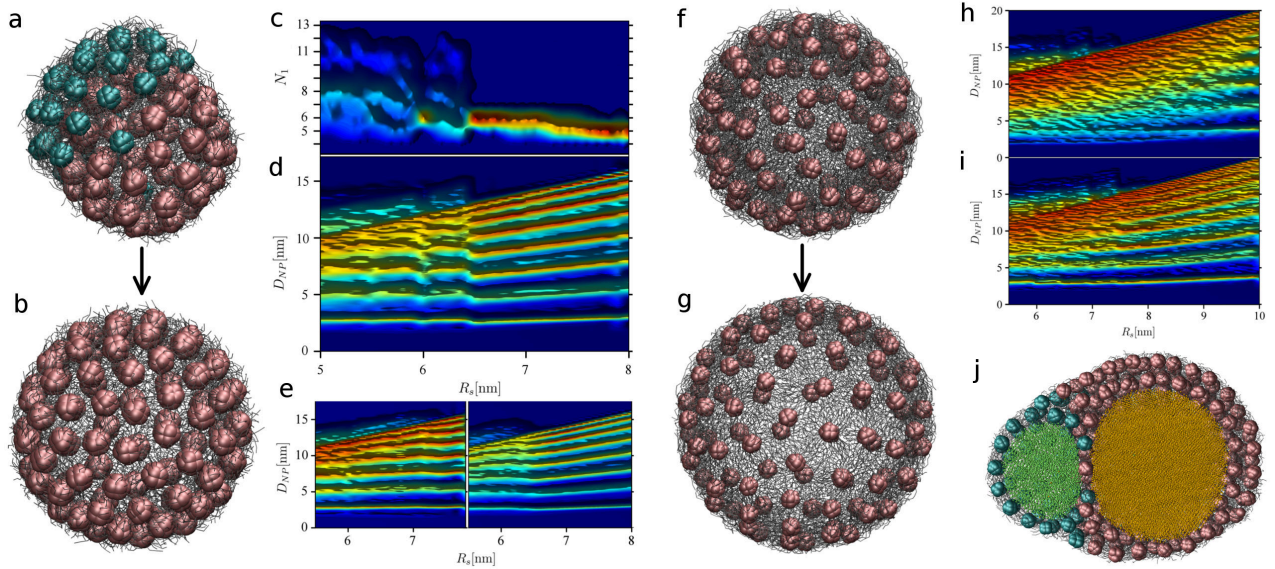


Figure 3: Spherical capsules formed by 96 NPs: (a) Capsule with 3-bead ligands at  $R_s = 5$  nm. A partial double-layer is formed. (b) Monolayer capsule with 3-bead ligands at  $R_s = 7$  nm. (c-e) Correlations of NP-distances in the capsule with 3-bead ligands as a function of the radius  $R_s$ : (c) the average number of first neighbors,  $N_1$ , and (d) the average distances to all the other NPs,  $D_{NP}$ . Lighter regions in the 2D maps signify higher probabilities. The red line on the right marks the transition from 5 first neighbor to 6 first neighbors. The red line on the left marks the point of double layer transition. The scale on the right show the relative heights of regions with different colors; all the distributions are normalized when integrated in the vertical direction. (e) The average distance between NPs,  $D_{NP}$ , for the NP-capsule with 3-bead ligands: (left) 10% defective NPs and (right) addition of 1,000 dodecane molecules. (f) Capsule with 6-bead ligands in monolayer form at  $R_s = 8$  nm and (g) fully stretched form at  $R_s = 10$  nm. (h,i) The average distance between NPs,  $D_{NP}$ , for the NP-capsule with 6-bead ligands (tetracosanethiol): (h) non-modified ligands and (i) modified ligands. (j) Sectional view of two water filled containers.

### Structural analysis of NP capsules

Next, we investigate the possibility of preparing stable NP-capsules. At the time of this study, novel routines have already been designed to prepare microsized and nanosized NP-capsules suitable for molecular storage and delivery [200]. For example, microsized spherical cavities have been assembled using CdSe NPs at a polymer-water interface [201], and well-defined nanocapsules have been prepared in emulsions [202].

We prepare highly elastic and potentially self-healing capsules from NPs with 3-bead and 6-bead ligands. The NP-capsules are formed by assembling 96 NPs on a spherical (hard-core) potential surface of variable radius. The potential is defined by the force

$$\vec{F}_{HS} = \theta(R_s - R) k_3 \vec{R}_0, \quad (3.5)$$

acting on the central bead in each NP, which mimics the presence of molecules in the capsule cavities. Here,  $\theta$  is the Heaviside step function ( $\theta = 1$  when  $R < R_s$ ,  $\theta = 0$  elsewhere),  $R_s$  is the variable radius of the potential surface,  $k_3 \approx 700$  pN is the magnitude of the applied force, and  $\vec{R}_0$  is a unit vector oriented along the direction of the position vector  $\vec{R} = (x, y, z)$ .  $k_3$  is chosen to be sufficiently large to make the sphere rigid. For smaller  $k_3$ , the NPs submerge into the soft boundary, depending on their stretching ( $R_s$ ).

In Figure 3 a,b,f,g, we show NP-capsules formed by NPs with 3-bead and 6-bead ligands. Each NP-capsule is prepared by blowing a cavity inside a NP-cluster using a spherical hard-core potential surface with increasing  $R_s$  of step size 0.1 nm. After 22 ns equilibration, we average the number of NP-neighbors and the NP-distances over all NPs in additional trajectories 20 ns in length to obtain the distributions shown in Figure 3 c,d,e,h,i. The capsule radius is changed in the interval of  $R_s = 5 - 10$  nm, with the step size of 0.1 nm, and the obtained plots are combined to form 2D maps.

The 3-bead capsule has partially a double-layer for  $R_s = 5$  nm, as seen in Figure 3 a, in analogy to the NP-membrane in Figure 2 e. With only 96 NPs, we do not observe a complete double-layer capsule even at  $R_s < 5$  nm. If we increase the capsule size to  $R_s = 7$  nm, it forms a monolayer, as seen Figure 3 b. When we further increase  $R_s$ , the coupling strength of the ligands is eventually exceeded, and the capsule ruptures. The capsule with 6-bead ligands is highly stretchable. As we

stretch it, the ligands become highly elongated and the NPs are more separated, thus covering only a small part of the capsule surface, as shown in Figure 3 (g).

We characterize the structure of NP-capsules by investigating the spatial correlations between NPs with different ligands and under different stretching. In Figure 3 c,d, we show for the capsule with the 3-bead ligands the number of first neighbors of a given NP and the distances to all the other NPs.

In planar membranes, NPs with small  $R_{LC}$  arrange in a close-packed hexagonal pattern, where each NP has 6 first neighbors. On curved surfaces, the number of first neighbors varies. In the NP-capsules, we define first neighbors as NPs that are within the chosen cutoff distance of 3.7 nm, based on the NP-correlations in Figure 3 d. As shown in Figure 3 c, when the capsule is a monolayer ( $R_s > 6.5$  nm), 5 neighbors ( $R_s > 7.3$  nm) and 6 neighbors ( $R_s < 7.2$  nm) predominate. This situation is analogous to  $C_{60}$  fullerene formed by pentagons and hexagons. We can obtain the approximate structure of such capsules if we replace every atom in  $C_{60}$  by a NP and add one more NP in the center of every pentagons and hexagons. When the capsule is formed by a partial double-layer ( $R_s < 6.4$  nm), the number of neighbors becomes less defined, with more neighbors present due to the second layer.

In Figure 3 d, we show a 2D map of the average NP distances for different capsule sizes. When the capsule is a monolayer ( $R_s > 6.5$  nm), we can see clear trend lines for the first 8 neighbors. All the NP separations linearly increase with  $R_s$ . Once a partial double-layer is formed on the NP-capsule ( $R_s < 6.5$  nm), the trend lines become less defined, occasionally breaking into several lines, and the NP separation almost does not depend on  $R_s$ .

In Figure 3 h, we show the same for the NP-capsule with 6-bead ligands. Here, we can see well the trend lines for the first few NP neighbors and only for  $R_s \approx 9 - 10$  nm, where the membrane is highly stretched. In this state, the ligands are fully extended and the cores are no longer able to translate. For smaller  $R_s < 9$ , the 2D map has irregular splittings and the NPs do not have well defined separation distances. In these capsules, the long ligands can wrap around any NP and form bundles. To enhance coupling of ligands from different NPs, we modify the 6-bead ligands by increasing their tip-to-tip coupling. We change the last bead in each ligand from the  $C_1$ -type to the  $C_2$ -type and define the vdW coupling strength of the  $C_1$ - $C_2$  and  $C_2$ - $C_2$  beads to be 1.5 and 2 times that of the  $C_1$ - $C_1$  beads, respectively. This results in more extended NP ligand shells, which leads to the reappearance of the trend lines, as shown in Figure 3 i.

To make our simulations more realistic, we also introduce defects in the NPs. First, we randomly remove a fixed percentile of ligands from the whole capsule with the 3-bead ligands, thus creating a variety of defective NPs with different ligand densities. In Figure 3 e (left), we show the distribution of NP-distances after removal of 10 % of ligands. At this ligand density, the overall structure of the capsule is similar to the defect-free capsule, since the NPs rotate to compensate for their ligand loss in certain regions. However, if we compare the distribution in Figure 3 e left with the results obtained in the non-defective capsule, we do not see a well defined transition between the monolayer and double-layer capsules, observed at  $R_s \approx 6.5$  nm in Figure 3 d. When 10 % and 20 – 25 % of ligands are removed, the capsule is stable for  $R_s < 7.8$  nm and 6.2 nm, respectively. When  $> 33$  % of ligands are removed, the capsule is unstable. Therefore, as the number of defects grow the capsules become less organized and less stable.

In Figure 3 e (right), we also study the effect of adding hydrophobic dodecane molecules to the non-defective capsule with 3-bead ligands. Initially the molecules are randomly added to the outer

surface of the capsule. The molecules are quickly absorbed between the NPs, since they are similar in nature to the alkanethiol ligands. They act as bridges/linkers that give more freedom to the NPs to adjust their positions. After equilibration, the capsule retains its structural regularity, as reflected by the sharp trend lines. The double-layer region, originally observed at  $R_s < 6.5$  nm, is slightly shifted to the left. This shows that the NP-coupling is more relaxed in the presence of dodecane molecules. Moreover, the maximum  $R_s$  is extended by  $\approx 0.5$  nm.

The large elasticity and potential self-healing ability of these NP-capsules suggest that they could be applied in molecular storage, transportation, and drug delivery. The capsules can only store molecules that do not break or solvate the ligated NPs. The nature of alkanethiol gold NPs limit the kind of substances that can be put into the capsule. Hydrophobic molecules dissolve the NPs and destroy the capsule.

We prepare two capsules, consisting of 96 NPs and 384 NPs, filled with coarse-grained water (one bead) [196]. After equilibrating these water-filled capsules, we merge them, as shown in Figure 3 j. The joined structure acquires the shape of a matryoska. The sectional view shows that a NP-monolayer separates waters in the two compartments. When we raise the temperature from  $T = 310$  K to  $T = 370$  K, the NP-monolayer breaks down and the two water compartments join each other. This has the possibility of realizing a controlled chemical reaction inside NP-capsules.

## Conclusions

We have performed CGMD simulations of NP-membranes and capsules to investigate their structure, stability, and mechanical properties for NPs with ligands of different lengths. We have shown that material properties of these nanosystems are largely controlled by the ratio  $R_{LC} = l_{ligand}/r_{core}$ . For smaller  $R_{LC}$  ( $< 1$ ), the systems form well organized monolayers that are relatively fragile and

less stretchable. For larger  $R_{LC}$  ( $> 1$ ), the structures are less organized, more stable, and highly elastic.

We found that characteristics of the membranes depend on the  $R_{LC}$  ratio. NPs with  $R_{LC} \approx 0.62$  form well ordered monolayers with hexagonal packing, in agreement with the experiments ( $R_{LC} \approx 0.44$ ). For  $R_{LC} \approx 1.6$ , the nanoparticles form less organized multilayers, which are more stable and flexible. The systems with large  $R_{LC}$  might potentially be used to form self-healing membranes and capsules. We show that these membranes could potentially form stable capsules for molecular storage and delivery.

### 3.2 Filtration properties of NP membranes

Adapted from Ref. [4] (*Nano Lett.* 2011, 11 (6), 4230–2435. DOI: 10.1021/nl200841a) with the permission from The American Chemical Society.

This study was performed in collaboration with the research group of Prof. Heinrich Jaeger from the University of Chicago. The main goal of the theoretical work in this study is to model the passage of small molecules through gold NP membranes and to derive the filtration mechanism based on experimental observations, simulation results, and free energy calculations. All the modeling and simulation work were performed by our group. Atomistic modeling of the NP membranes and MD simulations were performed by me, and free energy calculations were performed with Lela Vuković. All the experiments were performed by our collaborators.

#### Introduction

Ultrathin porous membranes with thickness of few nanometers are particularly advantageous for filtration applications due to their high throughput at low applied pressure [203–206]. In typical nanofiltration membranes, transport occurs through 0.5 – 2 nm diameter pores or channels. In reverse osmosis membranes, transport occurs by diffusion through polymeric networks [207]. Most ultrathin membranes, however, lack well controlled pore sizes and mechanical robustness due to their extreme thickness. Here, we present highly ordered NP membranes as a suitable candidate for high performance molecular filtration. These mechanically robust membranes are prepared using a drying-mediated method; they have well-defined ligand-filled spacing between NPs and can be suspended over micron-sized holes [190, 191, 208, 209].



## Filtration experiments

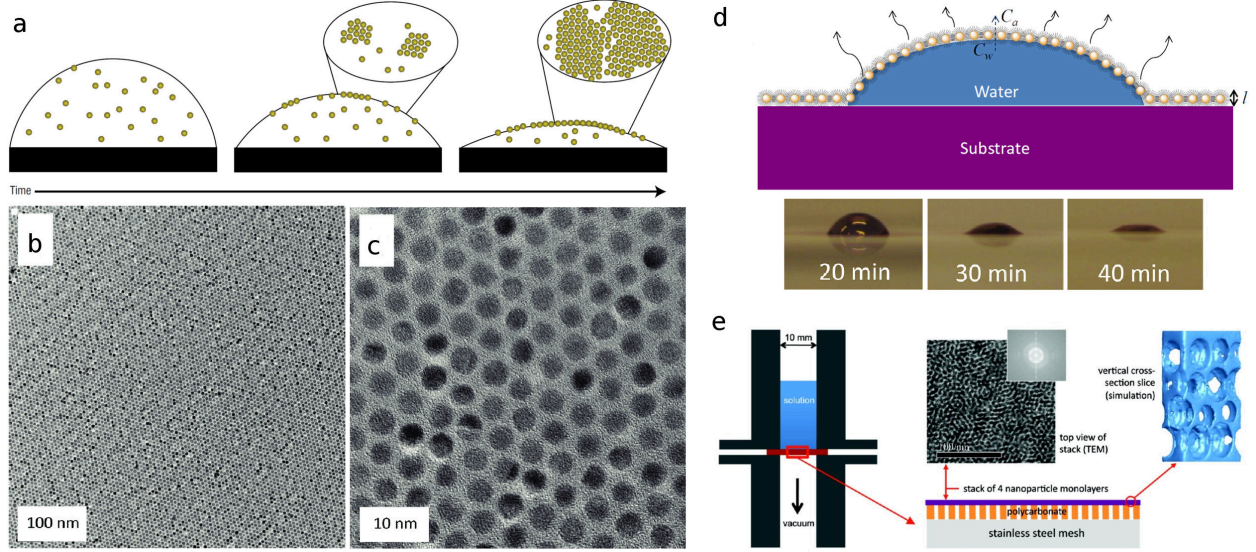


Figure 4: (a) Schematic diagram showing the drying-mediated self-assembly of dodecanethiol ligated gold NP at a liquid–air interface. (b) TEM image of the self-assembled NP monolayer. (c) TEM image of NP monolayer with magnified details. (d) top: Schematic diagram of the water flux experiment. After NP-containing solution (in toluene) has been applied to the top of a water droplet, the solution quickly spreads and, after evaporation of the solvent, forms a NP monolayer that completely covers the water droplet while it dries. bottom: Images of the covered water droplets at different drying times. (e) left: Schematic diagram of the filtration device. middle: TEM image (inset: computed diffraction pattern) and schematic diagram of four layers of NP monolayer stacked on a mechanical support consists of a polycarbonate filter and a stainless steel mesh. right: Cross-sectional slice of the NP membrane visualized using simulation. Void spaces represent volume occupied by NPs, colored volumes are accessible to solvent. Four layers of Lennard-Jones spheres with diameter distribution as in the experiments were prepared and equilibrated separately at  $T = 300$  K, then stacked on top of each other with random relative orientations but only briefly equilibrated.

The experiments carried out in Prof. Jaeger’s laboratory are briefly described here to provide the motivation for the simulations done by me. Gold NPs (average  $d = 5.0 \pm 0.5$  nm) coated with dodecanethiol ligands were prepared. Their self-assembly at a solvent-air interface (Figure 4 a) was mediated by drying of the solvent [48]. Upon complete drying, the NPs formed a mechanically robust freestanding monolayer that can span across micron sized holes (Figure 4 b). High magnification TEM images (Figure 4 c) show a hexagonal close-pack arrangement of the NPs, with a characteristic interparticle spacing that is determined by the type of ligand [191]. This spacing is comparable to the length of dodecanethiol ligands ( $l \approx 1.7$  nm), which implies that the NPs are connected by a

dense region of ligands that are possibly highly interdigitated. The triangular interstices between three neighboring NPs form a less densely packed ligand region where molecules can most likely pass through. Molecular passage through NP membranes can be by diffusion due to concentration gradients and by convection due to pressure gradients [210]. Both of these contributions were studied in these experiments.

In the first set of experiments, a droplet of toluene filled with NPs was deposited onto a droplet of water. NP monolayer covering the whole water droplet (Figure 4 d) formed at an early stage of the solvent drying process, after the evaporation of toluene. The natural rate of water diffusion through NP monolayer was then measured by mass loss over time (Figure 5 a).

In the second set of experiments, 4 NP monolayers were sequentially stacked on top of each other on a polycarbonate filter with 100 nm diameter holes (Figure 4 e). A stack of NP monolayers has a thickness of  $L \approx 34$  nm and the NPs in different layers are not in registry. The stacking of monolayers mitigates the effect of occasional defects in each layer (e.g., particle vacancies, dislocations, or grain boundaries). The stack of NP monolayers with the polycarbonate disk was then placed on a stainless steel mesh of a filtration device. A pressure differential of  $\delta P = 82$  kPa was applied across the membrane by pulling a vacuum downstream. The solutes to be tested were placed above the filtration membrane. Dyes and large fluorescent molecules with weights ranging from 200 to 43,000 and charge states ranging from +1 to -4 were used in the pressurized filtration experiments (Table 1).

The filtration performances of different molecules were quantified by a rejection fraction,  $R = 1 - C_p/C_f$ , which depends on solute concentration of the permeate solution,  $C_p$ , and the feeding solution,  $C_f$ , both determined by the peak intensities in UV-Vis spectra. The rejection rate as a function of the smallest cross-section diameter of each solute is shown in Figure 5 b. The plot

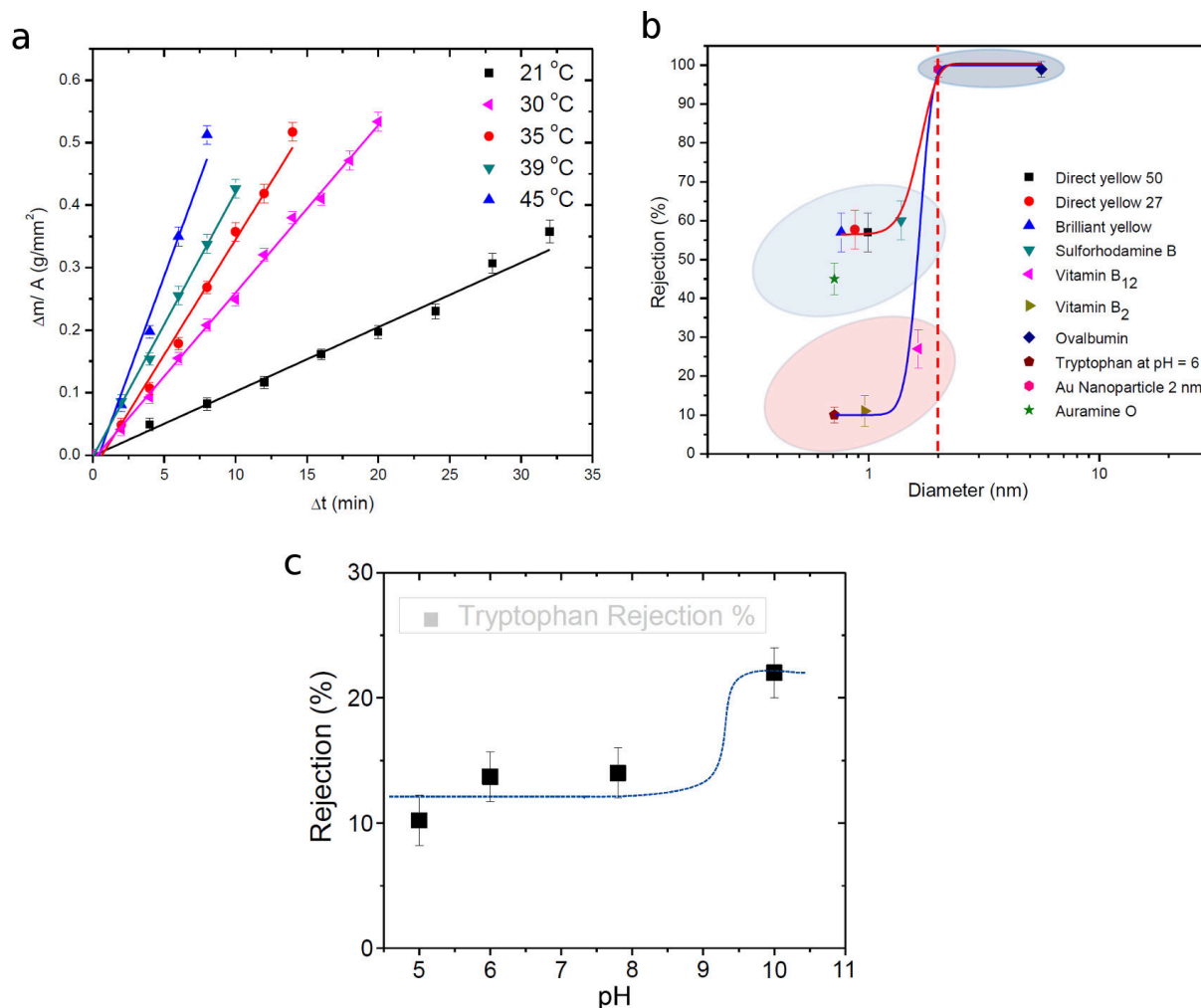


Figure 5: (a) Mass loss  $\Delta m$  of the water droplet as a function of time interval  $\Delta t$ . Here  $\Delta m$  is normalized by the drop surface area  $A$  (at time  $t$ ).  $\Delta t = 0$  corresponds to the point in time when the NP monolayer has fully formed and enveloped the water droplet. The lines represent best fits. (b) Nanofiltration performance. Rejection  $R$  is plotted as a function of the diameter  $d$  of the smallest cross section of each molecule. Data for molecular species with a wide molecular weight range, shape, and charge state are shown, as indicated by the legend. The oval shaded areas show total rejection for objects larger than 1.7 nm in diameter (gray),  $\approx 10\%$  rejection of smaller uncharged species (light blue), and 45 – 60% rejection for smaller charged species (pink). The red dashed line represents the upper limit diameter of pore size predicted by standard pore flow models. The red and blue lines are predictions from a model for  $R(d)$  based on sieving, as explained in the text. In this model, nanopores result from low ligand density regions in the interstices and the width of the transition in  $R(d)$  is determined by small variations in the diameter of the NPs. The lines correspond to a mean pore diameter  $d_p = 1.65$  nm and a pore diameter spread  $\sigma_p = 0.25$  nm, in line with TEM analysis of the NP diameter variation. To account for the effects of residual steric hindrance and for dielectric exclusion of the charged species, diameter-independent offsets were allowed for  $R(d)$ . This approach does not consider the shape of the solute; of the charged species tested only Auramine O is the most compact and spherical, which could be the reason for its lower  $R$  value. (c) The rejection of tryptophan at different pH values.

Name	Mol. weight	Approximate size, nm <sup>3</sup>	Charge
Vitamin B12	1355	$1.7 \times 1.5 \times 1.4$	0
Vitamin B2	377	$1.3 \times 1.2 \times 0.6$	0
Direct yellow 50	957	$2.0 \times 1.1 \times 0.7$	-4
Direct yellow 27	663	$2.2 \times 1.2 \times 0.5$	-2
Brilliant yellow	625	$2.9 \times 0.9 \times 0.5$	-2
Sulforhodamine B	559	$1.6 \times 1.5 \times 1.0$	-1
Auramine O	304	$1.5 \times 0.8 \times 0.5$	+1
Tryptophan	204	$1.0 \times 0.8 \times 0.5$	0
Au Nanoparticle (non-ligated)	—	$d \approx 2 - 5$ nm (spherical)	—
Ovalbumin	43,000	$d = 5.6$ nm (nearly spherical)	—

Table 1. List of solutes tested in the filtration experiments.

shows a remarkably sharp size cutoff of 1.6 nm, separating the highly rejected and partially rejected molecular groups.

Large solutes such as ovalbumin and water-soluble Au NPs ( $d \geq 2$  nm) have a rejection rate  $R > 99\%$ . Small charged solutes have  $R = 45 - 60\%$  and small uncharged solutes have  $R \approx 10\%$ . This sharp size cutoff indicates the absence of significant defects in the membrane stack which might lead to transport through large holes. The NP membranes exhibit a strikingly low size and shape sensitivity for small solutes. The rejection rates of small solutes also only depend on the presence of charges but not on the magnitude of their charging. The rejection rate of tryptophan in different pH conditions (Figure 5 c) was also measured as a reference for simulation studies.

### Atomistic modeling of the NP membranes

Gold cores of the NPs were modeled as icosahedral shells ( $d \approx 5$  nm), formed of non-interacting gold atoms. Dodecanethiol ligands were rigidly bonded onto the surface of the NP cores. The density of ligands on each NP was  $\chi = 1.0$ , where  $\chi$  is the number of sulphur atoms per three gold atoms. This density of ligands was determined by matching the average interparticle distance obtained in simulations of 7 NPs in vacuum (Figure 6 b) to the average interparticle distance derived from

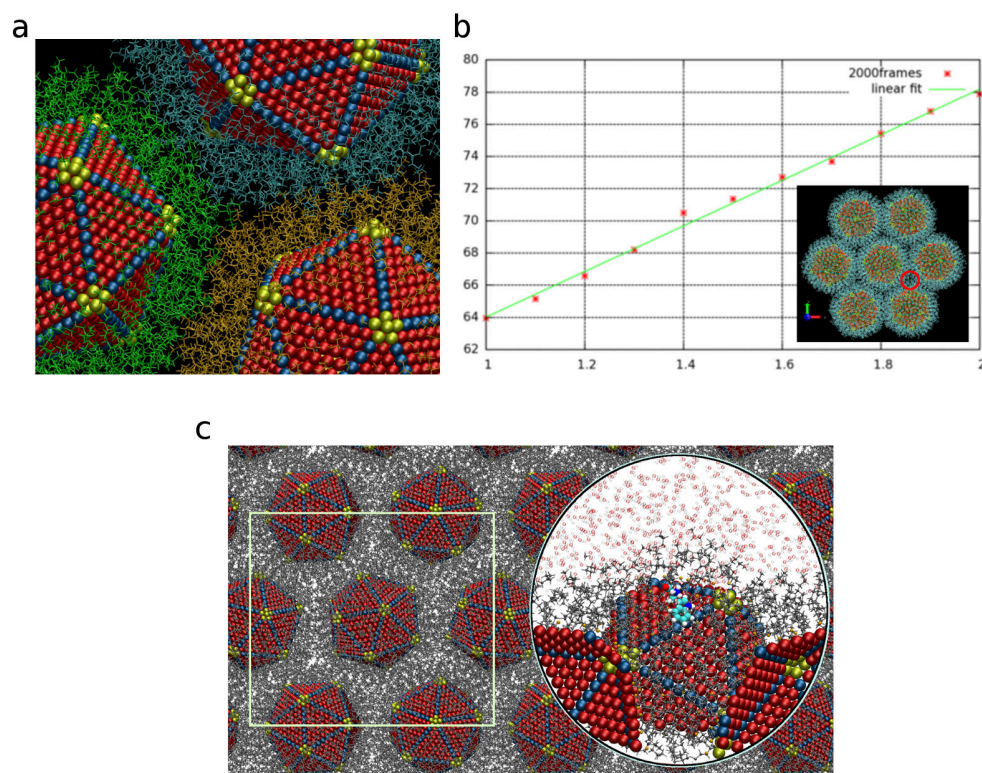


Figure 6: (a) Atomistic model of three gold NPs simulated in vacuum. Ligands on these NPs are colored differently to show the degree of interdigitation. (b) Simulation of 7 NPs in vacuum. The graph shows the interparticle distance as a function of ligand densities. (c) Solvated NP membrane monolayer consists of 4 NPs simulated under NPT condition with periodic boundary conditions applied. The simulation unit cell is highlighted. Inset shows a tryptophan molecule on top of the region between 3 NPs.

experimental TEM images. A solvated NP membrane layer was prepared by placing 4 NPs inside a  $12.5 \times 11.0 \times 8.4 \text{ nm}^3$  simulation box filled with water molecules. Periodic boundary conditions were applied to model an infinite size membrane. The NPs within the unit cell were positioned in a way that the periodic system reproduced a hexagonal NP arrangement. The NPs held on to each other by the vdW interactions of the ligands. The bulk vdW interaction between the NP cores were neglected. Partial charges and force field parameters of all atoms were assigned based on the CHARMM27 force field [171].

The simulations of the solvated NP membrane were performed using NAMD [175]. The isothermal-isobaric (NPT) ensemble was used with a flexible boundary condition to account for any lateral fluctuations of the membrane. A pressure of  $P = 1$  bar and temperature of  $T = 300$  K were set for the barostat and thermostat, both using Langevin dynamics with a damping coefficient  $\gamma_{Lang} = 1.0$  ps<sup>-1</sup>. Long-range electrostatics beyond a cutoff distance of 1 nm was computed using the particle mesh Ewald (PME) algorithm [172]. During a 5 ns equilibration, the NP membrane remained compact and planar. Dodecanethiol ligands extend into the interstices of three neighboring particles, and formed a less densely packed region. Water molecules surrounded the slightly corrugated surface of the membrane, but no water channels or water-filled pores were observed.

### **Free energy calculations**

Molecular passage through water-solvated membranes by diffusion is on a microsecond time scale [191], which exceeds the time scale currently attainable by unrestricted MD simulations. Instead of directly simulating the passage, we calculated the Gibbs free energy profile for selected solutes in the pore regions of the membranes. The chosen solutes were 1 TIP3P water molecule and 3 different charge states of tryptophan: zwitterion ( $-\text{NH}_3^+$ ,  $-\text{COO}^-$ ), neutral ( $-\text{NH}_2$ ,  $-\text{COOH}$ ), and negatively charged ( $-\text{NH}_2$ ,  $-\text{COO}^-$ ). These solutes are all defined in the CHARMM27 force field [171]. The negatively charged tryptophan was modeled in the presence of a simple counter ion ( $\text{Na}^+$ ) in order to preserve the overall neutrality of the unit cell. The adaptive biasing force (ABF) method [211–213] is used to perform the calculations.

Our free energy calculation was set up by dividing the system into horizontal slabs. For water, we used eight 0.5 nm-thick slabs, whereas for tryptophan, we used seven 0.6 nm-thick slabs. We prepared separate simulation runs for each slab, and the solute is placed in different slabs in the



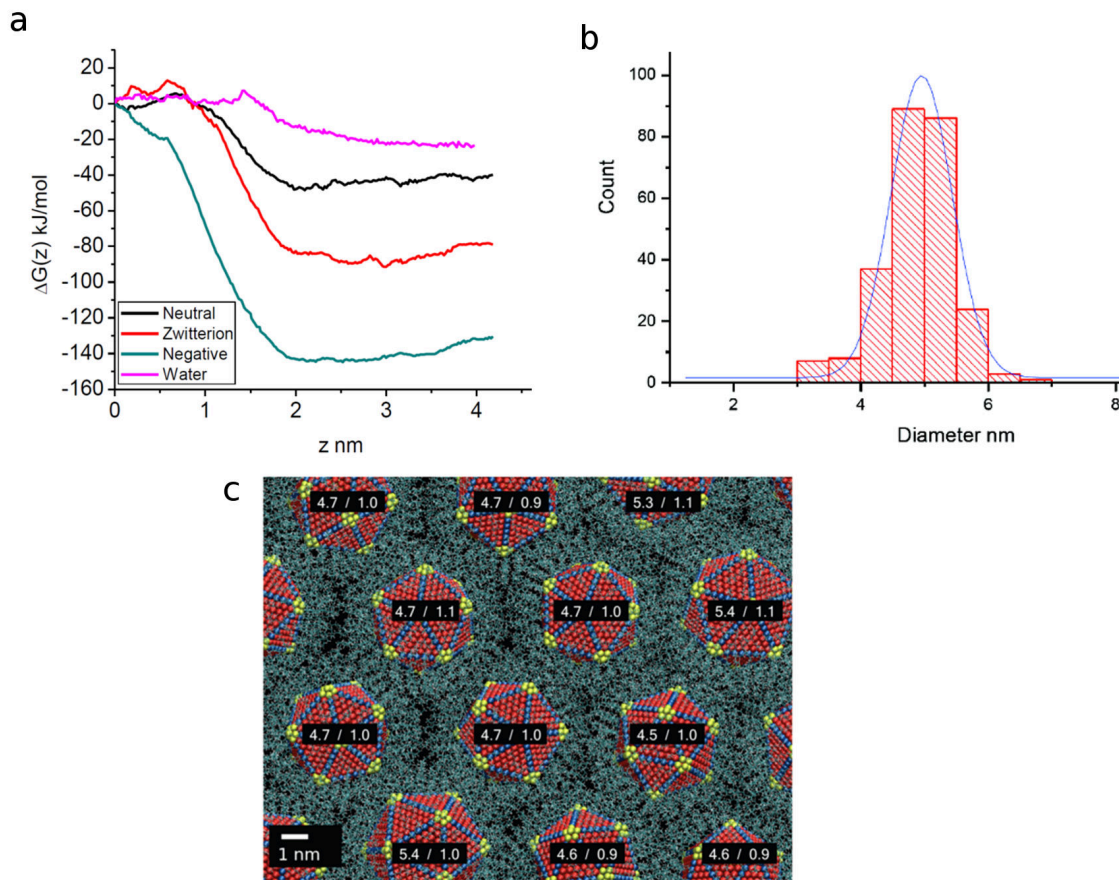


Figure 7: (a) Free energy profiles,  $\Delta G(z)$ , of water (pink) and different charge states of tryptophan – neutral (black), zwitterion (red), and negative (blue) – as a function of distance,  $z$ , between the solute and the mid-plane of the membrane ( $z = 0$ ). Bulk water region corresponds to  $z > 4$  nm. The solute approaches the membrane along a trajectory that goes through the interstitial region of 3 neighboring NPs. (b) Distribution of NP diameter measured from TEM images. (c) Model NP membrane formed of NPs with different sizes and ligand densities. The diameter and ligand density per 3 gold surface atom is shown for each NP.

separate runs. We defined the  $z$  axis as the reaction coordinate, and collected the average force exerted onto the solute in each of the simulation runs. These average forces were then integrated along the reaction coordinate to obtain the free energy profile,  $G(z)$ . It took about 3 to 7 ns in each run for the solute to sufficiently sample along the height of the slab.

The calculated free energy profile,  $\Delta G(z)$ , as a function of distance,  $z$ , is shown in Figure 7 a. This profile was used to evaluate the likelihood of solute passing through the membrane. The

energy difference,  $\Delta\Delta G = \Delta G(z)|_{z=4nm} - \Delta G(z)|_{z=0}$ , between the interfacial region and interior of the membrane is negative in all the cases, which indicates that the solute is more soluble in water than in the alkane environment of the membrane. Since the  $\Delta\Delta G$  for neutral tryptophan is already roughly twice the value for water, the passage rate for tryptophan of any charge states is exceedingly small. The free energy calculations predicted a significantly larger rejection rate than the experimentally observed 5-fold increase of  $R$  for uncharged species. A comparison experiment performed to test  $R$  for tryptophan at different pH values (Figure 5 c) confirmed that  $R$  only doubled when the pH is increased from 8 to 10 (about 70 - 80% of negatively charge tryptophan present). Therefore, the passage of solute through the interstices by diffusion is unlikely.

### **Filtration mechanism**

The results from experiment and simulations suggested a pore-slow mechanism. Pore-like regions can form for a variety of reasons, even if the NPs are well-ordered in a close-packed arrangement. Besides the possibility that ligands can dynamically reorganize during the passage of solute (something our simulations did not specifically include), other factors, such as (a) small variations in NP size and position and (b) temperature-driven fluctuations, can also lead to the formation of instantaneous pores. We tested the first idea by simulating a NP membrane formed of NPs with varying diameters,  $d$ , and ligand density,  $\chi$  (Figure 7 c). Both  $d$  and  $\chi$  were randomly distributed around their means of  $5 \pm 0.5$  nm (distribution is shown in Figure 7 b) and  $\chi = 1 \pm 0.1$ , respectively. We observed in these simulations the appearance of pore-like regions that are larger than in the completely regular lattice (Figure 6 c), which has no variations in core sizes and ligand density.

A picture of transport by means of the pore flow mechanism is also supported by the experimentally measured water flux through the 4-layer NP membrane of  $82 \times 10^{-6}$  m/s, at the pressure differential of  $\delta P = 82$  kPa. This flux is almost 50 times as large as the flux resulting from the



self-diffusion through a single monolayer. To estimate the approximate pore sizes, we use the standard expression [207]  $J_c = \epsilon \pi d_p^2 \delta P / (32 \mu L)$ , where  $J_c$  is the flux due to pressure-driven convection,  $\epsilon$  is the surface porosity,  $\mu$  the water viscosity, and  $L$  the pore channel length. With  $L = 4l \approx 34$  nm for the 4-layer membrane and by assuming that each nanocrystal is surrounded by six pores (so that  $\epsilon = (6\pi d_p^2/4)/(3\sqrt{3}/2s^2)$ , where  $s = 6.7$  nm is the average center-to-center spacing for our dodecanethiol-coated Au particles), we find that the pore size is  $d_p \approx 1.7$  nm. If instead only 50% of the possible pores were actually open,  $d_p$  would increase by a factor  $2^{1/4}$  to  $\approx 2.0$  nm (the diameter of the red circle in Figure 6 b). The obtained range of  $d_p$  values is in excellent agreement with the cut-off diameter for the molecular passage seen in Figure 5 b.

## Conclusions

Results from experiments, MD simulations, and free energy calculations demonstrated that NP membranes have desirable characteristics for nanofiltration, namely the strong size and charge selectivity at low pressure and the ease of fabrication. With improved processing, it should in principle be possible to provide filtration down to the extreme limit of single,  $\approx 10$  nm thin monolayers. Furthermore, different particle–ligand combinations could be used to control the pore size [191,208]. This makes NP membranes promising candidates for applications not only for nanofiltration and separation but also for controlled delivery and encapsulation [3,214,215].

### 3.3 Interfacial Localization and Voltage-Tunable Arrays of Charged NPs

Adapted from Ref. [5] (*Nano Lett.* 2014, 14 (12), 6816–6822. DOI: 10.1021/nl502450j) with the permission from The American Chemical Society.

This study was performed in collaboration with the research group of Prof. Mark Schlossman from University of Illinois at Chicago. The main goal of the theoretical work in this study is to simulate the submersion of a single NP at an aqueous-organic liquid interface, to understand the interactions between NP, ions, and solvent molecules. All the modeling and simulation work were performed by our group. In particular, the atomistic simulations and the analysis of simulation data were performed by me. All the experiments and analysis of related data were performed by our collaborators.

#### Introduction

Interfacial self-assembly of NP arrays with tunable lattice spacings are applicable in the development of nanoscale electro-variable optical devices. The interfacial stability of NPs and NP arrays depends on many factors including electrostatic interactions, balance of surface forces, solvation effects, capillary forces, and ion correlations. Multi-charged NPs, including proteins, viruses, and synthetic constructs, interact strongly with counterions in electrolyte solutions [216]. Electrostatic interactions produce spatial correlations between these NPs and counterions, which are responsible for the condensation of DNA and proteins [217,218], as well as for charge reversal in aqueous colloidal dispersions [219,220]. Charge reversal, also known as overcharging, occurs when the bare charge of a particle is overcompensated by the condensation onto its surface of oppositely charged counterions whose net charge exceeds that of the original charge [220].

Counterion condensation onto micrometer-sized colloidal particles in aqueous dispersions is enhanced in the presence of highly charged counterions, typically trivalent or greater, whose stronger

electrostatic interactions lead to stronger particle-counterion correlations [220]. Although charge reversal due to ion condensation is not expected to occur with monovalent counterions in aqueous solutions, recent experiments have demonstrated that condensation of monovalent counterions takes place on the organic side of an interface between aqueous and organic electrolyte solutions as a result of the stronger electrostatic interactions present in a low permittivity organic liquid [221].

### Probing the interfacial position of NPs by experiments

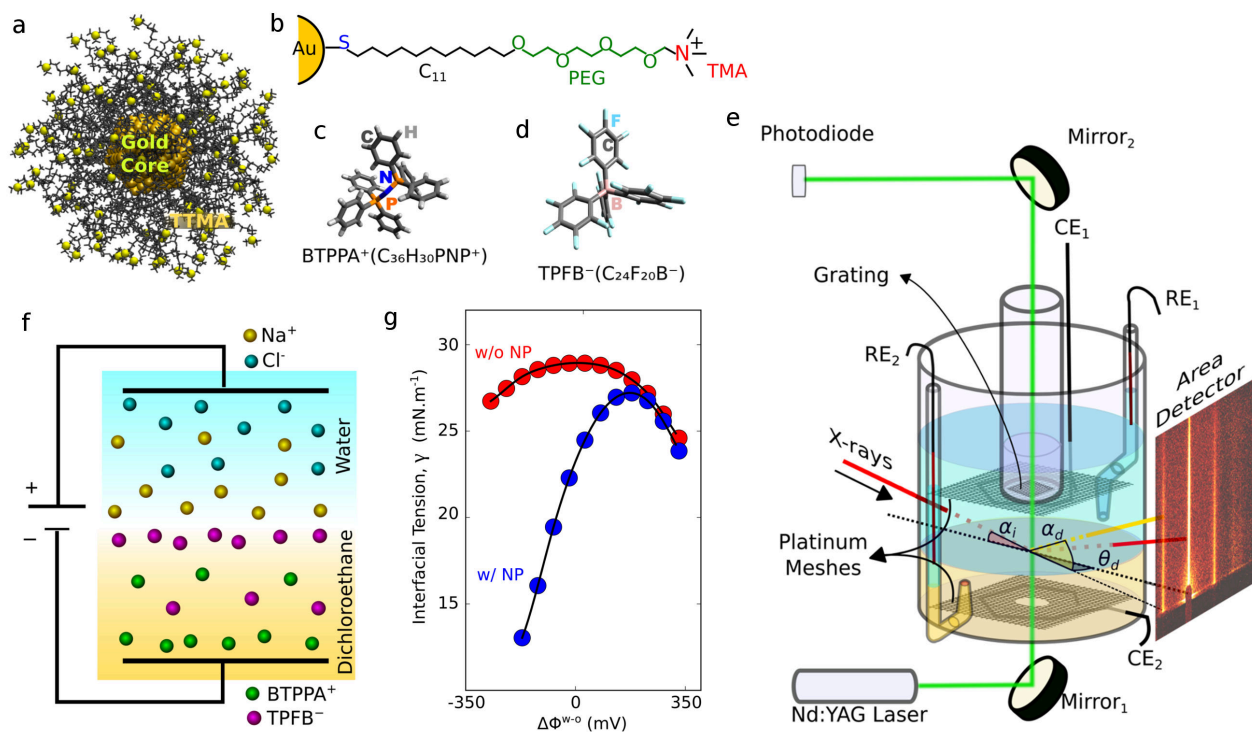


Figure 8: Sample and interfacial tension measurements (taken from [5]). (a) Gold NPs (2 nm core diameter) coated with  $\approx 100$  TTMA ligands. (b) Structure of TTMA ligands. (c,d) Molecular structure of the organic ions BTPPA<sup>+</sup> and TPFB<sup>-</sup>. (e) Electrochemical sample cell and experimental geometry for X-ray surface scattering measurements and quasi-elastic light scattering interfacial tension measurements (CE<sub>1</sub> and CE<sub>2</sub>, counter electrodes made of Pt mesh; RE<sub>1</sub> and RE<sub>2</sub>, reference electrodes are Ag wires coated with AgCl). (f) Cartoon of ion distribution near a liquid-liquid interface between two immiscible electrolyte solutions when an electric potential difference  $\Delta\phi^{w-o} > 0$  exists between the bulk phases, but without NPs. The supporting electrolytes are NaCl (5 mM) in water and BTPPA<sup>+</sup> TPFB<sup>-</sup> (5 mM, 54% dissociated) in 1,2-dichloroethane (DCE). (g) Interfacial tension measurements of the aqueous-organic interface as a function of electric potential difference  $\Delta\phi^{w-o}$  with NPs (blue) and without NPs (red). Error bars ( $\pm 0.1$  mN/m) are much smaller than the symbols.

We briefly describe here the experiments carried out in Prof. Schlossman's group to provide motivation for our simulation studies. Gold NPs ( $d = 2$  nm) coated with  $\approx 100$  positively charged TTMA ligands [222] (Figure 8 a,b) were injected into an electrochemical cell filled with water and DCE (Figure 8 e). Each solution phase contains its own supporting electrolytes (NaCl and BTTPATPFB, Figure 8 c,d) and the electrolyte solutions form an immiscible aqueous-organic liquid interface. Two planar Pt mesh electrodes were used to apply electric potential across the liquid-liquid interface, creating an electric field within a few nanometers of the interface (Figure 8 f). When the electric potential difference, defined as  $\Delta\phi^{w-o} = \phi(w) - \phi(o)$ , is positive, movements of the supporting electrolytes from the bulk phase to the interface produces an enhancement of  $\text{Na}^+$  on the water side of the interface and  $\text{TPFB}^-$  on the organic side of the interface (Figure 8 f) [223]. Even at a high potential of  $\Delta\phi^{w-o} = 100\text{mV}$  (electric field on the order of  $10^8$  V/m), these supporting electrolytes mostly do not cross the interface since they are essentially insoluble in the opposite phase.

Interfacial tension measurements (Figure 8 g) show a reduction in interfacial tension at small positive  $\Delta\phi^{w-o}$  (e.g., 30 mV) but not at negative  $\Delta\phi^{w-o}$ , which indicates that positive  $\Delta\phi^{w-o}$  induces interfacial adsorption of TTMA ligated gold NPs [224, 225]. A negative interfacial excess charge per area (positive slope in Figure 8 g),  $Q_{tot} = -(\partial\gamma/\partial\Delta\phi^{w-o})_{T,p,\mu_i}$  (temperature  $T$ , pressure  $p$  and chemical potential  $\mu_i$  of species  $i$ ), further indicates that the interfacial adsorption of NP and ions enhances charges on the organic side of the interface.

X-ray reflectivity measurements with sub-nanometer resolution were performed to directly probe the variation in electron density perpendicular to the interface [226]. The measurements performed using 30 keV X-rays at the ChemMatCARS beamline of the Advanced Photon Source (Figure 9 a) were fitted to a model of interfacial electron density profile to determine the interfacial depth of the NPs and their depth distribution (Figure 9 b). Two-nm spherical gold cores (measured from TEM

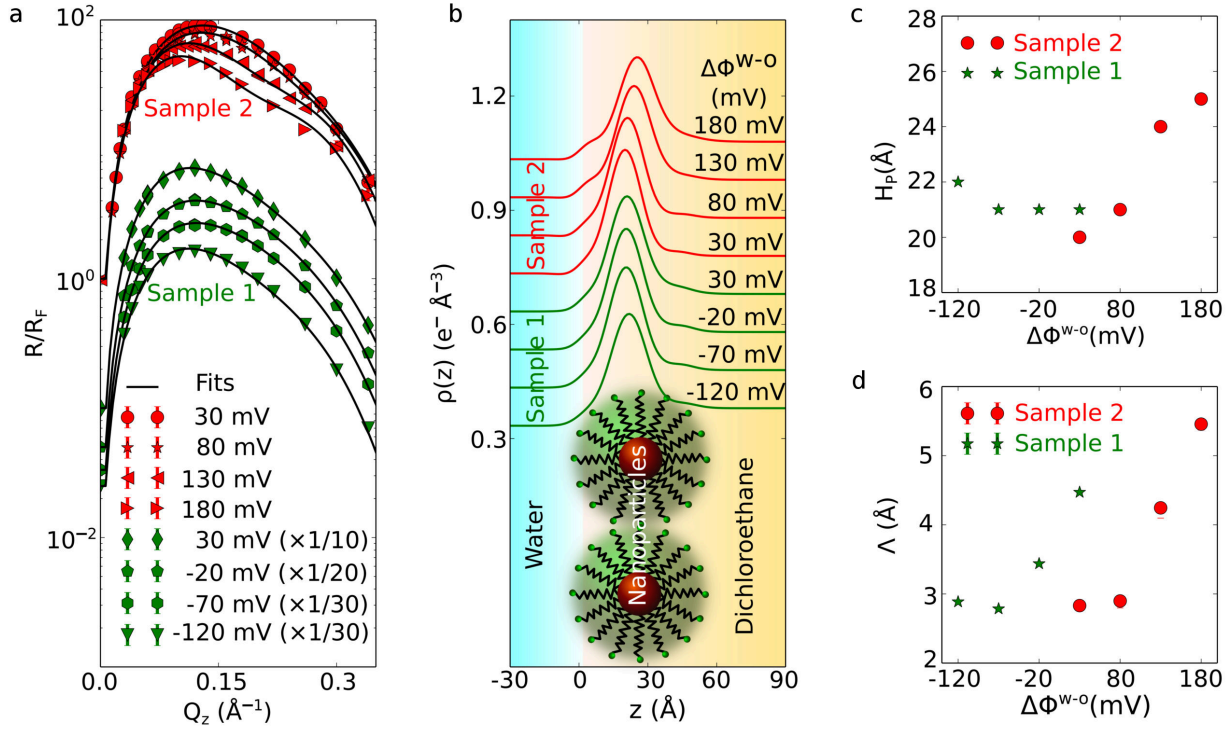


Figure 9: X-ray reflectivity measurements. The data shown are from samples that were initially equilibrated at  $\Delta\phi^{w-o} = 30$  mV, then  $\Delta\phi^{w-o}$  was increased (Sample 2) or decreased (Sample 1) from 30 mV. Cycling  $\Delta\phi^{w-o}$  back and forth reproduces the interfacial structure with small variations in interfacial coverage and height distribution. (a) X-ray reflectivity  $R$ , normalized to the Fresnel reflectivity  $R_F$  from an ideal interface for TTMA gold NPs at the electrified water–DCE interface as a function of wave vector transfer normal to the interface,  $Q_z$ , for different electric potential differences  $\Delta\phi^{w-o}$ . Solid lines represent best fits to the model discussed in the text. (b) Variation of electron density  $\rho(z)$  along the direction  $z$  (perpendicular to the interface) obtained from the fits in (a). A cartoon of NPs at the interface is shown. (c) The depth  $H_p$  of the NPs is given by the location of the peak maximum in (b). (d) The exponential decay length  $\Lambda$  of the depth distribution obtained from fitting X-ray reflectivity data. The discontinuity in  $\Lambda$  at  $\Delta\phi^{w-o} = 30$  mV is the result of slight differences in equilibrated structure observed for different samples. Error bars are smaller than the symbols for panels a, c, and d.

images) enclosed by 1.8 nm ligand shells were used in the fitting model and the variations of NP depth within the monolayer and NP polydispersity were modeled by an exponential variation with decay length  $\Lambda$ .

Peaks in the electron density profiles (Figure 9 b) represent the NP gold cores. The results of a sample initially equilibrated at  $\Delta\phi^{w-o} = 30$  mV show that the NPs are located almost entirely on the organic DCE side of the interface. The interfacial depth of the NP monolayer shows little

change for negative potentials, but a small increase into the DCE phase as  $\Delta\phi^{w-o}$  approaches +180 mV (Figure 9 c). The small increase in peak width observed in Figure 9 b as  $\Delta\phi^{w-o}$  increases is characterized by an increase in the decay length  $\Lambda$  of the NP depth distribution shown in Figure 9 d.

Over this range of potentials,  $-120 \text{ mV} \leq \Delta\phi^{w-o} \leq 180 \text{ mV}$ , some of the NP ligands in the monolayer appear to remain in contact with the aqueous phase, though the NPs are primarily immersed in the DCE phase (Figure 9 b). However, the interfacial tension at even higher potentials, up to 350 mV, approaches that of the pure interface without NPs (Figure 8 g). Although this is consistent with the increase in penetration of the NPs into the DCE phase as  $\Delta\phi^{w-o}$  approaches 180 mV, additional X-ray measurements are required to determine whether or not NPs leave the organic side of the interface at  $\Delta\phi^{w-o} > 180 \text{ mV}$ .

### Self-assembly of voltage-tunable arrays

Grazing-incidence small-angle X-ray scattering (GISAXS, Figure 10 a) reveals a 2D monolayer ordering of NPs at the interface [226]. The variation of Bragg rod intensity with  $Q_z$  (out-of-plane) is fit by a monolayer-thick 2D-array of NPs, which is consistent with the results from our X-ray reflectivity studies. The 2D array at  $\Delta\phi^{w-o} = 30 \text{ mV}$ , as determined by the presence of two symmetric first order ( $[1,0]/[0,1]$ ) Bragg rods at in-plane scattering wave vector  $Q_{xy} = Q_{[10]} \approx \pm 0.114 \text{ \AA}^{-1}$  and faint second and third order Bragg rods at  $Q_{xy} = Q_{[11]} \approx -0.197 \text{ \AA}^{-1}$  and  $Q_{xy} = Q_{[20]} \approx -0.228 \text{ \AA}^{-1}$ . Intensities of the GISAXS patterns integrated over  $Q_z$ , shown in Figure 10 b, demonstrate that the lattice remains hexagonal for all measured potentials but variations in peak position and shape reveal voltage-dependent changes in lattice spacing and in-plane correlation length. The narrowest peaks are obtained after initial equilibration of the samples at  $\Delta\phi^{w-o} = 30$

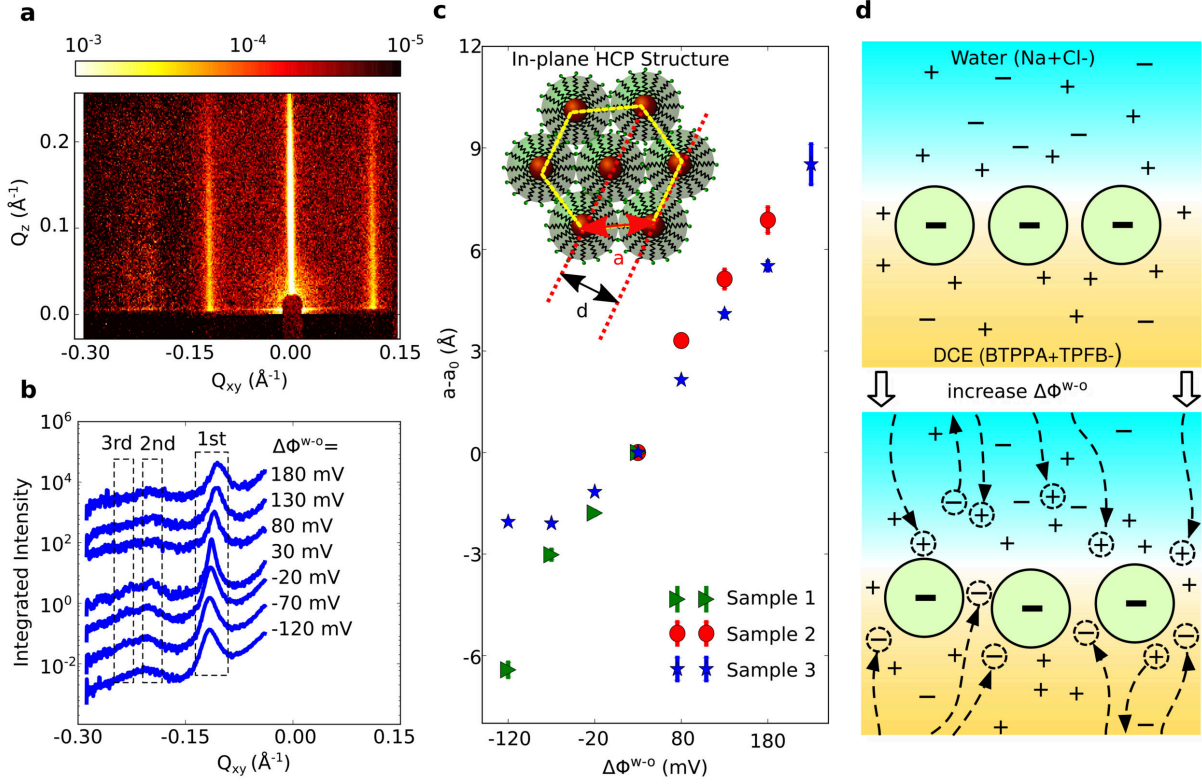


Figure 10: GISAXS measurements. (a) Bragg rods measured by grazing-incidence small angle scattering (GISAXS) from a 2D array of charged NPs at the electrified water–DCE interface for  $\Delta\phi^{w-o} = 30$  mV, where  $Q_z$  is the wave vector transfer in the direction out of the plane of the interface and  $Q_{xy}$  is in the plane. (b) Intensity integrated over  $Q_z$  from  $0\text{\AA}^{-1}$  to  $0.1\text{\AA}^{-1}$  plotted as a function of  $Q_{xy}$  for different values of  $\Delta\phi^{w-o}$  (measured from Sample 3). Each curve shows the equivalent of 2D grazing incidence diffraction with three diffraction peaks indicated. (c) Change in the nearest neighbor spacing  $a = 2d/\sqrt{3} = 4\pi/(\sqrt{3}Q_{[10]})$  for three different samples as a function of  $\Delta\phi^{w-o}$  referenced to the spacing  $a_0$  measured at  $\Delta\phi^{w-o} = 30$  mV of the same sample ( $a_0 = 67.2, 61.5$ , and  $64.5$   $\text{\AA}$  for samples 1, 2, and 3, respectively). Inset: Cartoon of the 2D hexagonal close-packed structure of NPs with nearest-neighbor spacing  $a$  and lattice spacing  $d$ . (d) As explained in the text, NPs indicated by a “-” sign are charge-reversed with a net negative charge. TPFB<sup>-</sup> anions that condense on the NPs to reverse their charge are not shown separately. As  $\Delta\phi^{w-o}$  increases, the net charge of the supporting electrolytes becomes more positive near the interface on the aqueous side and more negative on the organic side as a result of the re-distribution (indicated by arrows) of supporting electrolytes between bulk and interfacial regions.

mV. The peak width determines the in-plane correlation length  $\zeta$ , which measures the spatial extent of in-plane lattice order, to be 15 times the nearest-neighbor separation  $a$  for  $\Delta\phi^{w-o} = 30$  mV. The larger widths of the peaks in Figure 10 b at either larger or smaller  $\Delta\phi^{w-o}$  indicate a decrease in  $\zeta$ , which may be due to the creation of defects as the lattice expands or contracts.

Figure 10 c illustrates a nearly linear increase of in-plane nearest-neighbor spacing,  $a$ , as  $\Delta\phi^{w-o}$  is increased. This increase is not due to a loss of NPs from the interface, as demonstrated by an analysis of the percentage  $C$  of interface covered by NP unit cells ( $C \approx 75\%$ ), showing that the number of NPs on the interface is nearly constant as  $\Delta\phi^{w-o}$  varies from  $-120$  to  $180$  mV. Instead, the lattice spacing of the 2D NP array varies because  $\Delta\phi^{w-o}$  determines the concentration of electrolytes in the electrical double layers on either side of the interface and these electrolytes, in turn, modulate electrostatic interactions between NPs. In particular, increasing  $\Delta\phi^{w-o}$ , starting from either positive or negative values of  $\Delta\phi^{w-o}$ , makes the electrolyte environment on the organic side of the interface, that is, near the NPs, more negative (Figure 10 d). If the total charge of each NP (including the TPFB<sup>-</sup> anions condensed on its surface) is positive, then a more negative electrolyte environment will reduce electrostatic repulsive forces between NPs, thereby reducing the lattice spacing. However, this contradicts the observations. Therefore, we need to assume that the total NP charge is not positive. This alternative scenario is illustrated in Figure 3d, which shows a monolayer of negatively charged NPs whose lattice spacing will increase with increasing  $\Delta\phi^{w-o}$ , as observed experimentally. Although the bare charge on each NP is  $+100$ , ion condensation of TPFB<sup>-</sup> counterions could reverse their net charge, as has been observed for larger colloids [220]. Charge reversal, also known as overcharging, occurs when the bare charge of a particle is overcompensated by the condensation onto its surface of oppositely charged counterions whose net charge exceeds that of the original charge [220]. Our MD simulations discussed below will provide strong evidence for charge reversal of the NPs. This



heuristic explanation of the trend in lattice spacing with  $\Delta\phi^{w-o}$  relies upon the NPs effective charge remaining negative throughout the entire range of  $\Delta\phi^{w-o}$ .

The enhanced repulsion at larger  $\Delta\phi^{w-o}$  should also increase the out-of-plane distribution of NPs, an expectation that is confirmed by the increase in decay length shown in Figure 9 d. Note that the presence of NPs with negative effective charge does not contradict the results of interfacial tension discussed earlier, which probe the total excess charge of one (or the other) side of the interface. In that case, transport of a +100 bare-charged NP contributes +100 charges to the excess charge on the organic side of the interface whether or not organic counterions condense onto the NP and reverse its net charge.

### MD simulations of a submerging NP

The submersion and interfacial stability of a TTMA gold NP at an aqueous-organic interface was studied using MD simulations. The liquid interface was modeled inside a  $20 \times 20 \times 47$  nm<sup>3</sup> unit cell filled with water and DCE molecules plus 20 mM supporting electrolytes (100 pairs of ions) in each phase. The NP core was modeled as an icosahedral shell ( $d \approx 2$  nm), formed by rigidly bonded non-interacting gold atoms (no partial charges or vdW parameters,  $b_o = 2.74\text{\AA}$  and  $K_b$  is large). The NP core was covered by 100 TTMA<sup>+</sup> ligands, and initially placed in water with 50 Cl<sup>-</sup> ions and 50 TPFB<sup>-</sup> as counterions to achieve global charge neutrality. Partial charges and force field parameters of all atoms are assigned based on the CHARMM35 ethers force field and CHARMM36 general force field [171, 227, 228].

The model system (Figure 11 e) had a total of 100 Na<sup>+</sup> and 150 Cl<sup>-</sup> in the aqueous phase and 100 BTPPA<sup>+</sup> and 150 TPFB<sup>-</sup> in the organic phase, which simulated the experimental condition of small  $\Delta\phi^{w-o}$ . However, the electrolyte concentration in simulations was set higher than in experiments

to include enough ions in the small system for the NP to stabilize in either the water or the DCE phase. The larger number of counterions (150) in each phase than charges on the bare NP (100) also allowed for the possibility of charge reversal in either phase. A 5 nm thick layer at the top of the unit cell (65526 of the total 320908 water molecules) and a 2 nm thick layer at the bottom of the unit cell (6641 of the total 67888 DCE molecules) were spatially fixed throughout the simulation to prevent atoms inside the unit cell from shifting up and down. The thickness of these fixed layers was about the Debye length of the respective solvent at  $< 5$  mM ion concentration.

The simulations were performed in Canonical (NVT) ensemble using the NAMD package [175, 199]. A constant temperature of 295.15 K is chosen for all the systems and it was maintained by Langevin dynamics with a damping coefficient of  $0.01 \text{ ps}^{-1}$ . Long-range electrostatic interactions were employed using the particle mesh Ewald (PME) algorithm [172].

Simulation snapshots of the NP submersion are shown in Figure 11 (a-d). The height of the NP Figure 11 f (top), measured from the center of the gold core to the water–DCE interface, and the number of ions within 1 nm of the NP surface Figure 11 f (bottom) show that the submersion of the NP is accompanied by the adsorption of  $\text{TPFB}^-$  ions that replace  $\text{Cl}^-$  ions. Counterion adsorption onto the NP eventually alters the ion balance in our simulation cell, by releasing  $\text{Cl}^-$  ions into the aqueous phase and removing  $\text{TPFB}^-$  ions from the organic phase. This produces an electric field gradient that opposes further submersion. To reset the ion balance, 30  $\text{Cl}^-$  ions are removed from the aqueous phase and 30  $\text{TPFB}^-$  ions added to the DCE phase at  $\approx 96$  ns and again at  $\approx 127$  ns. Counterion condensation of  $\text{TPFB}^-$  onto the NP is likewise observed as it crosses the interface.

Figure 11 f (bottom) shows that the number of  $\text{TPFB}^-$  counterions within 1 nm of the NP surface is larger by  $\approx 13$  ions than the number of  $\text{TTMA}^+$  ligands exposed to the DCE phase by the end of the simulation. Many of these excess charges are located in the denser region of  $\text{TPFB}^-$

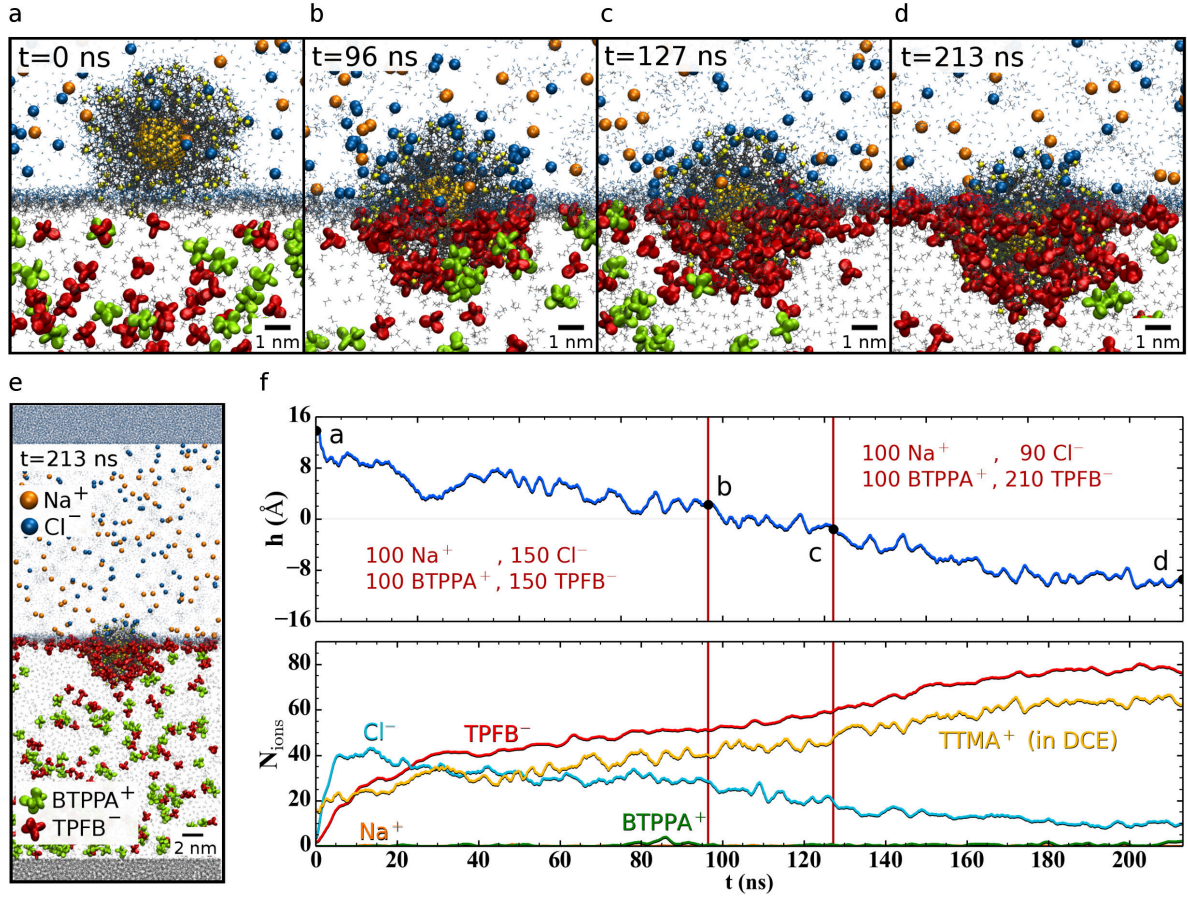


Figure 11: MD simulations (a-d) Time sequence snapshots taken from a 213 ns MD simulation show the submersion of a NP from an aqueous (top) to an organic (bottom) electrolyte phase accompanied by the exchange of loosely bound  $\text{Cl}^-$  ions (blue) in the aqueous phase for condensed organic  $\text{TPFB}^-$  ions (red) in the organic phase. (e) The simulation cell (snapshot at 213 ns). Most solvent molecules are not shown for clarity. Two spatially fixed solvent layers are shown in gray at the top and bottom. (f) Time dependence of the NP submersion height,  $h$ , measured from the center of the Au core to the interface, and the number of ions,  $N_{\text{ions}}$ , within 1 nm of the NP surface. The vertical lines at  $t = 96$  ns and  $t = 127$  ns indicate when the number of  $\text{Cl}^-$  and  $\text{TPFB}^-$  ions in the bulk phases are adjusted.

ions along the “ring” of 3-phase contact between NP and aqueous and organic phases. Excluding the excess charges in this ring, the remaining part of the NP exposed to the organic phase is charge reversed (Figure 12 a). The bottom panel of Figure 12 a shows that the net charge is approximately  $-2$  for cone angles between  $70^\circ$  and  $90^\circ$  that account for most of the NP submerged into the organic phase, but exclude the 3-phase contact ring. Likewise, an MD simulation of an isolated TTMA AuNP placed within a DCE electrolyte solution exhibits a small overcharging of  $-2$  (Figure 12 b).

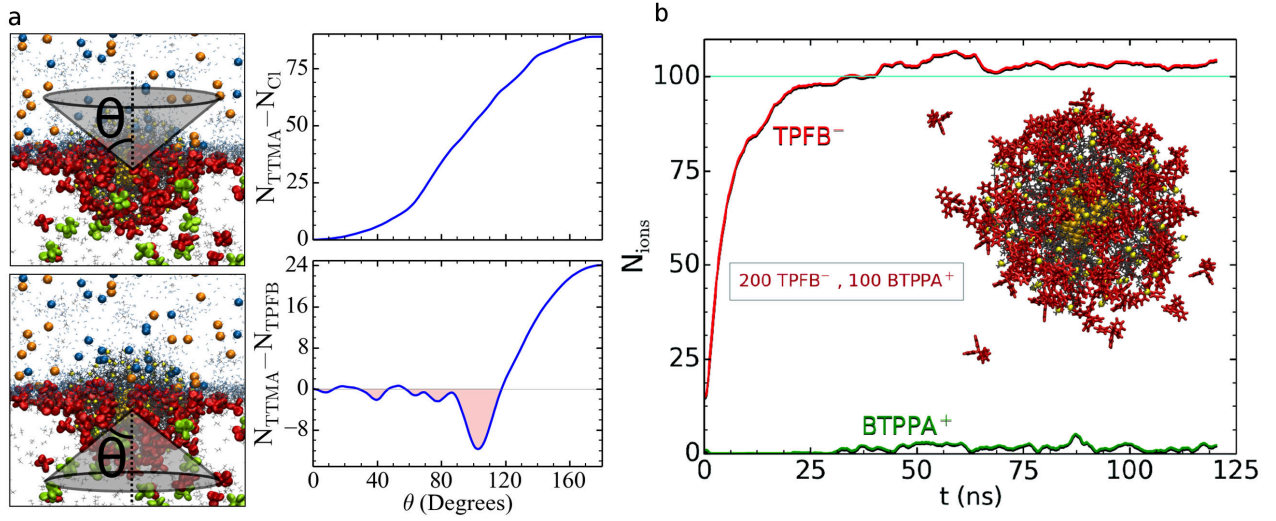


Figure 12: (a) Time averaged analysis of the last 40 ns MD simulation trajectory for the charge summed over NP surface cations (TTMA<sup>+</sup>) plus either Cl<sup>-</sup> (top) or TPFB<sup>-</sup> (bottom) that are within 1 nm of the NP surface and within the specified cone angle. The cone apex is located at the center of the Au core. The minimum at  $\approx 105^\circ$  in the lower panel contains TPFB<sup>-</sup> ions within the ring of three-phase contact line between NP and aqueous and organic phases. The pink fill shows that the portion of the NP exposed to the organic phase is charge reversed. (b) MD Simulation of a single NP in the Bulk Organic Phase. Variation with simulation time of the number of ions,  $N_{ions}$ , within 1 nm of nanoparticle surface. This figure illustrates the analysis of an MD simulation of a TTMA-Au nanoparticle in bulk DCE. A nanoparticle with a bare charge of +100 is placed at the center of a  $19.9 \times 19.9 \times 22.5 \text{ nm}^3$  simulation cell, which also contains 64555 DCE molecules, 200 TPFB<sup>-</sup> ions, and 100 BTPPA<sup>+</sup> ions. The simulation is performed under NPT conditions. Upon equilibration, the average net charge of the nanoparticle plus counter- and co-ions within 1 nm of its surface is -2, indicating that the nanoparticle undergoes charge reversal. Close observation of the snapshot image from the simulation reveals ring stacking of neighboring TPFB<sup>-</sup> ions on the surface of the nanoparticle. The inset shows only the nanoparticle and TPFB<sup>-</sup> ions within 2 nm of it.

Stacking of TPFB<sup>-</sup> rings, as observed in the simulation in Figure 12 b, allow TPFB<sup>-</sup> ions to pack more closely on the NP surface, potentially contributing to the efficiency of charge reversal. Charge reversal of the NP is consistent with the GISAXS results of lattice expansion with increasing  $\Delta\phi^{w-o}$  (Figure 10 c). As expected for monovalent ions in water, Figure 12 a shows that Cl<sup>-</sup> ions are not condensed on the water-side of the NP and that side is not charge-reversed. The simulation results provide clear evidence that NPs are transported from the polar aqueous phase to the organic phase, due to their stronger affinity to bind TPFB<sup>-</sup> ions than Cl<sup>-</sup> ions.

Two-NP systems were also simulated to study the interactions between NPs at the interface (Figure 13 a). The simulations were performed under the same conditions and in the same cell used for the single NP simulations. The simulation was prepared by adding 1 NP plus the nearest 30  $\text{Cl}^-$  and 70  $\text{TPFB}^-$  ions, as extracted from the single NP simulation, to the final equilibrated configuration of the single NP system. Ions that were initially positioned between the NPs were repositioned to the solution under them. The interparticle distance between the NPs stabilized at  $\approx 7.4$  nm within 50 ns and  $\text{TPFB}^-$  ions from the solution were observed to migrate to the region between the NPs (see Figure 13).

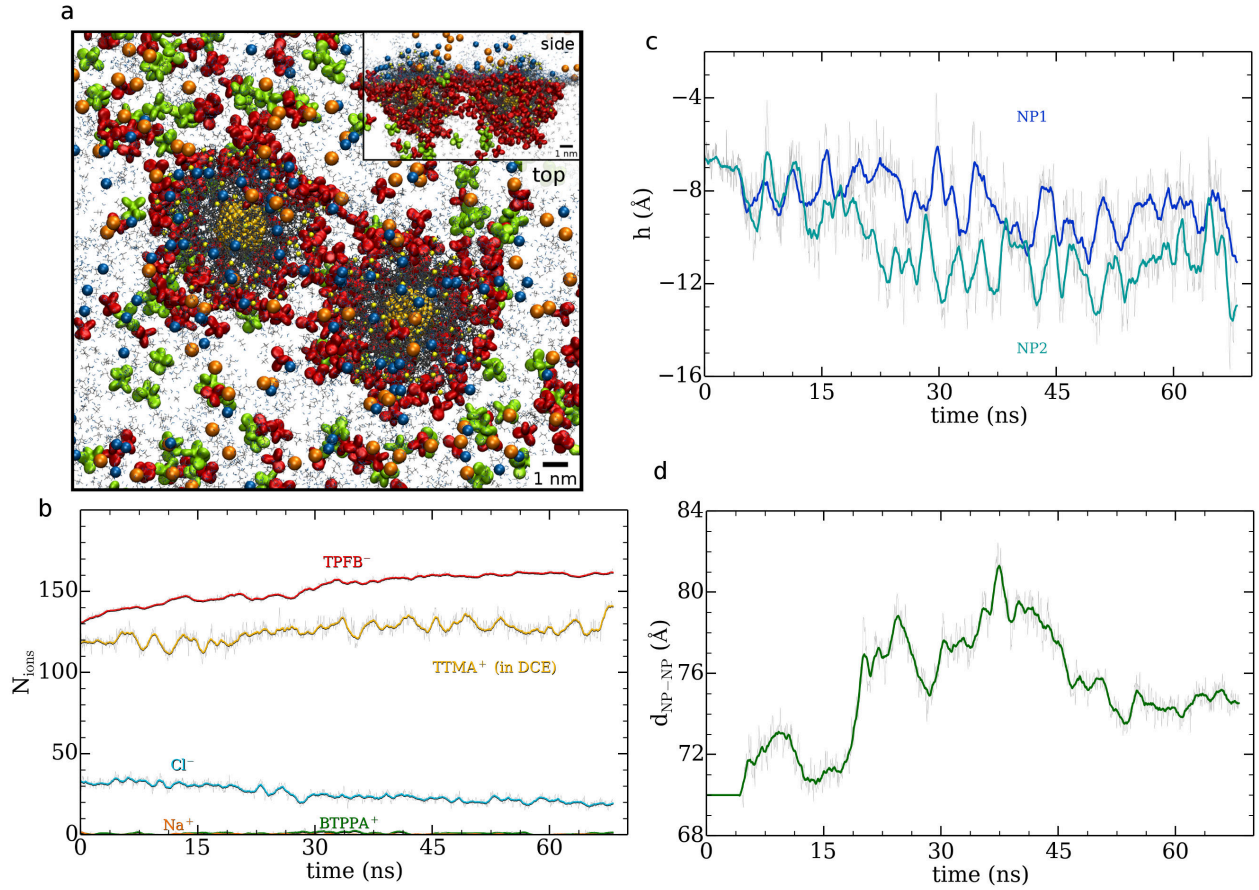


Figure 13: (a) Two NPs in the simulation cell in Figure 11 e form a stable pair at  $t = 68$  ns (top view with inset of side view). (b) The number of ions,  $N_{ions}$ , within 1 nm of the NP surface. (c) Time dependence of the submersion height,  $h$ , of both NPs measured from the center of the gold core to the interface. (d) The center-to-center interparticle distance between the two NPs.

The strength of correlations between a charged NP and a counterion, which can be measured by the ratio of electrostatic interaction energy to thermal energy, varies inversely with the permittivity of the solvent [216]. Sufficiently strong electrostatic interactions, such as those present in the low permittivity organic DCE phase ( $\epsilon_{r,DCE} = 10.43$ ), have been previously shown to produce condensation of TPFB<sup>-</sup> monovalent ions on the water–DCE interface without NPs [221]. The low permittivity of DCE can also produce ion condensation of TPFB<sup>-</sup> ions onto NPs and, subsequently, reverse their effective charge. Other effects, such as preferential chemical interactions between TPFB<sup>-</sup> ions and the NP, could contribute to the ion condensation.

Our simulations of a single NP show that ion condensation does occur in the bulk organic phase in the absence of an applied electric field (Figure 13 b). Related to this, their experiments show that NPs are transported to the organic side of the interface under the action of a small applied potential equal to 30 mV. Simulations with equal numbers of counterions on either side of the interface, which model a small  $\Delta\phi^{w-o}$ , confirm that a NP is spontaneously transported across the interface with ion condensation occurring on the organic side, as well as charge reversal of the portion of the NP exposed to the organic phase. Ion condensation thus provides a driving force to move TTMA gold NPs from the aqueous to the organic DCE phase.

These observations in simulations lead to our understanding that NPs are charge reversed due to ion condensation that occurs as a result of their presence in the low permittivity organic phase, not as a result of an applied electric field. The cartoon in Figure 10 d describes our suggestion that the voltage-tunability of the 2D array of NPs is the result of voltage-induced variations in the density of counterions in the vicinity of charge-reversed NPs. To summarize, ion condensation on NPs and their charge reversal occur when NPs are exposed to the organic phase, even at very low voltage, whereas voltage-tunability is due to counterion mediated interactions between the charge-reversed

NPs. The separation of these two effects arises because the electrostatic energies associated with the potential range of the experiment are much smaller than the electrostatic energy of attraction between a condensed counterion and its NP.

To address the existence of a 2D lattice of NPs, we carried out MD with two NPs in the simulation box, shown in Figure 13 a. The MD simulation results indicate that the two NPs stabilize within close proximity of each other, where they appear to share a few TPFB<sup>-</sup> ions in the condensed layer of counterions. Atomistic simulations of larger interfacial NP lattices tunable by voltages would necessitate significantly larger computational resources than we have at our disposal. Monte Carlo simulations of the liquid–liquid interface between immiscible electrolyte solutions may also provide an accessible computational scheme to study this lattice [229]. Although analytic theory has described voltage-tunable lattices at the liquid–liquid interface, the effects of ion condensation and charge reversal that we simulated have not been previously considered in this context [224]. Other theoretical works have discussed several correlation effects that could be important in stabilizing the observed lattice of charged NPs, including mechanisms to share multivalent counterions between neighboring surfaces or colloids [220,230], as observed in our two-NP simulation, as well as Coulomb-depletion [231] forces that arise due to excluded volume effects. In this context, it should be noted that the experiments demonstrate that the 2D crystallization cannot be due to pure repulsion, as previously observed for charged micrometer-sized colloids at the liquid–liquid interface [232]. The X-ray reflectivity measurements show that NPs are present over only 75% of the interface and the two-NP simulations confirm that NPs can be stably bound while occupying only a fraction of the interface. If exclusively repulsive forces stabilized the lattice, NPs would spread apart from each other as far as possible within the confinement of the interface, thereby leading to larger lattice constants than those measured experimentally.



## Conclusions

In this study, we found that strong correlations between charged NPs and counterions in electrolyte solutions can lead to novel transport and assembly behavior. Our MD simulations show that interfacial transport of NPs at liquid interfaces is mediated by counterion condensation onto the portion of the charged NP exposed to the organic phase. Experiments do show that the NPs, upon transport across the interface, become charge-reversed and form a nearly close-packed 2D array on the organic side of the interface, whose spacing can be tuned by varying the voltage.

When condensation of organic counterions onto highly charged NPs takes place at an aqueous–organic interface, the charge of the NP is shielded as it is drawn across the interface into the low polarity organic environment. In combination with water-borne transport of NPs [233], this route into organic phases adds to the possible pathways along which charged NPs, both synthetic and natural, can be transported through complex heterogeneous environments consisting of aqueous and organic regions that exist within biological organisms and the natural environment. The experiments also show that electrical control over interfacial transport leads to voltage-tunable self-assembly of NPs at the interface. Fine-tuning chemical and electrostatic interactions on both sides of the interface may ultimately lead to control over the location of charged NPs within the interfacial region, thereby providing new possibilities to control interactions with aqueous and organic components for purposes such as multiphase trace analyte detection [234]. NP arrays self-assembled at liquid interfaces are applicable to the development of electrovariable optical devices [235], plasmonics [236,237], and active elements controlling molecular transport across liquid interfaces.



### 3.4 Stabilization and Self-assembly of Nanoparticles in Lipid Bilayers

Adapted from Ref. [10], a submitted manuscript.

In this work, we performed coarse-grained molecular dynamics simulations to study the inclusion of alkanethiol-ligated gold nanoparticles, and their stabilization inside lipid bilayers. All the simulations in this study were performed by me.

#### Introduction

In biology, many functional superstructures are self-assembled from lipids, proteins, and other molecules [238]. Natural self-assembly processes have inspired the fabrication of materials from nanoscale components [239]. The self-assembly of versatile inorganic building units, such as nanoparticles (NPs) or graphene, offers a direct way to form complex nanostructures [240]. The integration of bio-molecules and inorganic nanostructures can extend the functionality of both systems [241,242].

NPs can be adsorbed onto, translocate through, or be embedded within bilayer membranes, depending on their sizes, shapes, and surface properties [243–245]. The organization of NPs can be guided by fluid membranes [246]. Embedding NPs into membrane bilayers can change their permeability [247,248], phase transition points [249,250], and mechanical responses [251]. Careful design of symbiotic biohybrid systems requires good understanding of the complex interactions acting between the individual sub-systems.

Gold NPs (diameter of  $d \approx 3.7$  nm) coated with alternating anionic and hydrophobic groups translocate through lipid membranes without breaking them down [141, 142, 246, 252, 253]. Small hydrophobic gold NPs ( $d \approx 2 - 4$  nm) have also been embedded inside lipid bilayers [254–257]. Here, we model the conditions under which clusters of hydrophobic NPs may enter and stabilize inside lipid

bilayers. This work expands our studies of micelle-lipid interactions [258] and NP membranes, related to their mechanical properties [3], molecular filtration [4], and self-assembly at liquid interfaces [5].

### Modeling of NP-lipid layered systems

To cover a long-range dynamics, we describe the NP-lipid systems using a coarse-grained molecular dynamics (CGMD) simulations [259]. In the model, roughly every four non-hydrogen atoms are represented by a CG bead. The bonded and non-bonded interactions between CG beads are parameterized using the MARTINI 2.0 force field [196]. The van der Waals (vdW) interactions are described by the Lennard-Jones potential,

$$V_{vdW}(r) = 4\epsilon \left\{ \left( \frac{\sigma}{r} \right)^{12} - \left( \frac{\sigma}{r} \right)^6 \right\}. \quad (3.6)$$

where  $\sigma$  is the effective minimum distance between two beads and  $\epsilon$  is the strength of their interaction.

The gold NP core ( $d = 1.4$  nm) is formed by 55 SC<sub>4</sub>-type beads arranged into a cuboctahedral shape of a *fcc* structure. The bonding distance between these beads is 4.08 Å, which is the lattice constant of gold. The gold core structure is maintained by a high bond strength (15 kcal/mol/Å<sup>2</sup>) and rigid SC<sub>4</sub>-SC<sub>4</sub>-SC<sub>4</sub> angles (60°, 2.988 kcal/mol/rad<sup>2</sup>). In a similar way, nanorods (NR) and triangular nanodiscs (ND) are modeled using SC<sub>4</sub>-type beads arranged into a *hcp* structure. Dodecanethiol ligands are attached onto all (42) SC<sub>4</sub>-type beads that are on the NP surface. Each ligand is represented as a linear chain of 3 apolar C<sub>1</sub>S-type beads, with force field parameters based on C<sub>1</sub>-type beads (tails of lipid molecules). The coupling strength between NPs is controlled by the vdW strength of C<sub>1</sub>S-C<sub>1</sub>S interactions, neglecting a direct vdW coupling between the NP cores [188,189].

The model lipid bilayer is formed by 1-palmitoyl-2-oleoyl-sn-glycero-3-phosphocholine (POPC) molecules. The amine head groups, phosphate head groups, and hydrophobic tails of the POPC

molecules are described by  $Q_0$ -type,  $Q_a$ -type, and  $C_1$ -type beads, respectively. the lipid bilayer is solvated in CG water ( $P_4$ -type beads), with one anti-freeze molecule ( $BP_4$ -type bead) added to every 9 CG water beads. This is done to prevent the undesirable crystallization of water at 310 K due to the simplified description of water molecules [196].  $BP_4$ -type beads are slightly modified  $P_4$ -type beads with  $\sigma = 5.7 \text{ \AA}$  for the  $BP_4$ - $P_4$  vdW interaction.

Our CGMD simulations were performed with NAMD [175, 196, 199, 260] in an NPT ensemble. A pressure of  $P = 1 \text{ atm}$  was maintained by the Langevin Piston method [261], with a decay period of 200 fs, a damping time of 50 fs, and a timestep of  $t = 20 \text{ fs}$ . The system was maintained at a temperature of  $T = 310 \text{ K}$  by a Langevin thermostat with a damping coefficient of  $1 \text{ ps}^{-1}$ .

### Insertion of NPs into lipid bilayers

First, we studied the insertion of individual NPs into the lipid bilayer. Small NPs with hydrophobic ligands can intercalate within lipid bilayers due to a favorable coupling between their ligands and lipid tails [262]. Initially, a  $13 \times 13 \text{ nm}^2$  POPC bilayer is equilibrated in water with a zero membrane surface tension [240]. The equilibrated bilayer has an approximated thickness of  $h_{mem} \approx 5 \text{ nm}$ , and a lipid density of  $d_{mem} \approx 2 \text{ lipids/nm}^2$ . One NP saturated with dodecanethiol ligands and covered by different number of solvation lipid molecules is placed in water, about  $0.1 - 0.2 \text{ nm}$  away from the POPC bilayer. We quantify the lipid coverage of the NP by a ratio defined as  $R_c = N_{lip}/N_{lig}$ , where  $N_{lip}$  is the number of solvation lipid molecules around the NP, and  $N_{lig} = 42$  is the number of NP ligands.

Figure 14 (a-d) shows an inclusion process of NP with a high lipid coverage ( $R_c = 2.6$ ). Right before the inclusion takes place ( $t = 0 \text{ ns}$ ), the NP with solvation lipids is in a close contact with the surface of the POPC bilayer, due to dipole-dipole coupling between oppositely oriented head groups

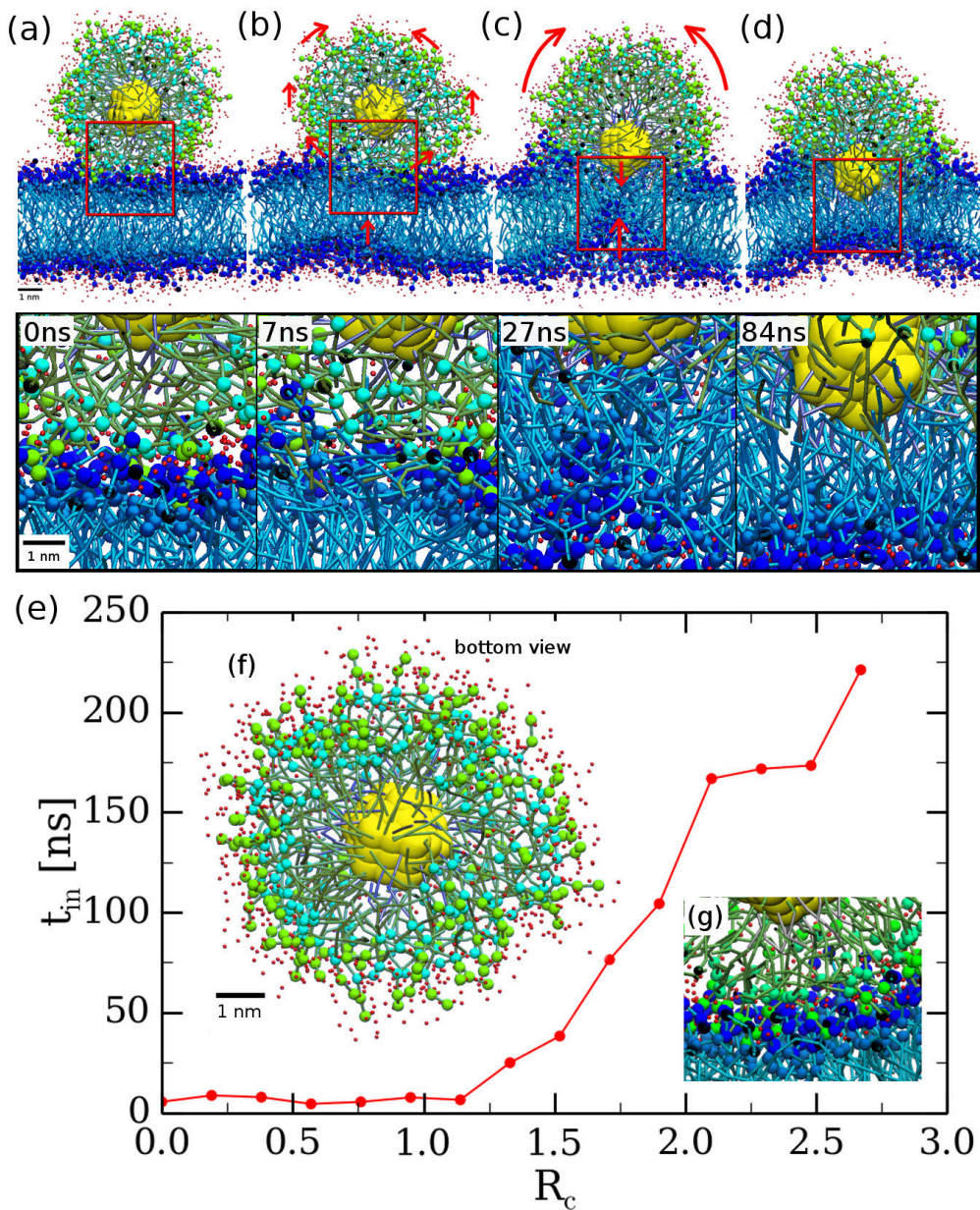


Figure 14: (a-d) Snapshots and close-up views of the first 84 ns of a NP inclusion process. The arrows indicate movements of the NP and lipid molecules. Initially, the NP is covered with 112 solvation lipids ( $R_c = 2.6$ ) which are colored in green to distinguish them from those of the bilayer. Nearby water molecules are shown in red. (e) The inclusion time of NP with different coverages of solvation lipids. (f) A bottom view of the NP at  $t = 7$  ns, which shows an opening of the structure due to bottom-to-top motion of lipid molecules. (g) A close-up view of the stable contact between polar head groups of the structure and those of the bilayer. This NP is solvated by 126 lipid molecules ( $R_c = 3.0$ ), and it does not penetrate the bilayer within our simulation time.

(positive amine, negative phosphate) of lipid molecules in the two sub-systems. This behavior is also observed at  $R_c > 3$ , where the NP, however, does not enter the bilayer (Figure 14 (g)). In the next  $t = 7$  ns, solvation lipid molecules gradually accumulate in the top region of the NP to cover all the NP ligands exposed to water. The bottom-to-top motion of solvation lipid molecules release lipids below the NP from both the NP and bilayer (Figure 14 (f)). At  $t = 27$  ns, a large enough hole is formed in the top leaflet of the bilayer, through which the NP enters into the membrane. During this process, the NP interacts with lipid tails of the bottom leaflet, creating a distinct funnel shape structure [240] (Figure 14 (c)). At  $t = 84$  ns, the funnel structure starts to disappear but the stabilization of NP within these asymmetrical lipid layers can take another  $\approx 100$  ns. The flip-flop motions of lipids between the top and bottom leaflets of the bilayer are not considered in our simulations, but they are expected to restore the symmetry of the bilayer.

We define a NP insertion time,  $t_{in}$ , as the time difference between the NP penetration of the top leaflet to its full stabilization within the bilayer. Figure 14 (e) shows that NPs with a higher lipid coverage have a larger  $t_{in}$ . When the lipid coverage is relatively low ( $R_c \leq 1$ ), the insertion time is constant,  $t_{in} \approx 6.5$  ns. Then, the NP insertion involves an abrupt penetration of the top bilayer leaflet. When  $R_c > 1$ , the insertion mechanism follows the previously described complex motion of lipids. The growth of  $t_{in}$  with  $R_c$  is caused by the increasing density of lipids on the NP surface and the related inability of the NP to suck lipids from the top leaf of the membrane. In our simulations, we do not see any NP insertions beyond  $R_c > 3$ .

### **Nanoparticles self-assembly inside bilayers**

The equilibrium arrangement of NPs within the lipid bilayer depends on the NP-NP, NP-lipid, and lipid-lipid coupling strengths. To examine this dependence, we model systems with a variable NP-NP coupling strength, while keeping the other coupling strengths fixed. We parametrize the

relative coupling strengths by a factor  $\alpha = \epsilon_1/\epsilon_0$ , where  $\epsilon_1$  is the C<sub>1</sub>S-C<sub>1</sub>S vdW (NP-NP) coupling strength and  $\epsilon_0$  is the initial (fixed) strength of C<sub>1</sub>S-C<sub>1</sub> and C<sub>1</sub>-C<sub>1</sub> vdW (NP-lipid, lipid-lipid) couplings (Equation 3.6).

We examined the stabilization of a 13 NP-cluster with  $\alpha = 0.5, 1.0$  and  $1.5$  inside a micelle and a lipid bilayer. The micelle can be used as a nanocarrier to deliver the NPs into the bilayer. For  $\alpha = 1, 1.5$  the NP-cluster remains compact within the micelle. However, for  $\alpha = 0.5$  the lipid-covered NP-cluster (micelle) reorganizes into a vesicle by sucking lipids from the outside to the inside, as shown in Figure 15 (a). This structure is more stable since it maximizes the relatively strong coupling between NP ligands and lipid tails. Its hydrophilic interior cavity also contains a few water molecules. The equilibrated structure looks similar to Janus-NP vesicles, observed experimentally [262].

In Figure 15 (b-d), we show the stabilization of a 13 NP-cluster within a lipid bilayer. When  $\alpha = 0.5$  and  $1.0$ , the cluster is flattened into a monolayer. However, the cluster stays compact only for  $\alpha = 1$ , while for  $\alpha = 0.5$  the NPs diffuse away one from another. For  $\alpha = 1.5$ , NPs which were initially scattered within the bilayer aggregate into a single globular cluster. To better understand this behavior, we simulate within the lipid bilayer 4 (tetrahedron), 5 (trigonal bipyramid), and 6 (octahedron) NP-clusters with  $\alpha = 0.5 - 2.4$ . We calculate the average height of a submerged and equilibrated NP-cluster,  $h_C$ , by subtracting the  $z$ -coordinate of the top-most and bottom-most SC<sub>4</sub> beads. Figure 15 (e) gives the result of  $h_C$  averaged over the last 75 ns of the  $t \approx 250$  ns simulations. NPs in larger clusters (5, 6 NPs) have more contact points with each other, which leads to stronger clusters that flatten only at small  $\alpha$ . Similar to the 13 NP-clusters, presented in Figure 15 (b-d), all these clusters flatten at  $\alpha \leq 1$  to a monolayer with a closed packed hexagonal arrangement, shown in Figure 15 (f) for 48 NPs and  $\alpha = 1$ .



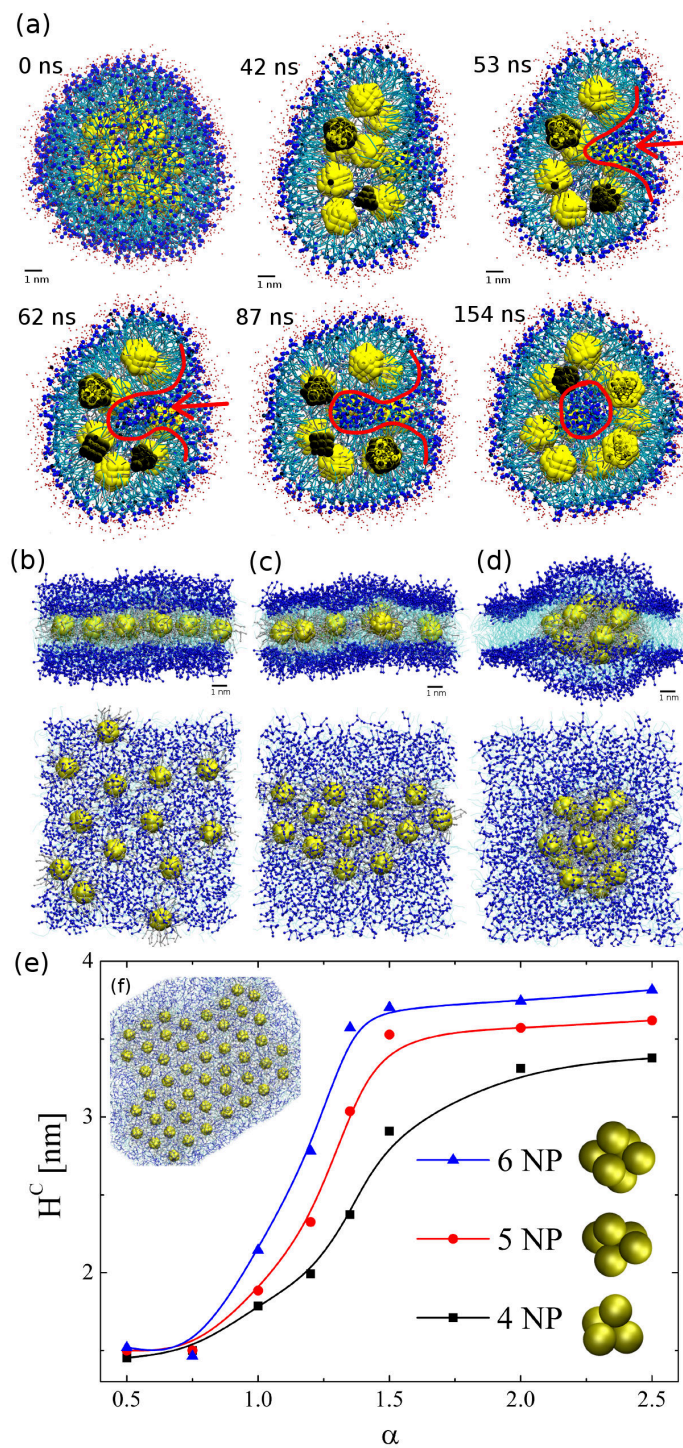


Figure 15: (a) Reorganization of lipid molecules in a vesicle carrying 13 NPs with  $\alpha = 0.5$ . (b-d) Stabilization of 13 NPs within a lipid bilayer: (b)  $\alpha = 0.5$  after 125 ns, (c)  $\alpha = 1.0$  after 814 ns, (d)  $\alpha = 1.5$  after 359 ns. (e) The height of small NP-clusters,  $h_C(\alpha)$ . (f) Hexagonal arrangement of 48 hydrophobic NPs with  $\alpha = 1$  equilibrated in the lipid bilayer for 500 ns.

Figure 15 can be clearly understood if we take into account that bilayer membranes are stabilized through a balance of positive and negative lateral tensions, generated by different molecular groups present at different heights [263, 264]. In equilibrium, the net lateral tension is close to zero. Once the membrane is deformed by adding a NP-cluster in its interior, the balance is changed and local tensions are formed in its two monolayers by the exposure of hydrophobic groups of the curved layers [265]. This tension generates a net vertical force on the inserted NP-cluster, which tends to flatten it and determines its equilibrium height,  $h_C$ .

### **Intercalation of nanorods and nanodiscs**

The self-assembly of many other types of nanoparticles has been studied [7, 189, 266, 267]. Here, we briefly examine the stabilization of nanodiscs (NDs) and nanorods (NRs) clusters with  $\alpha = 1$  inside the POPC bilayer. The large triangular ND has a side length of  $d \approx 7.2$  nm and a thickness of  $h \approx 0.6$  nm, while the small hexagonal ND has a diameter of  $d \approx 3.2$  nm and a thickness of  $h \approx 0.4$  nm. The NR has a diameter of  $d_{NR} \approx 1.4$  nm and a length of  $l_{NR} \approx 4.57$  nm. Similar  $\text{Gd}_2\text{O}_3$  nanoplates have been prepared experimentally [268].

First, we studied the self-assembly of small NDs inside a  $\approx 29.2 \times 29.2$  nm<sup>2</sup> POPC bilayer (Figure 16 (c-d)). These NDs are small enough to orient vertically or horizontally within the bilayer, which results in their non-uniform self-assembly. As seen in the figure marked by arrows, the lipid molecules wrap around any vacancy of the NP structure, forming funnel-shaped structures similar to those shown in Figure 14 (c) and Figure 15 (a) at  $t = 53$  ns. These structures on the two sides of the bilayer sometimes connect and form a channel. Although this is not observed for structure formed by 5 large triangular NDs (Figure 16 (a-b)), 6 of such NDs assembled into a pie structure leads to the formation of a relatively stable channel in the center after  $t \approx 85$  ns of equilibration (Figure 16



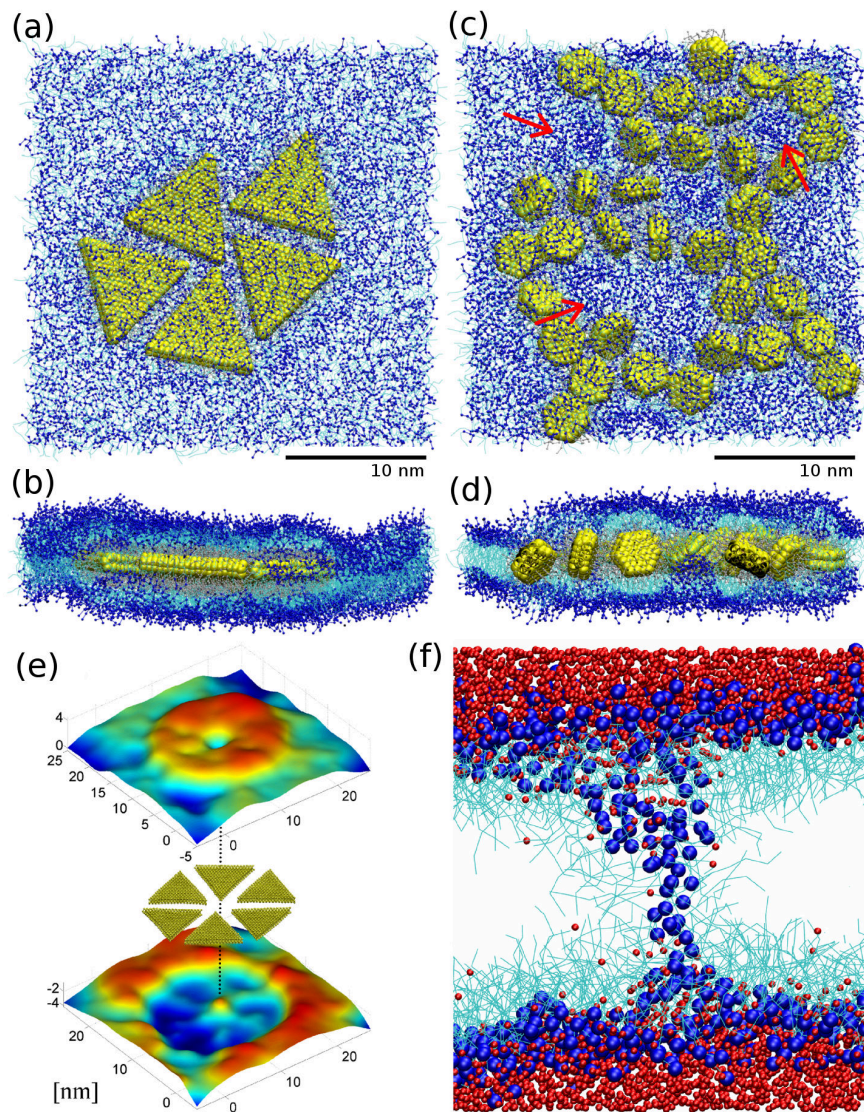


Figure 16: Stabilization of ND clusters with  $\alpha = 1$  inside a POPC bilayer. (a) Top view and (b) side view of a 5-large-triangular-ND cluster inside POPC bilayer. (c) Top view and (d) side view of 35 small NDs inside POPC bilayer. The arrows indicate some of the lipid pore formations induced by the NDs. (e) 6-large-triangular-ND cluster inside POPC bilayer. A color map surface is fitted to the polar heads of the lipid molecules to show the bilayer structure. (f) Side view of the central portion of the 6-large-triangular-ND cluster, showing few water molecules penetrated the perturbed bilayer.

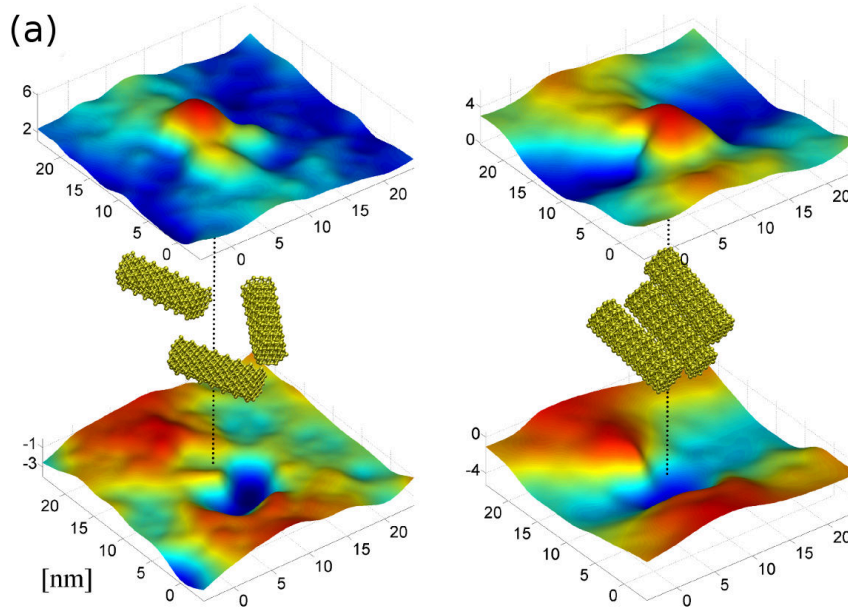


Figure 17: (a) Orientation of 3-NR cluster embedded inside the POPC bilayer. 3D surfaces are fitted to the polar heads of the lipids. (left)  $\alpha = 0.75$ , the NRs perturb the bilayer by  $< 2$  nm along the z-direction. (right)  $\alpha = 2$ , the tightly packed NR-cluster perturbs the bilayer by  $\approx 3 - 4$  nm.

(e-f)). This channel has polar groups arranged in a cylindrical fashion around its vertical axis, and it could facilitate transport of water and other solvated compounds through the membrane.

We have also studied the stabilization of a 3 NR-cluster inside a lipid bilayer. At  $\alpha > 2$ , the NR-cluster is tightly packed, where the NRs are aligned along each other. At weaker coupling,  $1 < \alpha < 2$ , the NRs start to slide along each other with their axes staying aligned. At even smaller values  $\alpha < 1$ , the NR-cluster becomes disintegrated, the NRs are separated from each other and eventually might diffuse within the membrane interior. Similar to the case of NPs, disintegration of the cluster is caused by the surface tension induced by a bent bilayer. In Figure 17 (a), we show 3D profiles of a weak ( $\alpha = 0.75$ ) and strong ( $\alpha = 2.0$ ) NR-clusters intercalated within a bilayer. In both cases, the NRs lead to membrane perturbations in the direction normal to the bilayer. The perturbed regions are localized about  $\approx 2 - 3$  nm and  $\approx 3 - 4$  nm around the NRs, respectively, for the two cases. The

anisotropy in the  $x - y$  directions is caused by the tilted orientation of the NR-cluster. Notice that even separated NRs stay tilted inside the bilayer.

## **Conclusions**

In summary, we have investigated the insertion of one NP and stabilization of NP clusters of different shapes inside lipid bilayers. The cluster structures formed inside the bilayer reflect the coupling strength between NPs. When the coupling strength is large enough to resist the membrane forces, the clusters are preserved, while in the opposite limit they are partially or fully disassembled.

### 3.5 Self-assembly of Platinum Nanocubes into Superlattices

Adapted from Ref. [6] (*ACS Nano* 2012, 6 (5), 4203–4213. DOI: 10.1021/nm3007338) with the permission from The American Chemical Society.

This study was performed in collaboration with Dr. Arnaud Demortière from Argonne National Laboratory. The main goal of this theoretical work is to examine the microscopic principles that control the self-assembly of colloidal octylamine-coated platinum nanocubes (NCs) into simple cubic (*sc*) and *fcc* superlattices, using mean-field and energy calculations from atomistic models. All the theoretical work including the analysis of supercrystal growth were performed by our group. Mean-field calculations of bulk van der Waals (vdW) coupling energy in different superlattices were performed by Lela Vuković, graduate student of Prof. Petr Král. Atomistic modeling and calculations of electric and surface vdW coupling energies between two nanocubes were performed by me. All the experiments were performed by our collaborators.

#### Introduction

In recent years, colloidal nanoparticles (NP) of different materials [269–272], sizes [273], shapes [90, 96, 166, 274–281], and coatings [77, 139, 187, 282] have been self-assembled into superlattices with many types of packing [138, 283, 284]. In most cases, the formations of superlattices are thermodynamically driven and are controlled by inter-particle forces which depend on the types of NPs [44], solvent molecules [285], substrates [63], and other experimental conditions [108, 159, 286]. The microscopic principles that govern the self-assembly of different superstructures of specific structural [287], chemical [288, 289], and physical properties [190, 290] are not well understood [281] but they are crucial for the preparation of meta-materials with functionalities in electronics [291], optics [292, 293], magnetism [294], and catalysis [89, 295].

Superlattices formed from non-spherical NPs extend beyond common face-centered cubic (*fcc*) and hexagonal close packing (*hcp*) structures observed for spherical NPs, or simple hexagonal (*sh*) and body-centered cubic (*bcc*) structures observed for NPs with anisotropic forces originating from electric/magnetic dipole-dipole coupling [188,189]. For example, polyhedral nanocrystals can self-assemble into open superlattices such as cubic and octahedral supercrystals [96,166,277–281,296]. Due to the different crystalline facets present on non-spherical NPs, their superlattices can have a wide range of packing densities and intriguing geometries of void spaces, which all can drastically influence the properties of their superlattices [297].

### Superlattices observed in experiments

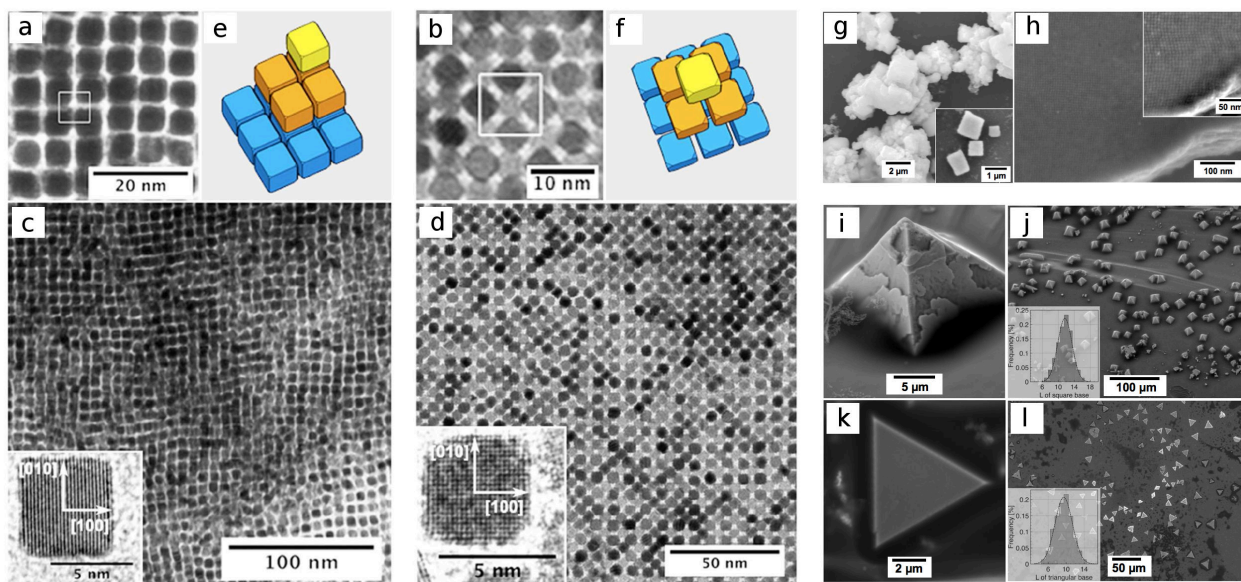


Figure 18: Experimentally observed superstructures of self-assembled regular (RCs) and truncated (TCs) colloidal octylamine-coated platinum nanocubes in toluene. (a, b) square array of RCs and TCs, (c, d) scheme of the simple cubic structure and fcc structure, (e, f) multilayer of organized RCs and TCs, (inset) TEM image of a RC and TCs. (g) SEM images of stacked sc supercrystals of RCs. (inset) Individual RC supercrystals. (h) SEM-FEG images of a RC supercrystal. (inset) Magnified SEM image showing the arrangement of RCs within the supercrystal. (i-l) SEM images of fcc supercrystals of TCs. (i) Superlattice of square pyramidal shape. (j) Ensemble of square pyramidal supercrystals and their size distributions (inset). (k) Superlattice of triangular prism shape. (l) Triangular prism supercrystals and their size distribution (inset).



Platinum NCs coated with octylamine ligands [298] were prepared in toluene using a liquid-liquid phase transfer method [279, 299]. These NCs formed uniform superlattices with long-range ordering when the toluene solvent ( $bp = 110^\circ\text{C}$ ) was slowly evaporated over a period of 8 days at  $25^\circ\text{C}$ , controlled by limiting the air/solution interface in a glass tube. TEM images (Figure 18 a-d) reveal two types of superlattices formed by NCs with only a small difference in shape. Regular NCs (RCs) with face-to-face length of  $l_{RC} = 5.5$  (8% polydispersity) form simple cubic ( $sc$ ) superlattices whereas corner truncated NCs (TCs) with  $l_{TC} = 4.7$  nm (9% polydispersity) form face center cubic ( $fcc$ ) superlattices. RCs are positioned in face-to-face ( $f - f$ ) configuration in  $sc$  superlattices with AAA stacking whereas TCs are positioned in shifted corner-to-corner ( $c - c$ ) configuration in  $fcc$  superlattices (Figure 18 b) with ABCABC stacking such that each successive layer is shifted by half the repetition distance. The lattice constant of the observed  $sc$  and  $fcc$  superlattices were  $a_{sc} \approx 7$  nm and  $a_{fcc} \approx 11$  nm measured using TEM with a carbon-coated grid, and  $A_{sc} \approx 8$  nm and  $A_{fcc} \approx 11$  nm measured using selected area electron diffraction (self-assemblyED) at 250 cm with a silicon wafer.

$sc$  structures have been observed in Po crystals [300] and  $\text{TiO}_2\text{-P}_2\text{O}_5$  NC supercrystals [301] but they are rare in Nature. Yamamuro *et al.* have shown that face-to-face assembly ( $sc$  structures) is the most stable configuration for RCs, based on evaluations of the vdW (ligand) potential energy of model NCs in different 2D [302] and 3D stacking [303]. Although this is in agreement with the experimental observations in Demortière's laboratory, it is still not clear how small modification of the NC shape can lead to the formation of a loose  $fcc$  structure. In the following sections, we will first analyze the NC self-assembly process and the forces that can lead to stabilization of their superstructures, and then provide an explanation based on modeling results.

## Analysis of the supercrystal growth

### *a) Supercrystal nucleation*

Spontaneous formation of seeds needed for the growth of colloidal NC supercrystals can take place homogeneously in solution or heterogeneously on a substrate [304]. The strength of inter-particle interactions, solvent evaporation rate, NC-substrate interfacial properties, and other factors can all influence the energy barrier,  $\Delta G_N$ , associated with the nucleation process. Since in general  $\Delta G_N^{homo} > \Delta G_N^{hetero}$ , it is likely that only *sc* superlattices which have strong vdW interactions between  $\{100\}$  faces of RCs can overcome the energy barrier and nucleate in solution. Loose *fcc* superlattices which are stabilized by much weaker corner-to-corner interactions of the TCs should only nucleate on a substrate.

In Figure 18 g, one can see that *sc* supercrystals are randomly positioned on the substrate, which indicates that the crystallite seeds were homogeneously formed in solution and subsequently attached to the substrate where they continue to grow. Consequently, their diffraction patterns reveal only homogeneous rings and small angle x-ray diffraction (self-assembly-XRD) pattern indicates an absence of a single-growth axis [279]. On the other hand, *fcc* crystallite seeds can grow into supercrystals of different morphologies depending on their relative orientation with respect to the substrate. For example, initial square arrangement of the  $\{100\}_{sp}$  basic plane yields a pyramidal *fcc* crystal, whereas a hexagonal layer with  $\{111\}_{sp}$  basic plane yields a triangular *fcc* crystal (no  $C_3$  symmetry due to NCs in the lattice points). This is all confirmed by previous self-assembly-XRD observations, which reveal the  $[001]_{sp}$  growth axis (perpendicular to the substrate) for the pyramidal supercrystals and the  $[111]_{sp}$  growth axis for the triangular supercrystals [279].

### *b) Deliberation of the NC coupling forces*

Superlattices that are nucleated in solution or on a substrate are further stabilized during the evaporation of solvent, leading to differences in the NC-binding Gibbs free energy,  $\Delta G = \Delta H - T\Delta S$ , in *solvent* (colloidal phase) and in *vacuum* (dried phase). In solution, one of the dominant contributions to this energy is the energy of dispersion forces between NC cores (bulk vdW coupling),  $\Delta H_{core}^{vdW}$ , which arise from the large polarizabilities of metal NC cores at room temperature [159, 305]. Since Pt NC cores are much more polarizable than toluene solvent molecules and the octylamine ligands on the NCs, the strength of vdW coupling (per unit volume) ranks as core-core > core-ligand > ligand-ligand  $\approx$  ligand-solvent. Hence, when the solvent and ligands are chemically similar, we can neglect the ligand-ligand vdW coupling and consider only the core-core vdW coupling [188, 189].

The vdW coupling associated with different densities of ligands between neighboring NC corners [287] is unlikely to create a local minima in  $\Delta G$  necessary for the stabilization of shifted corner-to-corner configuration in loose *fcc* superlattices. The stabilization of such configuration might require *directional forces* such as multipolar Coulombic coupling. These forces can originate from a partial charge transfer between ligands and the Pt NC-cores [306], where electrons in the vicinity of Pt atoms of the ligand binding sites can be transferred to the more electronegative N atoms of octylamine ligands (Figure 20 b). Inside the metal NC cores, charges can freely redistribute and locally charge the NC, as schematically shown in Figure 20 a. The (neutral) TCs can interact with each other in toluene at relatively large distances, as characterized by  $\Delta H_{NC}^{elec}$ , and direct the self-assembly of *fcc* superlattices.

When the superlattices are in a vacuum phase after complete evaporation of solvent, the ligand-ligand vdW coupling enthalpy,  $\Delta H_{ligand}^{vdW}$ , and the related entropy,  $\Delta S_{ligand}$ , can dominate in  $\Delta G$ . The growth of  $\Delta H_{ligand}^{vdW}$  is counter-balanced by  $\Delta S_{ligand}$  as the ligands become more compact in a



limited space. This balance of coupling between ligands might stabilize the loose *fcc* superstructures pre-formed in the colloidal phase by Coulombic coupling and bulk vdW core-core coupling.

### Microscopic modeling of bulk vdW coupling between NC cores

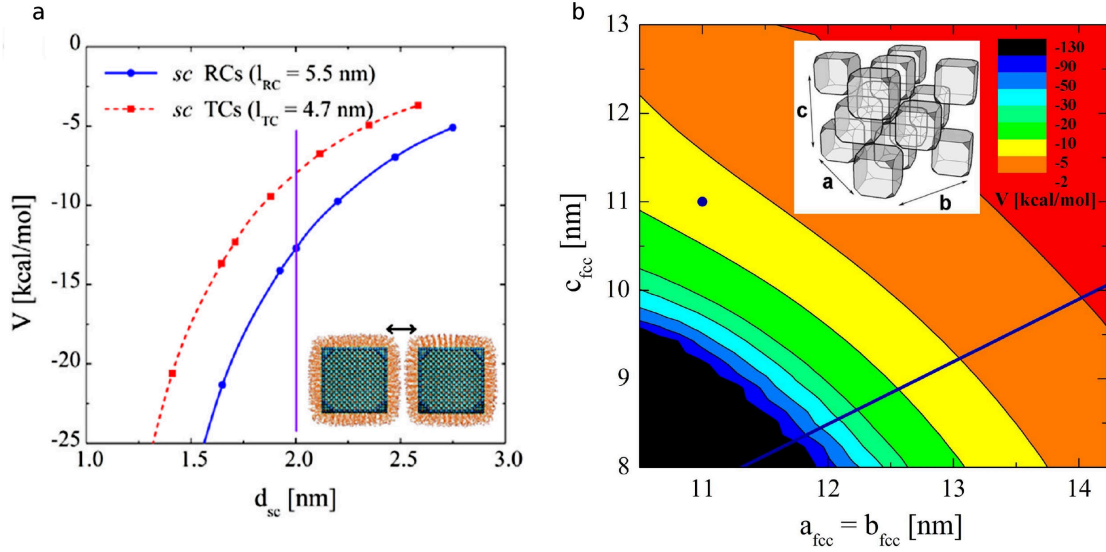


Figure 19: (a) vdW potential energy per particle for sc structures,  $V^{sc}$ , of RCs and TCs with respect to the face-to-face inter-nanocube distance,  $d_{sc}$ . The vertical line marks the experimentally observed  $d_{sc}$  for RCs in the sc superlattice. (b) vdW potential energy per particle for fcc structures,  $V_{fcc}$ , of TCs with respect to the parameters  $a_{fcc} = b_{fcc}$  and  $c_{fcc}$ . The line ( $a_{fcc} = b_{fcc} = \sqrt{2}c_{fcc}$ ) represents parameters for which the TCs have aligned corner facets.

The potential energy of vdW couplings between two NC cores (*i*th and *j*th) can be approximated by a pairwise Hamaker summation [174,189],

$$V = V_{core}^{vdW}(ij) = -\frac{A}{\pi^2} \int_{V_i} \int_{V_j} \frac{1}{r_{ij}^6} d\vec{r}_i d\vec{r}_j. \quad (3.7)$$

where,  $A$  is the Hamaker constant which depends on the type of NC core and  $r_{ij}$  is the distance between atoms (microscopic elements) of the two NC cores.

Since vdW couplings have a  $1/r^6$  distance dependence (fast decay), the vdW potential energy per NC core of *sc* or *fcc* superlattices can be obtained by all interactions between NCs and their first neighbors,

$$V^{sc} = \frac{1}{2} (6 V_{f-f} + 12 V_{e-e} + 8 V_{dc-dc}) , \quad (3.8)$$

where the subscripts in  $V$  indicate face-to-face ( $f-f$ ), edge-to-edge ( $e-e$ ), and aligned corner-to-corner ( $dc-dc$ ) NC coupling terms.

$$V^{fcc} = \frac{1}{2} (4 V_{f-f} + 4 V_{e-e} + 8 V_{c-c}) , \quad (3.9)$$

where the subscripts indicate intra-layer face-to-face ( $f-f$ ), intra-layer edge-to-edge ( $e-e$ ), and inter-layer shifted corner-to-corner ( $c-c$ ) NC coupling terms with the layers defined in the inset of Figure 19 b; the subscript  $dc-dc$  is replaced by  $c-c$  because the corner facets of TCs in *fcc* superlattices are not aligned.

Calculations of  $V^{sc}$  of varying inter-NC distances and  $V^{fcc}$  of varying intra-layer ( $a_{fcc}$ ,  $b_{fcc}$ ) and inter-layer ( $c_{fcc}$ ) distances were performed using the averaged experimental face-to-face lengths of  $l_{RC} = 5.5$  nm and  $l_{TC} = 4.7$  nm with  $\{111\}$  corner facets characterized by the experimental corner truncation  $\alpha = 0.85$  nm, measured along the NC edge. The Hamaker constant for Pt-Pt coupling (through octylamine ligands) was approximated by value of gold-gold coupling (through dodecanethiol),  $A \approx 2$  eV [307]. We consider  $a_{fcc} = b_{fcc}$  due to the  $C_4$  symmetry of *fcc* superlattices. The intra-layer distances of *fcc* superlattices are larger than *sc* superlattice but their inter-layer distances are smaller due to the ABCABC stacking pattern.

The results of  $V^{sc}$  (Figure 19 a) show that it is always smaller (more favorable) for RCs than TCs irrespective of the inter-NC distance. At the inter-NC distance of RCs in *sc* superlattices observed

in experiments (vertical line in Figure 19 a d),  $V_{RC}^{sc} = -13.1$  kcal/mol and  $V_{TC}^{sc} = -7.5$  kcal/mol. The difference is caused by different sizes of the NCs and the presence of small truncations in TCs.

Energy contour map of  $V^{fcc}$  (Figure 19 b) shows that  $V_{TC}^{fcc} = -6.7$  kcal/mol at the configuration ( $a_{fcc} = b_{fcc} = c_{fcc} = 11$  nm) observed in experiments. In this shifted corner-to-corner configuration, neighboring TCs have a sub-nanometer inter-layer distance of  $d_{fcc} = 0.8$  nm, which can in principle stabilize the large intra-layer distances ( $a_{fcc}$  and  $b_{fcc}$ ). Such distance separations also suggest a lower ligand density on the  $\{111\}$  corner facets of TCs than their  $\{100\}$  faces. The sloped line at the bottom of the contour map marks the configurations where the corner facets of the TCs are aligned ( $a_{fcc} = b_{fcc} = \sqrt{2}c_{fcc}$ ). Our mean-field modeling of bulk vdW coupling do not give a clear “visible” local minimum at large NC separations necessary to stabilize the  $fcc$  structure. The model also cannot explain why the corner of TCs are not aligned to maximize corner-to-corner couplings. Next, we explicitly model the NC ligands by atomistic molecular dynamics (MD) simulations to address some of these issues.

### Atomistic modeling of couplings between NC ligands

#### *a) Model of the NCs*

In Figure 20 a we show our atomistic model of two TCs in the shifted corner-to-corner ( $c - c$ ) configuration. Each TC has a Pt core protected by a monolayer of octylamine ligands, with the edge length (between two opposite  $\{100\}$  faces) of  $l_{TC} = 4.704$  nm, based on the experimental value of  $l_{TC} = 4.7$  nm. The  $\{111\}$  corner facets are characterized by the corner truncation parameter of  $\alpha = 0.784$  nm, obtained by removing 3 Pt layers; it is close to the experimental value of  $\alpha = 0.85$  nm.

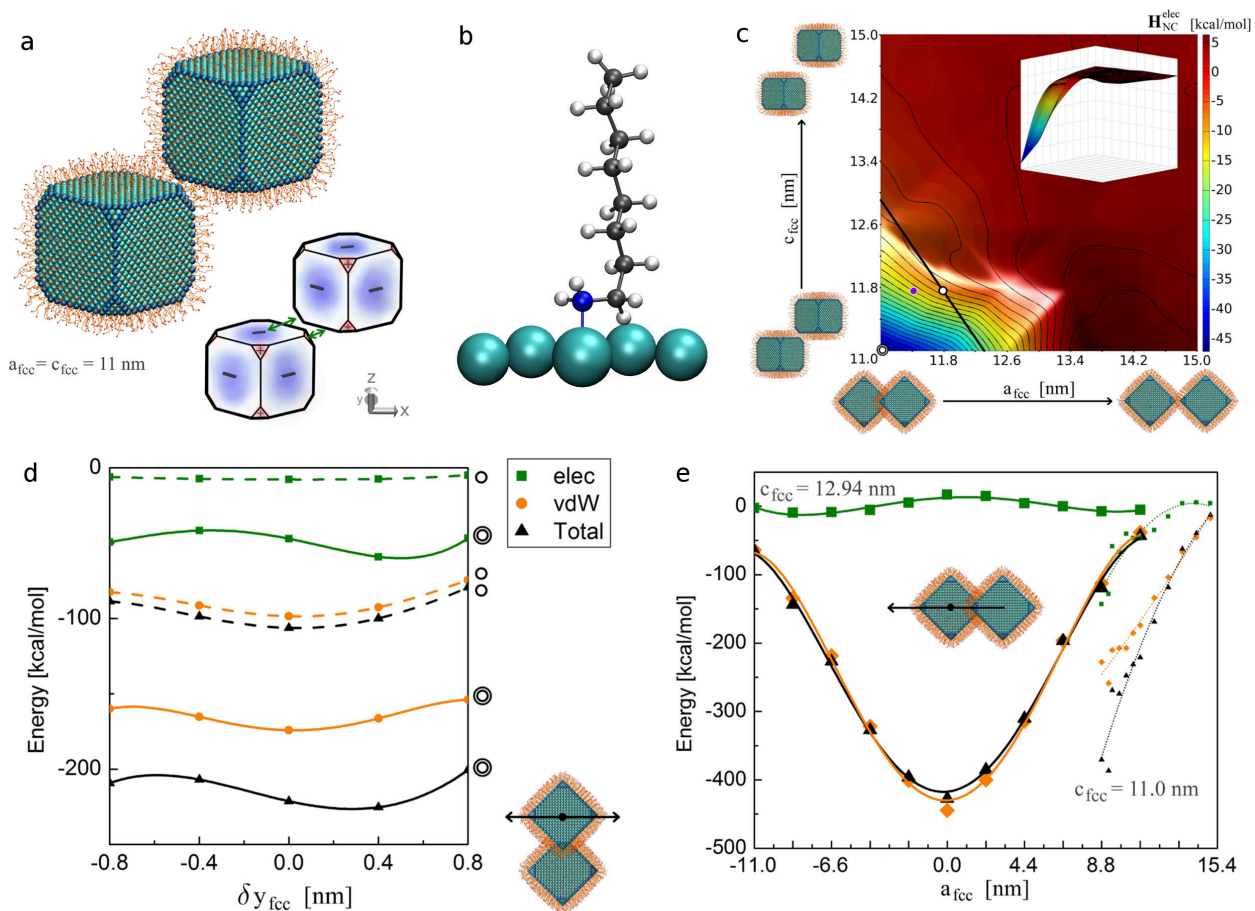


Figure 20: (a) Atomistic model of TCs in the experimentally predicted  $c$ - $c$  configuration, with H atoms hidden. The schematic drawing shows one possible charge distribution on the surface of the TCs that can stabilize the structure through the attractions shown by the arrows. (b) Model of a single octylamine ligand attached to the surface Pt atom. (c) Contour plot of the Coulombic coupling energy of TCs starting from the predicted  $c$ - $c$  configuration. The inset shows a 3D view of the energy surface. (d) Coulombic and vdW (ligand) coupling energies of TCs that are slightly shifted from the  $a_{fcc} = c_{fcc} = 11.0$  nm and  $a_{fcc} = c_{fcc} = 11.8$  nm configurations along the  $y$ -direction. The two configurations are labeled by a single-ring or double-ring icon on the right of each curve. (e) The Coulombic and vdW (ligand) coupling energies of NCs as a function of  $a_{fcc}$  are evaluated to cover the transition from the  $c$ - $c$  configuration to the  $f$ - $f$  configuration at the height of  $c_{fcc} = 12.94$  nm and  $c_{fcc} = 11.0$  nm.

In the MD simulations, we maintain the shape and rigidity of the core by Pt-Pt bonds with large bond strength of  $\approx 10^4$  kcal/mol  $\text{\AA}^2$ , added in the force field. The NC core has *fcc* packing with the lattice constant of  $a = 3.92$   $\text{\AA}$ , derived from the equilibrium Pt-Pt bond length of  $b_0 = 2.77$   $\text{\AA}$ . Each TC core has 7,758 Pt atoms, where 1,494 and 24 of them are exposed on the TC  $\{100\}$  faces and  $\{111\}$  facets, respectively, excluding the 180 Pt atoms that are on the edges.

Next, we attach octylamine ligands to the surface of the Pt core. The ligand densities and distributions cannot be observed from the TEM measurements, due to the low elemental contrast of molecular ligands. We estimate their local densities by assuming that ligands preferably bind to less coordinated Pt atoms. The coordination numbers for Pt atoms on the  $\{100\}$  faces, edges between two  $\{100\}$  faces,  $\{111\}$  facets, and edges around the  $\{111\}$  facets are 8, 5, 9, and 7 per atom, respectively; whereas bulk Pt atoms have the coordination number of 12. In our model, we attach 1 ligand onto each Pt atom on the edges and distribute ligands randomly and evenly on the faces with the density of 2 per 5 Pt atoms. We do not attach ligands on the small corner facets (3 Pt atoms per facet) due to the high steric hindrance between those ligands and ligands that are already attached to the edges. Even though these distributions are rather heuristic, their exact form does not seem to influence much the stability of the self-assembled TCs (see later).

Atomic charges on the (neutral) ligands are based on the CHARMM32 force field [171]. We model the Pt-N charge transfer by adding  $-0.4e$  to the Pt-bound N atoms of the ligands and  $0.4e$  to the ligand-hosting Pt atoms. The magnitude of the charge transfer is closely related to the results obtained from *ab initio* studies of  $\text{NH}_x$  species absorbed on Pt surfaces [306]. We keep the rest of the Pt atoms neutral and do not consider the (slight) charge redistribution on the metallic Pt core. If the positive charges on the Pt atoms are left to freely redistribute inside the metallic TC, they would cancel the field in its interior. Their repulsion would cause a slight shift from the area under the

ligands toward the corners and lead to the surface charge densities schematically shown in Figure 20 a. In our MD simulations, the presence of fixed Pt-N dipoles on the TC faces generates an electric field with the same multipolar symmetry but a smaller strength. When the TCs self-assemble in the *fcc* packing in the experimental system, their charge distribution might be further modified due to the rearrangement (detachment and reattachment) of ligands. Therefore, it is likely that the self-assembled structures have some tolerance with respect to the exact distribution of ligands and the core charging.

*b) Modeling of the NC coupling*

We will simulate these RCs and TCs as described in Methods. First, we search for additional local minima in  $\Delta G$  that can help to stabilize the self-assembled superstructures. As discussed above, the vdW ligand-ligand coupling should be relatively small in solvent (toluene) which is similar to the ligands. Therefore, the additional minima can potentially originate from the Coulombic coupling between the NCs.

During the MD simulations, we keep two adjacent NCs aligned and shifted with respect to each other in vacuum (to simulate a smaller number of atoms) and evaluate their corner-to-corner coupling. We mainly focus on their Coulombic coupling, which is not much affected by the lack of nonpolar solvent, while the vdW coupling is much stronger in its absence. The NCs are placed in a large cubic unit cell (20 nm in length), with periodic boundary conditions applied (NVT ensemble). This (simulation) unit cell is oriented the same way as the unit cells in the *sc* and *fcc* lattices (see Figure 18), so that  $a_{fcc}$ ,  $b_{fcc}$ , and  $c_{fcc}$  are distances along the simulation  $x$ ,  $y$ , and  $z$  axes, respectively. The centers of two adjacent NCs in the *sc* lattice are separated by the distance  $d_{NC-NC}$ , whereas those in the *fcc* lattice (inter-layer) are separated in the  $x$ ,  $y$ , and  $z$  directions by about one half of

the lattice parameters  $a_{fcc}$ ,  $b_{fcc}$ , and  $c_{fcc}$ , respectively. In the simulations, we vary some of these parameters (while fixing others) to evaluate the NC-binding energy.

In each simulation, we allow the ligands to relax while the NC-core atoms are spatially fixed. We first minimize the system energy for  $\approx 1$  ns and then equilibrate the system for  $\approx 2$  ns at the temperature of  $T = 300$  K. We use the last 1.5 ns of the simulation trajectories to evaluate the average Coulombic and vdW (ligand) coupling energy. When we optimize the binding position of the NCs, we briefly release the core atoms and run longer simulations to allow NC movements. We evaluate non-bonded (Coulombic and vdW) interactions of the TCs by pairwise summations of the coupling energies between atoms of both NCs.

We simulate the pairs of RCs and TCs by atomistic molecular dynamics simulations, using NAMD [175, 199] and the CHARMM32 force field [171]. During our simulations, we keep the temperature fixed by the Langevin dynamics with the damping constant of  $\gamma_{Lang} = 1 \text{ ps}^{-1}$ . The non-bonded interaction switching distance is set to 8 Å and the cutoff is set to 10 Å. The systems are simulated as NVT ensembles, where the Particle Mesh Ewald (PME) summation [172] is considered for the Coulombic coupling.

*The TC binding energies:*

We first calculate the Coulombic and vdW (ligand) binding energies between two adjacent TCs in the shifted corner-to-corner ( $c-c$ ) and face-to-face ( $f-f$ ) configurations. In Figure 20 c, we present the total Coulombic energy for TCs in the  $c-c$  configurations. We plot the potential energy surface as a function of the  $a_{fcc}$  and  $c_{fcc}$  parameters ( $b_{fcc}$  is not defined here), starting from the experimentally observed TC separation of  $a_{fcc} = c_{fcc} = 11.0$  nm. A 3D view of the energy surface is shown in the inset. In the studied range of the lattice parameters, the lowest value of the electrostatic energy,

$E_{elec} \approx -47.0$  kcal/mol, is obtained at the experimental TC separation,  $a_{fcc} = c_{fcc} = 11.0$  nm. If we remove the charges associated with the charge separation along the Pt-N bonds (ligand-NC), we get  $E_{elec} \approx 12.9$  kcal/mol for the same TC separation. These coupling energies are significantly larger than those found above for the bulk vdW coupling. Moreover, only the coupling between two NC neighbors is (so far) included in the energy.

If we let the ligated TCs to spontaneously stabilize their positions, we find that they go to the point of  $a_{fcc} = 11.4$  nm,  $c_{fcc} = 11.8$  nm (see point in Figure 20 c), rather than to the experimental point of  $a_{fcc} = c_{fcc} = 11.0$  nm. This is likely caused by the fact that in the experiment the ligands can migrate on the NC surfaces and be further redistributed upon the lattice formation to minimize the coupling energy [308]. The simulations of these relaxed TCs are only done for 2–3 ns to prevent their rotation. In this stabilization, both enthalpic and entropic contributions are involved in  $\Delta G$ .

To estimate the local stability of the TCs with shifted corners, we calculate the binding energy as their truncated corners “slide” on each other. In Figure 20 c, this motion goes along the straight line with the slope of  $-\sqrt{2}$ , which passes through the chosen point of  $a_{fcc} = c_{fcc} = 11.8$  nm. We evaluate  $E_{elec}$  along this line up to the point where the center of the two TC facets are at the closest distance and aligned ( $a_{fcc} = 13.8$  nm,  $c_{fcc} = 9.0$  nm). The lowest Coulombic energy along this line is  $E_{elec} \approx -21.4$  kcal/mol, which is found at the point  $a_{fcc} = 12.6$  nm and  $c_{fcc} = 10.7$  nm. This gives a small energy barrier of  $\Delta E_{elec} \approx 1.6$  kcal/mol that keeps the TC corners shifted. If we consider a free redistribution of the charges in the TCs, the energy barrier will likely be higher.

In Figure 20 d, we show the dependence of the total Coulombic and vdW energies in the TC pair, as we shift one TC with respect to the other along the  $y$ -direction. We define  $\delta y_{fcc}$  as the shift from the symmetric position. We choose two  $x$  and  $z$  positions of the TCs,  $a_{fcc} = c_{fcc} = 11.0$  nm (double ring in Figure 20 c,d) and  $a_{fcc} = c_{fcc} = 11.8$  nm (single ring in Figure 20 c,d). As discussed



earlier, the vdW energy mostly contributes to the NC stabilization after the removal of solvent (its value is then large, as seen here). We can see that for the experimental distances, the vdW energy has a minimum at  $\delta y_{fcc} = 0$ , while the Coulombic energy minimum is shifted to  $\delta y_{fcc} = 0.6$  nm. This slight asymmetry is caused by the random distribution of ligands on the TCs. At the larger separation (11.8 nm), the energy minima are already at  $\delta y_{fcc} = 0$ .

Upon the removal of the solvent, the vdW energy of the coupled ligands becomes large in the  $f - f$  configuration. The question is if the TCs stay in  $c - c$  configuration or spontaneously switch to the  $f - f$  configuration. To do so, the TCs would need to be lifted from the potential energy minimum at  $c_{fcc} = 11.8$  nm (equilibrium distance of the  $c - c$  configuration) to the elevation of  $c_{fcc} = 12.94$  nm (equilibrium distance of the  $f - f$  configuration), to be above the steric (ligand) barrier. This lifting is associated with a Coulombic barrier of  $\approx 14$  kcal/mol, which is not thermally accessible. The barrier is about 3 times larger if done from the experimentally observed height of  $c_{fcc} = 11.0$  nm. In Figure 20 e, we fix the TC height to  $c_{fcc} = 12.94$  nm, and show the Coulombic and vdW energies as the TCs slide on their faces. The variation of the Coulombic energy is very small, but the vdW energy has a deep minimum at  $a_{fcc} = 0$  nm ( $f - f$  configuration). We also show by dashed line the partial dependence of these energies calculated for the experimental TC height of  $c_{fcc} = 11$  nm (ligand repulsion prevents completion).

*Comparison of the TC and RC binding energies:*

In Figure 21, we compare the Coulombic and vdW (ligand) coupling energies of TCs (left) and RCs (right) in the  $c - c$  (top) and  $f - f$  (bottom) configurations. These energies are calculated as a function of the center-to-center distance of two (nearest) NCs with fixed cores, where  $a_{fcc} = c_{fcc}$  and  $\delta y_{fcc} = 0$ .

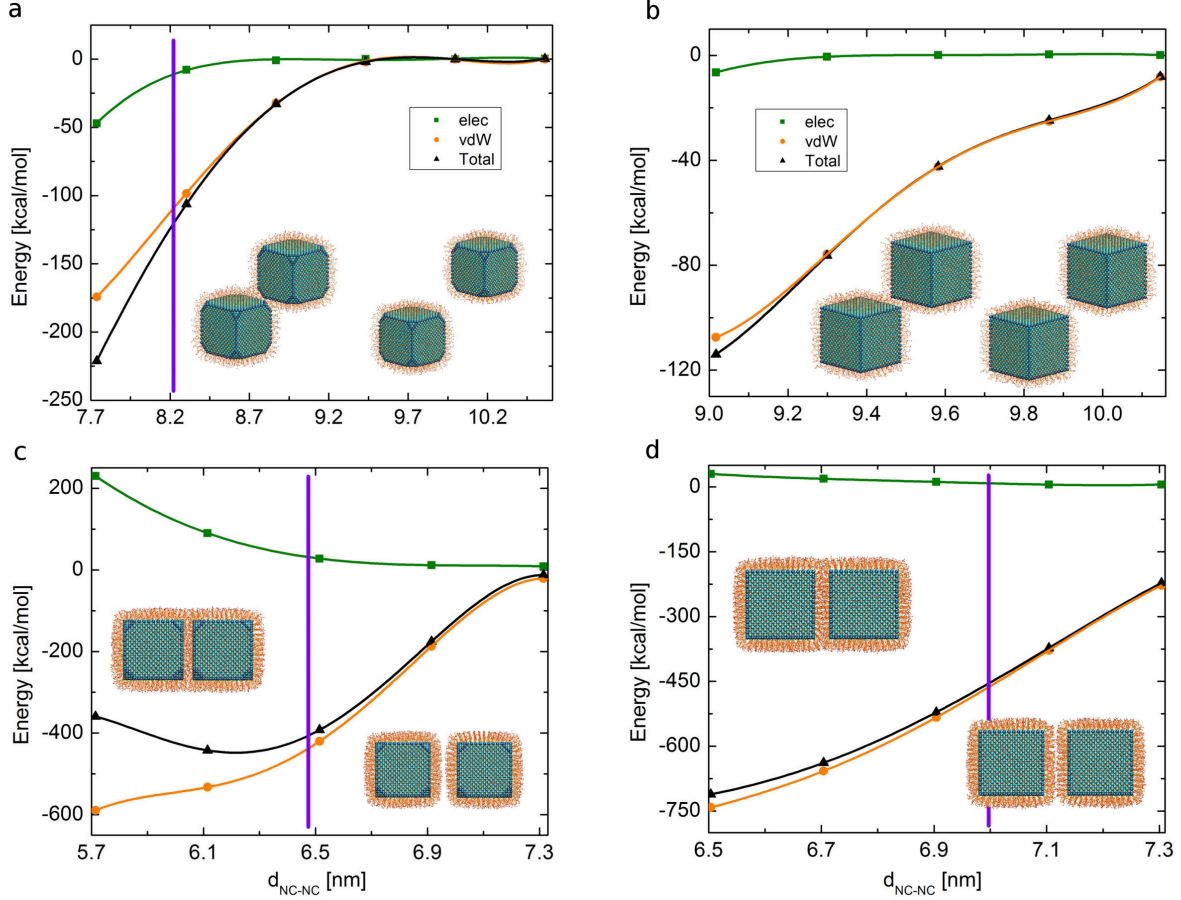


Figure 21: Coulombic and vdW (ligand) coupling energies of NCs as a function of the (interlayer) center-to-center inter-nanocube distance,  $d_{NC-NC}$ , for (a) TCs in the  $c-c$  configuration; (b) RCs in the  $c-c$  configuration; (c) TCs in the  $f-f$  configuration; (d) RCs in the  $f-f$  configuration. Schematic drawings in each plot show the configurations of the two end points. The vertical lines show the equilibrated distances of NCs with relaxed cores.

First, we consider the  $c-c$  configurations (Figure 21 a,b). If we align both the RCs and TCs in a similar way,  $d_{NC-NC}$  in TCs is by  $\approx 1$  nm smaller than in RCs, due to the smaller sizes of their cores ( $l_{TC} = 4.7$  nm and  $l_{RC} = 5.1$  nm). If the NC cores are free to move, the (relaxed) TCs tend to stabilize in the  $c-c$  configuration (the dark point in Figure 20 c at  $a_{fcc} = 11.4$  nm and  $c_{fcc} = 11.8$  nm), shown by the vertical line in Figure 21 a, while RCs continue to slide to the  $f-f$  configuration. In the  $c-c$  configuration the Coulombic coupling energy (relevant in solution) is negative and larger for TCs, while in the  $f-f$  configurations it is positive and larger for TCs (Figure 20 c,d). Both

NCs in vacuum can stabilize in the  $f-f$  configuration; their equilibrium  $d_{NC-NC}$  are shown by the vertical lines in Figure 20 c,d.

If we compare the vdW (ligand) energies in vacuum for both configurations, we can see that the  $f-f$  configuration is globally more stable for both RCs and TCs. In the solvent, the vdW coupling should be small, and the ligands might even cause repulsion between the NPs [309]. Therefore, it is the Coulombic coupling (together with the bulk vdW coupling) that can guide and stabilize the loose  $fcc$  structure of TCs.

## Conclusions

We have examined the microscopic principles governing the self-assembly of colloidal octylamine-coated platinum NCs. A self-assembly mechanism is deduced using averaged force fields and atomistic molecular dynamics simulations, which explains the formation of remarkably different  $sc$  and  $fcc$  superlattices of ligated regular and truncated Pt NCs ( $l_{RC} = 5.5$  nm,  $l_{TC} = 4.7$  nm) observed in experiments. Our detailed analysis shows that loose  $fcc$  packing is favored by TCs due to Coulombic couplings from multipolar electrostatic fields originated in a charge transfer between the octylamine ligands and the Pt cores and asymmetrically redistributed in the metal NC cores. This coupling creates a local energy minimum when the TCs have adjacent (shifted) corners, which can retain the  $fcc$  packing in solvent (toluene) and vacuum against global stabilization of the  $sc$  structure. These results could be used in guiding the experimental preparation of novel supercrystals with many potential applications.

### 3.6 Cadmium Sulfide NP Nanocapsules

**Adapted from Ref. [11], a submitted manuscript.**

This study was performed in collaboration with the research group of Prof. Nicholas Kotov from University of Michigan. The goal of the theoretical work in this study was to derive a mechanism that can explain the stabilization of self-assembled nanoshells formed of CdS NPs. The analysis of nanoshell formation, atomistic modeling, and simulations were performed by me. All the experiments were performed by our collaborators.

#### Introduction

A simple yet versatile geometry of nanoshells is at the foundation of their many special physical and chemical properties. Nanoshells with variable pore size are frequently used in nature to sustain gradients of pressure, pH, and ion concentration. They also allow compartmentalization of chemical components in liquid providing reaction control, selective transport, protection, and catalysis. Biomolecular nanoshells are typically formed by the self-assembly of tens to a few thousands of organic structural units that are either highly anisotropic, e.g., phospholipids, or bound together by highly specific lock-and-key interactions found, for instance, between structural proteins of viral capsids

Inorganic nanoshells are being actively studied for their unique optical, [310] mechanical [311], and catalytic characteristics [312] that often originate in shell-confined quantum mechanical effects. However, the methods for their preparation are limited. Templating composite films on spherical particles [93] is the leading synthetic approach for making artificial nanoshells [313], which results in rather large core-shell particles with diameters ranging from several hundreds of nanometers to several micrometers. Kirkendall effect, [94] nonequivalent stoichiometry reactions, [314] and Oswald ripening [315] lead to the formation of 10-200 nm nanoshells by chemical transformation of solid NPs

using mismatches between ion exchange/diffusion rates for different ions. As one can see, they are conceptually different from those utilized by nature.

Realization of biomimetic self-assembly of nanoshells from inorganic structural units would expand the current library of compartmentalized self-assembled materials but it may appear fundamentally prohibited without molecularly precise spherical tiling of the structural units. Compared to proteins, lipids or polymers [316], inorganic nanoscale building blocks will impart new properties and functions to nanoshells. Nanoshells with controlled porosities would be interesting for (bio)catalytic and structurally responsive systems. Self-assembly of inorganic shells from NPs may also allow for better understanding of the formation of inorganic nanoshell in living organisms. [317]

Studies in the past decade indicate that inorganic NPs display distinct ability to self-organize into both terminal (supraparticles, [318], nanostars [319], etc) and extended structures(chains [113], sheets [115], ribbons [320], superlattices [321] etc.), but they were not observed to form shells or other open structures with cavities. Here we demonstrate that simple CdS NPs produce porous spherical nanoshells and elaborate the mechanism of their formation. Their spontaneous assembly without pronounced hydrophobic/hydrophilic anisotropy, lock-and-key interaction, or molecular tiling between the constituent units is surprising and cannot be rationalized based on the traditional colloidal theories. However, it can be fully explained using atomistic molecular dynamics (MD) simulations with explicit molecular description of solvent and counter ions that confirm both structural and thermodynamic features of the nanoshell assemblies.

### **Experiment: Self-assembly of nanocapsule**

A brief description of the experiments performed by Prof. Kotov's group is given here. In this study CdS NPs were used as a model structural unit; these NPs are representative of other semicon-

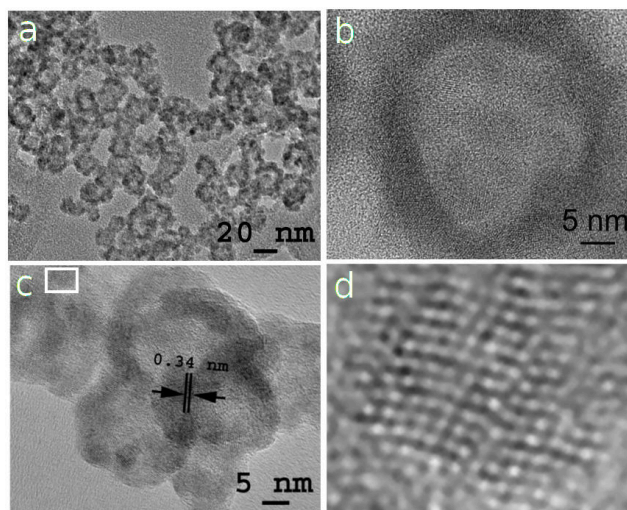


Figure 22: TEM images of CdS nanoshells obtained at pH 9.5. (d) The enlarged high-resolution image of the area in the white rectangle in (c).

ductor nanocolloids with respect to the size, shapes, and physical/chemical properties. Nanoshells with diameters of 10 – 20 nm (Figure 22 a,b) formed during the combined process of synthesis and assembly reminiscent of the protein-assisted self-assembly process. [322] The pH of the reaction medium and final nanoshell dispersion was controlled by 0.01 M NaOH solution and in most experimental series was 9.5. No extraneous organic molecules typically coating NP surfaces were used. This synthetic protocol is attractive by its simplicity but it was also essential for this study because it significantly decreases the ligand-to-ligand interactions. Individual NPs, as assembly units of the nanoshells, can also be identified in the TEM images by the presence of crystalline interfaces visible at high magnification. Their lattice spacing of 0.34 nm corresponds to the (111) crystal planes (Figure 22c,d) and is typical for cubic CdS. Oriented attachment observed for other NPs [113, 304, 323] might be taking place here as well, although slower than for CdTe [113] or PbSe. [112] The wall thickness of these nanoshells was 3 – 5 nm and is identical to the dimensions of the “building blocks”.

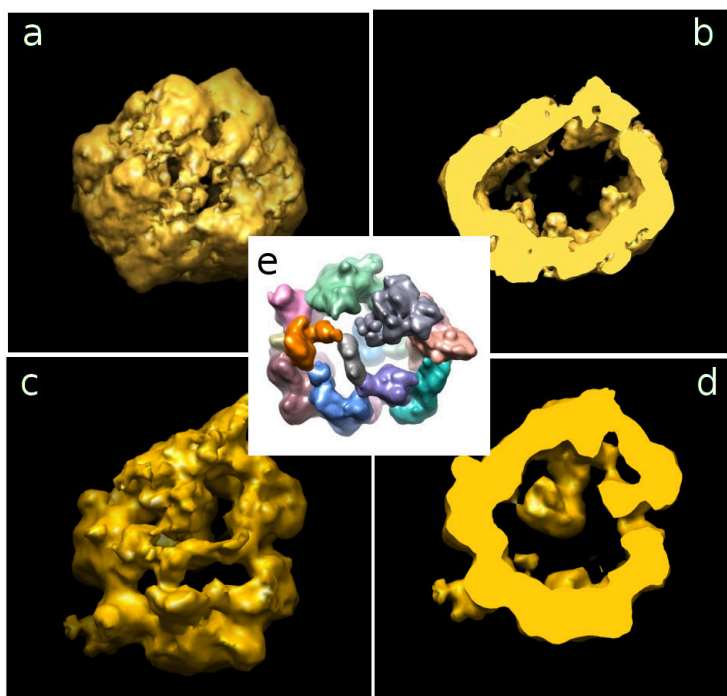


Figure 23: 3D surface rendering of the nanoshell (a, c) and cross-section of the nanoshell (b, d) at room temperature (a, b) and cryo conditions at 77°K (c, d). Scale bars are 5 nm. (e) 3D surface rendering of the nanoshell with different colored NP domains.

Uniformity of the nanoshell diameter and wall thickness is indicative of the self-limiting growth mode typical for terminal self-assembled structures previously observed for cavity-less supraparticles. [318]

Room-temperature and cryo-electron tomography of rapidly frozen samples captured the particles in their native hydrated state (Figure 23 a-d), unequivocally confirmed the formation of nanoshells, and accurately described their geometry. The accuracy in description of the three-dimensional arrangement of the constituent units enabled by this technique makes possible direct juxtaposition of the microscopy data with computer modeling. [324] The wall thickness of  $\approx 4 - 5$  nm and the diameter of  $\approx 10 - 15$  nm for the nanoshells determined by this technique were consistent with the data in Figure 22. The fact that the shells are composed of NPs without any special geometrical fit to each other is evident in these images and can be further highlighted by the 3D surface rendering

of the nanoshell with colored NP domains (Figure 23 e). TEM tomography also demonstrates that a nanoshell with a diameter of 20 nm accommodates ca. 90 NPs. The presence of nanoscale pores with a diameter of ca. 2 nm between the constituent units can also be observed (Figure 23 c,d).

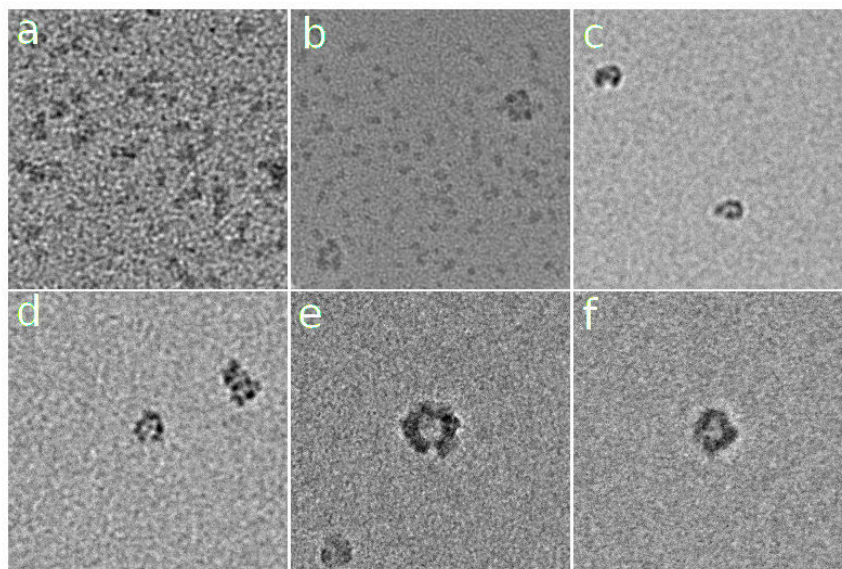


Figure 24: Representative TEM images of CdS nanoshells obtained after (a-b) 5 min, (c-d) 10 min and (e-f) 20 min of the assembly process at pH 9.5.

TEM images taken in the course of the nanoshell synthesis/assembly reveal intermediate geometrical shapes leading eventually to nanoshells. After 5 min, NPs form small arc-shaped agglomerates (Figure 24 a,b). After 10 min, they transform into incomplete crescent-like shells (Figure 24 c,d). The closing of the shells occurs in the last 20 min of the assembly (Figure 24 e,f). Again, no preferred contact surfaces, geometrically matching shapes, or substantially larger agglomerates – chains, sheets, ribbons, etc – can be identified at any stage of the process. Nanoshells and some individual NPs were exclusive products of this process with nanoshells containing over 90 %.

The self-organization of NPs into nanoshells was found to be pH-dependent. At pH 7.2, nanoshells with radii of 5 nm were observed that were smaller than the nanoshells formed at pH 9.5 with a radius of 10 nm. Solid supraparticles appeared when the assembly process was carried out at pH



5, which further supported the observation that lowering ambient pH reduces the size of cavities in nanoshells. At pH 4.3, predominantly single NPs were present.

Increase in pH coincides with the increase of zeta potential of the dispersions,  $\zeta$ . At pH 7.2, they observed nanoshells with  $\zeta = -11.2 \pm 1.1$  mV. This electrokinetic potential corresponds to total surface charge of  $Q_{CdS} = -7.2 \times 10^{-19}$  C, equivalent to  $\approx 4 - 5$  electrons per nanoshell. Since there are  $\approx 22$  single CdS NPs forming the nanoshell, the charge on the individual NPs approximates to  $q \approx -0.2e$ . At pH 9.2, they observed nanoshells with  $\zeta = -50.2 \pm 1.8$  mV, which corresponds to a total surface charge of  $Q_{CdS} = -8.9 \times 10^{-18}$  C, equivalent to  $\approx 55$  electrons per nanoshell or an average charge of  $q \approx -0.6e$  per NP. From these data and calculations one can surmise that increase of average NP charge leads to an increase of nanoshell size and the electrostatic repulsion between the “building blocks” causes the transition of the assembly pattern from cavity-less supraparticles [318, 319] to nanoshells.

### **Analysis of the formation of a nanoshell**

The formation of the nanoshells can be described at several levels of approximation to understand the mechanisms that lead to their formation and stabilization of their cavities. Based on a previous study [115], we know that the self-assembly of similar NPs is controlled by forces that mainly originate in van der Waals (vdW) and electrostatic interactions, with contribution of dipolar and hydrophobic attraction, hydrogen bonding, and other interactions. However, compared with the existing work [318], the notable difference here is the absence of stabilizers (capping agents) during the formation of nanoshells. Such effect may diminish the hydrogen bonding between NPs and hydrophobic interactions, which is typically originated from surface ligands but will strengthen CdS-CdS vdW attraction.

In the first approximation, the appearance of the nanoshells can be rationalized using the Gauss Law of electrostatics. In analogy to the stabilization of charged clusters [318], the strength of electrical field at the surface of the nanoshell when the nanoshell reaches the terminal size can be denoted as  $E_{term}$ . As the electrical field on the nanoshell surface,  $E$ , approaches  $E_{term}$ , it slows down the growth and reduces the stability of the assemblies, and eventually prohibits more NPs to join the terminal nanoshell. The assembly can acquire additional stability and take more NPs by changing the NP packing. As such, the nanoshells become porous because the partial perforation increases their diameter and reduces electrostatic repulsion of NPs stabilizing the structure. We can quantify all these effects by considering the total charge of assembled NPs:  $Q = Nq$  where  $N$  is the number of NPs in the assembly.  $N$  is proportional to the nanoshell surface area,  $S$ , and depends on the nanoshell radius, as  $Nq \approx Sq \approx R^2q$ . For porous nanoshells, however,  $Nq \approx R^\alpha q$ , where  $\alpha$  ranges from 1 to 2. One of the consequences of the Gauss Law,  $E \approx Q/R^2$  and thus  $E = R^\alpha q/R^2$ . So the terminal diameter  $R_{term} = (q/E_{term})^{1/(2-\alpha)}$ . When  $\alpha < 2$ , the denominator has finite value and for  $\alpha = 1$ ,  $R_{term} = q/E_{term}$ , which shows that the nanoshell size increases with the charge of the NPs, in analogy to the experimental observations.

### Models of the CdS NPs

The variety and complexity of NP-NP interactions in the described nanoshells can be accurately accounted for by atomistic molecular dynamics (MD) simulations. Considering the ever-increasing computational power and the improvements in 3D resolution of the nanoscale structures enabled by TEM tomography (Figure 23), the combination of MD with TEM methods represents a powerful toolbox for understanding of assembly mechanisms.

Based on previous studies, [325] the CdS NPs were modeled as tetrahedrons with a side length of  $l \approx 2.4$  nm, built from atoms of Cd and S in the atomically accurate crystal lattice (F43m space

group, lattice constant  $a = 0.582$  nm). Since NPs forming nanoshells in Figure 22 are not covered by any special organic stabilizer; the surface of MD NP models was composed of simple chemical groups typical for aqueous medium [326], which markedly simplified their simulations. In MD Model 1, the NP surface carried Cd-OH groups while the net charge of each NP  $q = 0e, 2e, 4e, \text{ or } 8e$  (Figure 25 a,b) was homogeneously distributed over the NP volume. The presence of surface  $-OH$  groups enabled local hydrogen bonding. To demonstrate generality of the observed self-assembly processes, we also used Model 2, in which the NP surfaces did not carry  $-OH$  ligands, i.e., bare CdS lattice, (Figure 27) and the overall charge was smaller:  $q = 0e, 0.6e, 1e, 2e$ . In both cases, the medium, i.e., molecules of water around the NPs, and the counterions were explicitly included in the atomistic model. In Model 1 and 2, we assigned positive partial charges of  $0.8e$  to all cadmium atoms and partial charges of  $0.15e, -0.37e, -0.72e, \text{ and } -0.8e$  to sulfur atoms on the vertex, edge, face, and bulk position of the NP core, respectively. These charges were assigned based on vacuum charges from *ab initio* (3-21g basis set) calculations performed using GPU-powered Terachem software [327].

**Model 1.** In Model 1, the NP core was covered by  $CdOH^+$ ,  $Cd(OH)_2$ , and  $Cd(OH)_3^-$  ligands in 1:2:1 ratio, respectively. The  $2e, 4e, \text{ and } 8e$  negatively charged NPs were obtained by replacing 1, 2, and 4  $CdOH^+$  ligands by  $Cd(OH)_3^-$ , respectively. The position of these ligands was optimized to minimize the total energy of electrostatic interactions between the NPs, which resulted in strong inter-locking between neighboring NPs. We assigned partial charges of  $2e, -1.32e, \text{ and } 0.32e$  to the cadmium, oxygen, and hydrogen atoms of the ligands. To allow a faster NP nanoshell equilibration, partial charges of all the atoms in the ligands were set to zero (depolarization); reinstatement of the removed ligand charges in the equilibrated systems led to locking of the assembled structure. Net charges of the NPs were evenly distributed onto all cadmium atoms of the NP cores to preserve the dominant electrostatic interactions between the NPs. Since the vdW interactions [188] between

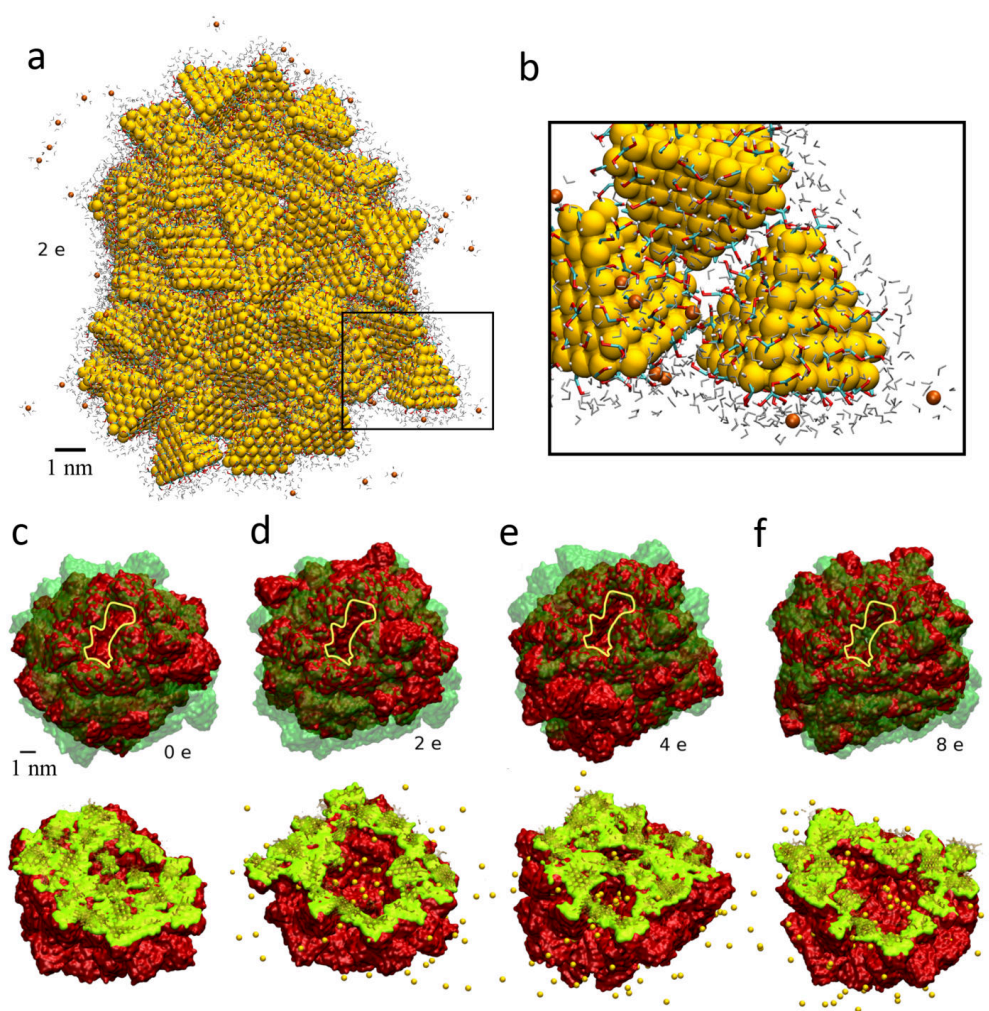


Figure 25: Detailed model of a 2e charged nanoshell (a). An enlarged view (b) shows the water molecules and counterions surrounding the NPs. Surface representation of simulated nanoshells obtained before (translucent green) and after (red) equilibration (c-f). The bottom figures show their cross-sections.

individual atoms in typical MD simulation software have a cutoff distance of  $10 \text{ \AA}$ , long-range vdW interactions between NPs need to be treated separately. In Model 1, they were considered to be less important than in the strong attractions between the molecular groups on NP surface and were neglected. However, they were explicitly included in Model 2.

**Model 2.** In Model 2, the NPs were “naked”, the atomic charges of Cd and S on the NP surface were halved reflecting reduced polarity due to the presence of some surface layer. The

London dispersion interactions between NPs were added by treating the NPs as spheres with volumes approximately equal to the volume of NPs used in the experiments (about three times larger volume than the simulated NPs). The vdW attraction between two spheres is described by [188]

$$V_{ij}^{vdW} = -\frac{A}{12} \left\{ \frac{R}{D_{ij} [1 + D_{ij}/4R]} + \frac{1}{1 + D_{ij}/R + D_{ij}^2/4R^2} + 2 \ln \left( \frac{D_{ij} [1 + D_{ij}/4R]}{R [1 + D_{ij}/R + D_{ij}^2/4R^2]} \right) \right\}, \quad (3.10)$$

where  $A$ , the Hamaker constant is  $5.24 \times 10^{-20}$  J (CdS-CdS in water),  $R$  is the radius of interacting spheres, and  $D_{ij}$  is their center-to-center distance. A cutoff of 70 Å is used to select the neighboring NPs in the calculations of vdW interactions between CdS lattices. The vdW attraction between neighboring NPs is re-evaluated every 1000 steps (2 pico-seconds) and it is applied to the atom closest to the NP center.

### **Atomistic MD simulations of nanoshells.**

Nanoshells with a radius of  $\approx 6$  nm were pre-assembled from 81 NPs. This capsule was solvated in 0.6 mM NaCl medium, where additional  $\text{Na}^+$  counter ions were homogeneously added to the system to neutralize the capsule charges. We also formed a  $\approx 8$  nm<sup>2</sup> wide opening on each nanoshell by removing two NPs and spatially fixing atoms of the NP cores located around the opening, in agreement with the observed porosity of nanoshells. The opening accelerated a free flow of ions and waters, and led to faster stabilization of the capsule sizes. The Gilbert–Johnson–Keerthi (GJK) distance algorithm [328] was used to determine the amount of water and ions within the nanoshell. Molecular Dynamics (MD) simulations of the NP nanoshells were performed using the NAMD software package [175] and the results were visualized with VMD software package [199]. Partial charges of the ions and water molecules were assigned based on the CHARMM36 force field [171, 228]. The vdW parameters of the atoms are directly transferred from available parameters in the CHARMM force

field, which were determined through Lennard-Jones optimization [329]. The systems were simulated in a NPT ensemble at  $T = 300$  K, maintained by Langevin dynamics with a damping coefficient of  $\gamma_{Lang} = 0.01 \text{ ps}^{-1}$ . Long range electrostatics was evaluated using periodic boundary conditions and a particle mesh Ewald (PME) summation [172]. Hydrophobic interactions and hydrogen bonding are implicitly described through electrostatic, vdW interactions, and atomistic description of the medium.

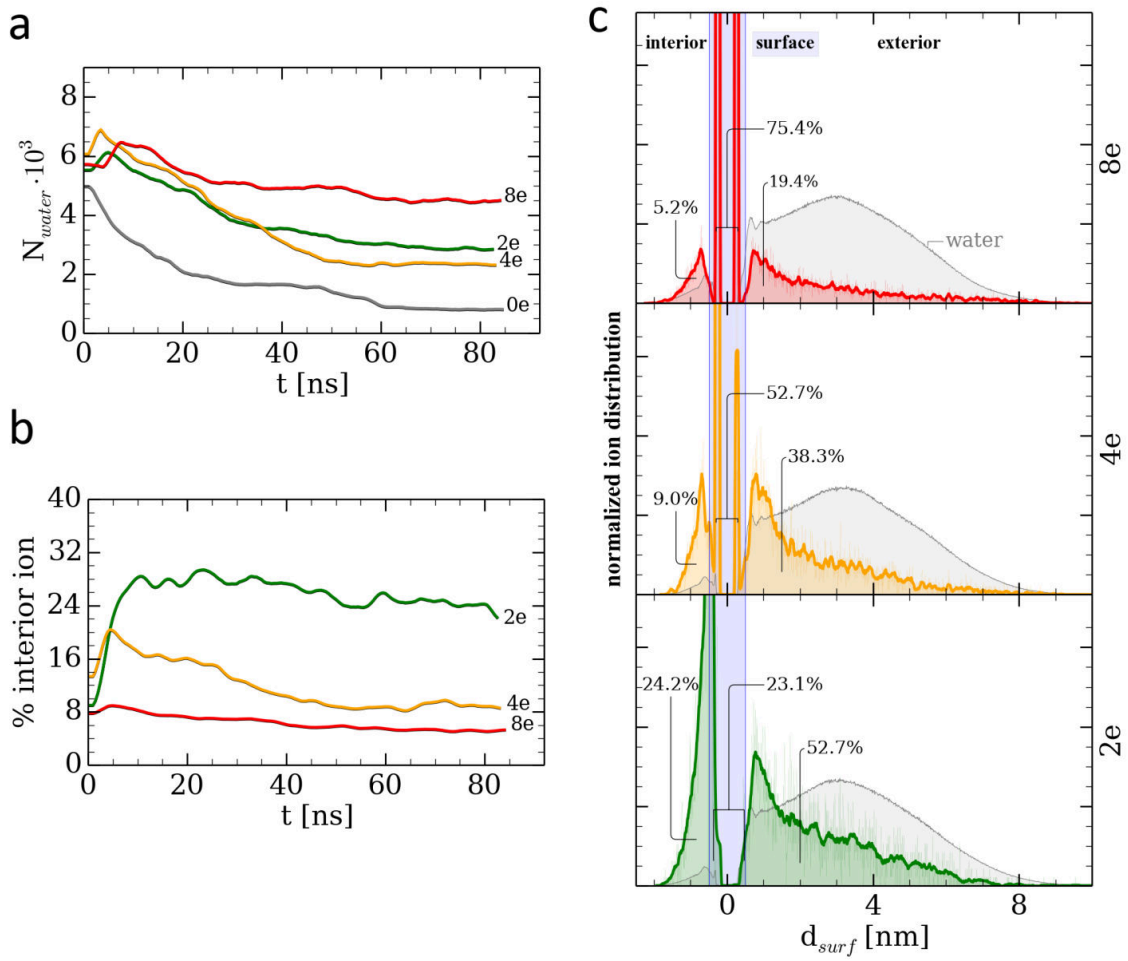


Figure 26: Plot (a) shows the time-dependent change in the number of water and plot (b) time-dependent change in percent of ions inside the nanoshells. Graphs in (c) show the distribution of ion inside (negative  $d_{surf}$ ) and outside (positive  $d_{surf}$ ) of the charged nanoshells.  $d_{surf}$  is the distance from the surface of the NPs.

In Model 1, we observed continuous reorganization of the NPs in the nanoshells that underwent slow “deflations” whose rate was dependent on  $q$  (Figure 25 c-f). Within  $\approx 85$  ns, the radii of nanoshells plateaued and the net flow of water and ions in/out the nanoshell approached zero (Figure 26 a,b), which was attributed to reaching the equilibrium state. Evaluation of the flux of water molecules and counter ions during the equilibration of the nanoshells (Figure 26 c) indicate that the hydrostatic force originating due to osmosis takes part in the stabilization of the cavity between the NPs. The number of ions inside the equilibrated nanoshells has a tendency to increase with  $q$ . Normalized distribution of water and ions calculated from the last 20 ns of the simulation (Figure 26 c) shows that the ratio of free ions and ion bound to the NP surface dramatically changes with  $q$ . The interior of a nanoshell made of NPs carrying  $q = 2e$  has a larger percentage of free ions (24.2 %) that are not adsorbed onto the NP surface than the nanoshells made from NP with  $q = 4e$  (9.0 %) and  $q = 8e$  (5.2 %), where ions are largely adsorbed on the shell surfaces. Importantly, nanoshells from NPs carrying  $q = 2e$  have a larger cavity than the nanoshell from NPs carrying  $q = 4e$ , despite the stronger Coulombic repulsion between the NPs. The large number of free ions forces influx of water molecules inside the nanoshells. The related increase of the osmotic pressure in the nanoshell may inflate it and increases its size.

In simulations, the nanoshells and the central cavity displayed a larger diameter as  $q$  increased, in agreement with the experiments. The generality of the phenomena can also be appreciated from the data obtained for Model 2, where the equilibrium nanoshell size in this case also grew when  $q$  increased. In both models, the equilibrated nanoshells displayed spontaneous formation of pores (Figure 25 and Figure 27). Comparison of the TEM data in Figure 22, tomography data in Figure 23 and simulation data in Figure 25 , indicates that the atomistic MD models give nearly perfect

agreement with the experiments. The comparison between Models 1 and 2 also shows that the local bonding [3] between, for instance, surface  $-OH$  groups decreases the porosity of the nanoshells.

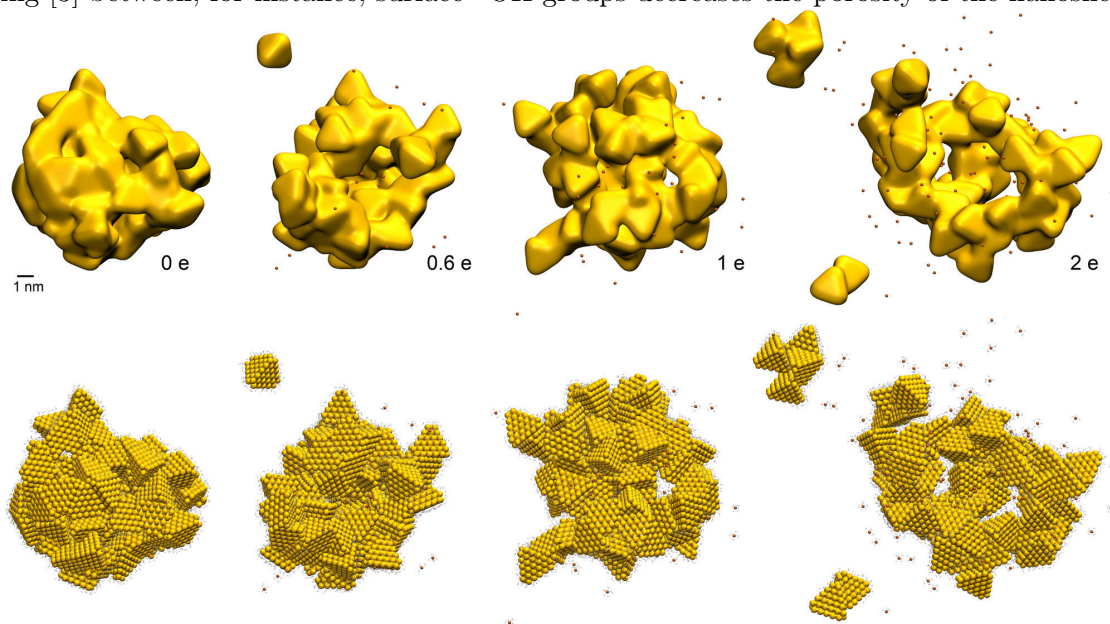


Figure 27: The equilibrated nanoshells having higher porosities obtained in the Model 2.

## Conclusions

CdS NPs can spontaneously assemble into thermodynamically stable nanoshells. They exemplify terminal self-organized nanostructures from inorganic “building blocks” as proven by atomistic MD simulations. It also demonstrates the emerging possibility to combine experiment, TEM imaging, and computer simulations in the powerful trifecta capable of atomically accurate descriptions of complex nanoscale assemblies, making possible conclusive elucidation of assembly mechanisms. The geometrical shape of nanoshells from NPs and their pH-induced behavior can be paralleled to that of some viral capsids [330] and other self-organized nanoshells without atomically sophisticated lock-and-key protein complexes. The simplicity of their formation and porous morphology facilitate their utilization for compartmentalization of chemical process and open the road to different biomimetic approaches to catalysis, [331] cascade reactions, [332] drug delivery, [333] and optical materials. [310]



### 3.7 Self-Assembly of NPs into Chiral Twisted Nanoribbons

Adapted from Ref. [7] (*Nat. Mat.* 2015, 14, 66–72. doi:10.1038/nmat4125) with the permission from The Nature Publishing Group.

This study was performed in collaboration with the research group of Prof. Nicholas Kotov from the University of Michigan. The goal of the simulation work was to test different arrangements of NPs that would lead to twisting of a nanoribbon, and also to identify the mechanism for the transfer of chirality from the NPs to the nanoribbon. Atomistic modeling and simulations were performed by me. The light absorption simulation, Derjaguin-Landau-Verwey-Overbeek theory, and all the experiments were performed by our collaborators.

#### Introduction

Materials with nanoscale chirality are known to strongly rotate the polarization of linearly polarized (LP) and circularly polarized light (CPL). Such optical effects in nanomaterials with different chiral geometries has been actively investigated as a part of chiral photonics and plasmonics [334–341]. The opposite effects – the transfer of spin angular momenta of circularly polarized photons to matter, followed by nanoscale or atomic restructuring and retaining the “memory” of circular polarization – are much less known. The possibility of such effects at the atomic and nanometer scale is indicated by, for instance, the formation of spiral nanoneedles with controlled helicity during laser ablation of bulk metallic tantalum with CPL [342]; however, the underlying mechanism is not well understood.

The transfer of spin angular momentum from photons of high-intensity CPL such as laser beams have been observed to induce circular or spiral motions in chromophores/scatterers of a wide range of sizes, including cold atom clusters (molar mass  $M \approx 10^2$ ) [343], Bose-Einstein condensates ( $M \approx 10^7$ ) [344], and micro-size colloidal particles ( $M \approx 5 \times 10^{22}$ ) [345]. However, the conversion of rotational motions into permanent structural changes is difficult to achieve due to achiral symmetry

of the particles, structural barriers for channelling rotational energies into chemical bonds, and fast quenching of rotational motion by the medium. NP dispersions that are stable at ambient conditions can be a more convenient and more reactive candidate for the study of CPL effects, as compared to most chromophores/scatterers, polymeric colloids [345], and bulk tantalum [342]. Owing to the unique length scale of NPs, they can also be more sensitive to photochemical effects of light with different handedness than chiral organic molecules [346,347].

CPL-induced restructuring of NP systems can provide a new, powerful, and versatile tool for the preparation of chiral nanomaterials. The synthesis of chiral nanostructures have potential applications in biosensing, telecommunication, display technologies, diffraction-free patterning, and chiral catalysis [335–338,340,340]. Furthermore, understanding of the CPL-induced restructuring process can lead to understanding of the origin of homochirality in natural compounds, i.e., the predominant existence of left-handed (LH) amino acids and right-handed (RH) sugars. Illumination with CPL has been suggested as one of the plausible causes of homochirality [348,349]. However, the mechanism of how CPL can lead to homochirality of organic molecules is not known; several chemical routes, including chiral amplification [350], are being debated [351].

### **CPL-induced transformations observed in experiments**

A brief description of the experiments carried out in Prof. Kotov's group is given here. A dispersion of CdTe NPs at ambient conditions, stabilized by an achiral capping agent, thioglycolic acid (TGA), is illuminated by either left- (LCP) or right-handed circularly polarized (RCP) light with a wavelength of 543 nm. Note that this CdTe dispersion revealed no circular dichroism (CD) peaks in the visible range and therefore has equal cumulative absorbance for LCP and RCP photons at 543 nm. CPL-induced transformations of NPs were examined after 1, 12, 28, 35 and 50 h of illumination (Figure 28 a,b). The temporal progression of the products included short 50–200 nm rods (1 h) that

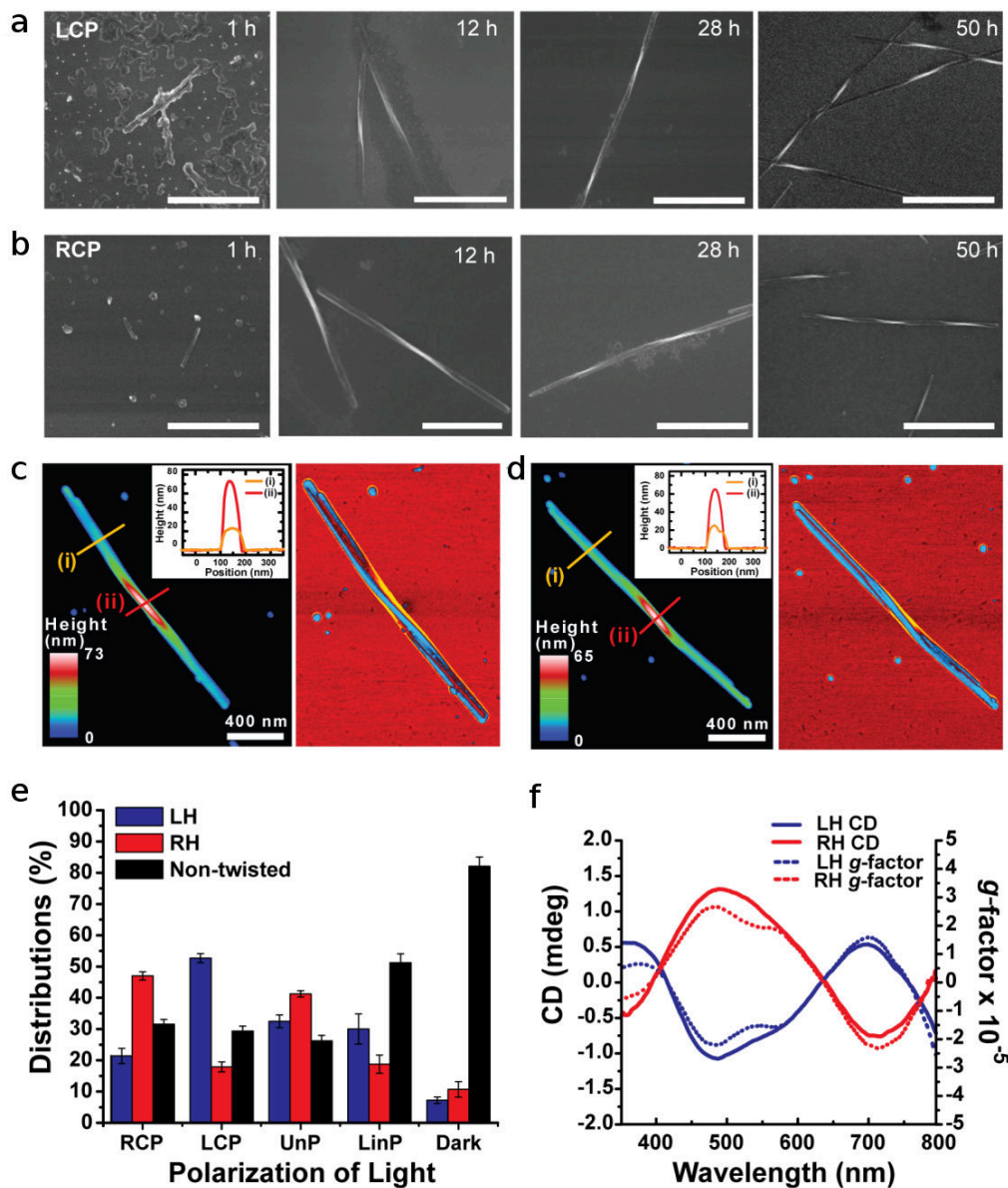


Figure 28: Self-assembly of CdTe NPs into twisted nanoribbons induced by illumination with CPL. (a,b) SEM images of ribbons assembled with LCP and RCP as a function of time exposure for 1 h, 12 h, 28 h and 50 h. All scale bars are  $1\mu m$ . (c,d) Tapping-mode atomic force microscopy (AFM) topographic (left) and phase (right) images of a LH nanoribbon (c) and a RH nanoribbon (d). (e) Distributions of LH, RH and non-twisted nanoribbons obtained after 50 h illumination with RCP, LCP, UnP, LP light, and in the dark. (f) Ensemble CD spectra (solid line) and g-factor (dotted line) of dispersions of left-handed (LH) nanoribbons and right-handed (RH) nanoribbons obtained after 50 h of CPL illumination. Linear dichroism effects that could be associated with adsorption on the walls of the cuvette and other spontaneous alignment of linear nanostructures have negligible contribution to the chiroptical properties, as indicated by the near identity of the CD spectra obtained with and without stirring of the dispersion.

evolved into 1–2  $\mu\text{m}$  twisted nanoribbons (12 h) and, subsequently, into 2–3  $\mu\text{m}$  longer nanoribbons (28 h). After 50 h of illumination, twisted nanoribbons with total lengths, pitch lengths and diameters of  $3 \pm 0.5 \mu\text{m}$ ,  $800 \pm 20 \text{ nm}$  and  $50 \pm 5 \text{ nm}$ , respectively, were the predominant products of the photo-induced reaction (Figure 28 c,d). When nanoribbons were exposed to CPL for more than 96 h, they started to become thinner, but retained their twisted shape. After 50 h of photo-induced assembly, and in the absence of further illumination, the nanoribbons retained their geometry.

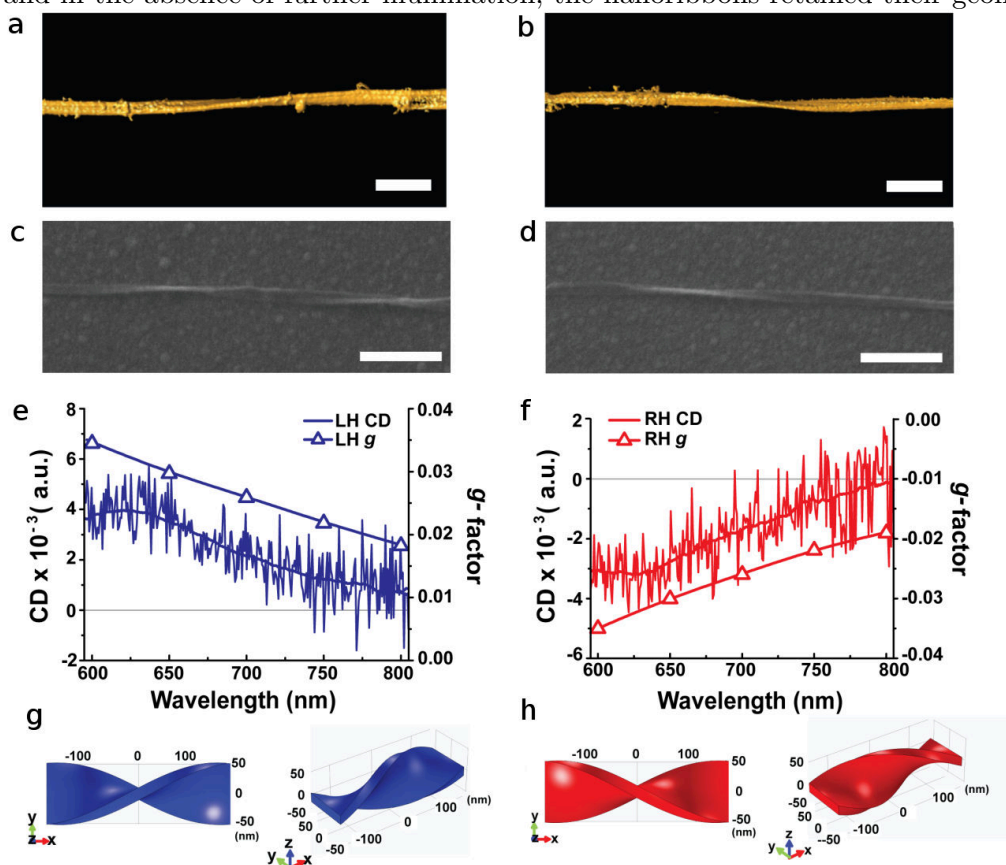


Figure 29: (a,b) Surface rendering of the 3D TEM tomographic reconstruction of a LH (a) and a RH (b) nanoribbon. Scale bars, 100 nm. (c,d) SEM images of single LH (c) and RH (d) nanoribbons. Scale bars, 500 nm. (e,f) CD spectra and calculated g-factor spectra for the single LH (e) and RH (f) nanoribbons in c,d, respectively. (g,h) Computational models of the LH (g) and RH (h) nanoribbons used in the FEM calculations of chiroptical properties on the basis of numerical solutions of the Maxwell equations.

Circular polarization of light exhibited an enantio-selective photochemical influence on NP dispersions and the geometry of self-assembled nanoribbons. Under LCP illumination, predominantly

LH nanoribbons were formed, as established by scanning electron microscopy (SEM) (Figure 28 a). When the NP dispersion was illuminated with RCP, RH nanoribbons of otherwise similar dimensions prevailed (Figure 28 b). In both cases, the differences between LH and RH nanoribbon fractions obtained after analysis of 100 SEM images of  $\approx 1,000$  nanoribbons were more than 30% (Figure 28 e), which was well in excess of the experimental error of  $\approx 5\%$ . Note that this is also much higher than a typical enantiomeric excess in CPL-stimulated organic reactions ( $0.5 - 2\%$ ; [347]). The chiral preference in nanoribbon geometry was also confirmed by CD spectroscopy. CD spectra of purified nanoribbons were measured in aqueous dispersions and revealed distinct chiroptical bands at 490, 590, and 700 nm (Figure 28 f). Comparison of CD and absorption spectra after 50 h illumination indicates that the first two bands in the CD spectra are associated with the absorption in the bandgap transition. Importantly, nanoribbon dispersions illuminated by LCP and RCP showed positive and negative CD signals, respectively. Transmission electron microscopy (TEM) tomography (Figure 29 a,b), capable of visualizing 3D structures of the nanoribbons, corroborated the conclusions regarding their chiral shape.

A control experiment involving illumination with unpolarized light (UnP) showed an equal distribution between right- and left-handed nanoribbons, in agreement with the previous study [320]. Illumination with LP light as well as incubation in the dark yielded straight nanowires that were the overwhelmingly dominant products in these two cases. Nanowires produced by exposure to UnP and LP light revealed no CD activity, consistent with the SEM data.

Another experimental series contributing to the understanding of the templating effect of photons on the mesoscale geometry of nanoribbons and nanowires was the illumination of CdTe dispersions with a different light source at 607 nm for 50 h. The efficiency of chiral induction by LCP is reduced as the difference between the yield of LH and RH nanoribbons drops to  $\approx 20\%$  compared to illumination

at 543 nm. This observation is consistent with the reduced intensity of NP absorbance at the fringes of the bandgap transition.

To avoid the effects of chirality arising from potential artefacts of small molecular weight compounds present in solution, they compared CD spectroscopy of ensembles of chiral structures in dispersion with CD measurements taken for single nanoribbons (Figure 29 e,f) for the 600 – 800 nm spectral window. The single LH and RH nanoribbons revealed correspondingly positive and negative mirror-image CD signals. A band located at  $\approx 660 - 700$  nm is spectrally similar to the band observed for dispersions (Figure 28 f; the effective spectral window of the quarter-wave plate used prevents single-particle CD measurements in the 400 – 600 nm region). CD spectra of the single twisted nanoribbons measured using dark-field microscopy are dominated by light scattering. Therefore, the “red” CD bands in Figure 28 f should be predominantly attributed to scattering of LCP and RCP photons on twisted nanoribbons with specific handedness and, in fact, may be considered in the framework of circular intensity differential scattering [352]. As a control experiment against potential artefacts they measured CD spectra from single nanoribbons at various rotational angles with respect to the long axis. The shape of the CD spectra remained unchanged regardless of the nanoribbon orientation. As another control experiment, confirming attribution of the origin of the CD bands, non-twisted nanoribbons showed no CD signals

The chiroptical properties of the twisted nanoribbons can be compared to those of microscale gold helices made by 3D lithography [341] which also exhibit broadband polarization rotation. Anisotropy factors of  $g = 0.02 - 0.04$  were obtained from numerical finite element method (FEM) solutions of the Maxwell equations for CdTe twisted ribbon models (Figure 29 c,d), which are comparable to the values obtained for Ag-enhanced Au nanohelices and Au nanorods/fibre composites of  $g \approx 0.025$  [335, 336]).

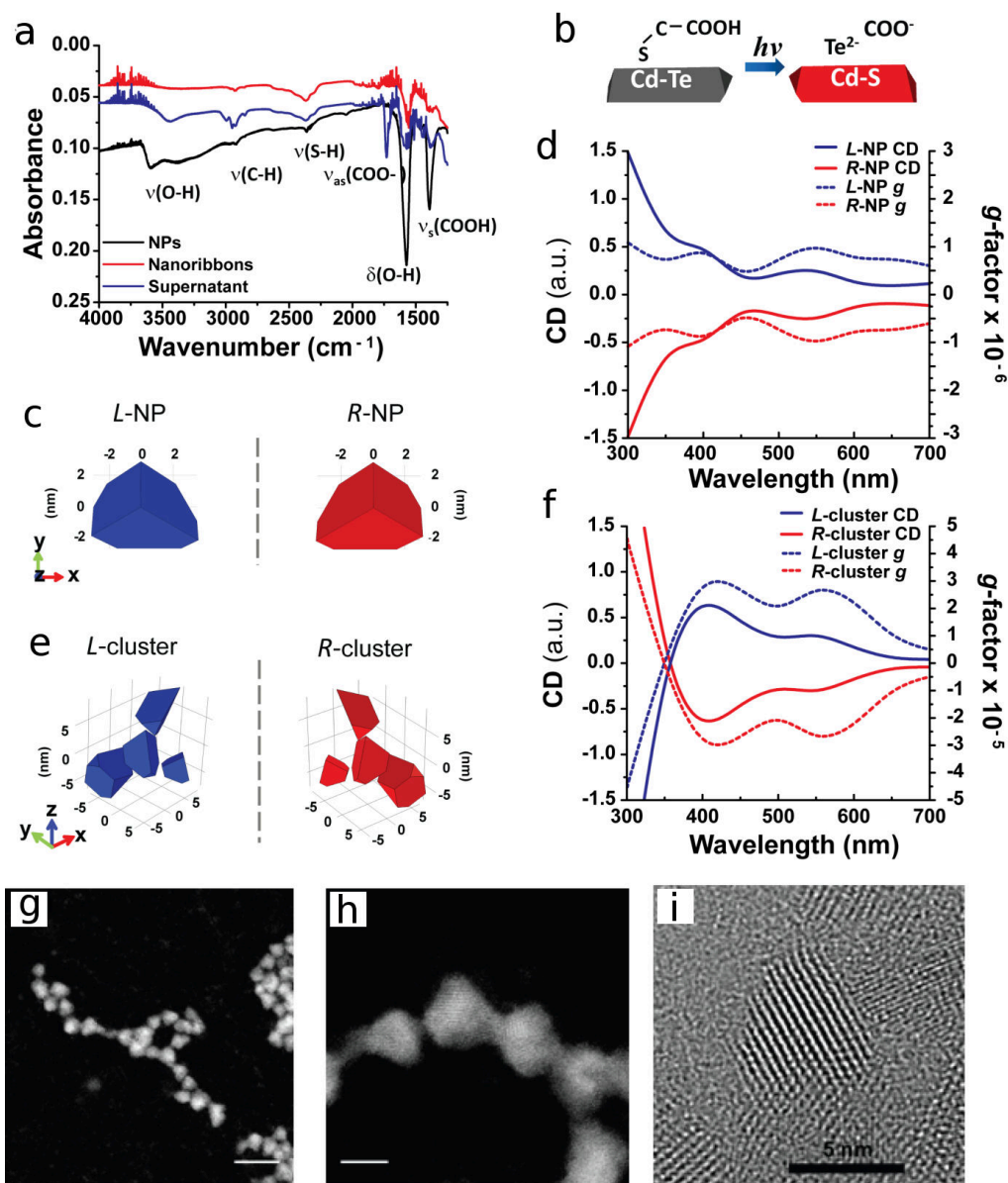


Figure 30: (a) FTIR spectra of original CdTe NPs, of the purified nanoribbons and of the supernatant obtained after 50 h of illumination time. (b) Schematic illustration of the CdTe phase transition to CdS. (c,e) Models of chiral NPs (c) and chiral NP clusters (e) used in calculations of the chiroptical properties. (d,f) Simulated spectra and g-factors for L = R-NPs (d) and L = R-clusters of NPs (f). The nomenclature for NPs and their clusters is based on their positive (L) or negative (R) optical activity. (g,h) HAADF STEM images of TGA-stabilized truncated tetrahedral CdTe NPs. Scale bars, 15nm (g) and 5nm (h). (i) High-resolution TEM image of TGA-stabilized truncated tetrahedral CdTe NPs.

### Mechanism of light-induced self-assembly

To understand how the circular polarization of photons causes distinct permanent differences in the shapes of nanoribbons, we first addressed the mechanism of light-induced self-assembly of CdTe NPs. From the optical properties and the relative content of NPs in the supernatant of nanoribbon dispersions assembled with and without light, it becomes apparent that, along with the spontaneous self-assembly of NPs [113,320], there is a parallel light-stimulated process of the formation of twisted ribbons. We found that Fourier transform infrared (FTIR) spectroscopy peaks for  $\mu(\text{O-H})$ ,  $\delta(\text{O-H})$  and  $\mu_s(\text{COOH})$ , characteristic of the TGA ligand, located at  $3500\text{ cm}^{-1}$ ,  $1567\text{ cm}^{-1}$  and  $1421\text{ cm}^{-1}$ , respectively, were drastically decreased in nanoribbons compared to the original CdTe NPs (Figure 30 a). A strong peak at  $1722\text{ cm}^{-1}$ , corresponding to  $\mu_{as}(\text{COO}^-)$  of carboxyl moieties, was observed in the supernatant obtained after separation of twisted nanoribbons and NPs by centrifugation. Concomitantly, the characteristic UV-Vis absorption peak of TGA at 276 nm decreased as the illumination time increased, indicating its decomposition. The presence of a S 2p signal from CdS in X-ray photoelectron spectra (XPS) of nanoribbons and the weakness of peaks for Te from CdTe indicate that illumination also results in the replacement of Te in the NPs by S; the elemental atomic composition of the nanoribbons was 51.5% Cd, 47.3% S, 1.2% Te. The mechanism for the photo-induced replacement of Te by S in NPs is likely to involve the ionic diffusion of  $\text{S}^{2-}$  ions formed by photo-induced oxidation of TGA into the NPs. TEM of the twisted region, atomic mapping images and energy dispersive spectroscopy (EDS) spectra confirmed the transformation of CdTe NPs into CdS NPs (Figure 30 b). These results are consistent with previous findings regarding the formation of a thin CdS shell around CdTe NPs due to the chemical decomposition of TGA and the photo-induced oxidation of CdTe [353].



X-ray photoelectron spectra indicated that there was no significant difference in the chemical composition of left- and right-handed nanoribbons. Therefore, the assembly mechanism should be the same for RCP and LCP illumination. Spectroscopy and microscopy data in Figure 30 and suggest that the mechanism of light-induced nanoribbon self-assembly starts with the photo-induced decomposition of TGA to form  $S^{2-}$ , which subsequently replaces  $Te^{2-}$  ions in NPs. The loss of the already sparse TGA shell is likely to be the trigger of the light-induced NP assembly into twisted structures. Such attribution of the self-assembly mechanism encounters, however, an unexpected complication. The electrokinetic zeta potential,  $\zeta$ , decreased from  $\approx -6$  mV to  $\approx -15$  mV on illumination; the increase in electrostatic repulsion must hinder the assembly process, contrary to the results observed. Calculations of the pair potentials between the NPs using extended Derjaguin-Landau-Verwey-Overbeek theory (E-DLVO) help to explain this discrepancy and confirm the light-induced assembly mechanism. Even though the zeta potential of “bare” CdS NPs are more negative, the loss of the TGA shell and increased ionic strength associated with the surface ligand photooxidation makes the overall pair potential more attractive.

Based on the above results, the effect of circular polarization of incident light on NP self-assembly originates in the optically selective activation of nanostructures with different handedness. Both individual CdTe NPs and their clusters can be chiral. As such, aberration-corrected TEM tomography indicates the existence of chiral dislocations of atoms in Pt NPs ([354]). Chirality of individual Au NPs in racemic mixtures capped with achiral ligands has been previously shown with liquid chiral chromatography [355]. With the help of high-angle annular dark-field (HAADF) scanning transmission electron microscopy (STEM; Figure 30 g,h), they found that the TGA-stabilized NPs have the shape of a truncated tetrahedron. The distinct truncated tetrahedron shape of CdTe-TGA NPs was also seen in high-resolution TEM images (Figure 30 i). Four uneven truncations result in

a chiral tetrahedron similar to a  $sp^3$  hybridized carbon atom with three different substituents. To confirm the chirality of individual NPs, they incubated the dispersion of TGA-stabilized CdTe NPs with bovine serum albumin (BSA, 66.5 kDa), serving here as an enantio-selective absorber. After 5 h of incubation, they separated BSA and unbound NPs using a centrifugal membrane (50 kDa) and measured the CD spectra of the obtained dispersions. In contrast to the original CdTe NPs, which have no CD signals, and Bself-assembly, which has a negative CD peak at around 215 nm, the separated NPs showed a positive CD band at 400 – 550 nm, coinciding with the excitonic transition of the NPs. This observation indicates that the starting NP dispersion is a racemic mixture of NP enantiomers with different chirality that can be enantio-selectively separated.

Simulation of light absorption showed that enantiomers of truncated NPs (Figure 30 c) should exhibit optical activity, as observed in the mirror-imaged simulated CD and  $g$ -factor spectra (Figure 30 d). Spontaneously formed small clusters of NPs similar to those in Figure 30 g can also be chiral. According to their simulations, the differences in absorption of LCP and RCP in such clusters (Figure 30 f) are even greater than in NPs (Figure 30 d). In both cases, there is a large difference in absorption of LCP and RCP at 543 nm for nanostructures of different handedness used for this study. Thus, the mechanism of chirality transfer from CPL to NP assemblies can be understood as follows. The original CdTe NP solution is racemic and contains equal amounts of left- and right-handed particles and small clusters. When a racemic mixture of CdTe NPs is illuminated by LCP at 543 nm, a subpopulation of LH NPs and clusters absorb light more effectively than RH NPs and clusters. The same is true for RH NPs/clusters when the dispersion is illuminated with RCP. The light-activated CdTe NPs undergo photooxidation of the TGA stabilizers that transforms them into “bare” CdS NPs. Photooxidation of multiple TGA ligands on the surface of NPs requires multiple photons and, therefore, the difference in the probability of absorption of L- and R- photons multiplies

over time. This process 'locks in' and amplifies the differences between NPs of opposite chirality in the initially racemic mixture.

The ligand-free CdS NPs exhibit a much stronger propensity to self-assemble than ligand-protected, non-light-activated CdTe NPs of opposite handedness. Because the self-assembly of NPs is very sensitive to the anisotropy of NP interactions [113], the chirality of the constituent building blocks is reflected in the helicity of the resulting assemblies, similar to the self-assembly of organic and biological macromolecules.

### Atomistic MD simulations

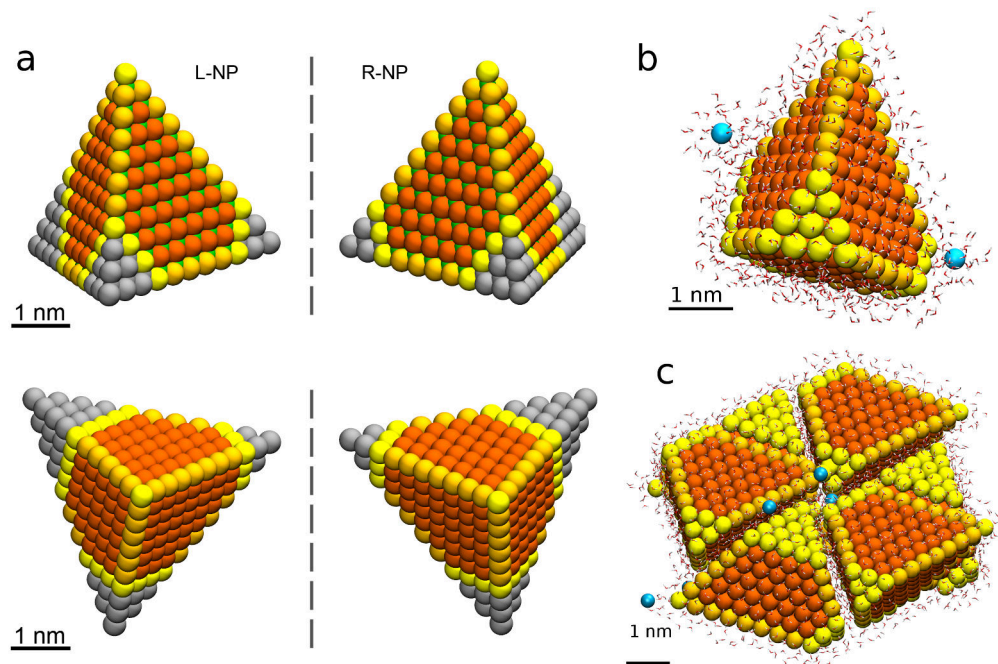


Figure 31: (a) Atomistic models of NPs with LH and RH truncations used in MD simulations. (b) Detailed view of a single NP in an aqueous environment and of the counterions used in the MD simulations. (c) Fragment of the simulated self-assembled ribbon from a top view, showing the packing of NPs. Scale bars in a-c are 1 nm

Atomistic molecular dynamics (MD) simulations were performed to further clarify the origin of the observed ribbon helicity. In the simulations, we start out with a model for individual NPs left- or right-handed and demonstrate the mechanism by which self-assembly of these individual NPs

lead to helical ribbons which are left- or right-handed. Individual NPs were modelled as slightly smaller 3.6 nm tetrahedrons with a cubic CdS crystal lattice and a lattice constant of  $a = 0.582$  nm. The tetrahedrons were asymmetrically truncated by the removal of 2-, 3- and 4-atom layers from three of the NP vertices to acquire a left or right chirality (Figure 31 a). The NP surfaces were not coated with stabilizers, in accordance with the experimental results presented in Figure 30, indicating ligand removal in the process of photoactivation. However, the large CdS lattice polarity was reduced at the NP surfaces to one half of the vacuum value to account for the potential presence of residual ligands. NPs at different (homogeneous) charging states were simulated in accordance with experimental observations. The MD simulations were carried out with explicit water molecules and  $\text{Cl}^-$  counterions of the charged NPs (Figure 31 b) to precisely describe the solvent environment of the NP self-assembly process.

Initially, NPs of the same (L or R) handedness (Figure 31 a) were pre-assembled into a planar piece of nanoribbon (Figure 32 a,b) with a packing similar to that observed before [320], assuming that NPs of predominantly one handedness were prepared by photoexcitation with circularly polarized light and self-assembled. Upon equilibration of the NP assemblies in an isothermal–isobaric ensemble at  $T = 300$  K for  $\approx 5 - 10$  ns, the planar nanoribbons acquired distinct twists. Importantly, the twist was opposite for NPs with opposite handedness. The average twist angle observed in the simulation of the nanoribbons made from CdS NPs was  $-3.1^\circ$  and  $+4.3^\circ$  for LH and RH NPs (Figure 32 c,d), respectively, which corresponds to a pitch length of  $\approx 1400 - 1900$  nm, similar to the experimental pitch length of nanoribbons observed after 28 h illumination in Figure 28 and Figure 29. These observations confirm the significance of NP chirality in guiding the ribbon assembly and the realism of the photon–matter chirality transfer via the geometry-specific photoactivation of NPs. The nanoribbon twists observed in the MD simulations clearly originate in the chirality (truncations) of

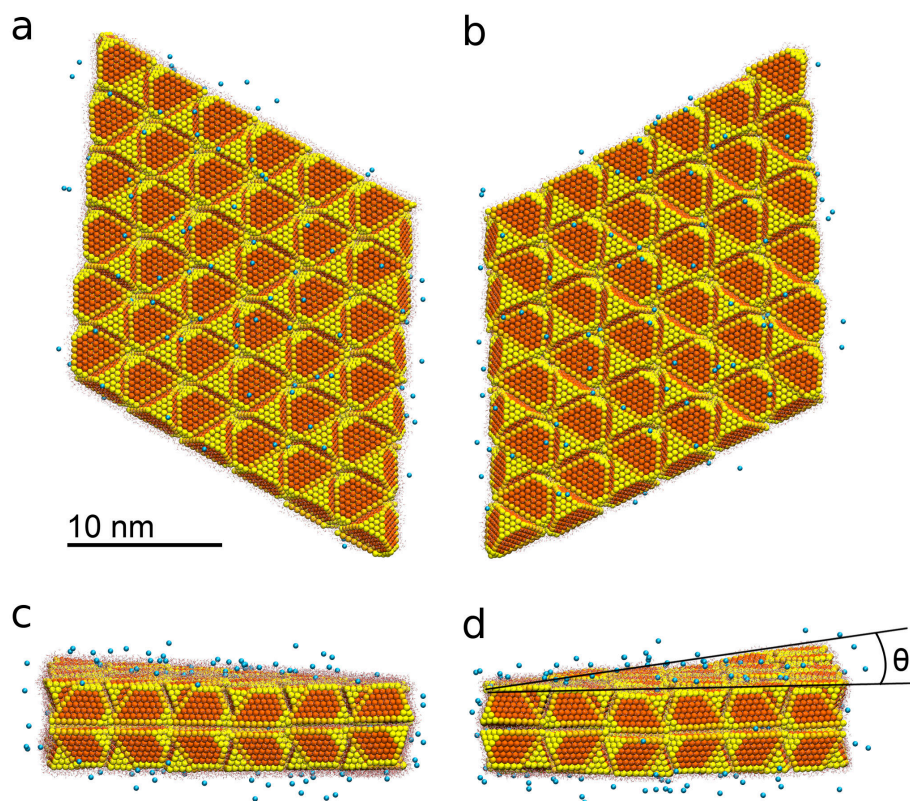


Figure 32: Top views (a,b) and side views (c,d) of simulated NP ribbons with LH (d) and RH (e) truncated NPs. The dihedral angle  $\theta$  determines the pitch of the nanoribbons.

the NPs, promoted via molecular-field-assisted NP–NP interactions into a cooperative phenomenon. As the light-transformed NPs are still largely solvated in water, their self-assembly into ribbons proceeds mostly via their bulk vdW coupling and partial hydrophobicity. However, water molecules form a soft “cushion” layer between the NPs within the ribbons, which allows the NPs to partially translate and reorient with respect to each other in accordance with the needs imposed by their chirality. The experimental structures are partially disordered owing to fluctuations of the NP size that translate into some variability of the pitch and non-close packing of the NP lattice in the ribbon.

## Conclusions

In the combination of experiments and simulations, it has been demonstrated that circular polarization of light can be “imprinted” on nanoscale structures by altering the chirality of NPs participating in the self-assembly process. Because light sensitivity is common in NPs, this study offers new methods of synthesis for chiral nanostructures using light as the primary parameter determining the asymmetry in the enantiomeric mixture of the products. Furthermore, geologic records suggest that inorganic NPs were present in primordial Earth conditions [356]; therefore, selective photonic activation of seemingly achiral NPs might represent the missing link between cosmic CPL ( [348,349,357] and inorganic/organic materials with preferential chirality.

The results present strong evidences that CPL-induced self-assembly of inorganic NPs can be achieved. We show that NPs are convenient building block for nanoscale synthesis, affording a variety of pathways to develop geometrically complex nanostructures. CPL-induced self-assembly is potentially influenced by the atomic and nanoscale chirality of individual NPs [354,358], amplification of CPL effects in NP assemblies [359,360], and the sensitivity of self-assembly processes to small changes in inter-particle interactions [361]. We present a plausible mechanism of the self-assembly process based on the results from experiments, spectroscopies, and simulations.

### 3.8 Field-Induced Self-Assembly of Magnetite Nanocubes

Adapted from Ref. [8] (*Science* 2014, 345 (6201), 1149–1153. DOI: 10.1126/science.1254132) with permission from The American Association for the Advancement of Science and Ref. [9] (*Faraday Discuss.* 2015, 181, 403–421. DOI: 10.1039/C4FD00265B) with permission from The Royal Society of Chemistry.

This study was performed in collaboration with the research group of Prof. Rafal Klajn from the Weizmann Institute of Science. The main goal of this theoretical study is to develop a realistic model that can describe the behavior of superparamagnetic (SPM) nanocubes, use the model to study experimentally observed structures such as belts and superhelices, and derive stabilization mechanisms that can explain their formation. All the theoretical work were performed by our group. The equations that model the magnetic interactions between magnetite nanocubes were derived by Artem Baskin and Nikita Repnin, graduate students of Prof. Petr Král, analytical calculations were performed by Artem Baskin, and atomistic modeling and Monte Carlo (MC) simulations were performed by me. All the experiments were performed by our collaborators.

#### Introduction

Nanoscale particles often self-assemble into superstructures with distinctive spatial arrangements that are difficult to predict based on the nature of their building blocks [110, 115, 149, 362–367]. This is because the stabilization of such self-assembled materials results from a delicate competition among forces of comparable magnitudes, originating in vdW, Coulombic, magnetic, and other types of particle interactions [44]. Although the structures of some systems are dominated by forces of a common origin (such as electrostatic interactions that govern the formation of open-lattice assemblies of peptide filaments [365] or colloidal crystals with a diamond-like lattice [149]), it is typically the interplay between various nanoscale forces that leads to the formation of highly complex materials, such as nanocrystal superlattices exhibiting polymorphism [368, 369].

Self-assembly of nanoparticles driven by competing forces can result in truly unique structures, with particularly striking diversity and complexity when the building blocks are simultaneously coupled by short- and long- range forces of different symmetries. Such frustration could arise in ensembles of magnetic nanocubes (NCs) whose axes of preferential magnetization (so-called “easy” axes) do not correspond to any of the directions favoring close packing. In the case of magnetite – the most abundant magnetic material on Earth, also present inside multiple living organisms in the form of NCs [370] – this condition is best fulfilled by cubic-shaped particles, whose easy axes (the [111] crystallographic direction; see Figure 33 b) connect two diagonally opposite corners of each cube. However, complex superstructures resulting from the competition between the shape anisotropy (favoring face-to-face interactions) and the magnetocrystalline anisotropy (favoring corner-to-corner interactions) have not been reported, perhaps because the former type of anisotropy typically dominates the latter [371,372]. Here, we investigated the self-assembly of magnetite NCs at the liquid-air interface in the presence of external magnetic fields. Depending on the density of the NCs, the experimentalists identified different types of self-assembled superstructures, including one-dimensional belts as well as single, double, and triple helices.

### **Superstructures observed in experiments**

We briefly describe the experimental work done in Prof. Klajn’s group to set the stage for the necessity of theoretical work. A drop of relatively monodisperse magnetite NCs [373–375] (average edge length = 13.4 nm, corner bluntness,  $\rho = 23\%$ ) solvated in hexane with an excess oleic acid (OA) was placed at a diethylene glycol (DEG)-air interface [209,376] under a magnetic field,  $H = 0 - 700$  G. The hexane solvent was allowed to evaporate within  $\approx 10$  min. These NCs are in the superparamagnetic (SPM) size regime, where collective dipoles of individual NCs thermally fluctuate



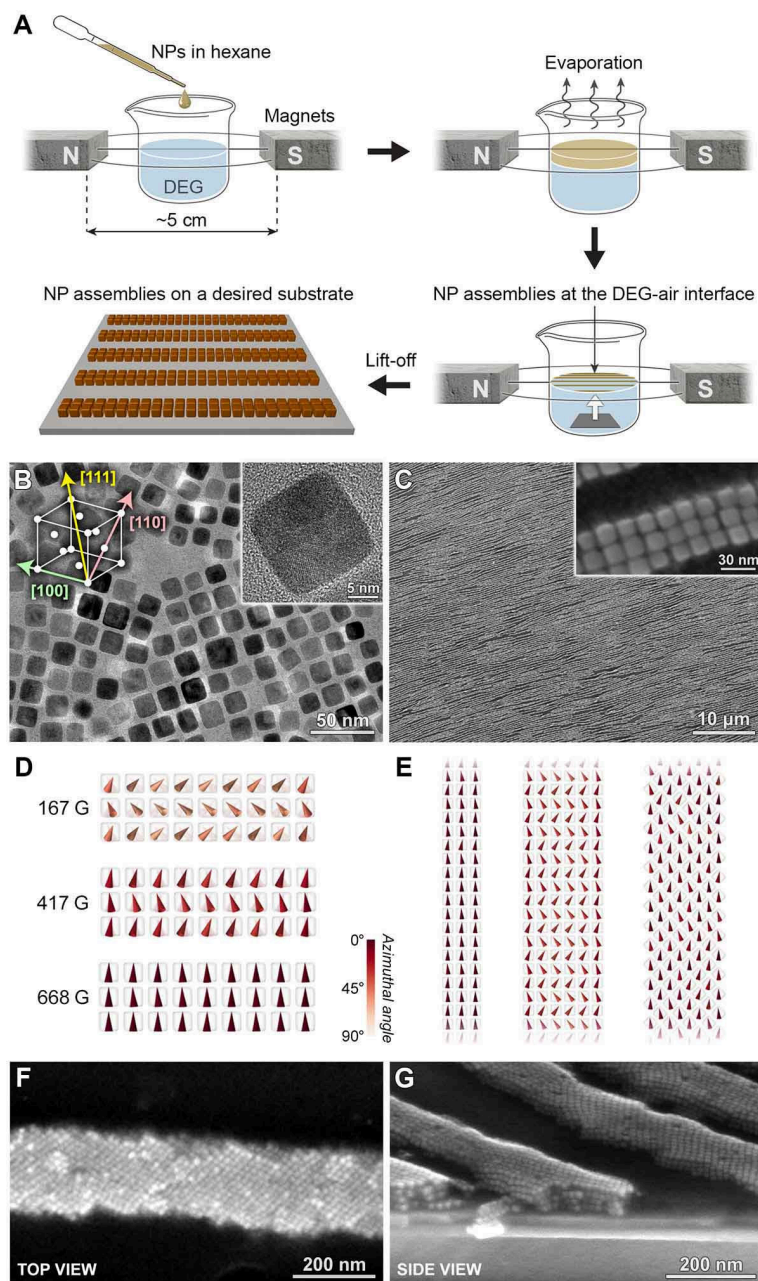


Figure 33: Self-assembly of one-dimensional nanocube belts. (A) Schematic representation of the experimental setup. (B) Low- and high-magnification transmission electron microscopy (TEM) images of the building blocks, ~ 13-nm  $\text{Fe}_3\text{O}_4$  nanocubes. The [111], [110], and [100] crystallographic directions correspond to the easy, intermediate, and hard axes of magnetization, respectively. (C) Low- and high-magnification scanning electron microscopy (SEM) images of belts<sub>100</sub>. (D) Averaged orientations of dipoles in a nine-cube wide belt<sub>100</sub> in the presence of increasing magnetic fields. (E) Orientations of dipoles in belts<sub>100</sub> of different widths and in a belt<sub>110</sub> under a relatively weak external field ( $H = 167\text{ G}$ ). (F and G) Top and side views of belts<sub>110</sub> by SEM.

and point in random directions. In the presence of an external magnetic field, the collective dipoles are partially aligned with the field direction, which allowed for the cooperative magnetic dipole-dipole coupling between the NCs. The resulting chains of single particles further aggregated as the solvent evaporated, ultimately giving rise to higher-order superstructures at the solvent-air interface. These superstructures were transferred onto a carbon-coated copper grid or a silicon wafer for inspection (Figure 33 a). On the basis of electron microscopy images, fewer than an estimated 1% of NCs remained unassembled.

The nature of these superstructures strongly depends on the surface concentration of NCs,  $\chi$ , where  $\chi = 1$  corresponds to a densely packed monolayer of NCs coated with inter-penetrating monolayers of OA. For  $\chi < 0.2$ , no long-range or well-defined structures were observed. However, when  $\chi \approx 0.2$ , NCs assembled into parallel arrays of one-dimensional (1D) belts [377] with high aspect ratios (2 to 3 NCs across and as long as  $100\ \mu\text{m}$ ; Figure 33 c), oriented parallel to the applied field. NCs within these belts had their [100] crystallographic axes oriented parallel to the belts (inset); we refer to them as belts<sub>100</sub>. This arrangement of NCs maximized the cube-cube contact within the assemblies, i.e., the assemblies were dominated by the shape anisotropy of the particles. The widths of these belts grew with increasing  $\chi$  and decreasing  $H$  values. The experimental formation of belts<sub>110</sub> was observed in a narrow range of  $1 < \chi < 1.5$  (Figure 33 f,g). The growth of belts superstructures tilted with respect to the liquid-air interface could be induced by modifying the direction of the applied magnetic field. When the field was perpendicular to the liquid-air interface, the NCs assembled into arrays of pillars. Similar to the belts parallel to the interface, individual

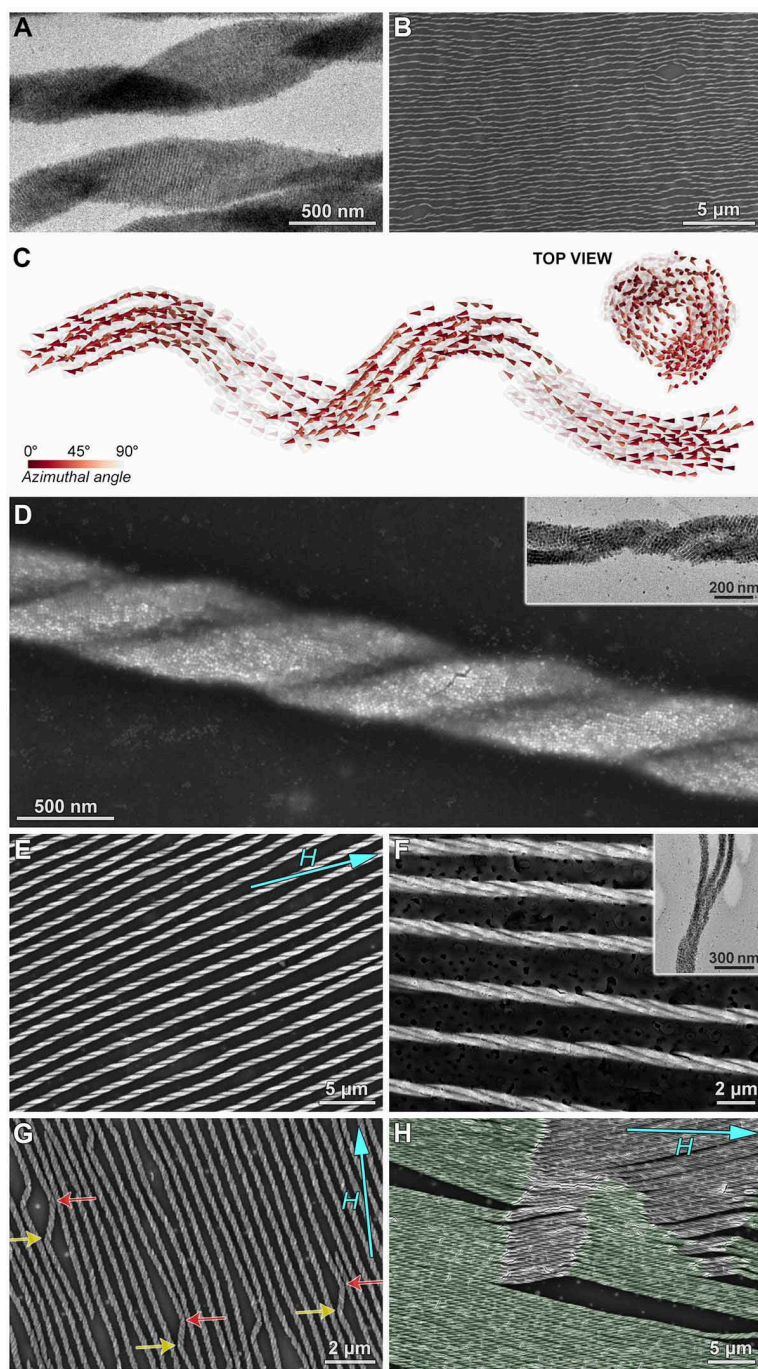


Figure 34: Self-assembly of helical nanocrystal superstructures. (A) TEM image of individual single stranded helices. (B) SEM image of a large array of single-stranded helices. (C) Snapshots from Monte Carlo simulations of a one-dimensional belt folding into a helix. (D) SEM image of a well-defined double helix. Inset shows a TEM image of two belts wrapping around each another. (E) SEM image of an array of double helices. (F) An array of triple helices and (inset) the end of a triple helix. (G) SEM image showing self-healing of double helices (“chirality self-correction”). Yellow and red arrows indicate sites of chirality inversion. (H) Collective switching of chirality. Gray and green colors indicate patches of right- and left-handed helices, respectively. In (E), (G), and (H), blue arrows show the direction of the applied magnetic field.

pillars repelled one another in the presence of the magnetic field, which resulted in their hexagonal close packing.

The most striking superstructures were observed at  $\chi > 1.5$ , where the NCs tend to orient their [111] axes – that is, the “easy” axes of magnetization – along the magnetic field lines (Figure 33b). Because of this arrangement, the belts spontaneously folded [378], giving rise to single-stranded helices [320] (Figure 34a). Similar to the belt superstructures discussed above, the experimentally observed helices were evenly spaced and spanned long distances of up to several hundred micrometers (for example, see Figure 34b). Apparently, the properties of these helices were mostly governed by the surface concentration of the NCs. High values of  $\chi$  entailed large effective magnetic fields, thus promoting a rearrangement of the NCs from the original belt<sub>100</sub> ensemble, i.e., gradually decreasing the helical pitch. At the same time, high  $\chi$  values contributed to the widening of the helices, i.e., decreasing inter-filament distances. We also observed that individual single-stranded helices tended to wrap around each other to form double- (Figure 34 d,e) or even triple- (Figure 34f) stranded helices.

The relatively thin helices prepared at  $1.5 < \chi < 2.0$  comprised equal populations of intermixed left- and right-handed structures, all oriented parallel to the applied field. A right-handed helix neighboring a left-handed one is shown in Figure 34a (top and bottom), respectively. At higher ( $\chi > 2.0$ ) coverages, however, long axes of the helices were tilted with respect to the external field, with the tilt angles  $\theta$  increasing with increasing  $\chi$  values. At the same time, they observed that the helices were mostly of the same handedness (e.g., Figure 34e). A clue to the origin of this selectivity is provided by experiments that yielded ill-defined mixtures of right- and left-handed helices (e.g., Figure 34g,h); these two types of helices were tilted at  $+\theta$  and  $-\theta$  angles with respect to the external magnetic field. All NC assemblies were oriented in the same direction and have the same handedness

probably to maximize packing within a given area. There was no intrinsic preference for helices of either handedness; each experiment began with the nucleation of either left- or right-handed helices with equal probabilities. As the assembly progressed from one side of the dish to the other, however, the chirality of pre-formed helices determined those of their neighbor, and this process continued to yield large (up to 1 mm<sup>2</sup>) domains of “enantiopure” helices.

However, defects were occasionally observed: the red arrows in the ensemble of right-handed helices in Figure 34g point to sites where chirality inversion took place, giving rise to segments of left-handed structures. Segments of the “wrong” chirality were relatively short; the tendency to maximize packing provided the helices with the ability to “correct” their chirality, as denoted by the yellow arrows in Figure 34g. They also observed “collective switching of chirality”: when a critical number of helices changed their handedness, a domain of inverted helices was stably propagated (see Figure 34h).

### Modeling the NCs and their interactions

To perform reliable simulations of the observed superstructures and phenomena, the SPM characteristics of NCs need to be properly described, as well as the experimental conditions under which they self-assemble. In experiments, the NCs self-assembly was triggered by a relatively fast evaporation of hexane. Therefore, both **kinetically** and **thermodynamically** controlled processes could, in principle, take part. As hexane evaporates, individual NCs are less prone to solvation and their bulk vdW coupling drives their self-assembly. However, magnetic forces are guiding these self-assembly processes: the Zeeman coupling tends to align the dipoles along the field, Magnetocrystalline anisotropy (MA) prefers them to be oriented along the NC body diagonals. The coupling between magnetic dipoles (*dd*-coupling) causes attraction dipoles when they are oriented within a cone with an azimuthal angle of  $\theta < \cos^{-1}(1/\sqrt{3}) \approx 54^\circ$ . The external magnetic field,  $H$ , also combines with



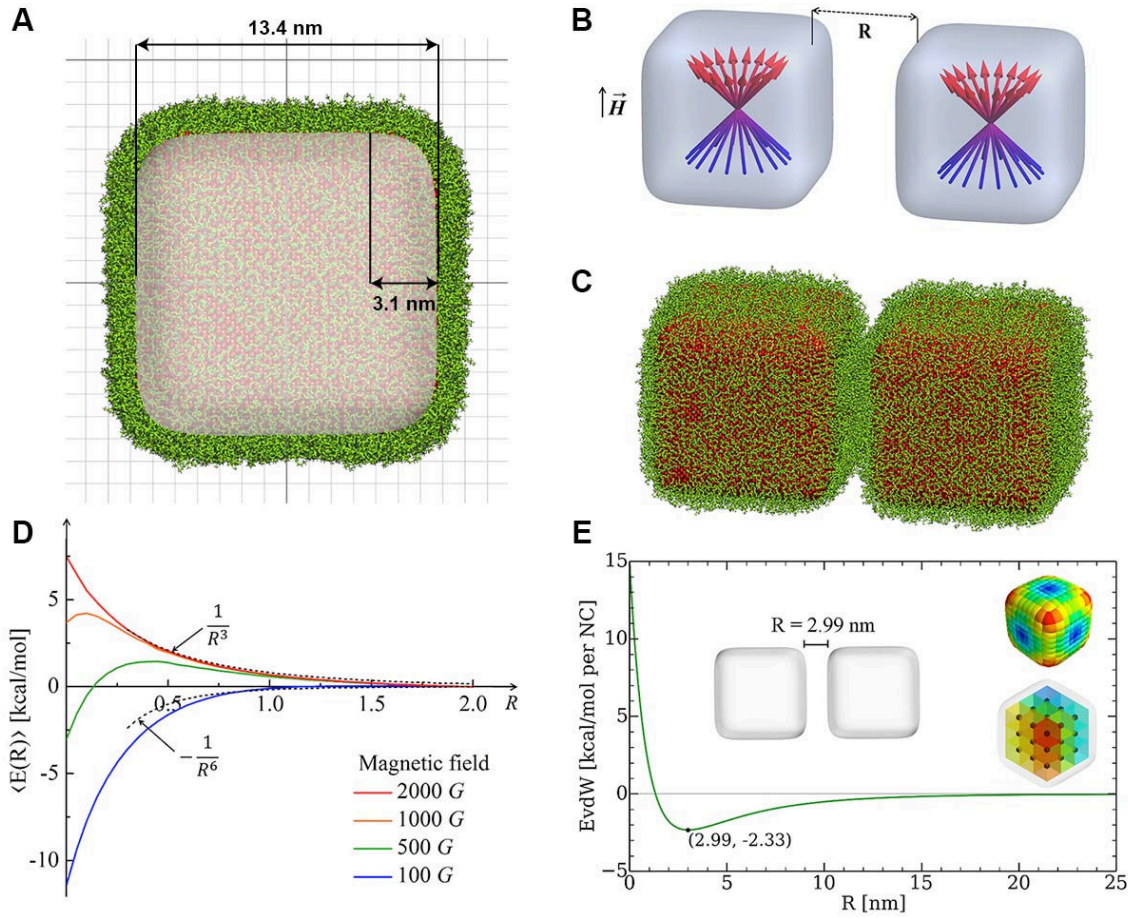


Figure 35: (A) Atomistic model of a single  $\text{Fe}_3\text{O}_4$  nanocube functionalized with oleic acid ligands. The shape of the inorganic core is based on averaging of multiple TEM images of individual nanocubes. Corner bluntness,  $\rho$ , is defined as the ratio of the rounding radius to the side length, and varies between 0% for a perfect cube and 50% for a sphere. (B) Two superparamagnetic nanocubes with side length  $a$  positioned side by side and aligned face-to-face. (C) Atomistic model of two nanocubes coated with oleic acid ligands. (D) Field-dependent average magnetic energy  $\langle E(R) \rangle$  of two nanocubes at temperature,  $T = 300$  K. The magnetic energy of two isolated cubes is set as zero. Weak- and strong-field asymptotic dependencies are shown by dashed black lines. (E) The effective vdW potential associated with bulk nanocube coupling. *Top inset:* surface elements (color scale from blue to red corresponds to the increase of the surface area per element) used in the repulsive part of the vdW coupling energy ( $E_W^{rep}$  in Equation 3.15). *Bottom inset:* subdivision of a nanocube by 27 identical volume elements (colored for clarity) used in the attractive part of the vdW coupling energy ( $E_W^{attr}$  in Equation 3.15).

*dd*-coupling (magnetic susceptibility) to form an effective local magnetic field,  $B$ , which affects the behavior of magnetic dipoles and the self-assembly of superstructures.

**Model of the NCs:** SPM NCs were modeled by a cuboid shape,  $x^6 + y^6 + z^6 = (a/2)^6$ , where  $a = 13.37$  nm is the edge length (Figure 35 A). An atomistic model of the NCs coated with oleic acid (OA) ligands was constructed to estimate their surface vdW coupling energy (Figure 35 C), which was  $\approx 700$  kcal/mol per NC surface in vacuum. Although this large surface vdW coupling could only take place upon a complete evaporation of excess solvent, it does provide a theoretical estimate of its limiting (maximum) value. The actual vdW coupling strength used in simulations was scaled down from this value since the NCs were supposed to self-assemble while in solvent. In our Monte Carlo (MC) simulations and semi-analytical studies, NCs are described as rigid bodies enclosing the NC cores.

At room temperature, small ( $d < 26$  nm [379]) magnetite SPM NCs possess a super-dipole (single magnetic domain) whose orientation is thermally fluctuating [380]. We modeled this by placing a single magnetic dipole at the center of each NC, as shown in Figure 35 b. In external magnetic fields, a magnetic super-dipole becomes partially locked to the field by a Zeeman coupling, and its motion is further constrained by a magnetocrystalline anisotropy (MA) [381–383]. Therefore, we included the description of NCs interacting at room temperature with the external magnetic field and with one another by van der Waals (vdW) and magnetic forces. Figure 35 D shows that the average *dd*-coupling energy between two fluctuating dipoles positioned side-by-side and affected by the MA and the Zeeman coupling changes with distance from  $-1/R^6$  (attraction) for randomly fluctuating magnetic dipoles (Keesom-like weak-field regime of SPM NCs) to  $+1/R^3$  (repulsion) for strongly coupled ferromagnetic dipoles [384] (strong-field regime of SPM NCs). These simple semi-analytical

results illustrate that a careful modeling is necessary to describe the rich spectrum of observed superstructures.

**NC interactions:** The total energy of an ensemble of NCs is given by:

$$E_T = \sum_{i=1}^{N_p} E_i + \sum_{i=1}^{N_p} \sum_{j=i+1}^{N_p} \left( E_{ij}^{dd} + E_{ij}^{vdW} \right) \quad (3.11)$$

where  $E_i$  is the total energy of an isolated NC in a given orientation defined as the sum of its Zeeman and MA energies,  $E_i = E_i^Z + E_i^A$ . The Zeeman energy is given by

$$E_i^Z = -K_Z (\vec{H} \cdot \vec{M}_i), \quad (3.12)$$

where  $K_Z = 1.647 \times 10^{-2}$  kcal mol<sup>-1</sup> ( $= 2.77 \times 10^{-2} kT$  at 300 K);  $\vec{H} = (0, 0, H_0)$  is the external magnetic field vector (in Gauss units), and  $\vec{M}_i$  is the magnetic dipole unit vector. Magnetocrystalline anisotropy of a nanocube was approximated by a quartic term [379, 385] appropriate to the bulk magnetite (Fe<sub>3</sub>O<sub>4</sub>) with a  $Fd3m$  crystal structure and is given by

$$E_i^A = K_{A1} [(M'_{ix} M'_{iy})^2 + (M'_{ix} M'_{iz})^2 + (M'_{iy} M'_{iz})^2], \quad (3.13)$$

where the quartic-order anisotropy constant,  $K_{A1} = -3.784$  kcal mol<sup>-1</sup> [380, 386, 387], and  $M'_{ix}$ ,  $M'_{iy}$ ,  $M'_{iz}$  are the  $\hat{x}$ ,  $\hat{y}$ ,  $\hat{z}$  components of the magnetic dipole unit vector in the reference NC coordinates. We neglected other corrections of the bulk MA energy related to the cubic shape of the NPs [387, 388]. The quartic term generates easy and hard magnetization axes of the NC, which are oriented along the cube body diagonals and edges, respectively.



In the local dipole approximation, the super-dipole of a single magnetic domain is a point dipole located in the center of each NC [44]. Then, the dipole-dipole coupling energy of dipoles in two cubes is given by

$$E_{ij}^{dd} = K_d \left( \frac{\vec{M}_i \cdot \vec{M}_j}{|\vec{r}_{ij}|^3} - \frac{3(\vec{M}_i \cdot \vec{r}_{ij})(\vec{M}_j \cdot \vec{r}_{ij})}{|\vec{r}_{ij}|^5} \right). \quad (3.14)$$

where  $K_d = \mu_0 m_s^2 / 4\pi = 7.973 \text{ kcal mol}^{-1}$ , when the distance between dipoles,  $|\vec{r}_{ij}|$ , is measured in the units of  $a$  (cuboid edge length),  $m_s = M_s \times V = 1.174 \times 10^{-18} \text{ A m}^2$  is the intrinsic magnetic moment of a homogeneously magnetized nanocube, where  $M_s = 480 \text{ kA m}^{-1}$  is the saturation magnetization of a bulk magnetite, and  $V \approx 0.9 a^3$  is the cube volume. Saturation magnetization of magnetite nanocubes can be significantly smaller than that of the bulk material due to the presence of non-collinear (canted) spins showing a spin-glass-like behavior [386, 389, 390]. We assumed that the saturation magnetization of our nanocubes is 10 – 20% smaller than in bulk magnetite because of the spin disorder near the NP surface within the outer 1 nm [391, 392].

We describe the vdW coupling between the NCs by an anisotropic potential that includes bulk vdW attraction of the NC cores in OA solvent, and the steric repulsion between the surface ligands (Figure 35 E),

$$E_{ij}^{vdW} = E_{ij}^{attr} + E_{ij}^{rep}, \quad E_W^{attr} = -\varepsilon_1 \frac{A}{\pi^2} \int \int_{V_i, V_j} \frac{dV_i dV_j}{r_1^6}, \quad E_W^{rep} = \varepsilon_2 K_W \int_{S_i} \frac{dS_i}{(r_2 + \beta)^8}. \quad (3.15)$$

The attraction term is a pairwise Hamaker expression (with a scaling constant  $\varepsilon_1$ ), in which the integral is taken over volumes of two interacting NCs. Each NC is divided into  $3^3 = 27$  identical volume elements over which the integral (sum) is performed,  $A = 3 \text{ kcal mol}^{-1}$  is the Hamaker constant of magnetite in hexane, and  $r_1$  is the distance between the centers of two volume elements in different NCs. The repulsion term is expressed as an integral (sum) over 386 surface elements

that subdivide the NC's cuboid surface (the elements have different surface areas). Here,  $r_2$  is the distance between the center of a surface element of a chosen NC and the surface element of the interacting NC. The shape of the vdW potential is tuned by fitting parameters  $\varepsilon_1 = 130$ ,  $\varepsilon_2 = 290$ , and  $\beta = 9.56$  nm, in such a way that the energy minimum of the effective vdW potential is located at the average surface-to-surface distance of two face-to-face NCs, as in the experiments (2.99 nm). The strength of the vdW coupling (the depth of the potential curve) is defined by a constant of  $K_W = \varepsilon_1 \frac{A}{\pi^2} \left( \frac{0.9a^3}{27} \right)^2 = 2.5 \times 10^5 \text{ nm}^6 \text{ kcal mol}^{-1}$ , which yields maximum vdW interaction energy of  $2.33 \text{ kcal mol}^{-1}$  per NC. The total energy,  $E_T$ , is used in simulations of the NC self-assembly performed with a Markov Chain Monte Carlo (MCMC) algorithm using the Metropolis scheme [393]. The Gilbert–Johnson–Keerthi (GJK) algorithm [328] is used to check for overlapping between NCs.

Artem Baskin performed semi-analytical simulations of systems comprising a small number (2 or 3) of NCs in frozen positions, to elucidate how magnetic interactions favor special NC orientations. Towards achieving this goal, he evaluated the magnetic energies averaged over magnetic degrees of freedom,

$$\langle E_T \rangle = \frac{\int E_T e^{-E_T/kT} \prod_i d\Omega_i}{\int e^{-E_T/kT} \prod_i d\Omega_i}. \quad (3.16)$$

Here,  $d\Omega_i = \sin \theta_i d\theta_i d\varphi_i$  and  $\theta_i, \varphi_i$  are the spherical angles of individual magnetic dipoles in the laboratory's system of coordinates.

### **MC simulations of belt structures**

MC simulations generate trajectories of configuration samples which should converge to an equilibrium state of the NCs system (canonical ensemble). In our MC simulations, we computed the total energy difference,  $\Delta E_T$ , between the system configurations before and after we perform the proposed nanocube or dipole movements. A new configuration is accepted when  $\Delta E_T \leq 0$  or when a random

number in the interval  $[0,1)$  is smaller than  $e^{-\Delta E_t/kT}$ . In each MC cycle, we varied the position, orientation, and magnetic dipole orientation for all NCs in random order. The MC codes handled the configurational entropy of the NCs and their spins. Other entropy contributions, such as solvent, ligands, depletion, etc. were not modeled, but could in principle be included [166, 394–403]. The expectation values can be obtained by averaging over the configurations in a stabilized trajectory, in analogy to averaging over an equilibrium ensemble (Equation 3.16).

Using a MC simulation code that we developed, we first modeled different belt structures observed in the experiments (Figure 33 C, F, G). We studied the orientations of magnetic dipole moments for spatially fixed and perfectly aligned NCs structures (Figure 36). The results in Figure 33 D show that dipole orientations in individual NCs of the belts are determined by the competition between dipole-dipole interactions, MA, and Zeeman coupling to an external field. Under a relatively weak field (167 G), the dipoles were arranged in a “zigzag” configuration favoring MA. As the field strength is increased to 417 G, the dipoles partially underwent a zigzag-to-parallel transition, and became more aligned with the external field. Eventually with a field strength of 668 G, all dipoles were oriented along the field lines.

Next, we investigated the magnetic dipole orientations as a function of belt thickness at a weak field strength of 167 G. The results in Figure 33 E show that the dipoles are increasingly decoupled from the external field due to large induced fields generated by the dipoles of other NCs, meaning that MA and  $dd$ -coupling has compensated for Zeeman coupling. Since a parallel arrangement of dipoles is not favorable due to repulsions, the belts could have gradually become thinner as the applied field is increased. When we rotated each cube by  $45^\circ$  such that their  $[110]$  axes were parallel to the field direction, the dipoles were again oriented along the field. Although this  $\text{belts}_{110}$  structure is less favorable than  $\text{belts}_{100}$  from the point of vdW interactions due to their ridged sides, magnetization

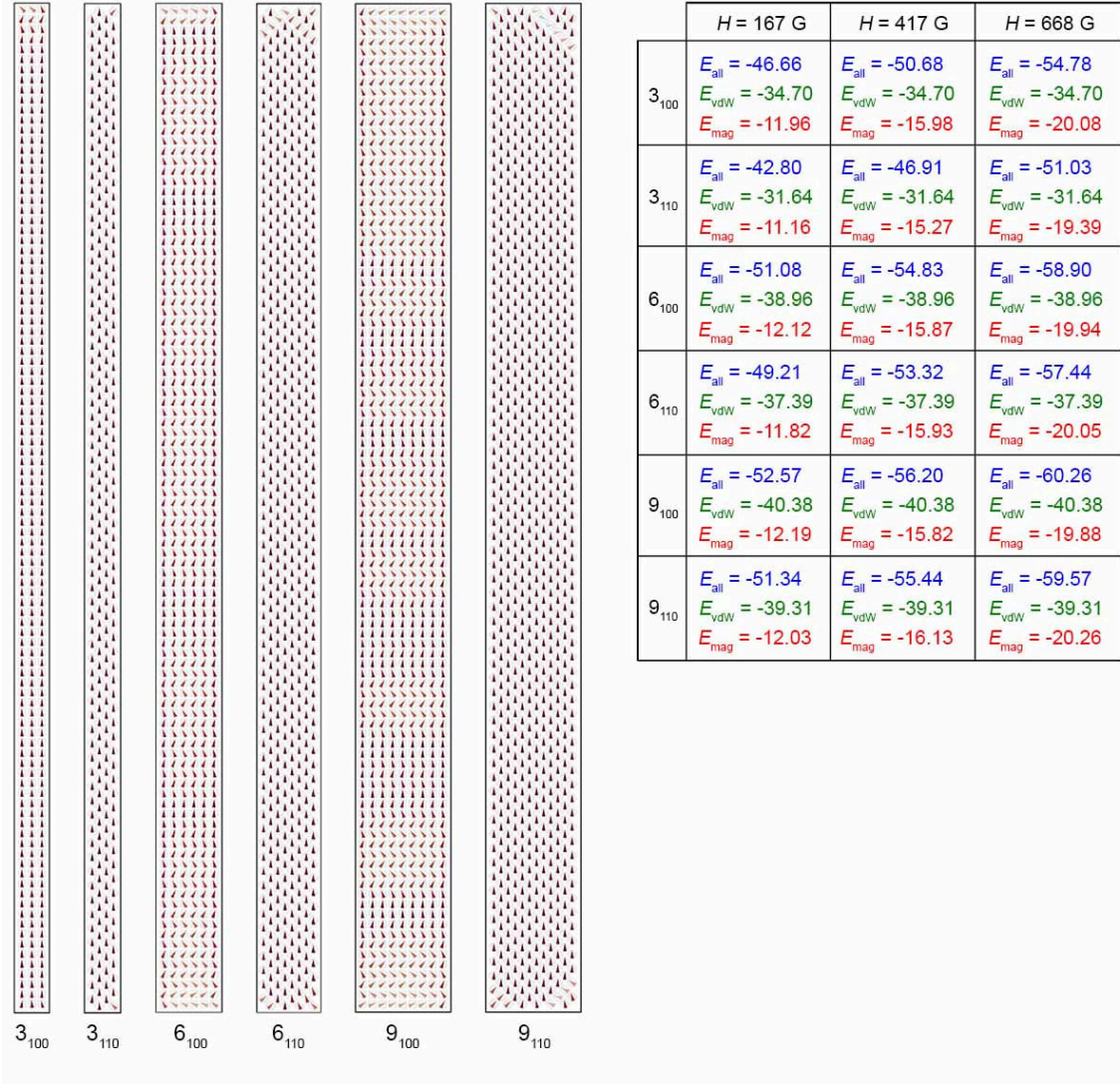


Figure 36: Potential energies of self-assembled belts as a function of belt thickness, arrangement of cubes, and strength of the external field. Total magnetic energy,  $E_{\text{mag}}$ , is the sum of the Zeeman energy,  $E_z$ , dipole-dipole energy,  $E_{dd}$ , and anisotropy energy,  $E_a$ :  $E_{\text{mag}} = E_z + E_{dd} + E_a$ . Total potential energy,  $E_{\text{all}}$ , is the sum of total magnetic energy and the van der Waals energy:  $E_{\text{all}} = E_{\text{vdW}} + E_{\text{mag}}$ . All values are in  $\text{kcal mol}^{-1}$  per nanocube. Averaged orientations of dipoles in different belts (left) are shown for weak external field ( $H = 167 \text{ G}$ ). The belts comprise the following numbers of nanocubes, from left to right: 300, 284, 600, 564, 900, 846. All energy values and dipole configurations shown in the figure are averaged over 10000 MC steps.

along the  $[110]$  direction (“intermediate” axis) occurs more easily than along the  $[100]$  (“hard”) axis  $[404, 405]$ . We have also simulated a multi-layered  $\text{belt}_{100}$  structure (Figure 37), where the dipoles are arranged in zigzag arrangement in two dimensions, leading to a complex formation of “onion-like” dipole configurations which has counter-propagating fluxes in neighboring flux-closure rings  $[188, 406]$ , a phenomenon previously studied in Prof. Kral’s group..

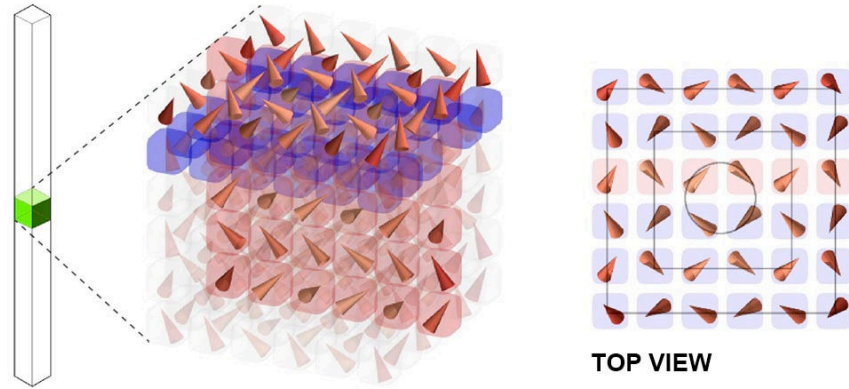


Figure 37: Averaged orientation of dipoles in a thick filament under a relatively weak external field ( $H = 167$  G). The top two layers are purposely separated from the structure (left) to better illustrate the dipole arrangement.

Next, we looked into the interactions between two  $\text{belt}_{100}$  structures. In experiments, belt structures not only have well defined width, but also a defined separation distance between them (Figure 33 C inset). The magnetic potential energy,  $E_{mag} = E_z + E_{dd} + E_a$ , as a function of separation distance of structures with different sizes is shown in Figure 38. The results on the left side of Figure 38 show that, under weak fields, narrow belts repel each other whereas the wide ones attract. Therefore, if the dipoles assume zigzag configurations the belts attract each other, while they repel when the dipoles are largely parallel. The results in Figure 38 right side show that slightly disorganized belt structures, prepared by letting the NCs move with vdW interactions for a short time, always repel each other.

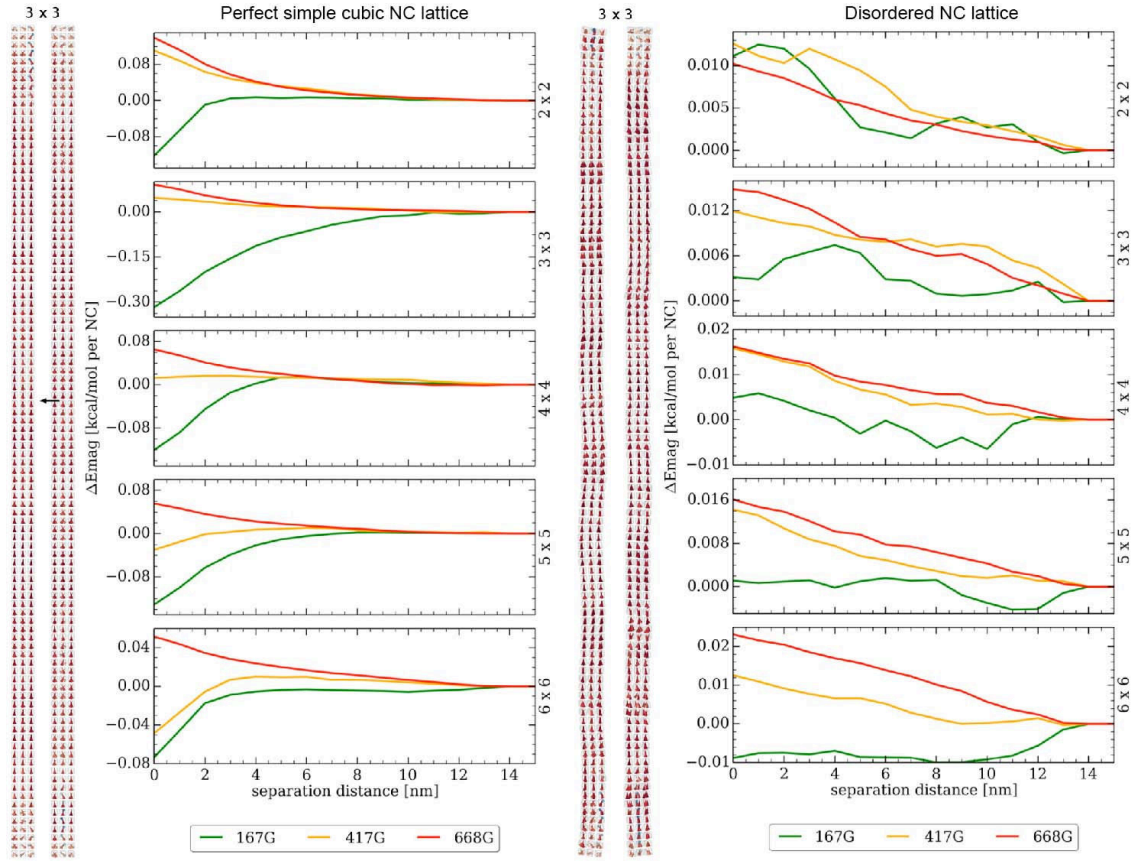


Figure 38: Potential energy dependence on the distance between two perfectly aligned and slightly disordered belts<sub>100</sub>. In each case, total magnetic energy,  $E_{mag} = E_z + E_{dd} + E_a$ , was averaged at each distance over 5000 MC steps of two belts approaching each other as a function of their separation.  $E_{mag}$  of two isolated belts was set as zero. The cases of weak, intermediate, and strong external magnetic fields ( $H = 167, 417, 688$  G, respectively) are shown for two  $n \times n \times 100$  belts, where  $n = 2, 3, 4, 5$ , and 6.

In summary, belts structures switch from zigzag dipole configurations (attraction) to parallel (repulsion) as the external field strength increases. This mechanism stops their width from increasing in high fields, which is in agreement with the experiments. However, in low fields, the zigzag configuration would widen their width indefinitely, which is contrary to observations. In reality, the slight disorder within the belt structures can lead to a small repulsion between two belts which can overcome the zigzag attraction.



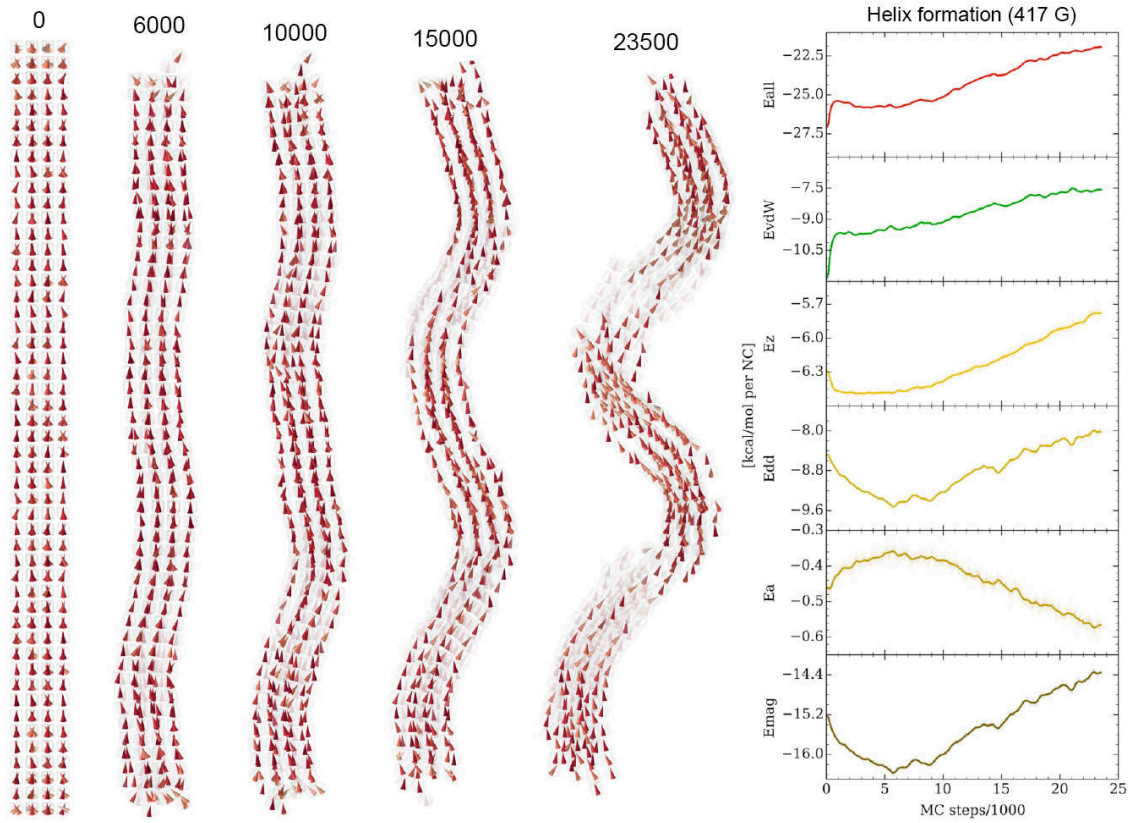


Figure 39: Snapshots of nanocube assemblies during helix formation (left) and the contributing energies (right) ( $E_z$ , Zeeman energy;  $E_{dd}$ , dipole-dipole energy;  $E_a$ , anisotropy energy;  $E_{mag} = E_z + E_{dd} + E_a$ , total magnetic energy;  $E_{vdW}$ , van der Waals energy;  $E_{all} = E_{vdW} + E_{mag}$ , total potential energy). The curves in the plots were obtained from smoothing (window = 500 steps) the original data (shown as thin lines).

### MC simulations of superhelices

We have shown that magnetic interactions favor belt<sub>110</sub> because of the arrangement of individual NCs enabling easy magnetization, whereas vdW interactions disfavor belt<sub>110</sub> because of its ridged sides. Despite the favorable arrangement of dipoles in the direction parallel to the long axis of belt<sub>110</sub>, the zigzag configuration is preserved in multi-layered belts<sub>110</sub> in the direction perpendicular to the liquid-air interface. A smooth (non-zigzag) connectivity of the dipoles following the nanocubes' easy axis can be resolved if the structures are further reconfigured by “side-stepping” of the NCs, which eventually leads to helical structures.

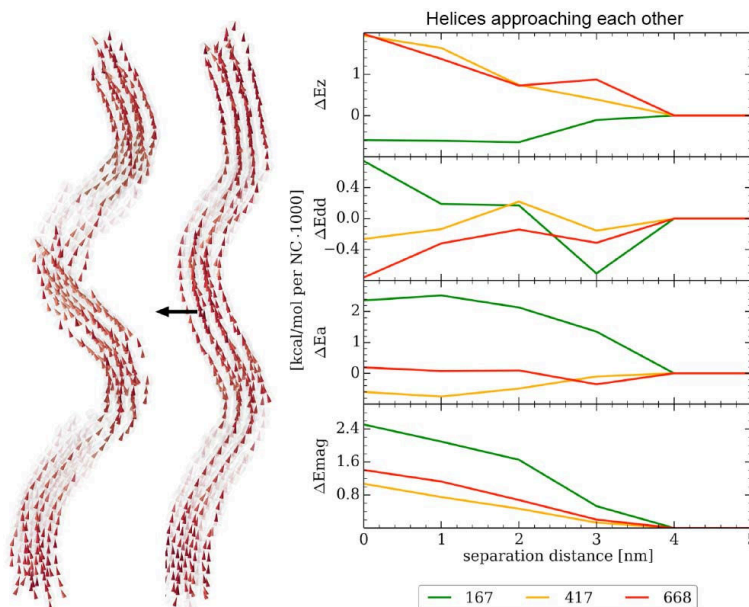


Figure 40: Potential energy dependence on the distance between two helices approaching each other. Zeeman energy,  $E_z$ ; dipole-dipole energy,  $E_{dd}$ ; anisotropy energy,  $E_a$ ; and total magnetic energy,  $E_{mag} = E_z + E_{dd} + E_a$  at each distance were averaged over 5000 MC steps. Colors correspond to different values of the applied magnetic field: 167 G (green), 417 G (yellow), 668 G (red).

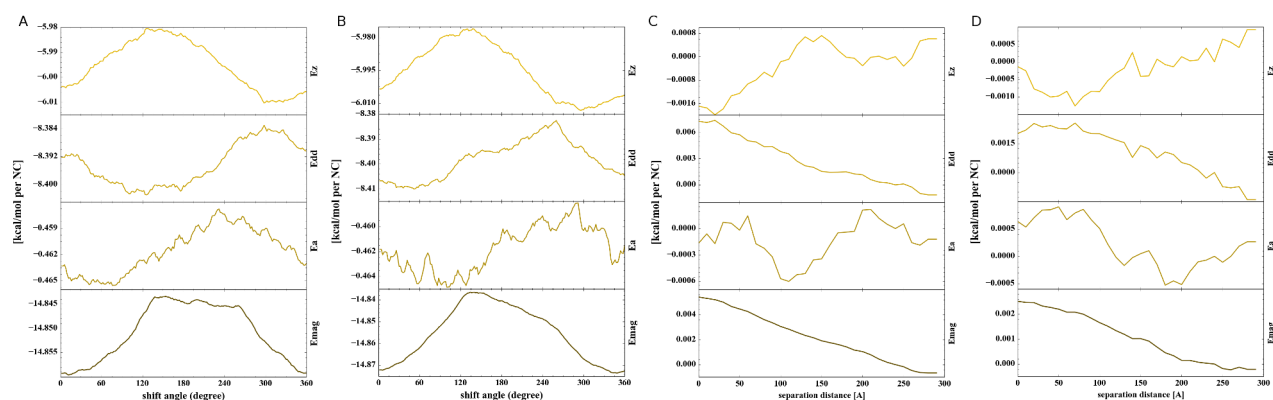


Figure 41: Potential energy dependence of helices of the same (A) and opposite (B) handedness as a function of the phase angle. Magnetic potential energy (in kcal/mol per particle) of helices of the same (C) and opposite (D) handedness as a function of reciprocal distance (the helices are parallel). The magnetic interaction energy at large distance is set as zero.



We prepared 4 by 4 by 100 filaments and investigated their deformation (helical formation) in MC simulations. Despite the small widths of the filaments, the simulation parameters (vdW interaction strength) have been scaled to favor helical formation. With the optimal set of parameters, we have observed the formation of helices at a much smaller scale than in the experiments (Figure 34 C). We observed that the magnetic dipoles mostly follow along the direction of the helices. Figure 39 shows snapshots from MC simulations of NC assemblies during the helix formation and the corresponding energies (Zeeman energy  $E_z$ , dipole-dipole energy  $E_{dd}$ , anisotropy energy  $E_a$ , total magnetic energy  $E_{mag} = E_z + E_{dd} + E_a$ , van der Waals energy  $E_{vdW}$ , and the total potential energy  $E_{all} = E_{vdW} + E_{mag}$ ). The loss of vdW coupling and, to some extent, the Zeeman and  $dd$ - coupling in helices is compensated by the gain in  $E_a$  and the growth of entropy of the looser and more randomly organized NCs similar to experiments (Figure 34 D inset). Helices formed by thick filaments should be less prone to entropic forces due to stronger effective magnetic fields.

Next, we took the helical structure from our MC simulation and modeled the interaction potential energies between a pair of helices, as a function of the separation distance (Figure 40) and phase angle (Figure 41), depending on their handedness (the same vs. the opposite chirality). These results show that the most favorable configuration of two neighboring helices is when they are in phase (i.e., shift angle =  $0^\circ$ ), irrespective of their reciprocal handedness (Figure 40 A, B). We also found that thin helices of the same handedness repel each other slightly stronger than helices of opposite handedness (Figure 42 C, D).

### MC simulations of NC self-assembly

To better understand the self-assembly of magnetic NCs, we studied the effect of NC concentration by MC simulations. We modeled systems containing 600 and 900 NCs randomly distributed within a cylindrical boundary with radius 150 nm and height 800 nm. These NCs interacted with each other

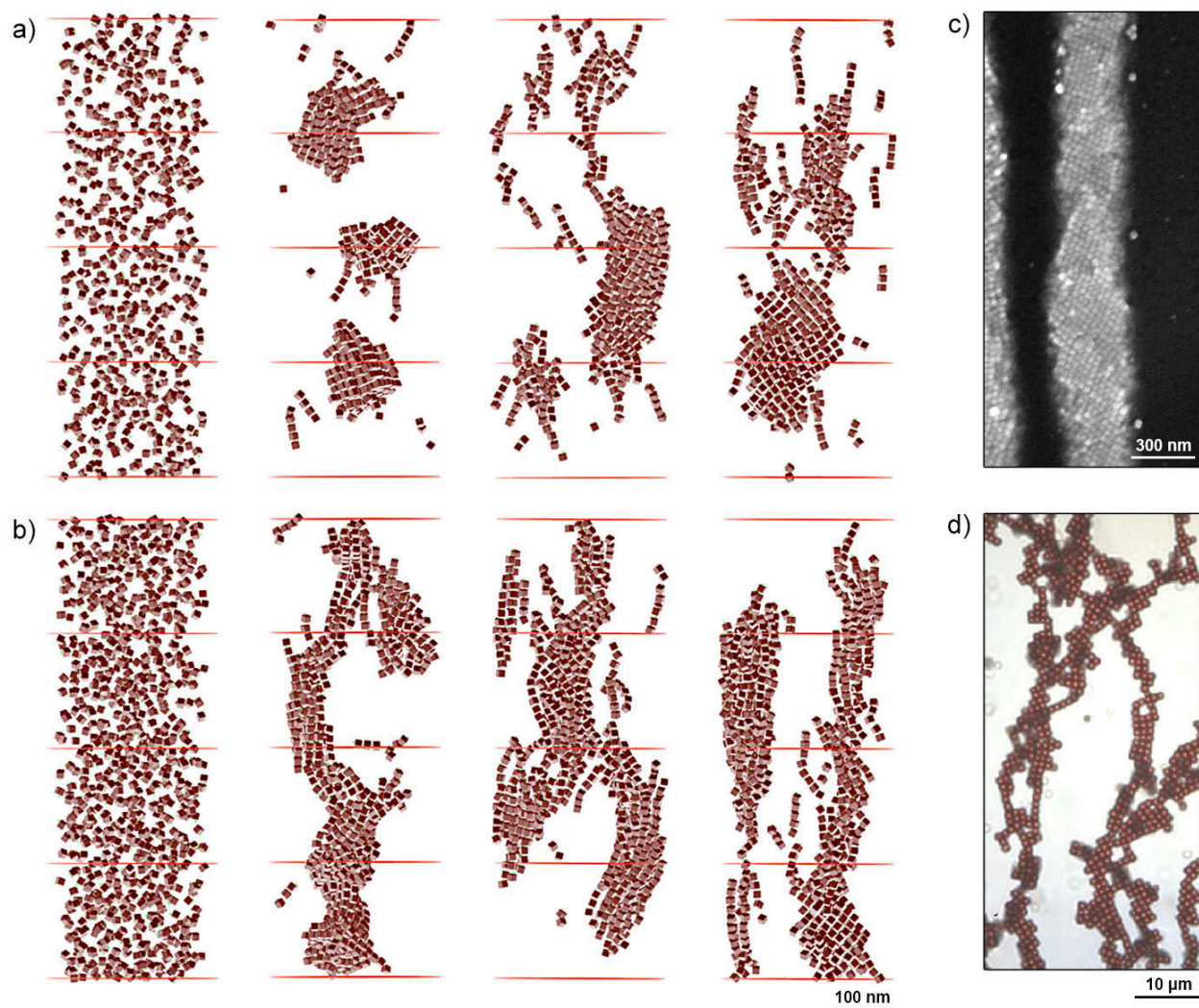


Figure 42: (a and b) MC simulations of NC self-assembly in different applied magnetic fields. (a) and (b) show systems comprising 600 and 900 particles, respectively. Left to right: initial configurations of the two systems, and configurations obtained under 167 G, 417 G, and 668 G. (c) SEM image showing a diamond-type arrangement of NCs within a one dimensional filament. (d) Optical micrograph of an ensemble of 0.9 nm  $\text{Fe}_2\text{O}_3$  NCs deposited on a glass slide in the presence of an applied magnetic field. In all simulations and experiments shown in this figure, the applied magnetic field was oriented vertically.

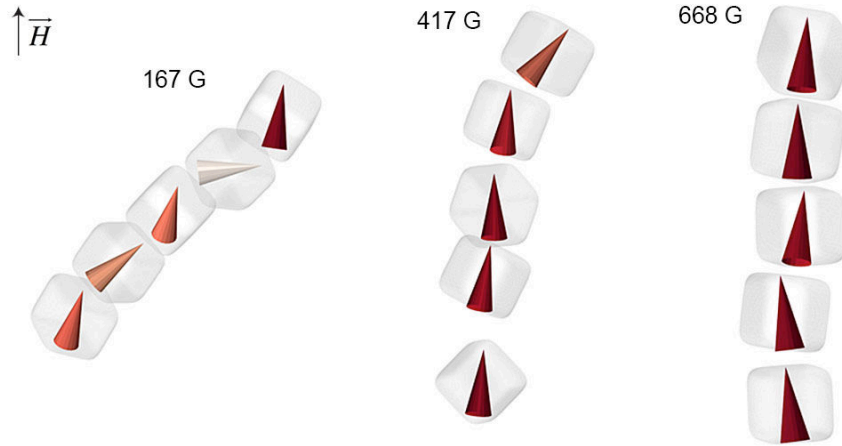


Figure 43: Short NC chains extracted from the MC simulation shown in Figure 42, showing the dependence of the magnetic dipole orientation on the strength of the applied magnetic field. The magnetic dipoles are colored based on their tilt angle with respect to the applied field (vertical). The dipoles within the chains assume a zigzag arrangement in weak fields and vertical arrangement in stronger fields.

by vdW and magnetic interactions under different field strengths. Figure 42 a and b show snapshots of our simulations obtained after more than 150000 MC steps. Depending on the field strength and concentration, different self-assembled structures emerged: in the 600-NC system, we observed the formation of short chains of several NCs tilted with respect to the applied field, as well as patches with a belt<sub>110</sub>-like structure (Figure 42 a right). The 900-NC systems have elongated structures that spanned the height of simulation box (similar to Fe<sub>2</sub>O<sub>3</sub> NC structures, Figure 42 d), and showed an increased tendency toward twisting. In general, all the structures that self-assembled in weaker fields were more tilted with respect to the field direction, as illustrated by short chains extracted from the simulations (Figure 43). These results are in agreement with the experiments: for example, one-dimensional belt<sub>110</sub>-like filaments (Figure 42 c) are assembled at lower NC concentrations, whereas helical superstructures are observed at higher NC concentrations. The resulting tilt angle of the self-assembled structures is clearly correlated with the mutual orientation of the neighboring magnetic dipoles.

### Finding the origin of chirality

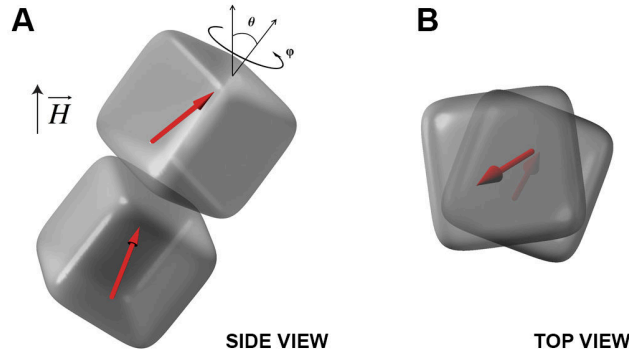


Figure 44: (A) Typical configuration of two cubes in an external field,  $H = 167$  G (vertical z-orientation) at  $T = 300$  K (bulk vdW coupling is reduced by 1/2 with respect to the nominal value). (B) View along the cube axis reveals that the NC pair is (transiently) chiral. Magnetic dipoles are represented by red arrows.

Based on the results we have so far, the formation of helical structures are believed to be induced by a transient chiral nucleus formed by two SPM nanocubes with vdW coupling in a magnetic field, as shown in Figure 44. NCs in this configuration can possess either left or right chirality. We have separately modeled two NCs, using both local and non-local dipole approximations, to evaluate the formation of this transient “chiral seed”. The non-local dipole approximations split the magnetic dipole of each NC into 27 smaller equivalent dipoles (all with the same orientation) distributed evenly in the NC volume, which is similar to the Hamaker summation approach for evaluating bulk vdW.

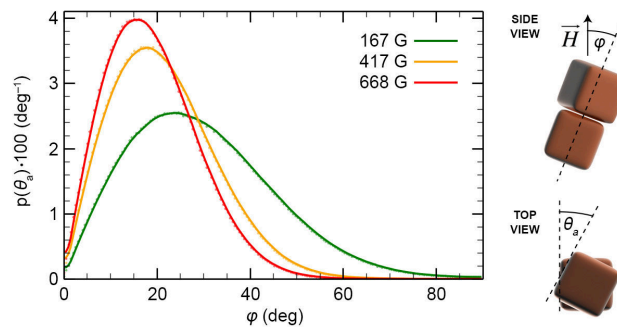


Figure 45: Tilt angle ( $\varphi$ ) distributions under various applied magnetic fields for a pair of two interacting cubes (in the case of the weak vdW bonds). The symbol  $\varphi$  is defined as the angle between the line connecting the centers of the cubes and the direction of the applied field.

The results in Figure 45 show that the pair of NCs as a whole (center-to-center) is tilted with respect to the applied magnetic field by about  $23^\circ$  in 167 G field,  $17^\circ$  in 417 G field, and  $15^\circ$  in 668 G field, whereas individual NCs are tilted with respect to their center-to-center axis by about  $11^\circ$ . The tilt angles are approximately the same in both the single and distributed magnetic dipole models.

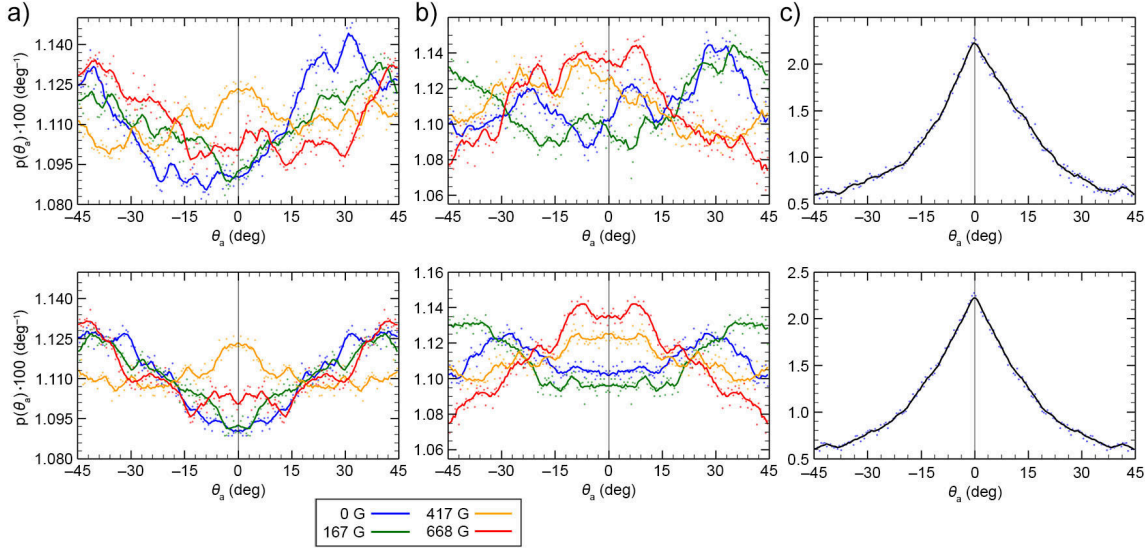


Figure 46: Distribution of the mutual rotation between two re-aligned NPs (see  $\theta_a$  in Figure 45) in external magnetic fields of 0 G (dark blue), 167 G (green), 417 G (dark yellow), and 668 G (red). (a) Results obtained from the single local magnetic dipole model. (b) Results obtained from the distributed dipole model. (c) Results obtained when no magnetic interactions were considered (vdW-only case). The top plots show the original statistically averaged data, and the bottom plots show symmetrized data.

To determine the tendency of NCs to exist in the chiral configuration, we performed statistical averaging over 500 MC trajectories each with 12000 steps, and obtained the NC mutual rotation angle,  $\theta_a$ , after realigning the NCs to a mutual plane. Positive and negative values of  $\theta_a$  indicate clockwise and counterclockwise rotations of one NC with respect to the other. The results in Figure 46 a b (top) show that there are relatively large fluctuations and asymmetry in the plots. This is likely the result of poor averaging (convergence), which can be attributed to a large configuration phase space and its partly biased sampling (repositioning of the two NCs and their separation). To obtain at least a qualitative measure of the NC pair's chirality, we averaged the original and the  $x = 0$  axis-

mirrored solutions. We can see that practically all the symmetrized curves presented in Figure 46 a b (bottom) exhibit features (local maxima at  $\theta_a$  different from  $0^\circ$  and  $45^\circ$ ) indicating preferential chiral arrangements of the NCs. Moreover, the obtained distributions also depend on the magnetic dipole model used. In order to examine the role of the vdW interactions in the formation of chiral configurations (mutual shifting and alignment of the faces of adjacent NCs), we have analyzed the arrangements of two NCs interacting solely by vdW forces. As expected, the plots of probability vs.  $\theta_a$  showed a pronounced peak at  $\theta_a = 0$ , indicating the importance of magnetic dipole interactions in the emergence of chiral assemblies.

Artem Baskin also studied the same 2-NC system using semi-analytical averaging over the dipole configurations in fixed NCs. He considered two NCs positioned one on top of the other, which were tilted as a rigid body with respect to the direction of the external field. Then, the top NC was allowed to rotate around the common axis without taking the vdW coupling into account.

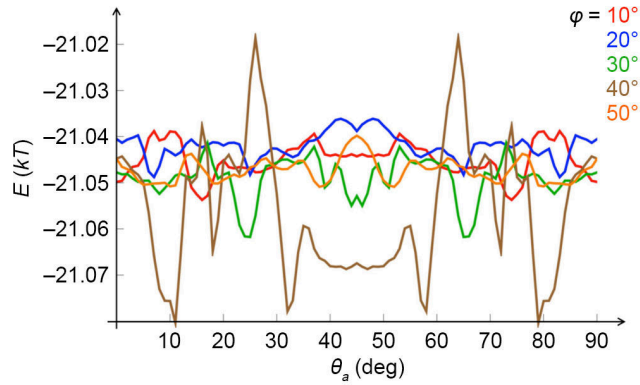


Figure 47: Average magnetic energies of two cubes tilted with respect to the external magnetic field (167 G) as a function of the mutual rotation of cubes around a common axis,  $\theta_a$ , at different tilt angles,  $\varphi$ . Energies are given in units of  $kT$  (at  $T = 298$  K).

Figure 47 shows a typical average magnetic energy profile as a function of the rotation angle  $\theta_a$  (spanning  $0^\circ$  to  $90^\circ$ ) for different tilt angles  $\varphi$  in a weak field (167 G). As one can see, there are sets of local energy minima signifying chiral configurations. For example, for  $\varphi = 30^\circ$  (the green

curve), there are prominent minima around  $25^\circ$  and  $65^\circ$ . For higher tilt angles ( $\varphi > 30^\circ$ ) the local minima are more prominent at  $\theta \approx 45^\circ$ . These conclusions are in agreement with the results of my MC simulations within the local dipole approximation.

These results, and the reasons for the emergence of chirality can be rationalized as follows: in an applied magnetic field, the NC dipoles tend to fluctuate less and prefer to be oriented along the NC diagonal, which points mostly along the field direction. For two such NCs, the dipoles tend to follow each other, ideally pointing along two parallel body diagonals positioned above each other. In contrast, vdW coupling tends to align the NC facets to the greatest extent possible. A compromise between those two extreme cases is a configuration where the two cubes are not in close contact, and are somewhat twisted in 3D with respect to each other. The dipole-dipole interaction is favored more in the twisted configuration (the two dipoles are closer to being parallel).

## Conclusions

We have modeled the SPM characteristics of magnetite NCs and supported the results with analytical calculations. The self-assembly of NCs and the stabilization mechanism of different belts structures and superhelices have been investigated using MC simulations. The results show that the formation of superhelical structures from achiral NCs is due to the complex interactions between magnetic interactions (Zeeman, MA, and  $dd$ -coupling) and vdW interactions, which lead to frustrations in the structures and the emergence of “chiral seeds”.

This study offered important insights in the self-assembly of magnetite NCs. Our observed helical assemblies are prepared from freely self-assembling achiral building blocks, which is in sharp contrast with the vast majority of helical assemblies of NPs reported previously. Most helical structures are made using pre-existing helical templates, such as peptide amphiphiles [407, 408], DNA [335,

409], lipids [410] and synthetic supramolecular templates [411], among others [412, 413]. In systems comprising micron-sized colloids, helical assemblies have been shown to form when packing frustration is induced, which can result either from selecting tailor-made particles or by confining colloids inside thin cylindrical channels. The first strategy is best exemplified in heterodimeric colloidal particles, each comprising a small paramagnetic domain and a large diamagnetic domain [403]. In external magnetic fields, the magnetic domains assembled into one-dimensional chains oriented along the applied field, where the steric bulkiness imposed by the diamagnetic domains forced the assembly into a helical structure [414–417]. The second way to induce packing frustration is to perform self-assembly inside one-dimensional cylinders having internal diameters slightly larger than the diameters of spherical colloids [418–423]. Notably, sharp transitions between disordered and ordered helical assemblies could be observed upon increasing the volume fraction of the spheres inside thin glass capillaries [424]. Analogously, spheres confined to the outer surface of a cylinder assumed a helical arrangement in order to maximize the commensurability with the cylinder circumference [425].



## CHAPTER 4

### CONCLUDING REMARKS

This thesis described several research projects that focused on the structures, properties, and stabilization mechanisms of different self-assembled systems. These projects aimed to provide fundamental understanding of self-assembly principles, and to explain the formation of new superstructures. We have applied mean-field calculations, Monte Carlo simulations, and classical molecular dynamics simulations at the atomistic and coarse-grained levels to study NP membranes and arrays, NP-lipid hybrid systems, superlattices, nanoshells, nanoribbons, and NP superhelices. The computational models used in these studies have accounted for all the interactions between atoms and nanoscale objects, which made them accurate enough for the description of experimental systems. In fact, most of the results from our simulations are in close agreement with experimental observations. By collaborating with other research groups, we have approached the problems from the perspective of a combination of experiments, theoretical analysis, and computational simulations, which provided a comprehensive view of the studied systems. The major contributions of the studies described in this thesis are summarized below:

**Section 3.1 - Coarse-grained MD simulations of NP membranes and capsules:** This study demonstrated the effect of ligands on the structural and mechanical behaviors of NP membranes and capsules. The results emphasized the importance to accurately describe ligand interactions in NP simulations.

**Section 3.2 - Atomistic MD simulations of NP filtration membranes:** Gibbs free energy calculations obtained from the simulation excluded the likelihood of molecular passage by diffusion

through the ligand-filled interstices region of NP monolayer, and led to the formulation of a size-exclusion and pore-flow based filtration mechanism. These results could be used to improve the development of NP membranes for filtration purposes.

**Section 3.3 - Atomistic MD simulation of interfacial NP submersion:** This study illustrated the interfacial transport of a supercharged NP across an aqueous-organic interface. The simulations revealed the overcompensation of NP charges by organic counterions, which helped to explain the experimentally observed dependence of NP submersion distance on an applied electric field. These results could help guide the development of new types of NP membranes with tunable interparticle distances.

**Section 3.4 - Coarse-grained MD simulation of NP–lipid systems:** This study illustrated the inclusion of small hydrophobic NPs into the interior of a lipid bilayer. The equilibrated structures of NP clusters inside a lipid bilayer was found to be dependent on the coupling strength between NPs. The simulations also explored new types of NP-lipid hybrid systems.

**Section 3.5 - Mean-field study of Pt nanocube superlattices:** This study explained the puzzling formation of two distinctive *sc* and *fcc* superlattices from nanocubes with only small shape differences. The calculations also revealed a multipolar electrostatic mechanism that can help to stabilize two nanocubes in a shifted corner-to-corner configuration (in *fcc* superlattices).

**Section 3.6 - Atomistic MD simulations of CdS nanoshells:** This study illustrated the formation of nanoshells by NPs that have slightly different surface chemistry. The results demonstrated that the sizes of nanoshell cavities are dependent on NP charges.

**Section 3.7 - Atomistic MD simulations of CdS nanoribbon:** This study revealed an arrangement of NPs in the nanoribbon that can lead to its twisting. The results showed that the

twisting direction is dependent on the NP chirality, and this transfer of chirality from the NPs to the nanoribbon relied on a thin layer of water molecules in between the NPs.

**Section 3.8 - Monte Carlo simulations of magnetic superstructures:** This study illustrated the stabilization of belt and superhelical structures formed of magnetite nanocubes, and rationalized them based on the balance between vdW and magnetic interactions. The results demonstrated the formation of a chiral center of two achiral nanocubes due to the frustration between shape anisotropy and magnetic degrees of freedom of the nanocubes.

In all the above studies, we have demonstrated the use of multiscale methods in modeling NP self-assembled systems. The fundamental understanding and knowledge gained from these studies can help guide the development of new bottom-up fabrication techniques for the preparation of multi-functional materials from nanoscale components.

## CITED LITERATURE

1. Tepavcevic, S., Liu, Y., Zhou, D., Lai, B., Maser, J., Zuo, X., Chan, H., Král, P., Johnson, C. S., Stamenkovic, V., *et al.* Nanostructured Layered Cathode for Rechargeable Mg-Ion Batteries. *ACS Nano* **9**, 8194 (2015).
2. Strauss, I., Chan, H., Král, P. Ultralong Polarization Chains Induced by Ions Solvated in Confined Water Monolayers. *J. Am. Chem. Soc.* **136**, 1170 (2014).
3. Chan, H., Král, P. Self-standing nanoparticle membranes and capsules. *Nanoscale* **3**, 1881 (2011).
4. He, J., Lin, X.-M., Chan, H., Vuković, L., Král, P., Jaeger, H. M. Diffusion and Filtration Properties of Self-Assembled Gold Nanocrystal Membranes. *Nano Lett.* **11**, 2430 (2011).
5. Bera, M. K., Chan, H., Moyano, D. F., Yu, H., Tatur, S., Amoanu, D., Bu, W., Rotello, V. M., Meron, M., Král, P., Lin, B., Schlossman, M. L. Interfacial Localization and Voltage-Tunable Arrays of Charged Nanoparticles. *Nano Lett.* **14**, 6816 (2014).
6. Chan, H., Demortiere, A., Vukovic, L., Král, P., Petit, C. Colloidal nanocube supercrystals stabilized by multipolar coulombic coupling. *ACS Nano* **6**, 4203 (2012).
7. Yeom, J., Yeom, B., Chan, H., Smith, K. W., Dominguez-Medina, S., Bahng, J. H., Zhao, G., Chang, W.-S., Chang, S.-J., Chuvilin, A., *et al.* Chiral templating of self-assembling nanostructures by circularly polarized light. *Nat. Mater.* **14**, 66 (2015).
8. Singh, G., Chan, H., Baskin, A., Gelman, E., Repnin, N., Král, P., Klajn, R. Self-assembly of magnetite nanocubes into helical superstructures. *Science* **345**, 1149 (2014).
9. Singh, G., Chan, H., Udayabhaskararao, T., Gelman, E., Peddis, D., Baskin, A., Leitius, G., Král, P., Klajn, R. Magnetic field-induced self-assembly of iron oxide nanocubes. *Faraday Discuss.* **181**, 403 (2015).
10. Chan, H., Král, P., Stabilization and Self-assembly of Nanoparticles in Lipid Bilayers. Submitted.
11. Yang, M., Chan, H., Zhao, G., Bahng, J. H., Zhang, P., Král, P., Kotov, N. A., Self-Assembly of Nanoparticles into Biomimetic capsid-like Nanoshells. Submitted.
12. Freestone, I., Meeks, N., Sax, M., Higgitt, C. The Lycurgus Cup – A Roman nanotechnology. *Gold Bulletin* **40**, 270 (2007).

## CITED LITERATURE (Continued)

13. Guloyan, Y. A. Colloidal coloring of glasses: unrecognized nanotechnologies (review). *Glass Ceram.* **68**, 171 (2011).
14. Rio, A. P.del , Roehrs, S., Aucouturier, M., Castaing, J., Bouquillon, A. Medinal Al-Zahra lustre ceramics: 10th century local nanotechnology or importation from middle east. *Arab. J. Sci. Eng* **35**, 157 (2010).
15. Reibold, M., Paufler, P., Levin, A. A., Kochmann, W., Patzke, N., Meyer, D. C. Materials: Carbon nanotubes in an ancient Damascus sabre. *Nature* **444**, 286 (2006).
16. Taniguchi, N. On the Basic Concept of ‘Nano-Technology’. *Proc. Intl. Conf. Prod. Eng. Tokyo, Part II, Japan Society of Precision Engineering* , 18 (1974).
17. Feynman, R. P., science, There’s plenty of room at the bottom. *Eng. Sci.* **23**, 22 (1960).
18. Binnig, G., Rohrer, H. Scanning tunneling microscopy. *IBM J. Res. Dev.* **40**, 4 (1986).
19. Binnig, G., Quate, C. F., Gerber, C. Atomic Force Microscope. *Phys. Rev. Lett.* **56**, 930 (1986).
20. Kroto, H. W., Heath, J. R., O’Brien, S. C., Curl, R. F., Smalley, R. E. C<sub>60</sub>: Buckminsterfullerene. *Nature* **318**, 162 (1985).
21. Iijima, S. Helical microtubules of graphitic carbon. *Nature* **354**, 56 (1991).
22. Roco, M. C. From vision to the implementation of the US National Nanotechnology Initiative. *J. Nanopart. Res.* **3**, 5 (2001).
23. Harriott, L. R. Limits of lithography. *Proc. IEEE* **89**, 366 (2001).
24. Biswas, A., Bayer, I. S., Biris, A. S., Wang, T., Dervishi, E., Faupel, F. Advances in top–down and bottom–up surface nanofabrication: Techniques, applications & future prospects. *Adv. Colloid Interface Sci.* **170**, 2 (2012).
25. Yu, B., Meyyappan, M. Nanotechnology: role in emerging nanoelectronics. *Solid-State Electron.* **50**, 536 (2006).
26. Lu, W., Lieber, C. M. Nanoelectronics from the bottom up. *Nat. Mater.* **6**, 841 (2007).
27. Balzani, V., Credi, A., Venturi, M. The Bottom-Up Approach to Molecular-Level Devices and Machines. *Chem. Eur. J.* **8**, 5524 (2002).
28. Baum, R. Nanotechnology: Drexler and Smalley make the case against ‘molecular assemblers’. *CENEAR* **81**, 37 (2003).

## CITED LITERATURE (Continued)

29. Halley, J., Winkler, D. A., *et al.* Consistent concepts of self-organization and self-assembly. *Complexity* **14**, 10 (2008).
30. Whitesides, G. M., Grzybowski, B. Self-assembly at all scales. *Science* **295**, 2418 (2002).
31. Roos, W. H., Bruinsma, R., Wuite, G. J. L. Physical virology. *Nat. Phys.* **6**, 733 (2010).
32. Dobson, C. M. Protein folding and misfolding. *Nature* **426**, 884 (2003).
33. Israelachvili, J. N., Mitchell, D. J., Ninham, B. W. Theory of self-assembly of hydrocarbon amphiphiles into micelles and bilayers. *J. Chem. Soc. Faraday Trans.* **72**, 1525 (1976).
34. Lara, C., Adamcik, J., Jordens, S., Mezzenga, R. General Self-Assembly Mechanism Converting Hydrolyzed Globular Proteins Into Giant Multistranded Amyloid Ribbons. *Biomacromolecules* **12**, 1868 (2011).
35. Bisoyi, H. K., Kumar, S. Liquid-crystal nanoscience: an emerging avenue of soft self-assembly. *Chem. Soc. Rev.* **40**, 306 (2011).
36. Gimzewski, J., Modesti, S., Schlittler, R. Cooperative self-assembly of Au atoms and C 60 on Au (110) surfaces. *Phys. Rev. Lett.* **72**, 1036 (1994).
37. Brinker, C. J., Lu, Y., Sellinger, A., Fan, H. Evaporation-induced self-assembly: nanostructures made easy. *Adv. Mater.* **11**, 579 (1999).
38. Whitesides, G. M., Boncheva, M. Beyond molecules: Self-assembly of mesoscopic and macroscopic components. *PNAS* **99**, 4769 (2002).
39. Gosline, J., Lillie, M., Carrington, E., Guerette, P., Ortlepp, C., Savage, K. Elastic proteins: biological roles and mechanical properties. *Philos. Trans. R. Soc. London B Biol. Sci.* **357**, 121 (2002).
40. Fratzl, P., Gupta, H., Paschalis, E., Roschger, P. Structure and mechanical quality of the collagen–mineral nano-composite in bone. *J. Mater. Chem.* **14**, 2115 (2004).
41. Gosline, J., Guerette, P., Ortlepp, C., Savage, K. The mechanical design of spider silks: from fibroin sequence to mechanical function. *J. Exp. Biol.* **202**, 3295 (1999).
42. Foo, C. W. P., Kaplan, D. L. Genetic engineering of fibrous proteins: spider dragline silk and collagen. *Adv. Drug Delivery Rev.* **54**, 1131 (2002).
43. Zhang, S. Fabrication of novel biomaterials through molecular self-assembly. *Nat. Biotechnol.* **21**, 1171 (2003).

## CITED LITERATURE (Continued)

44. Bishop, K. J. M., Wilmer, C. E., Soh, S., Grzybowski, B. A. Nanoscale Forces and Their Uses in Self-Assembly. *Small* **5**, 1600 (2009).
45. Nicolis, G., Prigogine, I., *Self-organization in nonequilibrium systems*, vol. 191977 (Wiley, New York, 1977).
46. Aoki, K., Chen, J., Yang, N., Nagasawa, H. Charge-transfer reactions of silver stearate-coated nanoparticles in suspensions. *Langmuir* **19**, 9904 (2003).
47. Lin, Y., Skaff, H., Böker, A., Dinsmore, A. D., Emrick, T., Russell, T. P. Ultrathin Cross-Linked Nanoparticle Membranes. *J. Am. Chem. Soc.* **125**, 12690 (2003).
48. Bigioni, T. P., Lin, X.-M., Nguyen, T. T., Corwin, E. I., Witten, T. A., Jaeger, H. M. Kinetically driven self assembly of highly ordered nanoparticle monolayers. *Nat. Mater.* **5**, 265 (2006).
49. Koryta, J., Vanýsek, P., Brezina, M. Electrolysis with an electrolyte dropping electrode. *J. Electroanal. Chem.* **67**, 263 (1976).
50. Gennis, R., *Biomembranes - Molecular Structure and Function* (Springer: New York, 1989).
51. Mälkiä, A., Liljeroth, P., Kontturi, A.-K., Kontturi, K. Electrochemistry at Lipid Monolayer-Modified Liquid-Liquid Interfaces as an Improvement to Drug Partitioning Studies. *J. Phys. Chem. B* **105**, 10884 (2001).
52. Samec, Z., Samcová, E., Girault, H. H. Ion amperometry at the interface between two immiscible electrolyte solutions in view of realizing the amperometric ion-selective electrode. *Talanta* **63**, 21 (2004).
53. S.A., D., A.M., B. Comparative analysis of alkali and alkaline-earth cation transfer assisted by monensin across the water—1,2-dichloroethane interface. *J. Electroanal. Chem.* **492**, 94 (2000).
54. Kneipp, K., Kneipp, H., Itzkan, I., Dasari, R. R., Feld, M. S. Ultrasensitive Chemical Analysis by Raman Spectroscopy. *Chem. Rev.* **99**, 2957 (1999).
55. Nam, J.-M., Thaxton, C. S., Mirkin, C. A. Nanoparticle-Based Bio-Bar Codes for the Ultrasensitive Detection of Proteins. *Science* **301**, 1884 (2003).
56. Sun, S., Zeng, H. Size-controlled synthesis of magnetite nanoparticles. *J. Am. Chem. Soc.* **124**, 8204 (2002).
57. Kim, K.-S., Demberehnyamba, D., Lee, H. Size-selective synthesis of gold and platinum nanoparticles using novel thiol-functionalized ionic liquids. *Langmuir* **20**, 556 (2004).

## CITED LITERATURE (Continued)

58. Hussain, I., Graham, S., Wang, Z., Tan, B., Sherrington, D. C., Rannard, S. P., Cooper, A. I., Brust, M. Size-Controlled Synthesis of Near-Monodisperse Gold Nanoparticles in the 1–4 nm Range Using Polymeric Stabilizers. *J. Am. Chem. Soc.* **127**, 16398 (2005).
59. Mohamed, M. B., Wang, Z. L., El-Sayed, M. A. Temperature-Dependent Size-Controlled Nucleation and Growth of Gold Nanoclusters. *J. Phys. Chem. A* **103**, 10255 (1999).
60. Wang, J., Neoh, K., Kang, E. Preparation of Nanosized Metallic Particles in Polyaniline. *J. Colloid Interface Sci.* **239**, 78 (2001).
61. Grzelczak, M., Pérez-Juste, J., Mulvaney, P., Liz-Marzán, L. M. Shape control in gold nanoparticle synthesis. *Chem. Soc. Rev.* **37**, 1783 (2008).
62. Yin, Y., Alivisatos, A. P. Colloidal nanocrystal synthesis and the organic-inorganic interface. *Nature* **437**, 664 (2005).
63. Min, Y., Akbulut, M., Kristiansen, K., Golan, Y., Israelachvili, J. The role of interparticle and external forces in nanoparticle assembly. *Nat. Mater.* **7**, 527 (2008).
64. Tao, A. R., Habas, S., Yang, P. Shape Control of Colloidal Metal Nanocrystals. *Small* **4**, 310 (2008).
65. Srivastava, S., Kotov, N. A. Nanoparticle assembly for 1D and 2D ordered structures. *Soft Matter* **5**, 1146 (2009).
66. Ghosh Chaudhuri, R., Paria, S. Core/shell nanoparticles: classes, properties, synthesis mechanisms, characterization, and applications. *Chem. Rev.* **112**, 2373 (2011).
67. Crooks, R. M., Zhao, M., Sun, L., Chechik, V., Yeung, L. K. Dendrimer-encapsulated metal nanoparticles: synthesis, characterization, and applications to catalysis. *Acc. Chem. Res.* **34**, 181 (2001).
68. Daniel, M.-C., Astruc, D. Gold nanoparticles: assembly, supramolecular chemistry, quantum-size-related properties, and applications toward biology, catalysis, and nanotechnology. *Chem. Rev.* **104**, 293 (2004).
69. Brust, M., Walker, M., Bethell, D., Schiffrin, D., Whyman, R. Synthesis of thiol-derivatised gold nanoparticles in a two-phase liquid-liquid system. *Chem. Commun.* **7**, 801 (1994).
70. Sun, Y., Xia, Y. Shape-Controlled Synthesis of Gold and Silver Nanoparticles. *Science* **298**, 2176 (2002).
71. Sun, S., Murray, C. B., Weller, D., Folks, L., Moser, A. Monodisperse FePt Nanoparticles and Ferromagnetic FePt Nanocrystal Superlattices. *Science* **287**, 1989 (2000).



## CITED LITERATURE (Continued)

72. Ahmadi, T. S., Wang, Z. L., Green, T. C., Henglein, A., El-Sayed, M. A. Shape-controlled synthesis of colloidal platinum nanoparticles. *Science* **272**, 1924 (1996).
73. Trindade, T., O'Brien, P., Pickett, N. L. Nanocrystalline Semiconductors: Synthesis, Properties, and Perspectives. *Chem. Mater.* **13**, 3843 (2001).
74. Bruchez, M., Moronne, M., Gin, P., Weiss, S., Alivisatos, A. P. Semiconductor Nanocrystals as Fluorescent Biological Labels. *Science* **281**, 2013 (1998).
75. Meulenkamp, E. A. Synthesis and Growth of ZnO Nanoparticles. *J. Phys. Chem. B* **102**, 5566 (1998).
76. Vaucher, S., Li, M., Mann, S. Synthesis of Prussian Blue Nanoparticles and Nanocrystal Superlattices in Reverse Microemulsions. *Angew. Chem. int. Ed.* **39**, 1793 (2000).
77. Murray, C. B., Kagan, C. R., Bawendi, M. G. Self-Organization of CdSe Nanocrystallites into Three-Dimensional Quantum Dot Superlattices. *Science* **270**, 1335 (1995).
78. Gref, R., Minamitake, Y., Peracchia, M., Trubetskoy, V., Torchilin, V., Langer, R. Biodegradable long-circulating polymeric nanospheres.. *Science* **263**, 1600 (1994).
79. Martin, C. R. Nanomaterials - a membrane-based synthetic approach. *Science* **266**, 1961 (1994).
80. Park, J., Joo, J., Kwon, S. G., Jang, Y., Hyeon, T. Synthesis of Monodisperse Spherical Nanocrystals. *Angew. Chem. int. Ed.* **46**, 4630 (2007).
81. Han, W., Fan, S., Li, Q., Hu, Y. Synthesis of Gallium Nitride Nanorods Through a Carbon Nanotube-Confined Reaction. *Science* **277**, 1287 (1997).
82. Dai, H., Wong, E. W., Lu, Y. Z., Fan, S., Lieber, C. M. Synthesis and characterization of carbide nanorods. *Nature* **375**, 769 (1995).
83. Vayssieres, L. Growth of Arrayed Nanorods and Nanowires of ZnO from Aqueous Solutions. *Adv. Mater.* **15**, 464 (2003).
84. Nikoobakht, B., El-Sayed, M. A. Preparation and Growth Mechanism of Gold Nanorods (NRs) Using Seed-Mediated Growth Method. *Chem. Mater.* **15**, 1957 (2003).
85. Wiley, B. J., Chen, Y., McLellan, J. M., Xiong, Y., Li, Z.-Y., Ginger, D., Xia, Y. Synthesis and Optical Properties of Silver Nanobars and Nanorice. *Nano Lett.* **7**, 1032 (2007).
86. Klajn, R., Pinchuk, A. O., Schatz, G. C., Grzybowski, B. A. Synthesis of Heterodimeric Sphere-Prism Nanostructures via Metastable Gold Supraspheres. *Angew. Chem. int. Ed.* **46**, 8363 (2007).

## CITED LITERATURE (Continued)

87. Kan, C., Zhu, X., Wang, G. Single-Crystalline Gold Microplates: Synthesis, Characterization, and Thermal Stability. *J. Phys. Chem. B* **110**, 4651 (2006).
88. Millstone, J. E., Métraux, G. S., Mirkin, C. A. Controlling the Edge Length of Gold Nanoprisms via a Seed-Mediated Approach. *Adv. Funct. Mater.* **16**, 1209 (2006).
89. Chen, S., Fan, Z., Carroll, D. L. Silver Nanodisks: Synthesis, Characterization, and Self-Assembly. *J. Phys. Chem. B* **106**, 10777 (2002).
90. Manna, L., Scher, E. C., Alivisatos, A. P. Synthesis of Soluble and Processable Rod-, Arrow-, Teardrop-, and Tetrapod-Shaped CdSe Nanocrystals. *J. Am. Chem. Soc.* **122**, 12700 (2000).
91. Fang, L., Park, J. Y., Cui, Y., Alivisatos, P., Shcrier, J., Lee, B., Wang, L.-W., Salmeron, M. Mechanical and electrical properties of CdTe tetrapods studied by atomic force microscopy. *J. Chem. Phys.* **127**, 184704 (2007).
92. Oldenburg, S., Averitt, R., Westcott, S., Halas, N. Nanoengineering of optical resonances. *Chem. Phys. Lett.* **288**, 243 (1998).
93. Caruso, F., Caruso, R. A., Möhwald, H. Nanoengineering of inorganic and hybrid hollow spheres by colloidal templating. *Science* **282**, 1111 (1998).
94. Yin, Y., Rioux, R. M., Erdonmez, C. K., Hughes, S., Somorjai, G. A., Alivisatos, A. P. Formation of hollow nanocrystals through the nanoscale Kirkendall effect. *Science* **304**, 711 (2004).
95. Chen, J., Wiley, B., Li, Z.-Y., Campbell, D., Saeki, F., Cang, H., Au, L., Lee, J., Li, X., Xia, Y. Gold Nanocages: Engineering Their Structure for Biomedical Applications. *Adv. Mater.* **17**, 2255 (2005).
96. Lu, X., Au, L., McLellan, J., Li, Z.-Y., Marquez, M., Xia, Y. Fabrication of Cubic Nanocages and Nanoframes by Dealloying Au/Ag Alloy Nanoboxes with an Aqueous Etchant Based on  $\text{Fe}(\text{NO}_3)_3$  or  $\text{NH}_4\text{OH}$ . *Nano Lett.* **7**, 1764 (2007).
97. Skrabalak, S. E., Chen, J., Sun, Y., Lu, X., Au, L., Cobley, C. M., Xia, Y. Gold Nanocages: Synthesis, Properties, and Applications. *Acc. Chem. Res.* **41**, 1587 (2008).
98. Wei, Y., Klajn, R., Pinchuk, A. O., Grzybowski, B. A. Synthesis, Shape Control, and Optical Properties of Hybrid Au/ $\text{Fe}_3\text{O}_4$  "Nanoflowers". *Small* **4**, 1635 (2008).
99. Teranishi, T., Inoue, Y., Nakaya, M., Oumi, Y., Sano, T. Nanoacorns: Anisotropically Phase-Segregated CoPd Sulfide Nanoparticles. *J. Am. Chem. Soc.* **126**, 9914 (2004).

## CITED LITERATURE (Continued)

100. Shi, W., Zeng, H., Sahoo, Y., Ohulchanskyy, T. Y., Ding, Y., Wang, Z. L., Swihart, M., Prasad, P. N. A general approach to binary and ternary hybrid nanocrystals. *Nano Lett.* **6**, 875 (2006).
101. Dinsmore, A. D., Hsu, M. F., Nikolaides, M. G., Marquez, M., Bausch, A. R., Weitz, D. A. Colloidosomes: Selectively Permeable Capsules Composed of Colloidal Particles. *Science* **298**, 1006 (2002).
102. Skaff, H., Lin, Y., Tangirala, R., Breitenkamp, K., Böker, A., Russell, T., Emrick, T. Crosslinked Capsules of Quantum Dots by Interfacial Assembly and Ligand Crosslinking. *Adv. Mater.* **17**, 2082 (2005).
103. Duan, H., Wang, D., Sobal, N. S., Giersig, M., Kurth, D. G., Möhwald, H. Magnetic Colloidosomes Derived from Nanoparticle Interfacial Self-Assembly. *Nano Lett.* **5**, 949 (2005).
104. Duan, H., Wang, D., Kurth, D. G., Möhwald, H. Directing Self-Assembly of Nanoparticles at Water/Oil Interfaces. *Angew. Chem. int. Ed.* **43**, 5639 (2004).
105. Wang, J., Wang, D., Sobal, N. S., Giersig, M., Jiang, M., Möhwald, H. Stepwise Directing of Nanocrystals to Self-Assemble at Water/Oil Interfaces. *Angew. Chem. int. Ed.* **45**, 7963 (2006).
106. Shimomura, M., Sawadaishi, T. Bottom-up strategy of materials fabrication: a new trend in nanotechnology of soft materials. *Curr. Opin. Colloid In.* **6**, 11 (2001).
107. Whitesides, G. M. Nanoscience, Nanotechnology, and Chemistry. *Small* **1**, 172 (2005).
108. Grzelczak, M., Vermant, J., Furst, E. M., Liz-Marzán, L. M. Directed Self-Assembly of Nanoparticles. *ACS Nano* **4**, 3591 (2010).
109. Coe, S., Woo, W.-K., Bawendi, M., Bulovic, V. Electroluminescence from single monolayers of nanocrystals in molecular organic devices. *Nature* **420**, 800 (2002).
110. Shevchenko, E. V., Talapin, D. V., Kotov, N. A., O'Brien, S., Murray, C. B. Structural diversity in binary nanoparticle superlattices. *Nature* **439**, 55 (2006).
111. Lin, S., Li, M., Dujardin, E., Girard, C., Mann, S. One-Dimensional Plasmon Coupling by Facile Self-Assembly of Gold Nanoparticles into Branched Chain Networks. *Adv. Mater.* **17**, 2553 (2005).
112. Cho, K.-S., Talapin, D. V., Gaschler, W., Murray, C. B. Designing PbSe nanowires and nanorings through oriented attachment of nanoparticles. *J. Am. Chem. Soc.* **127**, 7140 (2005).

## CITED LITERATURE (Continued)

113. Tang, Z., Kotov, N. A., Giersig, M. Spontaneous organization of single CdTe nanoparticles into luminescent nanowires. *Science* **297**, 237 (2002).
114. Tang, Z., Kotov, N. A. One-Dimensional Assemblies of Nanoparticles: Preparation, Properties, and Promise. *Adv. Mater.* **17**, 951 (2005).
115. Tang, Z., Zhang, Z., Wang, Y., Glotzer, S. C., Kotov, N. A. Self-assembly of CdTe nanocrystals into free-floating sheets. *Science* **314**, 274 (2006).
116. He, H. X., Zhang, H., Li, Q. G., Zhu, T., Li, S. F. Y., Liu, Z. F. Fabrication of Designed Architectures of Au Nanoparticles on Solid Substrate with Printed Self-Assembled Monolayers as Templates. *Langmuir* **16**, 3846 (2000).
117. Jiang, C., Tsukruk, V. V. Organized arrays of nanostructures in freely suspended nanomembranes.. *Soft Matter* **1**, 334 (2005).
118. Kalsin, A. M., Kowalczyk, B., Smoukov, S. K., Klajn, R., Grzybowski, B. A. Ionic-like Behavior of Oppositely Charged Nanoparticles. *J. Am. Chem. Soc.* **128**, 15046 (2006).
119. Xu, Y., Qin, Y., Palchoudhury, S., Bao, Y. Water-Soluble Iron Oxide Nanoparticles with High Stability and Selective Surface Functionality. *Langmuir* **27**, 8990 (2011).
120. Sylvestre, J.-P., Poulin, S., Kabashin, A. V., Sacher, E., Meunier, M., Luong, J. H. T. Surface Chemistry of Gold Nanoparticles Produced by Laser Ablation in Aqueous Media. *J. Phys. Chem. B* **108**, 16864 (2004).
121. Krauss, T. D., Brus, L. E. Charge, polarizability, and photoionization of single semiconductor nanocrystals. *Phys. Rev. Lett.* **83**, 4840 (1999).
122. Shim, M., Guyot-Sionnest, P. Permanent dipole moment and charges in colloidal semiconductor quantum dots. *J. Chem. Phys.* **111**, 6955 (1999).
123. Bassik, N., Stern, G. M., Jamal, M., Gracias, D. H. Patterning Thin Film Mechanical Properties to Drive Assembly of Complex 3D Structures. *Adv. Mater.* **20**, 4760 (2008).
124. Cho, J.-H., Gracias, D. H. Self-Assembly of Lithographically Patterned Nanoparticles. *Nano Lett.* **9**, 4049 (2009).
125. Won, Y.-Y., Davis, H. T., Bates, F. S. Giant Wormlike Rubber Micelles. *Science* **283**, 960 (1999).
126. Hartgerink, J. D., Beniash, E., Stupp, S. I. Self-Assembly and Mineralization of Peptide-Amphiphile Nanofibers. *Science* **294**, 1684 (2001).

## CITED LITERATURE (Continued)

127. Galush, W. J., Shelby, S. A., Mulvihill, M. J., Tao, A., Yang, P., Groves, J. T. A nanocube plasmonic sensor for molecular binding on membrane surfaces. *Nano Lett.* **9**, 2077 (2009).
128. El-Sayed, I. H., Huang, X., El-Sayed, M. A. Surface Plasmon Resonance Scattering and Absorption of anti-EGFR Antibody Conjugated Gold Nanoparticles in Cancer Diagnostics: Applications in Oral Cancer. *Nano Lett.* **5**, 829 (2005).
129. Kodama, R. Magnetic nanoparticles. *J. Mag. Mag. Matt.* **200**, 359 (1999).
130. Ku, J., Aruguete, D. M., Alivisatos, A. P., Geissler, P. L. Self-Assembly of Magnetic Nanoparticles in Evaporating Solution. *J. Am. Chem. Soc.* **133**, 838 (2010).
131. Terheiden, A., Dmitrieva, O., Acet, M., Mayer, C. Magnetic field induced self-assembly of gas phase prepared FePt nanoparticles. *Chem. Phys. Lett.* **431**, 113 (2006).
132. Snezhko, A., Aranson, I. S. Magnetic Manipulation of Self-Assembled Colloidal Asters. *Nat. Mater.* **10**, 698 (2011).
133. Scheele, M., Oeschler, N., Meier, K., Kornowski, A., Klinke, C., Weller, H. Synthesis and Thermoelectric Characterization of Bi<sub>2</sub>Te<sub>3</sub> Nanoparticles. *Adv. Funct. Mater.* **19**, 3476 (2009).
134. Dai, J., Bruening, M. L. Catalytic Nanoparticles Formed by Reduction of Metal Ions in Multilayered Polyelectrolyte Films. *Nano Lett.* **2**, 497 (2002).
135. Panyala, N. R., Méndez, E. M. P. na , Havel, J. Gold and nano-gold in medicine: overview, toxicology and perspectives. *J. Appl. Biomed.* **7**, 75 (2009).
136. Bain, C. D., Troughton, E. B., Tao, Y. T., Evall, J., Whitesides, G. M., Nuzzo, R. G. Formation of monolayer films by the spontaneous assembly of organic thiols from solution onto gold. *J. Am. Chem. Soc.* **111**, 321 (1989).
137. Dabbousi, B. O., Murray, C. B., Rubner, M. F., Bawendi, M. G. Langmuir-Blodgett Manipulation of Size-Selected CdSe Nanocrystallites. *Chem. Mater.* **6**, 216 (1994).
138. Murray, C. B., Kagan, C. R., Bawendi, M. G. Synthesis and Characterization of Monodisperse Nanocrystals and Close-Packed Nanocrystal Assemblies. *Annu. Rev. Mater. Sci.* **30**, 545 (2000).
139. Kovalenko, M. V., Scheele, M., Talapin, D. V. Colloidal Nanocrystals with Molecular Metal Chalcogenide Surface Ligands. *Science* **324**, 1417 (2009).
140. Lane, J. M. D., Grest, G. S. Spontaneous Asymmetry of Coated Spherical Nanoparticles in Solution and at Liquid-Vapor Interfaces. *Phys. Rev. Lett.* **104**, 235501 (2010).

## CITED LITERATURE (Continued)

141. Jackson, A. M., Myerson, J. W., Stellacci, F. Spontaneous assembly of subnanometre-ordered domains in the ligand shell of monolayer-protected nanoparticles. *Nat. Mater.* **3**, 330 (2004).
142. Verma, A., Uzun, O., Hu, Y. H., Hu, Y., Han, H. S., Watson, N., Chen, S. L., Irvine, D. J., Stellacci, F. Surface-structure-regulated cell-membrane penetration by monolayer-protected nanoparticles. *Nat. Mater.* **7**, 588 (2008).
143. Mirkin, C. A., Letsinger, R. L., Mucic, R. C., Storhoff, J. J. A DNA-based method for rationally assembling nanoparticles into macroscopic materials. *Nature* **382**, 607 (1996).
144. Macfarlane, R. J., Jones, M. R., Senesi, A. J., Young, K. L., Lee, B., Wu, J., Mirkin, C. A. Establishing the Design Rules for DNA-Mediated Programmable Colloidal Crystallization. *Angew. Chem. int. Ed.* **49**, 4589 (2010).
145. Broderick, J. B., Natan, M. J., O'Halloran, T. V., Van Duyne, R. P. Evidence for retention of biological activity of a non-heme iron enzyme adsorbed on a silver colloid: A surface-enhanced resonance Raman scattering study. *Biochemistry (Mosc.)* **32**, 13771 (1993).
146. McIntosh, C. M., Esposito, E. A., Boal, A. K., Simard, J. M., Martin, C. T., Rotello, V. M. Inhibition of DNA Transcription Using Cationic Mixed Monolayer Protected Gold Clusters. *J. Am. Chem. Soc.* **123**, 7626 (2001).
147. Katz, E., Willner, I. Integrated Nanoparticle–Biomolecule Hybrid Systems: Synthesis, Properties, and Applications. *Angew. Chem. int. Ed.* **43**, 6042 (2004).
148. Zheng, M., Davidson, F., Huang, X. Ethylene Glycol Monolayer Protected Nanoparticles for Eliminating Nonspecific Binding with Biological Molecules. *J. Am. Chem. Soc.* **125**, 7790 (2003).
149. Kalsin, A. M., Fialkowski, M., Paszewski, M., Smoukov, S. K., Bishop, K. J., Grzybowski, B. A. Electrostatic self-assembly of binary nanoparticle crystals with a diamond-like lattice. *Science* **312**, 420 (2006).
150. Kalsin, A. M., Grzybowski, B. A. Controlling the Growth of “Ionic” Nanoparticle Supracrystals. *Nano Lett.* **7**, 1018 (2007).
151. Drummond, T., Hill, M., Barton, J. Electrochemical DNA sensors. *Nat. Biotechnol.* **21**, 1192 (2003).
152. Chen, S., Ingram, R. S., Hostetler, M. J., Pietron, J. J., Murray, R. W., Schaaff, T. G., Khoury, J. T., Alvarez, M. M., Whetten, R. L. Gold Nanoelectrodes of Varied Size: Transition to Molecule-Like Charging. *Science* **280**, 2098 (1998).

## CITED LITERATURE (Continued)

153. Gittins, D. I., Bethell, D., Schiffrin, D. J., Nichols, R. J. A nanometre-scale electronic switch consisting of a metal cluster and redox addressable groups. *Nature* **408**, 67 (2000).
154. Jin, Y., Lu, W., Hu, J., Yao, X., Li, J. Site-specific DNA cleavage of EcoRI endonuclease probed by electrochemical analysis using ferrocene capped gold nanoparticles as reporter. *Electrochem. Commun.* **9**, 1086 (2007).
155. Ryan, K. M., Mastroianni, A., Stancil, K. A., Liu, H., Alivisatos, A. Electric-field-assisted assembly of perpendicularly oriented nanorod superlattices. *Nano Lett.* **6**, 1479 (2006).
156. Yuk, J. M., Park, J., Ercius, P., Kim, K., Hellebusch, D. J., Crommie, M. F., Lee, J. Y., Zettl, A., Alivisatos, A. P. High-resolution EM of colloidal nanocrystal growth using graphene liquid cells. *Science* **336**, 61 (2012).
157. Feldheim, D. L., Grabar, K. C., Natan, M. J., Mallouk, T. E. Electron Transfer in Self-Assembled Inorganic Polyelectrolyte/Metal Nanoparticle Heterostructures. *J. Am. Chem. Soc.* **118**, 7640 (1996).
158. Schmitt, J., Decher, G., Dressick, W. J., Brandow, S. L., Geer, R. E., Shashidhar, R., Calvert, J. M. Metal nanoparticle/polymer superlattice films: Fabrication and control of layer structure. *Adv. Mater.* **9**, 61 (1997).
159. Korgel, B. A., Fullam, S., Connolly, S., Fitzmaurice, D. Assembly and Self-Organization of Silver Nanocrystal Superlattices: Ordered "Soft Spheres". *J. Phys. Chem. B* **102**, 8379 (1998).
160. Bargeman, D., Van Voorst Vader, F. Van der Waals forces between immersed particles. *J. Electroanal. Chem.* **37**, 45 (1972).
161. Templeton, A. C., Hostetler, M. J., Kraft, C. T., Murray, R. W. Reactivity of Monolayer-Protected Gold Cluster Molecules: Steric Effects. *J. Am. Chem. Soc.* **120**, 1906 (1998).
162. Mau, S.-C., Huse, D. A. Stacking entropy of hard-sphere crystals. *Phys. Rev. E* **59**, 4396 (1999).
163. Williams, S. R., Snook, I. K., van Megen, W. Molecular dynamics study of the stability of the hard sphere glass. *Phys. Rev. E* **64**, 021506 (2001).
164. Zhang, Z., Horsch, M. A., Lamm, M. H., Glotzer, S. C. Tethered Nano Building Blocks: Toward a Conceptual Framework for Nanoparticle Self-Assembly. *Nano Lett.* **3**, 1341 (2003).
165. Zhang, Z., Glotzer, S. C. Self-Assembly of Patchy Particles. *Nano Lett.* **4**, 1407 (2004).
166. Glotzer, S. C., Solomon, M. J. Anisotropy of building blocks and their assembly into complex structures. *Nat. Mater.* **6**, 557 (2007).

## CITED LITERATURE (Continued)

167. Shaw, D. E., Dror, R. O., Salmon, J. K., Grossman, J., Mackenzie, K. M., Bank, J., Young, C., Deneroff, M. M., Batson, B., Bowers, K. J., *et al.*, *High Performance Computing Networking, Storage and Analysis, Proceedings of the Conference on* (IEEE, 2009), pp. 1–11.
168. Boltzmann, L., *Vorlesungen über Gastheorie*, vol. 1 (JA Barth, 1896).
169. Seminario, J. M. Calculation of intramolecular force fields from second-derivative tensors. *Quantum Chem. Sym.* **30**, 1271 (1996).
170. Mayne, C. G., Saam, J., Schulten, K., Tajkhorshid, E., Gumbart, J. C. Rapid parameterization of small molecules using the force field toolkit. *J. Comput. Chem.* **34**, 2757 (2013).
171. MacKerell, A. D., Bashford, D., Bellott, M., Dunbrack, R. L., Evanseck, J. D., Field, M. J., Fischer, S., Gao, J., Guo, H., Ha, S., Joseph-McCarthy, D., Kuchnir, L., Kuczera, K., Lau, F. T. K., Mattos, C., Michnick, S., Ngo, T., Nguyen, D. T., Prodhom, B., Reiher, W. E., Roux, B., Schlenkrich, M., Smith, J. C., Stote, R., Straub, J., Watanabe, M., Wiorkiewicz-Kuczera, J., Yin, D., Karplus, M. All-atom empirical potential for molecular modeling and dynamics studies of proteins. *J. Phys. Chem. B* **102**, 3586 (1998).
172. Darden, T., York, D., Pedersen, L. Particle mesh Ewald: An  $N^* \log(N)$  method for Ewald sums in large systems. *J. Chem. Phys.* **98**, 185503 (1993).
173. Parsegian, V., *Van der Waals Forces: A Handbook for Biologists, Chemists, Engineers, and Physicists* (Cambridge University Press, 2005).
174. Hamaker, H. The London–van der Waals attraction between spherical particles. *physica* **4**, 1058 (1937).
175. Phillips, J. C., Braun, R., Wang, W., Gumbart, J., Tajkhorshid, E., Villa, E., Chipot, C., Skeel, R. D., Kalé, L., Schulten, K. Scalable molecular dynamics with NAMD. *J. Comput. Chem.* **26**, 1781 (2005).
176. Case, D., Berryman, J., Betz, R., Cerutti, D., Cheatham III, T., Darden, T., Duke, R., Giese, T., Gohlke, H., Goetz, A., *et al.*, *AMBER 2015* (2015).
177. Plimpton, S. Fast parallel algorithms for short-range molecular dynamics. *J. Comput. Phys.* **117**, 1 (1995).
178. Metropolis, N., Rosenbluth, A. W., Rosenbluth, M. N., Teller, A. H., Teller, E. Equation of state calculations by fast computing machines. *J. Chem. Phys.* **21**, 1087 (1953).



## CITED LITERATURE (Continued)

179. Landman, U., Luedtke, W. D. Small is different: energetic, structural, thermal, and mechanical properties of passivated nanocluster assemblies. *Faraday Discuss.* **125**, 1 (2004).
180. Schapotschnikow, P., Pool, R., Vlugt, T. J. H. Coarse-grained model for gold nanocrystals with an organic capping layer. *Mol. Phys.* **105**, 3177 (2007).
181. Schapotschnikow, P., Vlugt, T. J. H. Understanding interactions between capped nanocrystals: Three-body and chain packing effects. *J. Chem. Phys.* **131**, 124705 (2009).
182. Bethell, D., Brust, M., Schiffrin, D., Kiely, C. From monolayers to nanostructured materials: an organic chemist's view of self-assembly. *J. Electroanal. Chem.* **409**, 137 (1996).
183. Musick, M. D., Keating, C. D., Keefe, M. H., Natan, M. J. Stepwise Construction of Conductive Au Colloid Multilayers from Solution. *Chem. Mater.* **9**, 1499 (1997).
184. Pradhan, S., Sun, J., Deng, F., Chen, S. Single-Electron Transfer in Nanoparticle Solids. *Adv. Mater.* **18**, 3279 (2006).
185. Taleb, A., Petit, C., Pileni, M. P. Optical Properties of Self-Assembled 2D and 3D Superlattices of Silver Nanoparticles. *J. Phys. Chem. B* **102**, 2214 (1998).
186. Weissman, J. M., Sunkara, H. B., Tse, A. S., Asher, S. A. Thermally Switchable Periodicities and Diffraction from Mesoscopically Ordered Materials. *Science* **274**, 959 (1996).
187. Martin, J. E., Wilcoxon, J. P., Odinek, J., Provencio, P. Control of the Interparticle Spacing in Gold Nanoparticle Superlattices. *J. Phys. Chem. B* **104**, 9475 (2000).
188. Talapin, D. V., Shevchenko, E. V., Murray, C. B., Titov, A. V., Král, P. Dipole-Dipole Interactions in Nanoparticle Superlattices. *Nano Lett.* **7**, 1213 (2007).
189. Titov, A. V., Král, P. Modeling the Self-Assembly of Colloidal Nanorod Superlattices. *Nano Lett.* **8**, 3605 (2008).
190. Mueggenburg, K. E., Lin, X.-M., Goldsmith, R. H., Jaeger, H. M. Elastic membranes of close-packed nanoparticle arrays. *Nat. Mater.* **6**, 656 (2007).
191. He, J., Kanjanaboos, P., Frazer, N. L., Weis, A., Lin, X.-M., Jaeger, H. M. Fabrication and Mechanical Properties of Large-Scale Freestanding Nanoparticle Membranes. *Small* **6**, 1449 (2010).
192. Rogers, J. A., Huang, Y. A curvy, stretchy future for electronics. *Proc. Natl. Acad. Sci. U.S.A.* **106**, 10875 (2009).

## CITED LITERATURE (Continued)

193. Pushparaj, V. L., Shaijumon, M. M., Kumar, A., Murugesan, S., Ci, L., Vajtai, R., Linhardt, R. J., Nalamasu, O., Ajayan, P. M. Flexible energy storage devices based on nanocomposite paper. *Proc. Natl. Acad. Sci. U.S.A.* **104**, 13574 (2007).
194. Ding, Y., Zhang, P., Long, Z., Jiang, Y., Xu, F., Di, W. Preparation of PVdF-based electrospun membranes and their application as separators. *Sci. Technol. Adv. Mat.* **9**, 015005 (2008).
195. Jiang, C., Markutsya, S., Pikus, Y., Tsukruk, V. V. Freely suspended nanocomposite membranes as highly sensitive sensors. *Nat. Mater.* **3**, 721 (2004).
196. Marrink, S. J., Risselada, H. J., Yefimov, S., Tieleman, D. P., Vries, A. H. de The MARTINI Force Field: Coarse Grained Model for Biomolecular Simulations. *J. Phys. Chem. B* **111**, 7812 (2007).
197. Bao, K., Goedecker, S., Koga, K., Lançon, F., Neelov, A. Structure of large gold clusters obtained by global optimization using the minima hopping method. *Phys. Rev. B* **79**, 041405 (2009).
198. Li, Z. Y., Young, N. P., Di Vece, M., Palomba, S., Palmer, R. E., Bleloch, A. L., Curley, B. C., Johnston, R. L., Jiang, J., Yuan, J. Three-dimensional atomic-scale structure of size-selected gold nanoclusters. *Nature* **451**, 46 (2008).
199. Humphrey, W., Dalke, A., Schulten, K. VMD: Visual molecular dynamics. *J. Mol. Graphics* **14**, 33 (1996).
200. Singh, R., Lillard Jr., J. W. Nanoparticle-based targeted drug delivery. *Exp. Mol. Pathol.* **86**, 215 (2009).
201. Boker, A., Lin, Y., Chiapperini, K., Horowitz, R., Thompson, M., Carreon, V., Xu, T., Abetz, C., Skaff, H., Dinsmore, A. D., Emrick, T., Russell, T. P. Hierarchical nanoparticle assemblies formed by decorating breath figures. *Nat. Mater.* **3**, 302 (2004).
202. Moinard-Checot, D., Chevalier, Y., Briancon, S., Beney, L., Fessi, H. Mechanism of nanocapsules formation by the emulsion-diffusion process. *J. Colloid Interface Sci.* **317**, 458 (2008).
203. Holt, J. K., Noy, A., Huser, T., Eaglesham, D., Bakajin, O. Fabrication of a carbon nanotube-embedded silicon nitride membrane for studies of nanometer-scale mass transport. *Nano Lett.* **4**, 2245 (2004).
204. Striemer, C. C., Gaborski, T. R., McGrath, J. L., Fauchet, P. M. Charge-and size-based separation of macromolecules using ultrathin silicon membranes. *Nature* **445**, 749 (2007).

## CITED LITERATURE (Continued)

205. Peng, X., Jin, J., Nakamura, Y., Ohno, T., Ichinose, I. Ultrafast permeation of water through protein-based membranes. *Nat. Nanotechnol.* **4**, 353 (2009).
206. Hinds, B. J., Chopra, N., Rantell, T., Andrews, R., Gavalas, V., Bachas, L. G. Aligned multi-walled carbon nanotube membranes. *Science* **303**, 62 (2004).
207. Baker, R. W., *Membrane technology* (Wiley Online Library, 2000).
208. Cheng, W., Campolongo, M. J., Cha, J. J., Tan, S. J., Umbach, C. C., Muller, D. A., Luo, D. Free-standing nanoparticle superlattice sheets controlled by DNA. *Nat. Mater.* **8**, 519 (2009).
209. Dong, A., Chen, J., Vora, P. M., Kikkawa, J. M., Murray, C. B. Binary nanocrystal superlattice membranes self-assembled at the liquid-air interface. *Nature* **466**, 474 (2010).
210. Otero, J., Mazarrasa, O., Villasante, J., Silva, V., Prádanos, P., Calvo, J., Hernández, A. Three independent ways to obtain information on pore size distributions of nanofiltration membranes. *J. Membr. Sci.* **309**, 17 (2008).
211. Darve, E., Pohorille, A. Calculating free energies using average force. *J. Chem. Phys.* **115**, 9169 (2001).
212. Darve, E., Rodríguez-Gómez, D., Pohorille, A. Adaptive biasing force method for scalar and vector free energy calculations. *J. Chem. Phys.* **128**, 144120 (2008).
213. Hénin, J., Chipot, C. Overcoming free energy barriers using unconstrained molecular dynamics simulations. *J. Chem. Phys.* **121**, 2904 (2004).
214. Lin, Y., Skaff, H., Emrick, T., Dinsmore, A., Russell, T. Nanoparticle assembly and transport at liquid-liquid interfaces. *Science* **299**, 226 (2003).
215. Russell, J. T., Lin, Y., Böker, A., Su, L., Carl, P., Zettl, H., He, J., Sill, K., Tangirala, R., Emrick, T., *et al.* Self-Assembly and Cross-Linking of Bionanoparticles at Liquid-Liquid Interfaces. *Angew. Chem. int. Ed.* **44**, 2420 (2005).
216. Levin, Y. Dynamics of myosin-v processivity. *Rep. Prog. Phys.* **65**, 1577 (2002).
217. Bloomfield, V. A. DNA condensation. *Curr. Opin. Struct. Biol.* **6**, 334 (1996).
218. Zhang, F., Skoda, M., Jacobs, R., Zorn, S., Martin, R. A., Martin, C., Clark, G., Weggler, S., Hildebrandt, A., Kohlbacher, O., *et al.* Reentrant condensation of proteins in solution induced by multivalent counterions. *Phys. Rev. Lett.* **101**, 148101 (2008).

## CITED LITERATURE (Continued)

219. James, R. O., Healy, T. W. Adsorption of hydrolyzable metal ions at the oxide–water interface. II. Charge reversal of SiO<sub>2</sub> and TiO<sub>2</sub> colloids by adsorbed Co (II), La (III), and Th (IV) as model systems. *J. Colloid Interface Sci.* **40**, 53 (1972).
220. Quesada-Pérez, M., González-Tovar, E., Martín-Molina, A., Lozada-Cassou, M., Hidalgo-Álvarez, R. Overcharging in colloids: beyond the Poisson–Boltzmann approach. *ChemPhysChem* **4**, 234 (2003).
221. Laanait, N., Mihaylov, M., Hou, B., Yu, H., Vanýsek, P., Meron, M., Lin, B., Benjamin, I., Schlossman, M. L. Tuning ion correlations at an electrified soft interface. *PNAS* **109**, 20326 (2012).
222. Miranda, O. R., Chen, H.-T., You, C.-C., Mortenson, D. E., Yang, X.-C., Bunz, U. H., Rotello, V. M. Enzyme-amplified array sensing of proteins in solution and in biofluids. *J. Am. Chem. Soc.* **132**, 5285 (2010).
223. Samec, Z. Electrochemistry at the interface between two immiscible electrolyte solutions (IUPAC Technical Report). *Pure Appl. Chem.* **76**, 2147 (2004).
224. Flatté, M., Kornyshev, A., Urbakh, M. Understanding voltage-induced localization of nanoparticles at a liquid–liquid interface. *J. Phys.: Condens. Matter* **20**, 073102 (2008).
225. Su, B., Abid, J.-P., Fermín, D. J., Girault, H. H., Hoffmannová, H., Krtíl, P., Samec, Z. Reversible Voltage-Induced Assembly of Au Nanoparticles at Liquid–Liquid Interfaces. *J. Am. Chem. Soc.* **126**, 915 (2004).
226. Pershan, P. S., Schlossman, M., *Liquid Surfaces and Interfaces: Synchrotron X-ray Methods* (Cambridge University Press, 2012).
227. Vorobyov, I., Anisimov, V. M., Greene, S., Venable, R. M., Moser, A., Pastor, R. W., MacKerell, A. D. Additive and classical drude polarizable force fields for linear and cyclic ethers. *J. Chem. Theory Comput.* **3**, 1120 (2007).
228. Vanommeslaeghe, K., Hatcher, E., Acharya, C., Kundu, S., Zhong, S., Shim, J., Darian, E., Guvench, O., Lopes, P., Vorobyov, I., *et al.* CHARMM general force field: A force field for drug-like molecules compatible with the CHARMM all-atom additive biological force fields. *J. Comput. Chem.* **31**, 671 (2010).
229. Guerrero-García, G. I., Jing, Y., Cruz, M. O. de la Enhancing and reversing the electric field at the oil–water interface with size-asymmetric monovalent ions. *Soft Matter* **9**, 6046 (2013).
230. Zwanikken, J. W., La Cruz, M. O. de Correlated electrolyte solutions and ion-induced attractions between nanoparticles. *Phys. Rev. E* **82**, 050401 (2010).

## CITED LITERATURE (Continued)

231. Allahyarov, E., D'Amico, I., Löwen, H. Attraction between like-charged macroions by Coulomb depletion. *Phys. Rev. Lett.* **81**, 1334 (1998).
232. Leunissen, M. E., Zwanikken, J., Roij, R. van, Chaikin, P. M., Blaaderen, A. van Ion partitioning at the oil–water interface as a source of tunable electrostatic effects in emulsions with colloids. *Phys. Chem. Chem. Phys.* **9**, 6405 (2007).
233. Lowry, G., Casman, E., *Nanomaterials: risks and benefits* (Springer, 2009), pp. 125–137.
234. Cecchini, M. P., Turek, V. A., Paget, J., Kornyshev, A. A., Edel, J. B. Self-assembled nanoparticle arrays for multiphase trace analyte detection. *Nat. Mater.* **12**, 165 (2013).
235. Flatté, M., Kornyshev, A., Urbakh, M. Electrovariable nanoplasmonics and self-assembling smart mirrors. *J. Phys. Chem. C* **114**, 1735 (2010).
236. Kinnan, M. K., Chumanov, G. Plasmon Coupling in Two-Dimensional Arrays of Silver Nanoparticles: II. Effect of the Particle Size and Interparticle Distance. *J. Phys. Chem. C* **114**, 7496 (2010).
237. Turek, V. A., Cecchini, M. P., Paget, J., Kucernak, A. R., Kornyshev, A. A., Edel, J. B. Plasmonic ruler at the liquid–liquid interface. *ACS Nano* **6**, 7789 (2012).
238. Kushner, D. Self-assembly of biological structures.. *Bacteriol. Rev.* **33**, 302 (1969).
239. Zhang, S. Building from the bottom up. *Mater. Today* **6**, 20 (2003).
240. Titov, A. V., Král, P., Pearson, R. Sandwiched Graphene-Membrane Superstructures. *ACS Nano* **4**, 229 (2010).
241. Webb, C. The body shops. *IEEE Spectrum* **42**, 34 (2005).
242. Van Lehn, R. C., Ricci, M., Silva, P. H., Andreozzi, P., Reguera, J., Voitchovsky, K., Stellacci, F., Alexander-Katz, A. Lipid tail protrusions mediate the insertion of nanoparticles into model cell membranes. *Nat. Commun.* **5**, (2014).
243. Ding, H.-m., Tian, W.-d., Ma, Y.-q. Designing Nanoparticle Translocation through Membranes by Computer Simulations. *ACS Nano* **6**, 1230 (2012).
244. Rocha, E. L. d., Caramori, G. F., Rambo, C. R. Nanoparticle translocation through a lipid bilayer tuned by surface chemistry. *Phys. Chem. Chem. Phys.* **15**, 2282 (2013).
245. Yang, K., Ma, Y.-Q. Computer simulation of the translocation of nanoparticles with different shapes across a lipid bilayer. *Nat. Nanotechnol.* **5**, 579 (2010).

## CITED LITERATURE (Continued)

246. Saric, A., Cacciuto, A. Self-assembly of nanoparticles adsorbed on fluid and elastic membranes. *Soft Matter* **9**, 6677 (2013).
247. Pogodin, S., Werner, M., Sommer, J.-U., Baulin, V. A. Nanoparticle-Induced Permeability of Lipid Membranes. *ACS Nano* **6**, 10555 (2012).
248. Song, B., Yuan, H., Pham, S. V., Jameson, C. J., Murad, S. Nanoparticle Permeation Induces Water Penetration, Ion Transport, and Lipid Flip-Flop. *Langmuir* **28**, 16989 (2012).
249. Paasonen, L., Sipilä, T., Subrizi, A., Laurinmäki, P., Butcher, S. J., Rappolt, M., Yaghmur, A., Urtti, A., Yliperttula, M. Gold-embedded photosensitive liposomes for drug delivery: Triggering mechanism and intracellular release. *J. Controlled Release* **147**, 136 (2010).
250. Santhosh, P. B., Pen, S., Genova, J., Igli, A., Kralj-Igli, V., Ulrih, N. P. A study on the interaction of nanoparticles with lipid membranes and their influence on membrane fluidity. *J. Phys. Conf. Ser.* **398**, 012034 (2012).
251. Lai, K., Wang, B., Zhang, Y., Zheng, Y. Computer simulation study of nanoparticle interaction with a lipid membrane under mechanical stress. *Phys. Chem. Chem. Phys.* **15**, 270 (2013).
252. Ginzburg, V. V., Balijepailli, S. Modeling the thermodynamics of the interaction of nanoparticles with cell membranes. *Nano Lett.* **7**, 3716 (2007).
253. Li, Y., Chen, X., Gu, N. Computational Investigation of Interaction between Nanoparticles and Membranes: Hydrophobic/Hydrophilic Effect. *J. Phys. Chem. B* **112**, 16647 (2008).
254. Binder, W. H., Sachsenhofer, R., Farnik, D., Blaas, D. Guiding the location of nanoparticles into vesicular structures: a morphological study. *Phys. Chem. Chem. Phys.* **9**, 6435 (2007).
255. Gopalakrishnan, G., Danelon, C., Izewska, P., Prummer, M., Bolinger, P.-Y., Geissbühler, I., Demurtas, D., Dubochet, J., Vogel, H. Multifunctional Lipid/Quantum Dot Hybrid Nanocontainers for Controlled Targeting of Live Cells. *Angew. Chem. int. Ed.* **45**, 5478 (2006).
256. Rasch, M. R., Yu, Y., Bosoy, C., Goodfellow, B. W., Korgel, B. A. Chloroform-Enhanced Incorporation of Hydrophobic Gold Nanocrystals into Dioleoylphosphatidylcholine (DOPC) Vesicle Membranes. *Langmuir* **28**, 12971 (2012).
257. Bothun, G. D. Hydrophobic silver nanoparticles trapped in lipid bilayers: Size distribution, bilayer phase behavior, and optical properties. *J. Nanobiotech.* **6**, A13 (2008).

## CITED LITERATURE (Continued)

258. Hsu, H.-j., Sen, S., Pearson, R. M., Uddin, S., Král, P., Hong, S. Poly(ethylene glycol) Corona Chain Length Controls End-Group-Dependent Cell Interactions of Dendron Micelles. *Macromolecules* **47**, 6911 (2014).
259. Marrink, S. J., Vries, A. H.de , Mark, A. E. Coarse-grained model for semiquantitative lipid simulations. *J. Phys. Chem. B* **108**, 750 (2004).
260. Shih, A. Y., Freddolino, P. L., Arkhipov, A., Schulten, K. Assembly of lipoprotein particles revealed by coarse-grained molecular dynamics simulations. *J. Struct. Biol.* **157**, 579 (2007).
261. Feller, S. E., Zhang, Y., Pastor, R. W., Brooks, B. R. Constant pressure molecular dynamics simulation: The Langevin piston method. *J. Chem. Phys.* **103**, 4613 (1995).
262. Rasch, M. R., Rossinyol, E., Hueso, J. L., Goodfellow, B. W., Arbiol, J., Korgel, B. A. Hydrophobic Gold Nanoparticle Self-Assembly with Phosphatidylcholine Lipid: Membrane-Loaded and Janus Vesicles. *Nano Lett.* **10**, 3733 (2010).
263. Derek, M. Lateral Pressure Profile, Spontaneous Curvature Frustration, and the Incorporation and Conformation of Proteins in Membranes. *Biophys. J.* **93**, 3884 (2007).
264. Gullingsrud, J., Schulten, K. Lipid Bilayer Pressure Profiles and Mechanosensitive Channel Gating. *Biophys. J.* **86**, 3496 (2004).
265. Andersen, O. S., Koeppe, R. E. Bilayer thickness and membrane protein function: An energetic perspective. *Annu. Rev. Biophys. Biomol. Struct.* **36**, 107 (2007).
266. Talapin, D. V., Nelson, J. H., Shevchenko, E. V., Aloni, S., Sadtler, B., Alivisatos, A. P. Seeded Growth of Highly Luminescent CdSe/CdS Nanoheterostructures with Rod and Tetrapod Morphologies. *Nano Lett.* **7**, 2951 (2007).
267. Baker, J. L., Widmer-Cooper, A., Toney, M. F., Geissler, P. L., Alivisatos, A. P. Device-Scale Perpendicular Alignment of Colloidal Nanorods. *Nano Lett.* **10**, 195 (2009).
268. Paik, T., Gordon, T. R., Prantner, A. M., Yun, H., Murray, C. B. Designing Tripodal and Triangular Gadolinium Oxide Nanoplates and Self-Assembled Nanofibrils as Potential Multimodal Bioimaging Probes. *ACS Nano* **7**, 2850 (2013).
269. Murray, C. B., Sun, S., Doyle, H., Betley, T. Monodisperse 3d transition-metal (Co, Ni, Fe) nanoparticles and their assembly into nanoparticle superlattices. *Mater. Res. Soc. Bull.* **26**, 985 (2001).
270. Alivisatos, A. P. Semiconductor Clusters, Nanocrystals, and Quantum Dots. *Science* **271**, 933 (1996).

## CITED LITERATURE (Continued)

271. Buck, M. R., Bondi, J. F., Schaak, R. E. A total-synthesis framework for the construction of high-order colloidal hybrid nanoparticles. *Nat. Chem.* **4**, 37 (2012).
272. Dong, A., Ye, X., Chen, J., Murray, C. B. Two-Dimensional Binary and Ternary Nanocrystal Superlattices: The Case of Monolayers and Bilayers. *Nano Lett.* **11**, 1804 (2011).
273. Chang, C.-C., Wu, H.-L., Kuo, C.-H., Huang, M. H. Hydrothermal Synthesis of Monodispersed Octahedral Gold Nanocrystals with Five Different Size Ranges and Their Self-Assembled Structures. *Chem. Mater.* **20**, 7570 (2008).
274. Peng, X., Manna, L., Yang, W., Wickham, J., Scher, E., Kadavanich, A., Alivisatos, A. P. Shape control of CdSe nanocrystals. *Nature* **404**, 59 (2000).
275. Puentes, V. F., Zanchet, D., Erdonmez, C. K., Alivisatos, A. P. Synthesis of hcp-Co Nanodisks. *J. Am. Chem. Soc.* **124**, 12874 (2002).
276. Jun, Y.-W., Casula, M. F., Sim, J.-H., Kim, S. Y., Cheon, J., Alivisatos, A. P. Surfactant-Assisted Elimination of a High Energy Facet as a Means of Controlling the Shapes of TiO<sub>2</sub> Nanocrystals. *J. Am. Chem. Soc.* **125**, 15981 (2003).
277. Wang, Z. L. Transmission Electron Microscopy of Shape-Controlled Nanocrystals and Their Assemblies. *J. Phys. Chem. B* **104**, 1153 (2000).
278. Tao, A. R., Ceperley, D. P., Sinsermsuksakul, P., Neureuther, A. R., Yang, P. Self-Organized Silver Nanoparticles for Three-Dimensional Plasmonic Crystals. *Nano Lett.* **8**, 4033 (2008).
279. Demortière, A., Launois, P., Goubet, N., Albouy, P.-A., Petit, C. Shape-Controlled Platinum Nanocubes and Their Assembly into Two-Dimensional and Three-Dimensional Superlattices. *J. Phys. Chem. B* **112**, 14583 (2008).
280. Zheng, R. K., Gu, H., Xu, B., Fung, K. K., Zhang, X. X., Ringer, S. P. Self-Assembly and Self-Orientation of Truncated Octahedral Magnetite Nanocrystals. *Adv. Mater.* **18**, 2418 (2006).
281. Quan, Z., Fang, J. Superlattices with non-spherical building blocks. *Nano Today* **5**, 390 (2010).
282. Demortière, A., Buathong, S., Pichon, B. P., Panissod, P., Guillon, D., Bégin-Colin, S., Donnio, B. Nematic-like Organization of Magnetic Mesogen-Hybridized Nanoparticles. *Small* **6**, 1341 (2010).
283. Puentes, V. F., Krishnan, K. M., Alivisatos, A. P. Colloidal Nanocrystal Shape and Size Control: The Case of Cobalt. *Science* **291**, 2115 (2001).



## CITED LITERATURE (Continued)

284. Burda, C., Chen, X., Narayanan, R., El-Sayed, M. A. Chemistry and properties of nanocrystals of different shapes. *Chem. Rev.* **105**, 1025 (2005).
285. Nie, Z., Fava, D., Kumacheva, E., Zou, S., Walker, G. C., Rubinstein, M. Self-assembly of metal-polymer analogues of amphiphilic triblock copolymers. *Nat. Mater.* **6**, 609 (2007).
286. Bodnarchuk, M. I., Kovalenko, M. V., Heiss, W., Talapin, D. V. Energetic and Entropic Contributions to Self-Assembly of Binary Nanocrystal Superlattices: Temperature as the Structure-Directing Factor. *J. Am. Chem. Soc.* **132**, 11967 (2010).
287. Choi, J. J., Bealing, C. R., Bian, K., Hughes, K. J., Zhang, W., Smilgies, D.-M., Hennig, R. G., Engstrom, J. R., Hanrath, T. Controlling Nanocrystal Superlattice Symmetry and Shape-Anisotropic Interactions through Variable Ligand Surface Coverage. *J. Am. Chem. Soc.* **133**, 3131 (2011).
288. Park, J., Kang, E., Son, S. U., Park, H. M., Lee, M. K., Kim, J., Kim, K. W., Noh, H.-J., Park, J.-H., Bae, C. J., *et al.* Monodisperse Nanoparticles of Ni and NiO: Synthesis, Characterization, Self-Assembled Superlattices, and Catalytic Applications in the Suzuki Coupling Reaction. *Adv. Mater.* **17**, 429 (2005).
289. Bell, A. T. The Impact of Nanoscience on Heterogeneous Catalysis. *Science* **299**, 1688 (2003).
290. Chen, C.-F., Tzeng, S.-D., Chen, H.-Y., Lin, K.-J., Gwo, S. Tunable Plasmonic Response from Alkanethiolate-Stabilized Gold Nanoparticle Superlattices: Evidence of Near-Field Coupling. *J. Am. Chem. Soc.* **130**, 824 (2007).
291. Andres, R. P., Bielefeld, J. D., Henderson, J. I., Janes, D. B., Kolagunta, V. R., Kubiak, C. P., Mahoney, W. J., Osifchin, R. G. Self-Assembly of a Two-Dimensional Superlattice of Molecularly Linked Metal Clusters. *Science* **273**, 1690 (1996).
292. Zaitseva, N., Dai, Z. R., Leon, F. R., Krol, D. Optical Properties of CdSe Superlattices. *J. Am. Chem. Soc.* **127**, 10221 (2005).
293. Grzelczak, M., Mezzasalma, S. A., Ni, W., Herasimenka, Y., Feruglio, L., Montini, T., Pérez-Juste, J., Fornasiero, P., Prato, M., Liz-Marzán, L. M. Antibonding plasmon modes in colloidal gold nanorod clusters. *Langmuir* **28**, 8826 (2011).
294. Ahnizay, A., Sakamoto, Y., Bergström, L. Magnetic field-induced assembly of oriented superlattices from maghemite nanocubes. *PNAS* **104**, 17570 (2007).
295. Huang, H.-T., Zhang, B.-T., He, J.-L., Yang, J.-F., Xu, J.-L., Yang, X.-Q., Zuo, C.-H., Zhao, S. Diode-pumped passively Q-switched Nd:Gd<sub>0.5</sub>Y<sub>0.5</sub>VO<sub>4</sub> laser at 1.34 $\mu$ m with V<sup>3+</sup>:YAG as the saturable absorber. *Opt. Express* **17**, 6946 (2009).

## CITED LITERATURE (Continued)

296. Henzie, J., Grünwald, M., Widmer-Cooper, A., Geissler, P. L., Yang, P. Self-assembly of uniform polyhedral silver nanocrystals into densest packings and exotic superlattices. *Nat. Mater.* **11**, 131 (2012).
297. Stebe, K. J., Lewandowski, E., Ghosh, M. Oriented Assembly of Metamaterials. *Science* **325**, 159 (2009).
298. Motte, L., Billoudet, F., Lacaze, E., Douin, J., Pileni, M. P. Self-Organization into 2D and 3D Superlattices of Nanosized Particles Differing by Their Size. *J. Phys. Chem. B* **101**, 138 (1997).
299. Demortière, A., Petit, C. First Synthesis by Liquid-Liquid Phase Transfer of Magnetic  $\text{Co}_x\text{Pt}_{100-x}$  Nanoalloys. *Langmuir* **23**, 8575 (2007).
300. Kraig, R. E., Roundy, D., Cohen, M. L. A study of the mechanical and structural properties of polonium. *Solid State Commun.* **129**, 411 (2004).
301. Li, F., Delo, S. A., Stein, A. Disassembly and Self-Reassembly in Periodic Nanostructures: A Face-Centered-to-Simple-Cubic Transformation. *Angew. Chem. Int. Ed.* **46**, 6666 (2007).
302. Yamamuro, S., Sumiyama, K. Why do cubic nanoparticles favor a square array? Mechanism of shape-dependent arrangement in nanocube self-assemblies. *Chem. Phys. Lett.* **418**, 166 (2006).
303. Yamamuro, S., Sumiyama, K., Kamiyama, T. Shape-induced simple cubic arrangement in three-dimensional nanocube self-assemblies. *Appl. Phys. Lett.* **92**, 113108 (2008).
304. Cölfen, H., Mann, S. Higher-Order Organization by Mesoscale Self-Assembly and Transformation of Hybrid Nanostructures. *Angew. Chem. int. Ed.* **42**, 2350 (2003).
305. Ohara, P. C., Leff, D. V., Heath, J. R., Gelbart, W. M. Crystallization of Opals from Polydisperse Nanoparticles. *Phys. Rev. Lett.* **75**, 3466 (1995).
306. Novell-Leruth, G., Valcárcel, A., Clotet, A., Ricart, J. M., Pérez-Ramírez, J. DFT Characterization of Adsorbed  $\text{NH}_x$  Species on Pt(100) and Pt(111) Surfaces. *J. Phys. Chem. B* **109**, 18061 (2005).
307. Luedtke, W. D., Landman, U. Structure, Dynamics, and Thermodynamics of Passivated Gold Nanocrystallites and Their Assemblies. *J. Phys. Chem.* **100**, 13323 (1996).
308. Ionita, P., Volkov, A., Jeschke, G., Chechik, V. Lateral Diffusion of Thiol Ligands on the Surface of Au Nanoparticles: An Electron Paramagnetic Resonance Study. *Anal. Chem.* **80**, 95 (2007).

## CITED LITERATURE (Continued)

309. Schapotschnikow, P., Pool, R., Vlugt, T. J. H. Molecular Simulations of Interacting Nanocrystals. *Nano Lett.* **8**, 2930 (2008).
310. Hirsch, L., Stafford, R., Bankson, J., Sershen, S., Rivera, B., Price, R., Hazle, J., Halas, N., West, J. Nanoshell-mediated near-infrared thermal therapy of tumors under magnetic resonance guidance. *PNAS* **100**, 13549 (2003).
311. Shan, Z., Adesso, G., Cabot, A., Sherburne, M., Asif, S. S., Warren, O., Chrzan, D., Minor, A., Alivisatos, A. Ultrahigh stress and strain in hierarchically structured hollow nanoparticles. *Nat. Mater.* **7**, 947 (2008).
312. Yu, J., Yu, X. Hydrothermal synthesis and photocatalytic activity of zinc oxide hollow spheres. *Envir. Sci. Tech.* **42**, 4902 (2008).
313. Caruso, F. Hollow capsule processing through colloidal templating and self-assembly. *Chem. Eur. J.* **6**, 413 (2000).
314. Sun, Y., Mayers, B., Xia, Y. Metal nanostructures with hollow interiors. *Adv. Mater.* **15**, 641 (2003).
315. Chang, Y., Teo, J. J., Zeng, H. C. Formation of colloidal CuO nanocrystallites and their spherical aggregation and reductive transformation to hollow Cu<sub>2</sub>O nanospheres. *Langmuir* **21**, 1074 (2005).
316. Antonietti, M., Förster, S. Vesicles and liposomes: a self-assembly principle beyond lipids. *Adv. Mater.* **15**, 1323 (2003).
317. Hamm, C. E., Merkel, R., Springer, O., Jurkojc, P., Maier, C., Pechtel, K., Smetacek, V. Architecture and material properties of diatom shells provide effective mechanical protection. *Nature* **421**, 841 (2003).
318. Xia, Y., Nguyen, T. D., Yang, M., Lee, B., Santos, A., Podsiadlo, P., Tang, Z., Glotzer, S. C., Kotov, N. A. Self-assembly of self-limiting monodisperse supraparticles from polydisperse nanoparticles. *Nat. Nanotechnol.* **6**, 580 (2011).
319. Zhou, H., Kim, J.-P., Bahng, J. H., Kotov, N. A., Lee, J. Self-Assembly Mechanism of Spiky Magnetoplasmonic Supraparticles. *Adv. Funct. Mater.* **24**, 1439 (2014).
320. Srivastava, S., Santos, A., Critchley, K., Kim, K.-S., Podsiadlo, P., Sun, K., Lee, J., Xu, C., Lilly, G. D., Glotzer, S. C. Light-controlled self-assembly of semiconductor nanoparticles into twisted ribbons. *Science* **327**, 1355 (2010).

## CITED LITERATURE (Continued)

321. Shevchenko, E. V., Talapin, D. V., Murray, C. B., O'Brien, S. Structural characterization of self-assembled multifunctional binary nanoparticle superlattices. *J. Am. Chem. Soc.* **128**, 3620 (2006).
322. Shenton, W., Pum, D., Sleytr, U. B., Mann, S. Synthesis of cadmium sulphide superlattices using self-assembled bacterial S-layers. *Nature* **389**, 585 (1997).
323. Banfield, J. F., Welch, S. A., Zhang, H., Ebert, T. T., Penn, R. L. Aggregation-based crystal growth and microstructure development in natural iron oxyhydroxide biomineralization products. *Science* **289**, 751 (2000).
324. Zhao, G., Perilla, J. R., Yufenyuy, E. L., Meng, X., Chen, B., Ning, J., Ahn, J., Gronenborn, A. M., Schulten, K., Aiken, C., *et al.* Mature HIV-1 capsid structure by cryo-electron microscopy and all-atom molecular dynamics. *Nature* **497**, 643 (2013).
325. Vossmeier, T., Reck, G., Katsikas, L., Haupt, E., *et al.* A "double-diamond superlattice" built up of Cd<sub>17</sub>S<sub>4</sub> (SCH<sub>2</sub>CH<sub>2</sub>OH) 26 clusters. *Science* **267**, 1476 (1995).
326. Rieke, P. C., Bentjen, S. B. Deposition of cadmium sulfide films by decomposition of thiourea in basic solutions. *Chem. Mater.* **5**, 43 (1993).
327. Ufimtsev, I. S., Martinez, T. J. Quantum chemistry on graphical processing units. 3. Analytical energy gradients, geometry optimization, and first principles molecular dynamics. *J. Chem. Theory Comput.* **5**, 2619 (2009).
328. Lindemann, P., The Gilbert-Johnson-Keerthi Distance Algorithm, *Algorithms in Media Informatics* (2009).
329. Chen, I. J., Yin, D., MacKerell, A. D. Combined ab initio/empirical approach for optimization of Lennard-Jones parameters for polar-neutral compounds. *J. Comput. Chem.* **23**, 199 (2002).
330. Kirnbauer, R., Booy, F., Cheng, N., Lowy, D., Schiller, J. Papillomavirus L1 major capsid protein self-assembles into virus-like particles that are highly immunogenic. *PNAS* **89**, 12180 (1992).
331. Rossbach, B. M., Leopold, K., Weberskirch, R. Self-Assembled Nanoreactors as Highly Active Catalysts in the Hydrolytic Kinetic Resolution (HKR) of Epoxides in Water. *Angew. Chem. int. Ed.* **45**, 1309 (2006).
332. Peters, R. J., Marguet, M., Marais, S., Fraaije, M. W., Hest, J. van, Lecommandoux, S. Cascade reactions in multicompartimentalized polymersomes. *Angew. Chem. int. Ed.* **126**, 150 (2014).

## CITED LITERATURE (Continued)

333. Rösler, A., Vandermeulen, G. W., Klok, H.-A. Advanced drug delivery devices via self-assembly of amphiphilic block copolymers. *Adv. Drug Delivery Rev.* **64**, 270 (2012).
334. Ren, M., Plum, E., Xu, J., Zheludev, N. I. Giant nonlinear optical activity in a plasmonic metamaterial. *Nat. Commun.* **3**, 833 (2012).
335. Kuzyk, A., Schreiber, R., Fan, Z., Pardatscher, G., Roller, E.-M., Högele, A., Simmel, F. C., Govorov, A. O., Liedl, T. DNA-based self-assembly of chiral plasmonic nanostructures with tailored optical response. *Nature* **483**, 311 (2012).
336. Guerrero-Martínez, A., Auguie, B., Alonso-Gómez, J. L., Džolić, Z., Gómez-Graña, S., Žinić, M., Cid, M. M., Liz-Marzán, L. M. Intense Optical Activity from Three-Dimensional Chiral Ordering of Plasmonic Nanoantennas. *Angew. Chem. int. Ed.* **50**, 5499 (2011).
337. Liu, S., Han, L., Duan, Y., Asahina, S., Terasaki, O., Cao, Y., Liu, B., Ma, L., Zhang, J., Che, S. Synthesis of chiral TiO<sub>2</sub> nanofibre with electron transition-based optical activity. *Nat. Commun.* **3**, 1215 (2012).
338. Chen, W., Bian, A., Agarwal, A., Liu, L., Shen, H., Wang, L., Xu, C., Kotov, N. A. Nanoparticle superstructures made by polymerase chain reaction: collective interactions of nanoparticles and a new principle for chiral materials. *Nano Lett.* **9**, 2153 (2009).
339. Mark, A. G., Gibbs, J. G., Lee, T.-C., Fischer, P. Hybrid nanocolloids with programmed three-dimensional shape and material composition. *Nat. Mater.* **12**, 802 (2013).
340. Ma, W., Kuang, H., Xu, L., Ding, L., Xu, C., Wang, L., Kotov, N. A. Attomolar DNA detection with chiral nanorod assemblies. *Nat. Commun.* **4**, (2013).
341. Gansel, J. K., Thiel, M., Rill, M. S., Decker, M., Bade, K., Saile, V., Freymann, G. von, Linden, S., Wegener, M. Gold helix photonic metamaterial as broadband circular polarizer. *Science* **325**, 1513 (2009).
342. Toyoda, K., Miyamoto, K., Aoki, N., Morita, R., Omatsu, T. Using optical vortex to control the chirality of twisted metal nanostructures. *Nano Lett.* **12**, 3645 (2012).
343. Tabosa, J., Petrov, D. Optical pumping of orbital angular momentum of light in cold cesium atoms. *Phys. Rev. Lett.* **83**, 4967 (1999).
344. Brachmann, J. F., Bakr, W. S., Gillen, J., Peng, A., Greiner, M. Inducing vortices in a Bose-Einstein condensate using holographically produced light beams. *Opt. Express* **19**, 12984 (2011).
345. Padgett, M., Bowman, R. Tweezers with a twist. *Nat. Photonics* **5**, 343 (2011).

## CITED LITERATURE (Continued)

346. Tang, Y., Cohen, A. E. Enhanced enantioselectivity in excitation of chiral molecules by super-chiral light. *Science* **332**, 333 (2011).
347. Feringa, B. L., Van Delden, R. A. Absolute asymmetric synthesis: the origin, control, and amplification of chirality. *Angew. Chem. int. Ed.* **38**, 3418 (1999).
348. Green, M. M., Selinger, J. V. Cosmic chirality. *Science* **282**, 880 (1998).
349. Giri, C., Goesmann, F., Meinert, C., Evans, A. C., Meierhenrich, U. J., *Biochirality* (Springer, 2013), pp. 41–82.
350. Prins, L. J., Timmerman, P., Reinhoudt, D. N. Amplification of chirality: the “sergeants and soldiers” principle applied to dynamic hydrogen-bonded assemblies. *J. Am. Chem. Soc.* **123**, 10153 (2001).
351. Cronin, J. R., Pizzarello, S. Enantiomeric excesses in meteoritic amino acids. *Science* **275**, 951 (1997).
352. Bustamante, C., Maestre, M. F., Tinoco Jr, I. Circular intensity differential scattering of light by helical structures. I. Theory. *J. Chem. Phys.* **73**, 4273 (1980).
353. Gaponik, N., Talapin, D. V., Rogach, A. L., Hoppe, K., Shevchenko, E. V., Kornowski, A., Eychmüller, A., Weller, H. Thiol-capping of CdTe nanocrystals: an alternative to organometallic synthetic routes. *J. Phys. Chem. B* **106**, 7177 (2002).
354. Chen, C.-C., Zhu, C., White, E. R., Chiu, C.-Y., Scott, M., Regan, B., Marks, L. D., Huang, Y., Miao, J. Three-dimensional imaging of dislocations in a nanoparticle at atomic resolution. *Nature* **496**, 74 (2013).
355. Dolamic, I., Knoppe, S., Dass, A., Bürgi, T. First enantioseparation and circular dichroism spectra of Au<sub>38</sub> clusters protected by achiral ligands. *Nat. Commun.* **3**, 798 (2012).
356. Hartland, A., Lead, J. R., Slaveykova, V. I., O’Carroll, D., Valsami-Jones, E. The environmental significance of natural nanoparticles. *Nat. Edu. Knowl.* **4**, 1 (2013).
357. Bailey, J., Chrysostomou, A., Hough, J., Gledhill, T., McCall, A., Clark, S., Ménard, F., Tamura, M. Circular polarization in star-formation regions: implications for biomolecular homochirality. *Science* **281**, 672 (1998).
358. Gautier, C., Bürgi, T. Chiral N-isobutyryl-cysteine protected gold nanoparticles: preparation, size selection, and optical activity in the UV-vis and infrared. *J. Am. Chem. Soc.* **128**, 11079 (2006).

## CITED LITERATURE (Continued)

359. Govorov, A. O., Fan, Z., Hernandez, P., Slocik, J. M., Naik, R. R. Theory of circular dichroism of nanomaterials comprising chiral molecules and nanocrystals: plasmon enhancement, dipole interactions, and dielectric effects. *Nano Lett.* **10**, 1374 (2010).
360. Ben Moshe, A., Szwarcman, D., Markovich, G. Size dependence of chiroptical activity in colloidal quantum dots. *ACS Nano* **5**, 9034 (2011).
361. Talapin, D. V., Shevchenko, E. V., Bodnarchuk, M. I., Ye, X., Chen, J., Murray, C. B. Quasicrystalline order in self-assembled binary nanoparticle superlattices. *Nature* **461**, 964 (2009).
362. Auyeung, E., Li, T. I. N. G., Senesi, A. J., Schmucker, A. L., Pals, B. C., de la Cruz, M. O., Mirkin, C. A. DNA-mediated nanoparticle crystallization into Wulff polyhedra. *Nature* **505**, 73 (2014).
363. Nykypanchuk, D., Maye, M. M., Lelie, D. van der , Gang, O. DNA-guided crystallization of colloidal nanoparticles. *Nature* **451**, 549 (2008).
364. Wang, T., Zhuang, J., Lynch, J., Chen, O., Wang, Z., Wang, X., LaMontagne, D., Wu, H., Wang, Z., Cao, Y. C. Self-assembled colloidal superparticles from nanorods. *Science* **338**, 358 (2012).
365. Cui, H., Pashuck, E. T., Velichko, Y. S., Weigand, S. J., Cheetham, A. G., Newcomb, C. J., Stupp, S. I. Spontaneous and X-ray-triggered crystallization at long range in self-assembling filament networks. *Science* **327**, 555 (2010).
366. Kostiainen, M. A., Hiekkataipale, P., Laiho, A., Lemieux, V., Seitsonen, J., Ruokolainen, J., Ceci, P. Electrostatic assembly of binary nanoparticle superlattices using protein cages. *Nat. Nanotechnol.* **8**, 52 (2013).
367. Miszta, K., Graaf, J. de , Bertoni, G., Dorfs, D., Brescia, R., Marras, S., Ceseracciu, L., Cingolani, R., Roij, R. van , Dijkstra, M. Hierarchical self-assembly of suspended branched colloidal nanocrystals into superlattice structures. *Nat. Mater.* **10**, 872 (2011).
368. Shevchenko, E. V., Talapin, D. V., O'Brien, S., Murray, C. B. Polymorphism in AB13 nanoparticle superlattices: an example of semiconductor-metal metamaterials. *J. Am. Chem. Soc.* **127**, 8741 (2005).
369. Ye, X., Chen, J., Murray, C. B. Polymorphism in self-assembled AB6 binary nanocrystal superlattices. *J. Am. Chem. Soc.* **133**, 2613 (2011).
370. Faivre, D., Schüler, D. Magnetotactic bacteria and magnetosomes. *Chem. Rev.* **108**, 4875 (2008).

## CITED LITERATURE (Continued)

371. Dunin-Borkowski, R. E., McCartney, M. R., Frankel, R. B., Bazylinski, D. A., Pósfai, M., Buseck, P. R. Magnetic microstructure of magnetotactic bacteria by electron holography. *Science* **282**, 1868 (1998).
372. Szyndler, M. W., Corn, R. M. Self-assembly of flux-closure polygons from magnetite nanocubes. *J. Phys. Chem. Lett.* **3**, 2320 (2012).
373. Kovalenko, M. V., Bodnarchuk, M. I., Lechner, R. T., Hesser, G., Schäffler, F., Heiss, W. Fatty acid salts as stabilizers in size-and shape-controlled nanocrystal synthesis: the case of inverse spinel iron oxide. *J. Am. Chem. Soc.* **129**, 6352 (2007).
374. Wang, T., Wang, X., LaMontagne, D., Wang, Z., Wang, Z., Cao, Y. C. Shape-Controlled Synthesis of Colloidal Superparticles from Nanocubes. *J. Am. Chem. Soc.* **134**, 18225 (2012).
375. Kim, D., Lee, N., Park, M., Kim, B. H., An, K., Hyeon, T. Synthesis of Uniform Ferrimagnetic Magnetite Nanocubes. *J. Am. Chem. Soc.* **131**, 454 (2008).
376. Aleksandrovic, V., Greshnykh, D., Randjelovic, I., Frömsdorf, A., Kornowski, A., Roth, S. V., Klinke, C., Weller, H. preparation and electrical properties of cobalt– platinum nanoparticle monolayers deposited by the langmuir– blodgett technique. *ACS Nano* **2**, 1123 (2008).
377. Dong, A., Chen, J., Oh, S. J., Koh, W.-K., Xiu, F., Ye, X., Ko, D.-K., Wang, K. L., Kagan, C. R., Murray, C. B. Multiscale periodic assembly of striped nanocrystal superlattice films on a liquid surface. *Nano Lett.* **11**, 841 (2011).
378. Baranov, D., Fiore, A., Huis, M. van , Giannini, C., Falqui, A., Lafont, U., Zandbergen, H., Zanella, M., Cingolani, R., Manna, L. Assembly of colloidal semiconductor nanorods in solution by depletion attraction. *Nano Lett.* **10**, 743 (2010).
379. Abe, K., Miyamoto, Y., Chikazumi, S. Magnetocrystalline anisotropy of low temperature phase of magnetite. *J. Phys. Soc. Jpn.* **41**, 1894 (1976).
380. McNab, T., Fox, R., Boyle, A. Some magnetic properties of magnetite (Fe<sub>3</sub>O<sub>4</sub>) microcrystals. *J. Appl. Phys.* **39**, 5703 (1968).
381. Chen, Z., Moore, J., Radtke, G., Sirringhaus, H., O'Brien, S. Binary nanoparticle superlattices in the semiconductor-semiconductor System: CdTe and CdSe. *J. Am. Chem. Soc.* **129**, 15702 (2007).
382. Ye, X., Chen, J., Engel, M., Millan, J. A., Li, W., Qi, L., Xing, G., Collins, J. E., Kagan, C. R., Li, J. Competition of shape and interaction patchiness for self-assembling nanoplates. *Nat. Chem.* **5**, 466 (2013).



## CITED LITERATURE (Continued)

383. Hasan, S. A., Kavich, D. W., Dickerson, J. H. Sacrificial layer electrophoretic deposition of free-standing multilayered nanoparticle films. *Chem. Commun.* **25**, 3723 (2009).
384. Scholten, P., Tjaden, D. Mutual attraction of superparamagnetic particles. *J. Colloid Interface Sci.* **73**, 254 (1980).
385. Landau, L. D., Bell, J., Kearsley, M., Pitaevskii, L., Lifshitz, E., Sykes, J., *Electrodynamics of continuous media*, vol. 8 (Elsevier, 1984).
386. El Ghandoor, H., Zidan, H., Khalil, M. M., Ismail, M. Synthesis and some physical properties of magnetite ( $\text{Fe}_3\text{O}_4$ ) nanoparticles. *Int. J. Electrochem. Sci* **7**, 5734 (2012).
387. Schabes, M. E., Bertram, H. N. Magnetization processes in ferromagnetic cubes. *J. Appl. Phys.* **64**, 1347 (1988).
388. Gubin, S. P., *Magnetic nanoparticles* (John Wiley & Sons, 2009).
389. Coey, J. M. D. Noncollinear spin arrangement in ultrafine ferrimagnetic crystallites. *Phys. Rev. Lett.* **27**, 1140 (1971).
390. Martinez, B., Obradors, X., Balcells, L., Rouanet, A., Monty, C. Low temperature surface spin-glass transition in  $\gamma\text{-Fe}_2\text{O}_3$  nanoparticles. *Phys. Rev. Lett.* **80**, 181 (1998).
391. Linderöth, S., Hendriksen, P. V., Bo, F., Wells, S., Davies, K., Charles, S., Mo, S., *et al.* On spin-canting in maghemite particles. *J. Appl. Phys.* **75**, 6583 (1994).
392. Morales, M., Veintemillas-Verdaguer, S., Montero, M., Serna, C., Roig, A., Casas, L., Martinez, B., Sandiumenge, F. Surface and internal spin canting in  $\gamma\text{-Fe}_2\text{O}_3$  nanoparticles. *Chem. Mater.* **11**, 3058 (1999).
393. Brooks, S., Gelman, A., Jones, G., Meng, X.-L., *Handbook of Markov Chain Monte Carlo* (CRC Press, 2011).
394. Woodcock, L. Entropy difference between the face-centred cubic and hexagonal close-packed crystal structures. *Nature* **385**, 141 (1997).
395. Cheng, Z., Russel, W. B., Chaikin, P. Controlled growth of hard-sphere colloidal crystals. *Nature* **401**, 893 (1999).
396. Eldridge, M., Madden, P., Frenkel, D. Entropy-driven formation of a superlattice in a hard-sphere binary mixture. *Nature* **365**, 35 (1993).
397. Snir, Y., Kamien, R. D. Entropically driven helix formation. *Science* **307**, 1067 (2005).

## CITED LITERATURE (Continued)

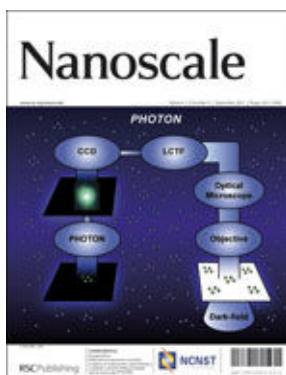
398. Anders, G.van , Ahmed, N. K., Smith, R., Engel, M., Glotzer, S. C. Entropically Patchy Particles: Engineering Valence through Shape Entropy. *ACS Nano* **8**, 931 (2013).
399. Young, K. L., Personick, M. L., Engel, M., Damasceno, P. F., Barnaby, S. N., Bleher, R., Li, T., Glotzer, S. C., Lee, B., Mirkin, C. A. A directional entropic force approach to assemble anisotropic nanoparticles into superlattices. *Angew. Chem. int. Ed.* **52**, 13980 (2013).
400. Zhang, Y., Lu, F., Lelie, D.van der , Gang, O. Continuous phase transformation in nanocube assemblies. *Phys. Rev. Lett.* **107**, 135701 (2011).
401. Anders, G.van , Ahmed, N. K., Klotsa, D., Engel, M., Glotzer, S. C., Unified theoretical framework for shape entropy in colloids, arXiv preprint arXiv:1309.1187 (2013).
402. Yin, Y., Xia, Y. Self-assembly of spherical colloids into helical chains with well-controlled handedness. *J. Am. Chem. Soc.* **125**, 2048 (2003).
403. Zerrouki, D., Baudry, J., Pine, D., Chaikin, P., Bibette, J. Chiral colloidal clusters. *Nature* **455**, 380 (2008).
404. Kakol, Z., Pribble, R., Honig, J. Magnetocrystalline anisotropy of  $\text{Fe}_{3(1-\delta)}\text{O}_4$ ,  $0 \leq \delta < 0.01$ . *Solid State Commun.* **69**, 793 (1989).
405. Özgür, Ü., Alivov, Y., Morkoç, H. Microwave ferrites, part 1: fundamental properties. *J. Mater. Sci.: Mater. Electron.* **20**, 789 (2009).
406. Baskin, A., Lo, W.-Y., Král, P. Clusters and Lattices of Particles Stabilized by Dipolar Coupling. *ACS Nano* **6**, 6083 (2012).
407. Chen, C.-L., Zhang, P., Rosi, N. L. A new peptide-based method for the design and synthesis of nanoparticle superstructures: construction of highly ordered gold nanoparticle double helices. *J. Am. Chem. Soc.* **130**, 13555 (2008).
408. Song, C., Blaber, M. G., Zhao, G., Zhang, P., Fry, H. C., Schatz, G. C., Rosi, N. L. Tailorable Plasmonic Circular Dichroism Properties of Helical Nanoparticle Superstructures. *Nano Lett.* **13**, 3256 (2013).
409. Sharma, J., Chhabra, R., Cheng, A., Brownell, J., Liu, Y., Yan, H. Control of self-assembly of DNA tubules through integration of gold nanoparticles. *Science* **323**, 112 (2009).
410. Lvov, Y. M., Price, R. R., Selinger, J. V., Singh, A., Spector, M. S., Schnur, J. M. Imaging nanoscale patterns on biologically derived microstructures. *Langmuir* **16**, 5932 (2000).

## CITED LITERATURE (Continued)

411. Jung, S. H., Jeon, J., Kim, H., Jaworski, J., Jung, J. H. Chiral arrangement of achiral Au nanoparticles by supramolecular assembly of helical nanofiber templates. *J. Am. Chem. Soc.* **136**, 6446 (2014).
412. Zhou, Y., Ji, Q., Masuda, M., Kamiya, S., Shimizu, T. Helical arrays of CdS nanoparticles tracing on a functionalized chiral template of glycolipid nanotubes. *Chem. Mater.* **18**, 403 (2006).
413. Guha, S., Drew, M. G., Banerjee, A. Construction of Helical Nanofibers from Self-Assembling Pseudopeptide Building Blocks: Modulating the Handedness and Breaking the Helicity. *Small* **4**, 1993 (2008).
414. Chakrabarti, D., Fejer, S. N., Wales, D. J. Rational design of helical architectures. *PNAS* **106**, 20164 (2009).
415. Chakrabarti, D., Wales, D. J. Tilted and helical columnar phases for an axially symmetric discoidal system. *Phys. Rev. Lett.* **100**, 127801 (2008).
416. Fejer, S. N., Chakrabarti, D., Wales, D. J. Self-assembly of anisotropic particles. *Soft Matter* **7**, 3553 (2011).
417. Prybytak, P., Frith, W., Cleaver, D. Hierarchical self-assembly of chiral fibres from achiral particles. *Interface focus* **2**, 651 (2012).
418. Erickson, R. O. Tubular packing of spheres in biological fine structure. *Science* **181**, 705 (1973).
419. Tymczenko, M., Marsal, L. F., Trifonov, T., Rodriguez, I., Ramiro-Manzano, F., Pallares, J., Rodriguez, A., Alcubilla, R., Meseguer, F. Colloidal crystal wires. *Adv. Mater.* **20**, 2315 (2008).
420. Pickett, G. T., Gross, M., Okuyama, H. Spontaneous chirality in simple systems. *Phys. Rev. Lett.* **85**, 3652 (2000).
421. Mughal, A., Chan, H., Weaire, D., Hutzler, S. Dense packings of spheres in cylinders: Simulations. *Phys. Rev. E* **85**, 051305 (2012).
422. Mughal, A. Screw symmetry in columnar crystals. *Philos. Mag.* **93**, 4070 (2013).
423. Jiang, L., Folter, J. W.de , Huang, J., Philipse, A. P., Kegel, W. K., Petukhov, A. V. Helical Colloidal Sphere Structures through Thermo-Reversible Co-Assembly with Molecular Microtubes. *Angew. Chem. int. Ed.* **52**, 3364 (2013).

## CITED LITERATURE (Continued)

- 424. Lohr, M. A., Alsayed, A. M., Chen, B. G., Zhang, Z., Kamien, R. D., Yodh, A. G. Helical packings and phase transformations of soft spheres in cylinders. *Phys. Rev. E* **81**, 040401 (2010).
- 425. Wood, D., Santangelo, C., Dinsmore, A. Self-assembly on a cylinder: a model system for understanding the constraint of commensurability. *Soft Matter* **9**, 10016 (2013).



**Title:** Self-standing nanoparticle membranes and capsules  
**Author:** Henry Chan, Petr Král  
**Publication:** Nanoscale  
**Publisher:** Royal Society of Chemistry  
**Date:** Mar 3, 2011  
 Copyright © 2011, Royal Society of Chemistry

Logged in as:  
 Henry Chan  
 Account #: 3001004244

LOGOUT

This reuse request is free of charge. Please review guidelines related to author permissions here:  
<http://www.rsc.org/AboutUs/Copyright/Permissionrequests.asp>

BACK

CLOSE WINDOW

Copyright © 2016 Copyright Clearance Center, Inc. All Rights Reserved. [Privacy statement](#). [Terms and Conditions](#).  
 Comments? We would like to hear from you. E-mail us at [customercare@copyright.com](mailto:customercare@copyright.com)



# RightsLink®

[Home](#)
[Account Info](#)
[Help](#)


**ACS Publications**  
Most Trusted. Most Cited. Most Read.

**Title:** Diffusion and Filtration Properties of Self-Assembled Gold Nanocrystal Membranes

**Author:** Jinbo He, Xiao-Min Lin, Henry Chan, et al

**Publication:** Nano Letters

**Publisher:** American Chemical Society

**Date:** Jun 1, 2011

Copyright © 2011, American Chemical Society

Logged in as:

Henry Chan

[LOGOUT](#)

## PERMISSION/LICENSE IS GRANTED FOR YOUR ORDER AT NO CHARGE

This type of permission/license, instead of the standard Terms & Conditions, is sent to you because no fee is being charged for your order. Please note the following:

- Permission is granted for your request in both print and electronic formats, and translations.
- If figures and/or tables were requested, they may be adapted or used in part.
- Please print this page for your records and send a copy of it to your publisher/graduate school.
- Appropriate credit for the requested material should be given as follows: "Reprinted (adapted) with permission from (COMPLETE REFERENCE CITATION). Copyright (YEAR) American Chemical Society." Insert appropriate information in place of the capitalized words.
- One-time permission is granted only for the use specified in your request. No additional uses are granted (such as derivative works or other editions). For any other uses, please submit a new request.

[BACK](#)
[CLOSE WINDOW](#)

Copyright © 2016 [Copyright Clearance Center, Inc.](#) All Rights Reserved. [Privacy statement.](#) [Terms and Conditions.](#)  
Comments? We would like to hear from you. E-mail us at [customercare@copyright.com](mailto:customercare@copyright.com)



RightsLink®

Home

Account  
Info

Help

ACS Publications  
Most Trusted. Most Cited. Most Read.**Title:**Interfacial Localization and  
Voltage-Tunable Arrays of  
Charged Nanoparticles**Author:**Mrinal K. Bera, Henry Chan,  
Daniel F. Moyano, et al**Publication:**

Nano Letters

**Publisher:**

American Chemical Society

**Date:**

Dec 1, 2014

Copyright © 2014, American Chemical Society

Logged in as:

Henry Chan

Account #:

3001004244

LOGOUT

**PERMISSION/LICENSE IS GRANTED FOR YOUR ORDER AT NO CHARGE**

This type of permission/license, instead of the standard Terms & Conditions, is sent to you because no fee is being charged for your order. Please note the following:

- Permission is granted for your request in both print and electronic formats, and translations.
- If figures and/or tables were requested, they may be adapted or used in part.
- Please print this page for your records and send a copy of it to your publisher/graduate school.
- Appropriate credit for the requested material should be given as follows: "Reprinted (adapted) with permission from (COMPLETE REFERENCE CITATION). Copyright (YEAR) American Chemical Society." Insert appropriate information in place of the capitalized words.
- One-time permission is granted only for the use specified in your request. No additional uses are granted (such as derivative works or other editions). For any other uses, please submit a new request.

BACK

CLOSE WINDOW

Copyright © 2016 [Copyright Clearance Center, Inc.](#) All Rights Reserved. [Privacy statement.](#) [Terms and Conditions.](#)  
Comments? We would like to hear from you. E-mail us at [customercare@copyright.com](mailto:customercare@copyright.com)



# RightsLink®

[Home](#)
[Account Info](#)
[Help](#)


**ACS Publications**  
Most Trusted. Most Cited. Most Read.

**Title:**

Colloidal Nanocube  
Supercrystals Stabilized by  
Multipolar Coulombic Coupling

**Logged in as:**

Henry Chan  
Account #:  
3001004244

**Author:**

Henry Chan, Arnaud  
Demortière, Lela Vukovic, et al

[LOGOUT](#)

**Publication:** ACS Nano

**Publisher:** American Chemical Society

**Date:** May 1, 2012

Copyright © 2012, American Chemical Society

## PERMISSION/LICENSE IS GRANTED FOR YOUR ORDER AT NO CHARGE

This type of permission/license, instead of the standard Terms & Conditions, is sent to you because no fee is being charged for your order. Please note the following:

- Permission is granted for your request in both print and electronic formats, and translations.
- If figures and/or tables were requested, they may be adapted or used in part.
- Please print this page for your records and send a copy of it to your publisher/graduate school.
- Appropriate credit for the requested material should be given as follows: "Reprinted (adapted) with permission from (COMPLETE REFERENCE CITATION). Copyright (YEAR) American Chemical Society." Insert appropriate information in place of the capitalized words.
- One-time permission is granted only for the use specified in your request. No additional uses are granted (such as derivative works or other editions). For any other uses, please submit a new request.

[BACK](#)
[CLOSE WINDOW](#)

Copyright © 2016 [Copyright Clearance Center, Inc.](#) All Rights Reserved. [Privacy statement.](#) [Terms and Conditions.](#)  
Comments? We would like to hear from you. E-mail us at [customercare@copyright.com](mailto:customercare@copyright.com)





# RightsLink®

[Home](#)
[Account Info](#)
[Help](#)


**Title:** Chiral templating of self-assembling nanostructures by circularly polarized light

**Author:** Jihyeon Yeom, Bongjun Yeom, Henry Chan, Kyle W. Smith, Sergio Dominguez-Medina, Joong Hwan Bahng

Logged in as:  
Henry Chan  
Account #:  
3001004244

[LOGOUT](#)

**Publication:** Nature Materials  
**Publisher:** Nature Publishing Group  
**Date:** Nov 17, 2014

Copyright © 2014, Rights Managed by Nature Publishing Group

## Author Request

If you are the author of this content (or his/her designated agent) please read the following. If you are not the author of this content, please click the Back button and select an alternative [Requestor Type](#) to obtain a quick price or to place an order.

Ownership of copyright in the article remains with the Authors, and provided that, when reproducing the Contribution or extracts from it, the Authors acknowledge first and reference publication in the Journal, the Authors retain the following non-exclusive rights:

- a) To reproduce the Contribution in whole or in part in any printed volume (book or thesis) of which they are the author(s).
- b) They and any academic institution where they work at the time may reproduce the Contribution for the purpose of course teaching.
- c) To reuse figures or tables created by them and contained in the Contribution in other works created by them.
- d) To post a copy of the Contribution as accepted for publication after peer review (in Word or Text format) on the Author's own web site, or the Author's institutional repository, or the Author's funding body's archive, six months after publication of the printed or online edition of the Journal, provided that they also link to the Journal article on NPG's web site (eg through the DOI).

NPG encourages the self-archiving of the accepted version of your manuscript in your funding agency's or institution's repository, six months after publication. This policy complements the recently announced policies of the US National Institutes of Health, Wellcome Trust and other research funding bodies around the world. NPG recognises the efforts of funding bodies to increase access to the research they fund, and we strongly encourage authors to participate in such efforts.

Authors wishing to use the published version of their article for promotional use or on a web site must request in the normal way.

If you require further assistance please read NPG's online [author reuse guidelines](#).

For full paper portion: Authors of original research papers published by NPG are encouraged to submit the author's version of the accepted, peer-reviewed manuscript to their relevant funding body's archive, for release six months after publication. In addition, authors are encouraged to archive their version of the manuscript in their institution's repositories (as well as their personal Web sites), also six months after original publication.

v2.0

[BACK](#)
[CLOSE WINDOW](#)



# RightsLink®

[Home](#)
[Account Info](#)
[Help](#)


**Title:** Self-assembly of magnetite nanocubes into helical superstructures

**Author:** Gurvinder Singh, Henry Chan, Artem Baskin, Elijah Gelman, Nikita Repnin, Petr Král, Rafal Klajn

Logged in as:  
Henry Chan  
Account #: 3001004244

[LOGOUT](#)

**Publication:** Science

**Publisher:** The American Association for the Advancement of Science

**Date:** Sep 5, 2014

Copyright © 2014, The American Association for the Advancement of Science

## Order Completed

Thank you very much for your order.

This is a License Agreement between Henry Chan ("You") and The American Association for the Advancement of Science ("The American Association for the Advancement of Science"). The license consists of your order details, the terms and conditions provided by The American Association for the Advancement of Science, and the [payment terms and conditions](#).

[Get the printable license.](#)

License Number	3818070943985
License date	Feb 29, 2016
Licensed content publisher	The American Association for the Advancement of Science
Licensed content publication	Science
Licensed content title	Self-assembly of magnetite nanocubes into helical superstructures
Licensed content author	Gurvinder Singh, Henry Chan, Artem Baskin, Elijah Gelman, Nikita Repnin, Petr Král, Rafal Klajn
Licensed content date	Sep 5, 2014
Volume number	345
Issue number	6201
Type of Use	Thesis / Dissertation
Requestor type	Author of the AAAS published paper
Format	Print and electronic
Portion	Full Text
Order reference number	None
Title of your thesis / dissertation	Multiscale Modeling of Self-assembled Nanoparticle Superstructures
Expected completion date	Feb 2016
Estimated size(pages)	200
Total	0.00 USD

[ORDER MORE...](#)
[CLOSE WINDOW](#)

Copyright © 2016 [Copyright Clearance Center, Inc.](#) All Rights Reserved. [Privacy statement](#). [Terms and Conditions](#).  
Comments? We would like to hear from you. E-mail us at [customer@copyright.com](mailto:customer@copyright.com)

# Magnetic field-induced self-assembly of iron oxide nanocubes

G. Singh, H. Chan, T. Udayabhaskararao, E. Gelman, D. Peddis, A. Baskin, G. Leitus, P. Král and R. Klajn, *Faraday Discuss.*, 2015, **181**, 403

DOI: 10.1039/C4FD00265B

This article is licensed under a [Creative Commons Attribution 3.0 Unported Licence](#). Material from this article can be used in other publications provided that the correct acknowledgement is given with the reproduced material.

Reproduced material should be attributed as follows:

- For reproduction of material from NJC:  
[Original citation] - Published by The Royal Society of Chemistry (RSC) on behalf of the Centre National de la Recherche Scientifique (CNRS) and the RSC.
- For reproduction of material from PCCP:  
[Original citation] - Published by the PCCP Owner Societies.
- For reproduction of material from PPS:  
[Original citation] - Published by The Royal Society of Chemistry (RSC) on behalf of the European Society for Photobiology, the European Photochemistry Association, and RSC.
- For reproduction of material from all other RSC journals:  
[Original citation] - Published by The Royal Society of Chemistry.

Information about reproducing material from RSC articles with different licences is available on our [Permission Requests page](#).

## HENRY CHAN

**Work Address:** 845 West Taylor Street, Room 4500, Chicago, IL 60607

**Webpage:** [www.linkedin.com/in/hyiprc](http://www.linkedin.com/in/hyiprc)

**Office Phone:** (312) 996-5393

**E-mail:** [hchan20@uic.edu](mailto:hchan20@uic.edu)

---

### Education

- 2010 – 2015    **Ph. D. in Physical Chemistry** with focus on Computational Chemistry,  
University of Illinois at Chicago, Advisor: Prof. Petr Král  
Thesis: “Multiscale Modeling of Self-assembled Nanoparticle Superstructures”
- 2006 – 2009    **B. Sc. in Chemistry and minor in Mathematics**, *Cum Laude*, University of Illinois at Chicago
- 

### Research Experience

- 2015 – present    **Research Aide**, Nanoscience and Technology Division, Argonne National Laboratory,  
Supervisor: Subramanian Sankaranarayanan
- Coarse-graining and force field fitting of thermo sensitive polymer (PNIPAM).
  - Applied machine learning principles (GA, clustering, etc) in molecular simulations.
- 2010 – 2016    **Graduate Researcher**, Department of Chemistry, University of Illinois at Chicago
- Collaborated with 5 research groups on the topic of nanoparticle self-assembly.
  - Studied nanomaterial systems using molecular dynamics (MD) simulations.
  - Developed a Monte Carlo (MC) code to simulate magnetic nanocubes.
  - Analyzed long timescale simulation data using statistical techniques.
  - Summarized research results in 9 publications, 2 submitted papers, and 9 presentations.
- 2008 – 2010    **Undergraduate Researcher**, Department of Chemistry, University of Illinois at Chicago
- Performed coarse-grained MD simulations of nanoparticle-lipid system.

### Teaching Experience

- 2010 – 2015    **Teaching Assistant**, Department of Chemistry, University of Illinois at Chicago
- Led tutoring, lab, and/or discussion sessions for the following classes:
- |                                      |  |
|--------------------------------------|--|
| Summer Enrichment Chemistry Workshop | : 2012Su, 2015Su (as an instructor)    |
| 101 - Preparatory Chemistry          | : 2010F                                |
| 112 - General College Chemistry I    | : 2011S, 2011Su                        |
| 114 - General College Chemistry II   | : 2012Su, 2013S, 2013Su, 2014Su, 2015S |
| 342 - Physical Chemistry I           | : 2014S                                |
| 343 - Physical Chemistry Laboratory  | : 2011F, 2012S                         |
| 542 - Quantum Mechanics              | : 2012F, 2013F, 2014F                  |

### IT Experience

- 2010 – 2016    **System Administrator**, Department of Chemistry, University of Illinois at Chicago
- Installed and maintained departmental Linux CPU and GPU Beowulf type clusters.
  - Managed software installations and users on the clusters.
- 2012 – 2013    **On call IT support**, Mary Crane Center
- Installed drivers and performed software updates.

### Other Activities

- 2015    **Visiting Student**, Electronic Visualization Laboratory, University of Illinois at Chicago
- Performed porting of molecular systems to CAVE2.
- 

### Honors and Awards

- 2015    TA Appreciation Awards, University of Illinois at Chicago (nominated by students)
- 2007 – 2009    Dean’s list, University of Illinois at Chicago
- 2010    Merck Award, University of Illinois at Chicago

---

**Publications**

1. H. Chan and P. Král, "Self-Standing Nanoparticle Membranes and Capsules", *Nanoscale* 2011, **3** (4), 1881–1886.
  2. J. He, X-M. Lin, H. Chan, L. Vuković, P. Král, and H. Jaeger, "Diffusion and Filtration Properties of Self-Assembled Gold Nanocrystal Membranes", *Nano Lett.* 2011, **11** (6), 2430–2435.
  3. H. Chan, A. Demortiere, L. Vuković, P. Král, and C. Petit, "Colloidal Nanocube Supercrystals Stabilized by Multipolar Coulombic Coupling", *ACS Nano* 2012, **6** (5), 4203–4213.
  4. I. Strauss, H. Chan, and P. Král, "Ultralong Polarization Chains Induced by Ions Solvated in Confined Water Monolayers", *J. Am. Chem. Soc.* 2014, **136** (4), 1170–1173.
  5. G. Singh, H. Chan, A. Baskin, E. Gelman, N. Repnin, P. Král, and R. Klajn, "Self-Assembly of Magnetite Nanocubes into Helical Superstructures", *Science* 2014, **345** (6201), 1149–1153.
  6. J. Yeom, B. Yeom, H. Chan, S. Dominguez-Medina, J. H. Bahng, G. Zhao, W.-S. Chang, S. J. Chang, P. Zhang, S. Link, P. Král, and N. A. Kotov, "Chiral Templating of Self-Assembling Nanostructures by Circularly Polarized Light", *Nat. Mat.* 2015, **14**, 66–72.
  7. M. K. Bera, H. Chan, D. F. Moyano, H. Yu, S. Tatur, D. Amoanu, W. Bu, V. M. Rotello, M. Meron, P. Král, B. Lin, and M. L. Schlossman, "Interfacial Localization and Voltage-Tunable Arrays of Charged Nanoparticles", *Nano Lett.* 2014, **14** (12), 6816–6822.
  8. G. Singh, H. Chan, T. Udayabhaskararao, E. Gelman, D. Peddis, A. Baskin, G. Leitus, P. Král, and R. Klajn, "Magnetic field-induced self-assembly of iron oxide nanocubes", *Farad. Discuss* 2015, **181**, 403–421.
  9. S. Tepavcevic, Y. Liu, D. Zhou, B. Lai, J. Maser, X-B Zu, H. Chan, P. Kral, C. Johnson, V. Stamenkovic, N. Markovic, T. Rajh, "Nanostructured Layered Cathode for Rechargeable Mg-ion Batteries", *ACS Nano* 2015, **9** (8), 8194–8205.
  10. M. Yang, H. Chan, G. Zhao, P. Zhang, P. Král, and N. A. Kotov, "Self-Assembly of Colloidal Nanoparticles into Shells", submitted to *Nature Chem.*
  11. H. Chan, A. Titov, and P. Král, "Stabilization of Nanoparticle Clusters inside Phospholipid Bilayers", submitted to *J. Chem. Phys.*
  12. H. Chan, A. Baskin, L. Vukovic, and P. Král, "Multiscale Simulations of Nanoparticle Self-Assemblies", review paper, in preparation.
- 

**Oral Presentations**

H. Chan, A. Titov, R. Pearson, and P. Král "Encapsulation of Graphene and Nanoparticles in Phospholipid Membranes." 2nd Annual UIC Chemistry Undergraduate Research Symposium, Chicago, Illinois: September 2, 2009.

H. Chan, P. Král, L. Vuković, and N. Patra "Self-assembly of functional superstructures: From graphene origami to nanoparticle membranes." Pacificchem 2010, Honolulu, Hawaii: December 15–20, 2010

H. Chan, M. Bera, H. Yu, S. Tatur, W. Bu, D. Amoanu, D. Moyano, V. Rotello, P. Král, B. Lin, M. Meron, P. Vanýsek, and M. Schlossman "Modeling of experimentally studied charged nanoparticle at electrified liquid/liquid interface." 245th ACS National Meeting, New Orleans, Louisiana: April 7–11, 2013

H. Chan, P. Král "Controlled self-assembly of colloidal nanoparticles into finite-sized superstructures." 247th ACS National Meeting, Dallas, Texas: March 16–20, 2014

---

**Poster Presentations**

H. Chan, A. Titov, R. Pearson, and P. Král, "Encapsulation of Graphene and Nanoparticles in Phospholipid Membranes." UIC Student Research Forum, Chicago, Illinois: April 20, 2010.

H. Chan, A. Titov, R. Pearson, and P. Král, "Encapsulation of Graphene and Nanoparticles in Phospholipid Membranes." From Computational Biophysics to Systems Biology (CBSB) workshop, Traverse City, Michigan, June 6–8, 2010.

H. Chan, L. Vuković, P. Král, J. He, and H. Jaeger, "Modeling Material Properties of Freestanding Nanoparticle Membranes and Capsules." Workshop on Self-Assembled Bio-Inspired Materials for Energy, ANL, Lemont, Illinois: February 4–5, 2011.

H. Chan, L. Vuković, J. He, P. Král, and H. Jaeger, "Nanoparticle superlattices: Self-assembly and molecular filtration." 243rd ACS National Meeting, San Diego, California: March 25–19, 2012.

H. Chan and P. Král, "Multiscale Modeling of Material Self-assembly Controlled by External Fields." Nanoparticle Synthesis and Assembly: Faraday Discussion 181, ANL, Lemont, Illinois: April 20-22, 2015.

### **Attended Workshops**

Parallel Programming with MPI, Theory and Computing Sciences Conference Center, ANL, June 6, 2014.

### **Expertises**

#### *Computer*

<b>Concepts</b>	: Programming Paradigms, OS (Abstractions, Data Structures), Development Cycle
<b>Languages</b>	: Bash (UNIX shell), Fortran, Tcl, Python, C, LaTeX, HTML, CSS, SQL, GLSL, JavaScript
<b>Operating Systems</b>	: Windows (Win95 and up), Linux (Fedora 12 and up), Mac OS
<b>Software</b>	: MS office, Vi, scientific python stack (NumPy, SciPy, matplotlib, MayaVi., ipython notebook, pandas, Bokeh), Simulation & Visualization (NAMD, LAMMPS, VMD, VisPy, D3.js), Image Manipulation (Photoshop, Gimp), Software Version Control (git, github)

#### *Language*

<b>Spoken</b>	: English (bilingual), Cantonese (native), Mandarin (elementary), Japanese (elementary)
<b>Written</b>	: English (read & write), Traditional Chinese (read & write), Simplified Chinese (read)

### **Professional Affiliations**

2007-present	National Society Collegiate Scholars
2011-present	American Chemical Society